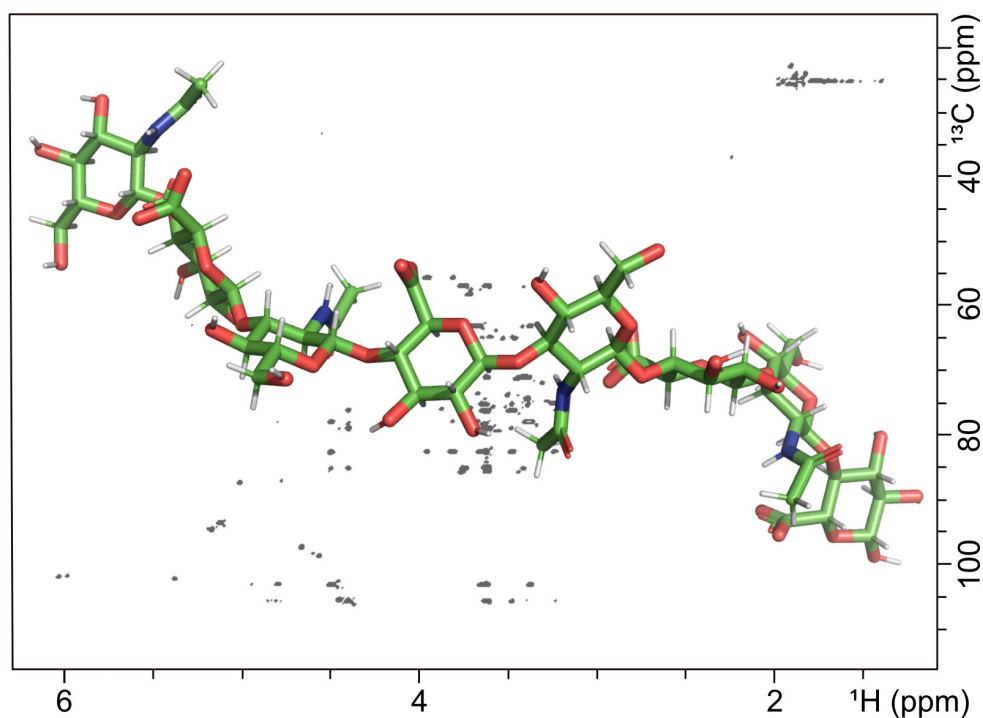




DOCTORAL THESIS No. 2023:57
FACULTY OF NATURAL RESOURCES AND AGRICULTURAL SCIENCES

Studies of Hyaluronan and Related Structures by NMR Spectroscopy

YAN XUE



Studies of Hyaluronan and Related Structures by NMR Spectroscopy

Yan Xue

Faculty of Natural Resources and Agricultural Sciences
Department of Molecular Sciences
Uppsala



SWEDISH UNIVERSITY
OF AGRICULTURAL
SCIENCES

DOCTORAL THESIS

Uppsala 2023

Acta Universitatis Agriculturae Sueciae
2023:57

Cover: 3D model of hyaluronan octasaccharide (PDB ID: 2BVK) generated by PyMol superimposed on a 2D- ^1H , ^{13}C]-HSQC-NOESY spectrum of hyaluronan octasaccharide in D_2O at 5 °C.

ISSN 1652-6880

ISBN (print version) 978-91-8046-166-5

ISBN (electronic version) 978-91-8046-167-2

<https://doi.org/10.54612/a.4daped2rv8>

© 2023 Yan Xue, <https://orcid.org/0000-0002-4234-1642>

Swedish University of Agricultural Sciences, Department of Molecular Sciences, Uppsala, Sweden

The summary chapter of this thesis is licensed under CC BY 4.0, other licences or copyright may apply to illustrations and attached articles.

Print: SLU Grafisk Service, Uppsala 2023

Studies of hyaluronan and related structures by NMR spectroscopy

Abstract

Hyaluronan (HA) is a natural polysaccharide in the glycosaminoglycan (GAG) family with repeating units of *N*-acetylglucosamine (GlcNAc) and glucuronic acid (GlcA), which are linked by $\beta(1\rightarrow4)$ and $\beta(1\rightarrow3)$ glycosidic linkages. HA has many important regulatory functions in the human body, but comprehension of its structure-function relationship remains limited. Nuclear magnetic resonance (NMR) spectroscopy is the method of choice for studying complex biomolecules at atomic level and also holds great potential for advancing understanding of HA. This thesis investigated various forms of HA in aqueous solution using NMR spectroscopy, to gain insights into structural and dynamic behaviors.

First, correlations between physicochemical properties of cross-linked HA hydrogels and the dynamic behavior of water in the samples were examined. The results showed that transverse relaxation (T_2) of water protons was dominated by the chemical exchange between water protons and exchangeable protons of HA. Based on the temperature profile of T_2 , it was possible to distinguish samples with different concentrations and, to some extent, hydrogels with different physicochemical properties.

Detailed conformational analysis of the GlcNAc monosaccharide was conducted, focusing on the *N*-acetyl group. Amide *cis* conformations were observed for the first time by ^1H NMR. The two torsion angles that define the conformation of the *N*-acetyl group were evaluated based on the measurement of eight 3J -couplings. In addition, conformations of the $\beta(1\rightarrow4)$ and $\beta(1\rightarrow3)$ glycosidic linkages and the *N*-acetyl group in HA-8mer and HA-20mer were compared. As in GlcNAc, the orientation between H2 and NH was determined to be in *anti* conformation for both chain lengths. The NMR data supported one predominant conformation of the $\beta(1\rightarrow3)$ glycosidic linkage and suggested a conformational equilibrium at the $\beta(1\rightarrow4)$ glycosidic linkage. Overall, the glycosidic linkage conformations of the two chain lengths exhibited subtle differences.

To overcome the low natural abundance of the ^{13}C and ^{15}N nuclei, ^{13}C , ^{15}N -enriched HA polysaccharide was produced biosynthetically. The level of ^{13}C and ^{15}N isotope enrichment was determined quantitatively by NMR and confirmed by high-resolution mass spectrometry.

Keywords: Hyaluronan, NMR spectroscopy, *N*-acetylglucosamine, hydrogel, oligosaccharide, polysaccharide, isotope labeling

Author's address: Yan Xue, SLU, Department of Molecular Sciences,
P.O. Box 7015, 750 07 Uppsala, Sweden.

E-mail: yan.xue@slu.se

Studier av hyaluronan och relaterade strukturer med NMR-spektroskopi

Abstract

Hyaluronan (HA) är en naturlig polysackarid i glykosaminoglykanfamiljen (GAG). HA är uppbyggd av upprepade enheter av *N*-acetylglukosamin (GlcNAc) och glukuronsyra (GlcA), som är sammankopplade med $\beta(1\rightarrow4)$ - och $\beta(1\rightarrow3)$ -glykosidbindningar. HA har många viktiga regulatoriska funktioner i människokroppen, men kunskapen om sambandet mellan dess struktur och funktion är fortfarande begränsad. Kärnmagnetisk resonans (NMR)-spektroskopi är en lämplig metod för att studera komplexa biomolekyler på atomnivå och har även stor potential för att öka förståelsen av HA. I denna avhandling undersöktes olika former av HA i vattenlösning med hjälp av NMR-spektroskopi för att studera deras strukturella och dynamiska egenskaper.

Först undersöktes sambandet mellan tvärbundna HA-hydrogelers fysikalisk-kemiska egenskaper och vattnets dynamiska egenskaper i proverna. Resultaten visade att T_2 -relaxationen för vattenprotoner framför allt påverkas av kemiskt utbyte mellan vattenprotoner och utbytbara protoner av HA. Baserat på temperaturprofilen av T_2 kunde prover med olika koncentrationer och i viss mån hydrogeler med olika fysikalisk-kemiska egenskaper särskiljas.

Detaljerad konformationsanalys av GlcNAc-monosackariden genomfördes med fokus på *N*-acetylgruppen. Amid-*cis*-konformationer observerades med ^1H NMR för första gången. De två torsionsvinklarna som definierar konformationen av *N*-acetylgruppen utvärderades baserat på mätningen av åtta 3J -kopplingar. Dessutom jämfördes konformationen av $\beta(1\rightarrow4)$ - och $\beta(1\rightarrow3)$ -glykosidbindningarna samt *N*-acetylgruppen i HA-8mer och HA-20mer. Precis som i GlcNAc fastställdes att orienteringen mellan H2 och NH var i *anti*-konformation för båda kedjelängderna. NMR-data bekräftade en dominerande konformation av $\beta(1\rightarrow3)$ -glykosidbindningen och antydde en jämvikt mellan olika konformationer för $\beta(1\rightarrow4)$ -glykosidbindningen. Sammantaget uppvisade konformationen av glykosidbindningarna för de två kedjelängderna subtila skillnader.

För att övervinna den låga naturliga förekomsten av ^{13}C - och ^{15}N -kärnor producerades ^{13}C , ^{15}N -inmärkt HA-polysackarid biosyntetiskt. Nivån av ^{13}C - och ^{15}N -isotopanrikning kvantifierades med hjälp av NMR och bekräftades med högupplöst masspektrometri.

Nyckelord: Hyaluronan, NMR-spektroskopi, *N*-acetylglukosamin, hydrogel, oligosackarid, polysackarid, isotopmärkning

Författarens adress: Yan Xue, SLU, Institutionen för molekylära vetenskaper, Box 7015, 750 07 Uppsala, Sverige.

E-post: yan.xue@slu.se

Dedication

To my parents

“A journey of a thousand miles begins with a single step.”

Lao Tzu

Contents

List of publications	9
List of tables	11
List of figures	13
Abbreviations	15
1. Introduction	19
2. Hyaluronan	21
2.1 Structure of hyaluronan.....	22
2.2 Biosynthesis and degradation of hyaluronan	26
2.2.1 Biosynthesis of hyaluronan.....	26
2.2.2 Degradation of hyaluronan	27
2.3 Chemical modification of hyaluronan	30
3. Methods	33
3.1 NMR spectroscopy.....	33
3.1.1 Principle	33
3.1.2 Relaxation.....	35
3.1.3 Diffusion.....	37
3.1.4 Scalar spin-spin coupling.....	38
3.1.5 Nuclear Overhauser effect.....	39
3.1.6 Analysis of carbohydrates by NMR spectroscopy	40
3.2 Mass spectrometry.....	48
3.2.1 Ionization	49
3.2.2 Mass analyzers.....	50
4. Aims.....	53
5. Results and Discussion.....	55

5.1	Relaxation and diffusion of water protons in BDDE cross-linked hyaluronic acid hydrogels investigated by NMR spectroscopy - Comparison with physicochemical properties (Paper I).....	55
5.1.1	Longitudinal relaxation and diffusion coefficient of water protons	56
5.1.2	Transverse relaxation of water protons	57
5.2	Determination of amide <i>cis/trans</i> isomers in <i>N</i> -acetyl-D-glucosamine: Tailored NMR analysis of the <i>N</i> -acetyl group conformation (Paper II).....	61
5.2.1	Conformation of the <i>N</i> -acetyl group.....	61
5.2.2	First observation of amide <i>cis</i> conformation by ¹ H NMR	62
5.2.3	Tailored NMR experiments for GlcNAc conformation analysis.....	64
5.2.4	³ <i>J</i> -couplings sensitive to the θ_1 angle (H2-C2-N-NH)	64
5.2.5	³ <i>J</i> -couplings sensitive to the θ_2 angle (C2-N-C1'-C2')	67
5.3	Solution conformational analysis of hyaluronan with different chain lengths by NMR spectroscopy (Paper III)	69
5.3.1	Experimental interproton distances and ³ <i>J</i> -couplings.....	69
5.3.2	Conformation of the acetamido group	70
5.3.3	Conformation of the β (1→3) glycosidic linkage	72
5.3.4	Conformation of the β (1→4) glycosidic linkage	74
5.4	Metabolic labeling of hyaluronan: Biosynthesis and quantitative analysis of ¹³ C, ¹⁵ N-enriched hyaluronan by NMR and MS-based methods (Paper IV).....	76
5.4.1	Quantitative 1D ¹ H NMR.....	77
5.4.2	Quantitative 1D ¹³ C NMR.....	79
5.4.3	Mass spectrometry analysis	80
6.	Conclusions and Outlook	83
	References.....	85
	Popular science summary	99
	Populärvetenskaplig sammanfattning	101
	Acknowledgements	103

List of publications

This thesis is based on the work contained in the following papers, referred to by Roman numerals in the text:

- I. Frida J. Wende[#], **Yan Xue**[#], Gustav Nestor, Åke Öhrlund and Corine Sandström* (2020). Relaxation and diffusion of water protons in BDDE cross-linked hyaluronic acid hydrogels investigated by NMR spectroscopy—Comparison with physicochemical properties. *Carbohydrate Polymers*, 248, 116768.
- II. **Yan Xue** and Gustav Nestor* (2022). Determination of amide *cis/trans* isomers in *N*-acetyl-D-glucosamine: Tailored NMR analysis of the *N*-acetyl group conformation. *ChemBioChem*, 23 (17), e202200338.
- III. **Yan Xue**, Corine Sandström and Gustav Nestor. Solution conformational analysis of hyaluronan with different chain lengths by NMR spectroscopy (manuscript).
- IV. **Yan Xue**^{*}, Karolina Ucieklak, Suresh Gohil, Tomasz Niedziela, Gustav Nestor and Corine Sandström (2023). Metabolic labeling of hyaluronan: Biosynthesis and quantitative analysis of ¹³C,¹⁵N-enriched hyaluronan by NMR and MS-based methods. *Carbohydrate Research*, 531, 108888.

Papers I, II and IV are reproduced with the permission of the publishers.

*Corresponding author

[#]First authorship shared

The contribution of Yan Xue to the papers included in this thesis was as follows:

- I. Devised and planned the project together with the co-authors.
Performed NMR analysis, processing and interpretation of data.
Wrote the manuscript together with the co-authors.
- II. Devised and planned the project together with the co-author.
Performed NMR analysis, processing and interpretation of data.
Wrote the manuscript together with the co-author.
- III. Devised and planned the project together with the co-authors.
Planned and performed experimental work (NMR, HPLC and SEC) and processing and interpretation of NMR data. Wrote the manuscript together with the co-authors.
- IV. Devised and planned the project together with the co-authors.
Performed NMR analysis, processing and interpretation of NMR and MS data. Wrote the manuscript together with the co-authors and, as corresponding author, was responsible for all correspondence with the journal.

List of tables

Table 1. Physicochemical parameters of HA-BDDE hydrogels	56
Table 2. ^1H , ^{13}C and ^{15}N chemical shifts (ppm) of α - and β -GlcNAc in amide <i>trans</i> and <i>cis</i> forms	62
Table 3. ^3J -coupling constants (Hz) of torsion angle θ_1 in α - and β -GlcNAc	66
Table 4. ^3J -coupling constants (Hz) of torsion angle θ_2 in α - and β -GlcNAc	68
Table 5. Interproton distances (Å) and ^3J -couplings (Hz) sensitive to torsion angle θ_1	71
Table 6. Interproton distances (Å) and ^3J -couplings (Hz) sensitive to the $\beta(1\rightarrow3)$ glycosidic linkage	72
Table 7. Interproton distances (Å) and ^3J -couplings (Hz) sensitive to the $\beta(1\rightarrow4)$ glycosidic linkage	74
Table 8. Three minimal conformations and two weighted ratios with their corresponding interproton distances (Å) and ^3J -couplings (Hz).....	75
Table 9. Mean level of isotope enrichment (%) of ^{13}C and ^{15}N in ΔHA_2 determined by quantitative ^1H NMR	78
Table 10. Mean level of isotope enrichment (%) of ^{13}C in ΔHA_2 determined by quantitative ^{13}C NMR.....	80
Table 11. Summary of the results of ESI-orbitrap-MS measurement of ^{13}C , ^{15}N -enriched ΔHA_2	81

List of figures

Figure 1. Schematic structure of HA	23
Figure 2. Schematic representations of transient hydrogen bonds and water bridges over the glycosidic linkages of HA.....	25
Figure 3. The three families of HA degradation enzymes and their corresponding major end-products.....	28
Figure 4. Scheme of cross-linking reactions of HA with BDDE.....	31
Figure 5. Illustration of a spinning nucleus.....	34
Figure 6. Fourier transformation of the time domain to the frequency domain	35
Figure 7. The inversion recovery pulse sequence.	36
Figure 8. The Carr-Purcell-Meiboom-Gill pulse sequence	37
Figure 9. The pulsed field gradient spin-echo pulse sequence.....	38
Figure 10. General schemes for measuring steady-state and transient NOEs	39
Figure 11. Water suppression schemes.....	42
Figure 12. Schematic representations of the basic pulse sequences of COSY, TOCSY and NOESY.	43
Figure 13. Homonuclear 2D NMR spectra of sucrose	44
Figure 14. Schematic representations of the basic pulse sequences of INEPT, HSQC and HMBC.....	46
Figure 15. Heteronuclear 2D NMR spectra of sucrose	47

Figure 16. Longitudinal relaxation and diffusion coefficient as a function of temperature at low HA concentration	57
Figure 17. Transverse relaxation as a function of temperature at low, medium and high HA concentration	58
Figure 18. Transverse relaxation as a function of temperature for four representative samples at low, medium, and high HA concentration	59
Figure 19. Chemical structure of GlcNAc with two torsion angles of the <i>N</i> -acetyl group	61
Figure 20. Selected region of 2D-[¹ H, ¹⁵ N]-HSQC and 1D ¹ H spectra of GlcNAc.....	63
Figure 21. Comparison between the protein backbone and the <i>N</i> -acetyl group.....	64
Figure 22. Selected regions of E.COSY spectra used to measure ³ J _{NH,H2} . 65	
Figure 23. Difference plot and root mean square deviation related to H2-C2-N-NH torsion angle	66
Figure 24. Selected regions of E.COSY spectra used to measure ³ J _{NH,C2'} 67	
Figure 25. Root mean square deviation versus C2-N-C1'-C2' torsion angle	68
Figure 26. Schematic structure of HA oligomers.....	69
Figure 27. Selected regions of 2D NMR spectra for the interior residues of HA-20mer	70
Figure 28. Root mean square deviation versus H2-C2-N-NH torsion angle of HA-8mer and HA-20mer.....	72
Figure 29. Conformational heatmaps showing the (φ , ψ) distribution of the $\beta(1\rightarrow3)$ glycosidic linkage of HA-8mer and HA-20mer	73
Figure 30. Schematic representation of Δ HA ₂	77
Figure 31. 1D ¹ H NOESY pre-saturation spectrum of ¹³ C, ¹⁵ N-enriched Δ HA ₂	78
Figure 32. 1D ¹³ C NMR spectrum of ¹³ C, ¹⁵ N-enriched Δ HA ₂	79
Figure 33. ESI-orbitrap-MS [M+H] ⁺ spectrum of ¹³ C, ¹⁵ N-enriched Δ HA ₂ ...	80

Abbreviations

BDDE	1,4-butanediol diglycidyl ether
BDPE	1,4-butanediol di-(propan-2,3-dioly)ether
BTH	Bovine testicular hyaluronidase
ChABC	Chondroitinase ABC
CI	Chemical ionization
COSY	Correlation spectroscopy
CPMG	Carr-Purcell-Meiboom-Gill
CrD	Degree of cross-linking
CTI	<i>cis-trans</i> isomerization
DD	Dipole-dipole
DMSO	Dimethyl sulphoxide
DSS	2,2-dimethyl-2-silapentane-5-sulfonate sodium salt
E.COSY	Exclusive correlation spectroscopy
ECM	Extracellular matrix
EI	Electron ionization
EIC	Extracted ion chromatogram
ESI	Electrospray ionization
FID	Free induction decay
FT	Fourier transformation

GAG	Glycosaminoglycan
GC	Gas chromatography
GelC	Gel content
GlcA	Glucuronic acid
GlcNAc	<i>N</i> -acetylglucosamine
HA	Hyaluronan
HAS	Hyaluronan synthase
HMBC	Heteronuclear multiple bond correlation
HSQC	Heteronuclear single quantum coherence
INEPT	Insensitive nuclei enhanced by polarization transfer
LC	Liquid chromatography
<i>m/z</i>	Mass-to-charge ratio
MALDI	Matrix-assisted laser desorption/ionization
MD	Molecular dynamics
MoD	Degree of modification
MS	Mass spectrometry
MS ⁿ	Multiple mass spectrometry
MW	Molecular weight
NMR	Nuclear magnetic resonance
NOE	Nuclear Overhauser effect
NOESY	Nuclear Overhauser effect spectroscopy
PDB	Protein data bank
PFG	Pulsed field gradient
QTOF	Quadrupole time-of-flight
RF	Radiofrequency
RMSD	Root mean square deviation

ROS	Reactive oxygen species
<i>S/N</i>	Signal-to-noise ratio
SNFG	Symbol nomenclature for glycans
SwD	Swelling Degree
TMS	Tetramethylsilane
TOCSY	Total correlation spectroscopy
TOF	Time-of-flight
TSP	3-(trimethylsilyl)propanoic acid
UDP	Uridine diphosphate
WATERGATE	Water suppression by gradient-tailored excitation
Δ GlcA	Glucuronic acid with C4-C5 unsaturation
Δ HA ₂	Hyaluronan disaccharide with Δ GlcA at the non-reducing end

1. Introduction

Carbohydrates, the most widely distributed and naturally occurring organic substances on Earth, have been overshadowed in the past by proteins and nucleic acids in terms of biological significance. Compared with those two classes of biomolecules, carbohydrates are more complex and hence more difficult to study (Flitsch & Ulijn, 2003). The complexity lies in the rich diversity of carbohydrate structures, which normally arises from the number of chemically similar (and often isomeric) monosaccharide building blocks, the position and orientation of glycosidic linkages, and branching (Gray *et al.*, 2019). To put this into perspective, any three amino acids could produce 27 peptides, while the same number of hexoses could theoretically yield 38,016 different trisaccharides (Laine, 1997; Bubb, 2003). Consequently, understanding of endogenous carbohydrate structure and function still lags behind that of other biomolecules (Gray *et al.*, 2019).

Glycosaminoglycans (GAGs, formerly known as mucopolysaccharides) are negatively charged heteropolysaccharides composed of repeating disaccharide units of *N*-acetylated hexosamine and uronic acid (Afratis *et al.*, 2012). Based on the type of monosaccharide in the repeating unit and the result of its sulfation, GAGs are classified into four different families: heparin/heparan sulfate; chondroitin/dermatan sulfate; keratan sulfate; and hyaluronan (Song *et al.*, 2021). GAGs are present in all mammalian tissues and their functions within the body are widespread and determined by their molecular structure (Casale & Crane, 2019).

Hyaluronan (HA) is unique in the GAG family because of its nonsulfated nature and lack of a covalently bound protein core. In addition, the sulfated GAGs are synthesized in the Golgi apparatus, whereas HA is synthesized on the intracellular surface of the plasma membrane (Song *et al.*, 2021). Although HA is a seemingly simple molecule, its true nature and full

function are still far from being fully unraveled. Different lengths of HA can adopt various conformations, including extended, relaxed and condensed states (Cowman *et al.*, 2005). Small changes in the local environment readily alter the conformation of HA and also affect the role of the GAG in biological processes (Bohaumilitzky *et al.*, 2017). A typical example is that low-molecular-weight HA has a pro-inflammatory response to regulation of macrophage activation, while high-molecular-weight HA has an anti-inflammatory response (Rayahin *et al.*, 2015). Furthermore, HA concentrations are usually higher in tumors than in the surrounding healthy tissues, with enhanced HA deposition accompanied by changes in the polymer size of HA being a reliable predictor for malignancy (Bohaumilitzky *et al.*, 2017). Therefore, it is essential to understand how the size of HA and its local surroundings cause conformational changes and how conformational changes further affect its biological functions *in vivo*.

High-field nuclear magnetic resonance (NMR) spectroscopy is a powerful analytical technique that allows detailed structural and dynamic studies of molecules at atomic level. Over the years, NMR spectroscopy has become one of the most important methods for structural analysis of carbohydrates. The aim in this thesis was to study various forms of HA by NMR spectroscopy, in order to improve understanding of their structural and dynamic behaviors. The work comprised: investigating the correlations between physicochemical properties of cross-linked HA hydrogels and the dynamic behavior of their water molecules (Paper I); examining the amide *cis* conformation of *N*-acetylglucosamine (GlcNAc, one of the repeating units of HA), and performing comprehensive conformational investigations of the *N*-acetyl group (Paper II); comparing conformations of glycosidic linkages and the *N*-acetyl group for different HA chain lengths (Paper III); and biosynthesis of ^{13}C , ^{15}N -enriched HA and quantitative determination of the level of isotopic incorporation (Paper IV).

2. Hyaluronan

“It is my opinion that the mucopolysaccharides will never be a highly popular field in biochemistry, but they will probably not be relegated again to the insignificance and disregard in which they were held not so long ago.”

- Karl Meyer, American Society of Biological Chemists Symposium on ‘Acid Mucopolysaccharides of Animal Origin’, 1958

Hyaluronic acid (HA) was first isolated from bovine vitreous humor by Karl Meyer and his assistant John Palmer in 1934. They described HA as a novel, high molecular weight (MW) polysaccharide acid consisting of “a uronic acid, an amino sugar, and possibly a pentose”, where the last constituent is incorrect. They proposed “for convenience, the name hyaluronic acid, from hyaloid (vitreous) + uronic acid ” (Meyer & Palmer, 1934). It took Meyer and his colleagues another 20 years to correctly establish the primary structure of HA (Linker & Meyer, 1954). The term “hyaluronan” was later proposed by Endre Balazs to conform with the international nomenclature of polysaccharides (Balazs *et al.*, 1986), and is used in the remainder of this thesis.

Hyaluronan is present in all tissues and body fluids of vertebrates and it also appears as a protective disguise in some bacteria (Fraser *et al.*, 1997). It is an important component of the extensive extracellular matrix (ECM) in tissues such as skin and cartilage, where it acts to bind and organize tissue proteoglycans, thus providing a highly hydrated network to resist tissue compression (Cowman, 2017). In synovial fluid, the role of HA is to form a film between cartilage surfaces, to protect adjacent tissues (Laurent *et al.*, 1996). Furthermore, HA is responsible for lubrication between tissue surfaces and for water transport in body fluids (Fakhari & Berklund, 2013). The high abundance of HA in the human body (~15 g in a 70-kg adult) and

the fact that nearly one-third of HA is replaced and removed daily suggest that it is a highly regulated molecule with functional importance (Fraser *et al.*, 1997; Maytin, 2016).

Due to its intrinsic properties, such as biocompatibility, biodegradability, hydrophilicity and viscoelasticity, HA has a wide range of applications in various biomedical fields. The first medical application of HA for humans was as a vitreous humor substitute during eye surgery in the late 1950s (Necas *et al.*, 2008). Since then, HA has been implemented in multiple fields of medicine, such as vascular, cartilage, bone and skin tissue engineering, and cancer therapy (Dovedytis *et al.*, 2020). In addition, HA and its derivatives have been applied alone or in combination with other substances to produce pro-drug, surface-modified liposomes, nanoparticles, hydrogels and other drug carriers (Fallacara *et al.*, 2018). However, while HA has a large number of potential applications, it has different and sometimes contradictory effects on many biological functions (Dicker *et al.*, 2014). Therefore, gaining a profound understanding of its structure-function relationship is crucial.

2.1 Structure of hyaluronan

Hyaluronan is a natural polysaccharide in the glycosaminoglycan (GAG) family and it has simple repeating disaccharide units of *N*-acetylglucosamine (GlcNAc) and glucuronic acid (GlcA) residues, which are linked by $\beta(1\rightarrow4)$ and $\beta(1\rightarrow3)$ glycosidic linkages (Figure 1). When both GlcNAc and GlcA are in the β -configuration, an energetically preferred state is formed where all the bulky functional groups (acetamido, carboxyl and hydroxyl) are in sterically favorable equatorial positions (Fallacara *et al.*, 2018). It is commonly believed that GlcA and GlcNAc mostly exist in a stable 4C_1 ring conformation (Cowman & Matsuoka, 2005; Pogány & Kovács, 2010; Pomin, 2014; Guvench, 2022). However, a rigid 4C_1 chair conformation of GlcNAc monosaccharide has been challenged due to ring puckering (Sattelle & Almond, 2011). HA is a linear non-sulfated molecule without any heterogeneity or branching. Since the pK_a of the carboxyl acid group is 3.2, it is ionized at physiological pH, so HA is a polyanion associated with cations (Cowman, 2017).

In early studies on HA, evidence obtained using various analytical techniques suggested that in dilute aqueous solutions at neutral pH, HA

behaves as a “somewhat stiff random coil” (Laurent, 1955; Laurent *et al.*, 1960). In the 1970s, left-handed 2-, 3- and 4-fold (both single and double) helical structures of HA in the solid state were discovered by X-ray diffraction under different experimental conditions, with each of the fiber diffraction refinement structures exhibiting intramolecular hydrogen bonds, specifically between the amide and carboxylate groups of neighboring residues (Atkins & Sheehan, 1972; Guss *et al.*, 1975; Sheehan & Atkins, 1983; Lapčik *et al.*, 1998). The conformation of HA in the solid state is not discussed in detail in this thesis, except when the data are relevant to those obtained in solution.

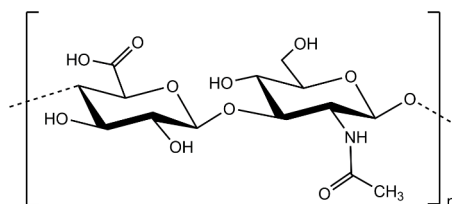


Figure 1. Schematic structure of hyaluronan, which is composed of repeating disaccharide unit of $\rightarrow 4$ -D-GlcpA- β (1 \rightarrow 3)-D-GlcpNAc- β (1 \rightarrow).

In the 1970s–1980s, Scott and his colleagues conducted a series of NMR studies, commencing with monosaccharides and extending to the entire polymer, in order to examine the secondary and tertiary structure of HA in solution. They first selected deuterated dimethyl sulphoxide (DMSO) as a solvent to avoid exchange of amide and hydroxyl protons in HA with protons from the solvent (Heatley *et al.*, 1979). They proposed a secondary structure of HA with intramolecular amide-carboxylate hydrogen bonds across the β (1 \rightarrow 4) glycosidic linkage and an extended 2-fold helical conformation (Scott *et al.*, 1984). Subsequent NMR analysis in deuterated DMSO with 12% (v/v) water suggested that the orientation of the acetamido group differed in aqueous solution from that in pure DMSO. Instead, Heatley & Scott (1988) proposed a structure with hydrogen-bonded water bridge between the acetamido and carboxylate groups in the secondary structure of HA.

Cowman *et al.* (1984) found no evidence of the existence of hydrogen bonds between the amide proton and the carboxylate oxygen across the β (1 \rightarrow 4) glycosidic linkage in HA oligomers in aqueous solution. If a stable amide-carboxylate hydrogen bond is present, a deviation of 35–40° from the

perfect *anti* orientation between H2 and NH would result in a reduction in the amide proton vicinal coupling constant (${}^3J_{\text{NH,H2}}$) to about 7.5 Hz. However, Cowman *et al.* (1984) found that the coupling constant was essentially constant (9–10 Hz) for both the α - and β -configurations. In a later study, they suggested absence of any stabilizing hydrogen bonds across the $\beta(1\rightarrow3)$ glycosidic linkage in HA in aqueous solution (Cowman *et al.*, 1996). Another NMR study concluded that cooperative intramolecular hydrogen bonds probably play a minor role in determining the conformation of HA in water (Toffanin *et al.*, 1993).

Although NMR spectroscopy is the method of choice for dynamic and conformational studies of complex biomolecules, it has limitations in detecting individual intramolecular hydrogen bonds directly (Hargittai & Hargittai, 2008). The presence of strong couplings and overlapping resonances in NMR spectra makes examination of solution conformation and dynamic properties more problematic. Moreover, analysis of high-MW HA samples is difficult because of the high viscosity and rapid relaxation resulting in low sensitivity and severe line broadening. Therefore, most studies on HA conformation and dynamics have been performed on low-MW derivatives or on short- and medium-sized oligomers, usually up to 12-mer (Pomin, 2014).

Different studies combining NMR and molecular dynamics (MD) simulation have investigated the structure of HA in aqueous solution (Holmbeck *et al.*, 1994; Donati *et al.*, 2001; Gargiulo *et al.*, 2010). Almond *et al.* (2006) were the first to utilize ${}^{15}\text{N}$ -isotope-labeled HA oligomers and computer modeling based on NMR experimental data to develop a comprehensive solution conformation of HA. In that study, the average conformation of HA in aqueous solution was predicted to be a contracted left-handed 4-fold helix (Almond *et al.*, 2006), and other studies agreed with the left-handed helix shape (Holmbeck *et al.*, 1994; Gargiulo *et al.*, 2010). However, Gargiulo *et al.* (2010) proposed that the 3-fold helix is favored over the 4-fold helix in an approximate 4:1 ratio. Almond *et al.* (2006) suggested that there are weak, transient hydrogen bonds that are in interchange with water-bridged arrangements for both $\beta(1\rightarrow4)$ and $\beta(1\rightarrow3)$ linkages. They predicted specifically that the frequency of the hydrogen bond between $\text{H}^{\text{O}3}\text{-O}^5$ is 49% and the water bridge between $\text{H}^{\text{N}}\text{-O}^6$ is present 58% of the time at the $\beta(1\rightarrow4)$ linkage (Figure 2a), and that the frequency of the hydrogen bond ($\text{H}^{\text{O}4}\text{-O}^5$) is 35% and the water bridge between $\text{H}^{\text{O}2}\text{-O}^7$ is

present 24% of the time at the $\beta(1\rightarrow3)$ linkage (Figure 2b). Thus, they concluded that interactions with water molecules are favored over strong and direct hydrogen bonding and that it is unlikely that the conformation of HA polysaccharides is stabilized by strong intramolecular hydrogen bond networks (Almond *et al.*, 2006).

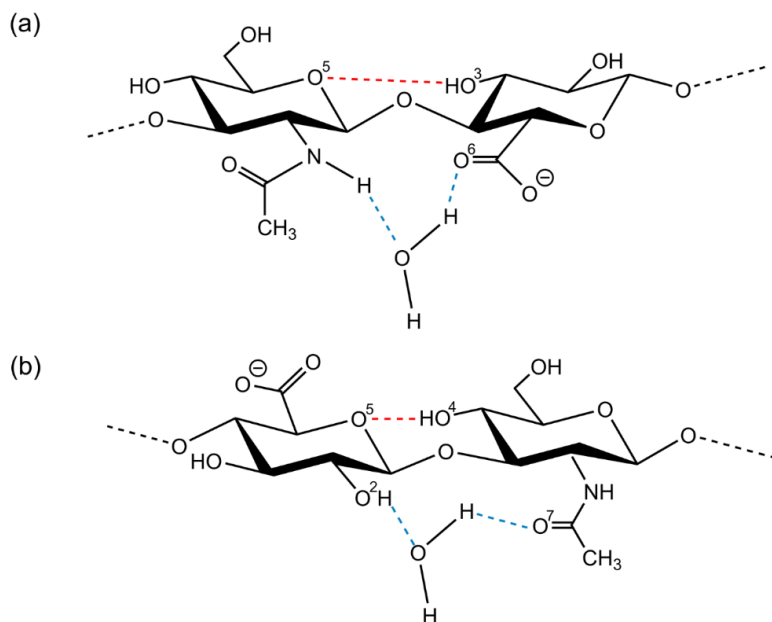


Figure 2. (a) Transient hydrogen bond ($H^{O^3}-O^5$) and water bridge between amide and carboxylate group (H^N-O^6) at the $\beta(1\rightarrow4)$ linkage and (b) transient hydrogen bond ($H^{O^4}-O^5$) and water bridge ($H^{O^2}-O^7$) at the $\beta(1\rightarrow3)$ linkage. Hydrogen bonds and water bridges are labeled according to commonly used nomenclature (Almond *et al.*, 2006).

In addition, comparisons of the properties of oligomeric and polymeric HA indicated no significant difference in the amide proton environment between the octasaccharide center and the polymer (Blundell *et al.*, 2006a). Terminal residues of the oligomer chain are typically more mobile than the interior residues (Cowman *et al.*, 2001), and subtle chemical shift perturbations observed have been explained by the different conformations and dynamic processes at the end of HA oligomers (Blundell *et al.*, 2006b).

The main origin of the structural flexibility of HA is the two β -glycosidic linkages, the carboxylate on GlcA and the acetamido group on GlcNAc. Previous findings on conformational changes and rigidity of the two β -

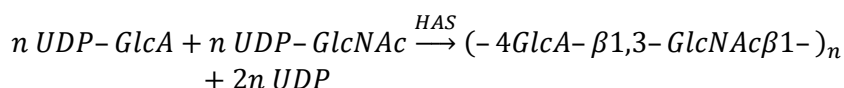
glycosidic linkages have been inconsistent (Holmbeck *et al.*, 1994; Cowman *et al.*, 1996; Furlan *et al.*, 2005; Taweechat *et al.*, 2020), and to this day the debate on which glycosidic linkage is more flexible is still ongoing. On the other hand, there is consensus that the amide proton typically adopts an *anti* orientation towards H2 (Holmbeck *et al.*, 1994; Cowman *et al.*, 1996; Donati *et al.*, 2001; Almond *et al.*, 2006; Blundell *et al.*, 2006a). In conclusion, while previous research has shed light on the conformational behaviors of HA, further studies are required to clarify the nature and extent of the structural flexibility associated with glycosidic linkages, side groups and molecular size.

2.2 Biosynthesis and degradation of hyaluronan

2.2.1 Biosynthesis of hyaluronan

Currently, two processes are available to obtain HA polymers: extraction from animal tissues, typically rooster comb, human umbilical cord and bovine synovial fluid, or more recently through the use of bacterial expression systems in *Streptococcus* (Sze *et al.*, 2016). Microbial fermentation is gradually replacing extraction as the preferred source of HA, due to lower production costs and environmental impact (Liu *et al.*, 2011).

Most GAGs are synthesized in the intracellular Golgi network and are attached to proteins. In contrast, HA is synthesized at the plasma membrane by a group of highly specialized membrane proteins, HA synthases (HASs), and is not associated with any core protein (Laurent & Fraser, 1992; DeAngelis *et al.*, 1993; Weigel *et al.*, 1997; Dicker *et al.*, 2014; Shikina *et al.*, 2022). The HASs assemble high-MW HA that is simultaneously extruded through the membrane into the ECM (or to make the cell capsule in the case of bacteria), which also allows unconstrained polymer growth, thereby achieving exceptionally large size of HA (Weigel *et al.*, 1997). The uniqueness of HAS lies in its ability to employ four substrates (two sugar-nucleotides and two types of uridine diphosphate (UDP)-HA chains) and two glycosyltransferase activities within the same protein (Weigel, 2015). The overall reaction for synthesizing one HA disaccharide unit is described by the following equation (Weigel & DeAngelis, 2007):



Streptococcus zooepidemicus is the strain most commonly used in industrial production of HA, but this has limited biomedical application of HA because *Streptococci* are pathogenic (Liu *et al.*, 2011). In recent years, recombinant systems have been developed to address this issue (Widner *et al.*, 2005; Chien & Lee, 2007; Mao & Chen, 2007; Mao *et al.*, 2009). However, HA biosynthesis has several other limitations, such as increased viscosity and low oxygen mass transfer in the medium, competition between HA synthesis and cell growth for precursors, and accumulation of lactic acid inhibiting cell growth (Liu *et al.*, 2011). The mechanism of how HAS couples HA synthesis with translocation remains unclear and production of HA polymers with very high MW and low polydispersity still faces great challenges (Weigel, 2015).

2.2.2 Degradation of hyaluronan

Hyaluronan degradation has functional implications, since the biological activity of HA is size-dependent. High-MW HA has anti-inflammatory properties, while medium-to-low MW HA has pro-inflammatory or variable effects, depending on which cell-surface receptor binds HA (Maytin, 2016). The estimated half-life of HA is 1–2 days in the epidermis and only 2–5 min in the blood circulation (Stern *et al.*, 2007). Degradation of HA can occur through a variety of mechanisms with an enzymatic, free radical or chemical basis.

Enzymatic degradation

Hyaluronan is degraded by hyaluronidases, which are endoglycosidases that predominately degrade HA polymer by cleaving its glycosidic linkages (El-Safory *et al.*, 2010). Hyaluronidases can be classified into three families based on their catalytic mechanisms and end-products: (i) hyaluronan 4-glycanohydrolases (mammalian hyaluronidases, EC 3.2.1.35) (Figure 3a); (ii) hyaluronan 3-glycanohydrolases (leech hyaluronidases, EC 3.2.1.36) (Figure 3b) and (iii) hyaluronan lyases (EC 4.2.2.1) (Figure 3c and d). In addition, HA can be degraded by chondroitin lyases (EC 4.2.2.4 and EC 4.2.2.5), which predominately cleave chondroitin sulfates (Figure 3c) (El-Safory *et al.*, 2010; Šimek *et al.*, 2020).

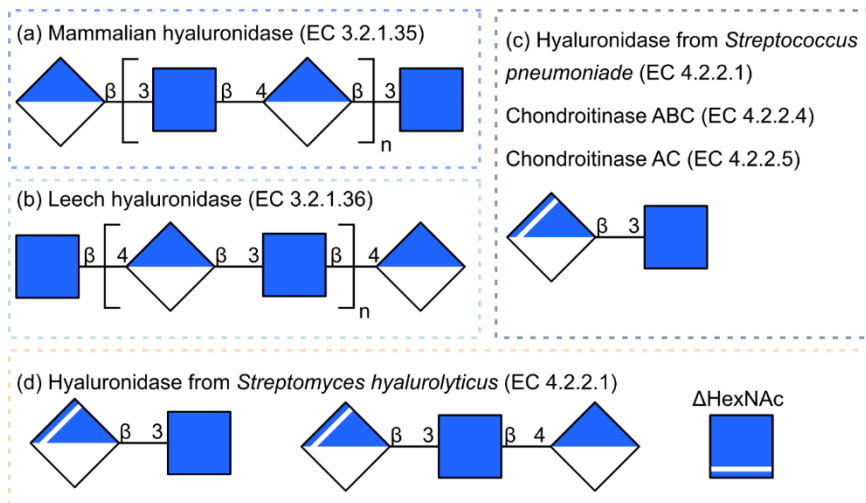


Figure 3. The three families of HA degradation enzymes and their corresponding major end-products ($n = 1$ or 2). *N*-acetylglucosamine (GlcNAc) and glucuronic acid (GlcA) are presented in Symbol Nomenclature for Glycans (SNFG) format (Neelamegham *et al.*, 2019). The white lines indicate a double bond between C4 and C5 of GlcA (Δ GlcA) at the non-reducing end and a double bond between C2 and C3 of Δ HexNAc monosaccharide.

Hyaluronan 4-glycanohydrolases (EC 3.2.1.35) cleave HA through hydrolysis of the $\beta(1\rightarrow4)$ glycosidic linkage and this group of enzymes can degrade HA, chondroitin, chondroitin sulfate and dermatan sulfate. The best-known enzymes from this family are testicular, lysosomal and bee venom hyaluronidase, of which bovine testicular hyaluronidase (BTH) is the most widely used animal hyaluronidase to prepare shorter oligomers (El-Safory *et al.*, 2010). BTH also shows transglycosylation activity and the final product consists mainly of tetra- and hexa-saccharides (Saitoh *et al.*, 1995).

The second family, hyaluronan 3-glycanohydrolases (EC 3.2.1.36), which are extracted from leeches, cleave HA through hydrolysis of the $\beta(1\rightarrow3)$ glycosidic bond, yielding GlcA at the reducing end (Linker *et al.*, 1957). These enzymes also produce tetra- and hexa-saccharides as end-products. In contrast to BTH, leech hyaluronidases have no transglycosylation properties and no activity toward chondroitin sulfate (Šimek *et al.*, 2020).

The third family, hyaluronan lyases (EC 4.2.2.1), as well as chondroitin lyases (chondroitinase ABC, EC 4.2.2.4; chondroitinase AC, EC 4.2.2.5), derive from a variety of bacterial sources. Lyases degrade HA by cleaving

the $\beta(1\rightarrow4)$ glycosidic linkages via a β -elimination reaction to yield an unsaturated disaccharide with a double bond between C4 and C5 of GlcA (Δ GlcA) at the non-reducing end (Suzuki *et al.*, 2002). This family of enzymes is used to characterize the structure of HA (Lauder *et al.*, 2000; Grøndahl *et al.*, 2011). A noteworthy feature is that hyaluronidase from *Streptomyces hyalurolyticus* (EC 4.2.2.1) is the only specific hyaluronidase that can distinguish HA from other GAGs and cleaves both $\beta(1\rightarrow4)$ and $\beta(1\rightarrow3)$ glycosidic linkages. These enzymes can produce a similar amount of even- and odd-numbered unsaturated oligosaccharides, as well as unsaturated monosaccharide Δ HexNAc (2-acetamido-2,3-di-deoxy- β -D-erythro-hex-2-enopyranose) (Tao *et al.*, 2017; Šimek *et al.*, 2020).

Non-enzymatic degradation

Ultrasonic degradation of HA is caused by cleavage of glycosidic linkages by free radicals $\text{OH}\cdot$ and $\text{H}\cdot$, which can be generated by the action of ultrasonic waves in water and the collapse of cavitation bubbles (Hafsa *et al.*, 2017). Ultrasonic degradation is essentially specific for high-MW HA, but the process is slow and never leads to complete HA degradation into monomers or oligomers (Kubo *et al.*, 1993). Interestingly, this type of degradation occurs in a non-random manner, with a bimodal MW distribution. However, many other methods can reduce the MW more efficiently down to 100 kDa, without major chemical modifications to the primary structure (Stern *et al.*, 2007). Several studies have examined the degradation of HA in the presence of reactive oxygen species (ROS), such as ozone, UV radiation and hydrogen peroxide (Wu, 2012; Chen *et al.*, 2019; Grabska & Sionkowska, 2019).

Hyaluronan can be degraded by acid or alkaline hydrolysis but, unlike ultrasonic degradation, chemical hydrolysis proceeds randomly and gives rise to mixtures of oligo- and monosaccharides (Stern *et al.*, 2007). In general, alkaline hydrolysis produces a complex mixture including both even- and odd-numbered oligosaccharides, while acid hydrolysis at high concentrations produces mainly even-numbered oligosaccharides (Šimek *et al.*, 2020). In the presence of acid, GlcA moieties are affected and cleavage of the glycosidic linkage takes place in one step. In contrast, base-catalyzed hydrolysis occurs on the GlcNAc moieties and cleavage occurs in a two-step reaction (Tokita & Okamoto, 1995). In addition, even brief exposure of HA polymers to acidic or alkaline environments can cause degradation, including

"peeling" from the reducing end and β -elimination (Kiss, 1974; Stern *et al.*, 2007).

The mechanism of thermal degradation of HA is a random chain scission (Snetkov *et al.*, 2020). Although HA is not very sensitive to temperature changes, degradation is much more significant at high temperatures (90 and 120 °C) than at moderate temperatures (30 and 60 °C), while degradation of low-MW HA occurs more quickly than degradation of high-MW HA at moderate temperature (Mondek *et al.*, 2015). Two recent studies investigated the degradation of HA under different conditions during the storage process (Simulescu *et al.*, 2015, 2016). Kinetic results indicated that storage conditions have a greater effect on degradation than initial MW of the sample (Simulescu *et al.*, 2015). Aqueous solutions of HA were found to be very stable to degradation (up to 60 days) when stored in a refrigerator without protection against microorganisms (Simulescu *et al.*, 2016).

2.3 Chemical modification of hyaluronan

Chemical modification of HA has been widely used in biomedical applications, due to the limited mechanical properties and rapid turnover rate of native HA *in vivo*. The main functional sites of HA that can be modified are the hydroxyl and the carboxyl groups. In addition, deacetylation of the acetamido group can restore the functionality of the amino group (Schanté *et al.*, 2011). There are two ways to chemically modify HA: conjugation or cross-linking. Conjugation is when one compound is grafted onto the HA chain through a single covalent bond. Conjugation of various active ingredients to HA allows the development of pro-drugs with better physicochemical properties, stability and therapeutic effects than free drugs (Fallacara *et al.*, 2018). Cross-linking means that the different HA chains are linked together by two or more covalent bonds (Schanté *et al.*, 2011). When the cross-linked network of HA is reduced to the microscopic scale, microgels and nanogels are created. These are ideal drug delivery carriers because of their adjustable size, colloidal stability, low cytotoxicity, large surface area and protection from enzymatic degradation (Xu *et al.*, 2012). Conjugated and cross-linked HA hydrogels enable HA-based biomaterials with modifiable structure, improved mechanical properties and diverse biological functions.

Cross-linking

There are many available methods for HA cross-linking, such as esterification on both hydroxyl and carboxyl groups (Huin-Amargier *et al.*, 2006; Larrañeta *et al.*, 2018), amidation, oxidation and Ugi condensation on the carboxyl group (Jia *et al.*, 2004; Young *et al.*, 2004; Maleki *et al.*, 2007), as well as ether and hemiacetal formations on the hydroxyl group (Laurent *et al.*, 1964; Tomihata & Ikada, 1997; Zhao, 2006; Collins & Birkinshaw, 2007).

Epoxides and bisepoxides such as 1,4-butanediol diglycidyl ether (BDDE) have been widely used to synthesize ether derivatives of HA in alkaline aqueous solution (Fallacara *et al.*, 2018). HA-BDDE derivatives are one of the most commonly modified HA hydrogels. At high pH (pH >13), hydroxyl groups are all deprotonated (pK_a of the hydroxyl group is ~ 10) and thus more nucleophilic than the deprotonated carboxyl group. The deprotonated hydroxyl groups of HA react with the epoxide groups of BDDE to form stable covalent ether bonds between HA and the cross-linkers. Thus, one or both ends of BDDE can be attached to HA and produce mono- or cross-linked 1,4-butanediol di-(propan-2,3-diolyl)ether (BDPE) (Zhang *et al.*, 2023) (Figure 4). NMR- and MS-based studies by Wende *et al.* (2016, 2017) showed that the most common substitution position of BDDE in different HA hydrogels is GlcNAc-OH4, followed by GlcA-OH2 and GlcNAc-OH6. The degradation products of HA-BDDE do not show any cytotoxicity and the epoxide compounds are hydrolyzed to simple diols (Schanté *et al.*, 2011).

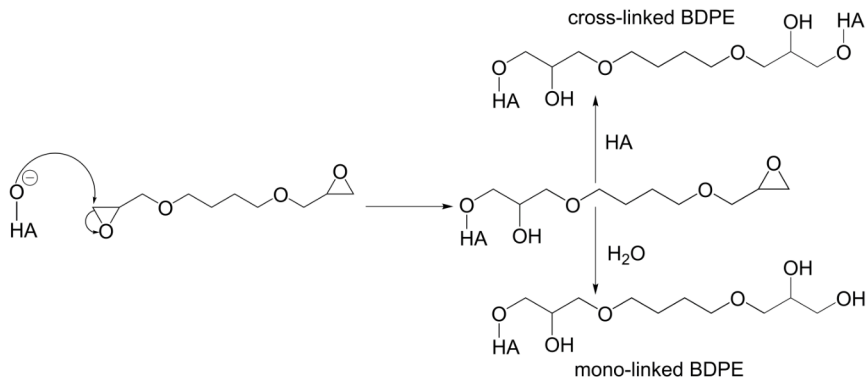


Figure 4. Scheme of cross-linking reactions of HA with 1,4-butanediol diglycidyl ether (BDDE) under alkaline conditions. BDPE = 1,4-butanediol di-(propan-2,3-diolyl)ether.

3. Methods

In this thesis, nuclear magnetic resonance (NMR) spectroscopy was used as the primary method to investigate the structural and dynamic properties of HA in aqueous solution. Mass spectrometry (MS) was used as a complementary method to corroborate some of the NMR data or to provide additional structural information.

3.1 NMR spectroscopy

The first observations of proton magnetic resonance in water and in paraffin were made independently by Bloch *et al.* (1946) and Purcell *et al.* (1946), who were awarded the Nobel Prize for Physics in 1952 “for their development of new methods for nuclear magnetic precision measurements and discoveries in connection therewith”. The development of NMR has undergone significant advancements since that time. From its beginnings with chemical shifts and scalar coupling constants as structural indicators to the recent utilization of machine learning, NMR has evolved into one of the most important analytical methods in numerous disciplines, including chemistry, biology, materials science, medicine and geology.

3.1.1 Principle

The nuclei of all atoms may be described by the nuclear spin quantum number I , which is either equal to zero or multiples of $\frac{1}{2}$. Those nuclei with $I = 0$, such as ^{12}C and ^{16}O , have no nuclear spin and therefore show no NMR signal. The spinning nuclei ($I \neq 0$) possess angular momentum P and this gives rise to magnetic moment μ , which is defined as the product of γ and P , where γ is the gyromagnetic ratio. Both P and μ are vectors whose magnitude and direction are quantized. When nuclei are placed in a static external

magnetic field (B_0 , referred to as + z-axis), they align themselves relative to B_0 in a discrete number of orientations. There are $2I+1$ possible spin states. For the spin- $\frac{1}{2}$ nucleus (such as ^1H , ^{13}C and ^{15}N), two spin states are possible: parallel or low energy state (α state) and antiparallel or high energy state (β state). When B_0 is applied to the nucleus, it creates a circular path known as Larmor precession, which is dependent on the field strength and gyromagnetic ratio of the spin (Figure 5). The rate of precession is defined by the angular velocity (ω rad s^{-1} or ν Hz):

$$\omega = -\gamma B_0 \text{ rad s}^{-1} \text{ or } \nu = \frac{-\gamma B_0}{2\pi} \text{ Hz}$$

This is known as Larmor frequency of the nucleus. If the nuclei are perturbed by applying a radiofrequency (RF) pulse whose frequency matches the Larmor frequency of the spin, energy transitions occur between different spin states. When the nuclei return to their equilibrium state, the RF signal emitted from the excited nuclear spins, also known as free induction decay (FID), is detected as a time-dependent voltage. By Fourier transformation (FT), the FID is converted from the time domain to the frequency domain, giving the NMR spectrum (Figure 6).

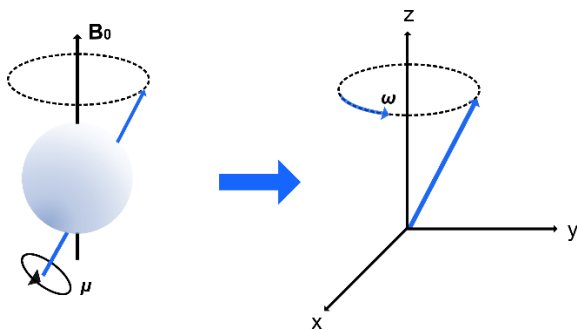


Figure 5. A spinning nucleus possesses a magnetic moment μ . When an external magnetic field (B_0) is applied to the nucleus, it experiences a Larmor precession, represented as a vector (ω) moving over the surface of the cone defined by μ . The magnetic field (B_0) is applied along the z-axis of the coordinate frame.

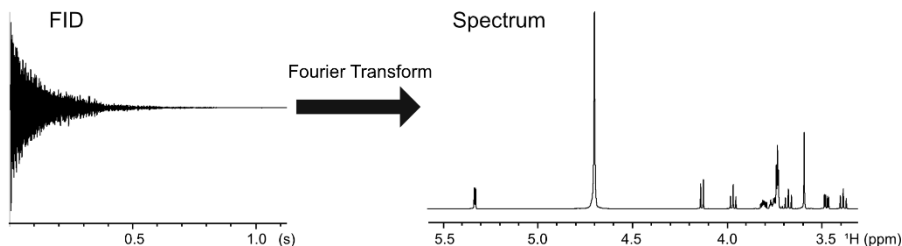


Figure 6. Fourier transformation of the time domain (FID) to the corresponding frequency domain spectrum. The FID and 1D ^1H NMR spectrum of sucrose in D_2O at 25 $^\circ\text{C}$ are shown.

Nuclei are also affected by local magnetic fields from surrounding electron clouds. As a result, nuclei with different microenvironments resonate at slightly different frequencies. The frequency deviation of a nucleus (ν_{sample}) from a standard nucleus (ν_{ref}) is measured as the chemical shift (δ) and expressed in parts per million (ppm) (Harris *et al.*, 2001):

$$\delta = \frac{\nu_{\text{sample}} - \nu_{\text{ref}}}{\nu_{\text{ref}}}$$

In ^1H and ^{13}C NMR spectroscopy, tetramethylsilane (TMS), 3-(trimethylsilyl)propanoic acid (TSP) and 2,2-dimethyl-2-silapentane-5-sulfonate sodium salt (DSS) are commonly used as references.

3.1.2 Relaxation

The process of re-establishing thermal equilibrium conditions of the excited nuclear spins after an applied RF perturbation is called relaxation. The relatively long lifetime of the excited nuclear spins (seconds to minutes) provides an opportunity to manipulate the spin system after their initial excitation. In addition, the relaxation process can provide insights into the structure of a molecule and its dynamics.

Longitudinal relaxation

Longitudinal relaxation (T_1) is the recovery of magnetization along the z-axis. During T_1 relaxation, the equilibrium population is restored, resulting in an overall loss of energy that is dissipated into the surrounding lattice, and hence T_1 relaxation is also known as spin-lattice relaxation. The most important mechanism for spin-lattice relaxation is dipole-dipole (DD) relaxation, which is due to the motion of neighboring magnetic dipoles,

causing alteration in the local magnetic field. Dipole-dipole relaxation is also the source of the nuclear Overhauser effect (NOE) (*vide infra*).

The NMR experiment most commonly used to determine T_1 is the inversion recovery experiment (Figure 7). An 180° pulse induces the initial population inversion. Since magnetization along the z-axis is unobservable, recovery is observed in the transverse plane with a 90° pulse after a certain period of τ . When τ is zero, the magnetization vector terminates with full intensity, resulting in the maximum negative signal. The experiment is then repeated multiple times with increasing τ . When τ is sufficiently long ($\tau > 5 \times T_1$), complete relaxation occurs, resulting in the maximum positive signal.

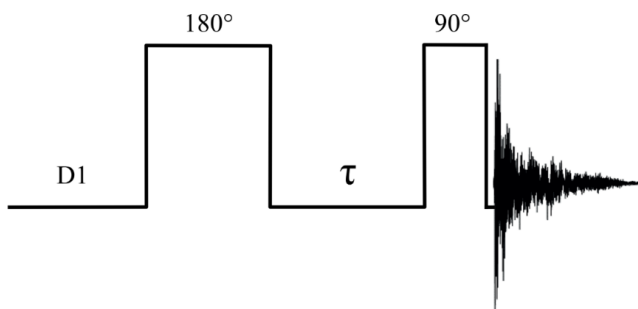


Figure 7. The inversion recovery pulse sequence.

The intensity of the detected magnetization, M_Z follows:

$$M_Z = M_0(1 - 2e^{\frac{-\tau}{T_1}})$$

where M_0 corresponds to the magnetization at the thermal equilibrium.

Transverse relaxation

Transverse relaxation (T_2) is the progressive loss of phase coherence of magnetization in the x-y plane. In other words, nuclear spin-spin interactions lead to local magnetic field differences, with spins precessing at slightly different frequencies, ultimately resulting in zero bulk magnetization in the transverse plane. Hence, T_2 relaxation is also known as spin-spin relaxation. Another source of T_2 relaxation is inhomogeneity of the static magnetic field (B_0). Therefore, the apparent transverse relaxation time T_2^* is:

$$\frac{1}{T_2^*} = \frac{1}{T_2} + \frac{1}{T_{2(\Delta B_0)}}$$

where T_2 refers to the natural relaxation process and $T_{2(\Delta B_0)}$ refers to the inhomogeneity of the static magnetic field. In addition, the width of the resonance signal in NMR is inversely proportional to T_2^* :

$$\Delta\nu_{1/2} = \frac{1}{\pi T_2^*}$$

However, it is not common practice to measure T_2 directly from the linewidths, because for most spin- $\frac{1}{2}$ nuclei, field inhomogeneity provides the dominant contribution to the linewidth. Instead, T_2 can be obtained using a spin-echo sequence that refocuses the blurring in the x-y plane caused by field inhomogeneity. The most commonly used spin-echo sequence is the Carr-Purcell-Meiboom-Gill (CPMG) pulse sequence (Figure 8). It starts with a 90° pulse to shift the magnetization into the transverse plane followed by a loop of echoes (τ - 180° - τ) to refocus the signal where τ is relatively short to reduce the effects of diffusion and J -evolution. By repeating the same procedure with different values of τ , the exponential decay of the signal can be recorded.

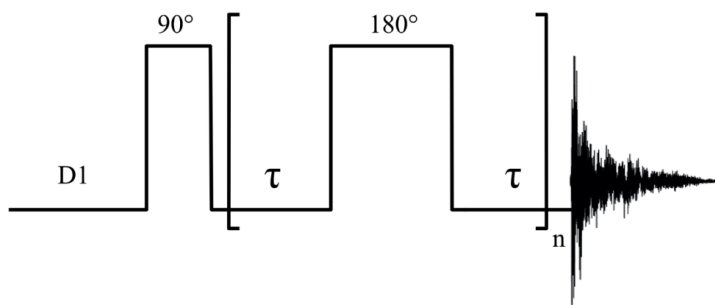


Figure 8. The Carr-Purcell-Meiboom-Gill pulse sequence.

The intensity of the detected magnetization, M_{xy} follows:

$$M_{xy} = M_0 e^{\frac{-t}{T_2}}$$

where $t = 2\tau, 4\tau \dots$

3.1.3 Diffusion

Molecular diffusion arises from translational (Brownian) motion, which depends on several physical parameters such as molecular size, solution viscosity and temperature. Pulsed field gradient (PFG) NMR can be used to

characterize molecular diffusion along the direction of the field gradient (z -axis), and spins can thereby become spatially labeled. After the encoding gradient pulse (δ), the spins move during the diffusion time (Δ) and their new position can be decoded by a second gradient pulse. This encoding/decoding procedure leads to attenuation of the NMR signal. The diffusion coefficient (D) can be measured by the PFG spin-echo sequence (Figure 9).

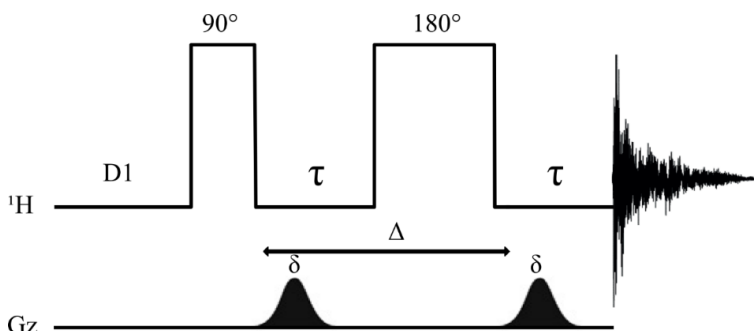


Figure 9. The pulsed field gradient spin-echo pulse sequence.

The intensity of the detected signals can be expressed as:

$$I(g) = I_0 \exp[-(\gamma g \delta)^2 D (\Delta - \frac{\delta}{3})]$$

where $I(g)$ is the observed intensity, I_0 is the intensity after a single 90° pulse, γ is the gyromagnetic ratio, g is the gradient strength and δ is the length of the gradient pulse.

3.1.4 Scalar spin-spin coupling

Scalar couplings or J -couplings arise from spin-spin interactions that occur via bonding electrons between nuclei as their nuclear magnetic moments interact through the electron cloud. Scalar coupling occurs due to the indirect interaction of two coupled nuclei through the chemical bonds, leading to splitting of the resonance signal. The magnitude of the splitting is called the coupling constant, denoted ${}^nJ_{AX}$ (Hz), where n is the number of covalent bonds between the coupled nuclei A and X . The magnitude of the coupling constant depends on the gyromagnetic ratio of the coupled nuclei and is independent of the external magnetic field B_0 . Coupling constants can provide insights into chemical connectivity between atoms, one-bond distances and dihedral angles.

3.1.5 Nuclear Overhauser effect

Nuclear Overhauser effect (NOE) occurs through dipolar couplings between two spatially close nuclei. When the population differences of a spin are perturbed from their equilibrium values by saturation or inversion, the change in intensity of dipolar-coupled neighbors after DD relaxation (ultimately leading to longitudinal relaxation) can be observed as NOE. There are two mechanisms of NOE: steady-state and transient. Steady-state NOE is when the perturbation is brought by saturation, which means equalizing spin population differences by weak RF radiation across the corresponding transitions. Steady-state NOE cannot be readily converted into internuclear separations because it results from a balance between the influences of all neighboring spins. On the other hand, transient NOE can be used to obtain kinetic data by perturbing the spin system by inverting the spin population differences in the corresponding transitions, which allows NOE to develop independently during the mixing time (τ_m), and eventually disappear due to spin relaxation. The general schemes of these two types of NOE are compared in Figure 10. Transient NOE is commonly used for 1D and 2D NOE spectroscopy (NOESY) experiments. Furthermore, it is useful for estimating internuclear distances (r) using build-up curves, since the growth of NOE has a linear dependence on mixing time ($\propto r^{-6}$) at the initial region ($\tau_m \ll T_1$).

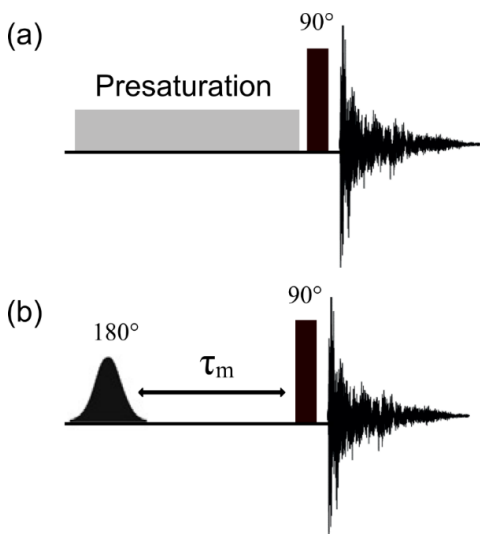


Figure 10. General schemes for measuring (a) steady-state nuclear Overhauser effect (NOE) and (b) transient NOE. τ_m = mixing time.

3.1.6 Analysis of carbohydrates by NMR spectroscopy

Nuclear magnetic resonance spectroscopy is one of the most powerful analytical methods for structural, conformational and dynamic analysis of carbohydrates. The ^1H , ^{13}C and ^{15}N nuclei can be employed to detect nuclear spin correlations from a combination of multidimensional NMR experiments.

Characteristic chemical shifts

In ^1H NMR spectra, anomeric resonances for the protons of aldoses are generally found between $\delta_{\text{H}} \sim 4.4$ and 6.0 ppm, where signals from anomeric protons with the β -configuration are usually found in a more upfield region than signals from protons with the α -configuration. Protons attached to carbons bearing hydroxyl or amide groups are usually found at $\delta_{\text{H}} \sim 3.2$ –4.2 ppm, while methyl protons from *N*- or *O*-acetyl groups appear as singlets at $\delta_{\text{H}} \sim 2.0$ –2.2 ppm (Fontana & Widmalm, 2023). In H_2O solution, exchangeable protons can be observed with hydroxyl protons at $\delta_{\text{H}} \sim 5.0$ –7.5 ppm and amide protons at ~ 8.0 ppm.

In ^{13}C NMR spectra, the anomeric carbons are found at $\delta_{\text{C}} \sim 95$ –110 ppm. The δ_{C} at the glycosidic linkage sites move to higher frequencies in oligo- and polysaccharides than in the corresponding monosaccharides. This shift called glycosylation shift is usually between δ_{C} 4–10 ppm (Söderman *et al.*, 1998). Carbons with secondary hydroxyl groups are observed at $\delta_{\text{C}} \sim 65$ –85 ppm, hydroxymethyl carbons at $\delta_{\text{C}} \sim 60$ –65 ppm, and nitrogen-bearing carbons at $\delta_{\text{C}} \sim 50$ –60 ppm. Carbonyl carbons appear at $\delta_{\text{C}} \sim 170$ –180 ppm and methyl carbons from acetyl groups are at $\delta_{\text{C}} \sim 20$ –25 ppm (Fontana & Widmalm, 2023).

Characteristic scalar couplings

Scalar coupling constants can be used to establish the anomeric configuration and to determine the conformation of pyranose rings. The relationship between the vicinal coupling constant (3J) and the dihedral angle (θ) can be described by the Karplus equation (Karplus, 1959; Haasnoot *et al.*, 1980):

$$J(\theta) = A \cos^2 \theta + B \cos \theta + C$$

where A, B and C are constants that are dependent on the type of atom to which the proton is attached and the nearby substituents. These parameters are usually adjusted to specific molecular systems and conditions, to improve the accuracy and applicability of the Karplus equation.

In the aldopyranosyl ring, the magnitude of $^3J_{H1,H2}$ is routinely used to determine the stereochemistry of the anomeric carbon. When sugar residues are in *gluco-*, *allo-*, *galacto-* and *gulo-* configuration, a larger value of $^3J_{H1,H2}$ at $\sim 7\text{--}9$ Hz in β -configuration and a smaller value of $^3J_{H1,H2}$ at $\sim 2\text{--}4$ Hz in α -configuration is detected. For other configurations (*manno-*, *altro-*, *talo-* and *ido-* configuration), since H2 is in the equatorial position, the value of $^3J_{H1,H2}$ is too small and/or not resolved. Therefore, $^1J_{C1,H1}$ can be used instead with a value of ~ 170 Hz for the α -configuration and ~ 160 Hz for the β -configuration (Bubb, 2003). The average one-bond CH coupling ($^1J_{CH}$) of non-anomeric positions is around 145 Hz, while the one-bond CH coupling of methyl groups in acetyl saccharides is around 130 Hz (Bubb, 2003). The value of $^1J_{CC}$ is generally in the range 37–47 Hz and the values of $^2J_{CC}$ and $^3J_{CC}$ are usually less than 5 Hz in the aldopyranosyl ring (Bose-Basu *et al.*, 2007). In addition, transglycosidic $^3J_{C,H}$ interpreted via Karplus equations is particularly useful for determination of dihedral angles over the glycosidic linkages.

Water suppression

Many structural studies of carbohydrates need to be performed in H₂O/D₂O solution, in order to observe exchangeable protons and study the possible formation of hydrogen bonds and water bridges. The strong signal from the water protons causes problems with the dynamic range of the NMR signals, due to the large difference between the water proton concentration (110 M) and the typical solute concentration (\sim mM), leading to baseline distortion, radiation damping and t_1 noise in 2D experiments.

The goal of water suppression is to reduce the magnitude of the water signal before reaching the receiver and the simplest way to achieve this is by pre-saturation of water. This is achieved by applying weak RF radiation at the water frequency prior to excitation and acquisition, equalizing the spin population differences and thereby suppressing the water signal. Another very effective method is to use PFG to suppress the water signal. One approach, called water suppression by gradient-tailored excitation (WATERGATE), is shown in Figure 11a. The first gradient pulse (G_1) is designed to defocus all spins, followed by a 180° selective pulse or a pulse train (S), and then the solute spins are refocused after the second gradient while the water signal remains dephased. The two identical gradient pulses act in the opposite way and refocus the selected magnetization, so it is considered a gradient echo. However, phase distortion can occur due to the

selective pulses for the water signal. Therefore, an improved approach called excitation sculpting with double gradient echoes can be applied (Figure 11b). Repeating the gradient echo with a different gradient strength (G_2) eliminates all remaining phase errors and produces a pure phase excitation profile that depends only on the selective pulse.

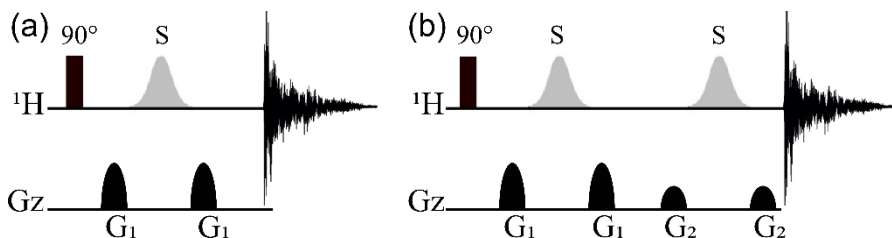


Figure 11. Water suppression schemes employing pulse field gradient, based on (a) water suppression by gradient-tailored excitation (WATERGATE, single-echo) and (b) excitation sculpting (double-echo). The element S represents a combination of soft and hard pulses or a pulse train that inverts all other spins, but has zero net effect on the solvent resonance.

2D NMR experiments for structural analysis of carbohydrates

2D- ^1H , ^1H -correlation spectroscopy (COSY) is used for correlating protons coupled over two or three bonds. The basic pulse sequence consists of two 90° hard pulses and a variable evolution time t_1 , during which magnetization transfer occurs through adjacent bonds (Figure 12a). The peaks of interest are the off-diagonal cross-peaks, which show the direct connectivity of protons sharing a mutual J -coupling.

2D- ^1H , ^1H -total correlation spectroscopy (TOCSY) yields proton correlations like those in COSY, but it creates correlations between all protons within the same spin system (in principle). The TOCSY sequence is similar to the COSY sequence, the only difference being the use of a spin-lock instead of a single pulse (Figure 12b). The spin-lock can be considered as a discrete δ - 180° - δ period, which keeps all spin vectors in the transverse plane, and the evolution of chemical shifts and homonuclear J -couplings continues during the mixing time τ_m . As τ_m increases, the magnetization can be gradually transferred from the vicinally coupled protons to the most distant protons within each monosaccharide spin system. A mixing time of 20 ms (one-step transfer) will essentially give the same information as the COSY experiment, whereas a mixing time of 80–120 ms will give a 5–6 step transfer and allow assignment of all spin systems from H1 to H6 in sugars

with the glucose configuration. The magnetization transfer can be interrupted by small 3J coupling constants. This property is advantageous for deducing the configuration of sugars (*manno*, *galacto* or *gluco*).

TOCSY is a powerful NMR experiment for analyzing complex proton spectra by (a) varying τ_m , so that signals can appear in a stepwise manner to avoid spectral overlap, (b) combining with other 2D NMR techniques and (c) using spectral editing techniques to create *e.g.* band-selective TOCSY, which can target certain spectral regions.

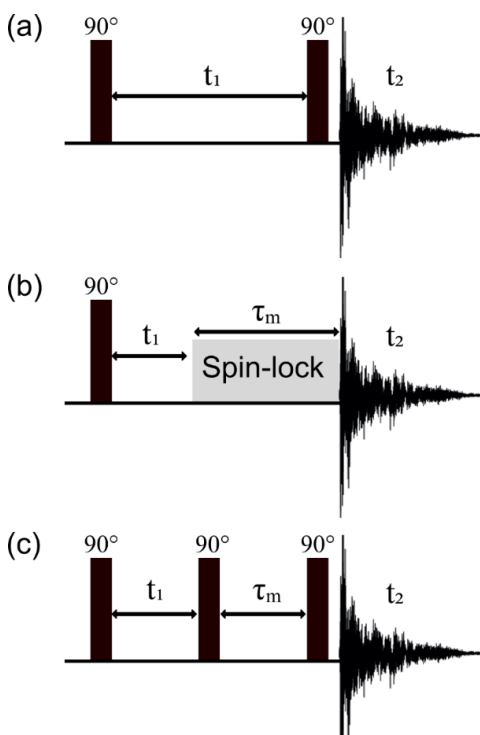


Figure 12. Schematic representations of the basic pulse sequences of (a) correlation spectroscopy (COSY), (b) total correlation spectroscopy (TOCSY) and (c) nuclear Overhauser effect spectroscopy (NOESY). t_1 = evolution time; τ_m = mixing time; t_2 = detection time.

The through-space correlation $[^1\text{H}, ^1\text{H}]$ -NOESY pulse sequence is closely related to COSY. The difference lies in the mixing period τ_m , during which the NOE develops via cross-relaxation (Figure 12c). As mentioned, NOESY spectra can be used to obtain interproton distances (r) that are less than 5 Å and it is therefore an effective way to establish correlations between sugar

residues in polysaccharides. Different types of correlations obtained for sucrose by these three NMR experiments are illustrated in Figure 13.

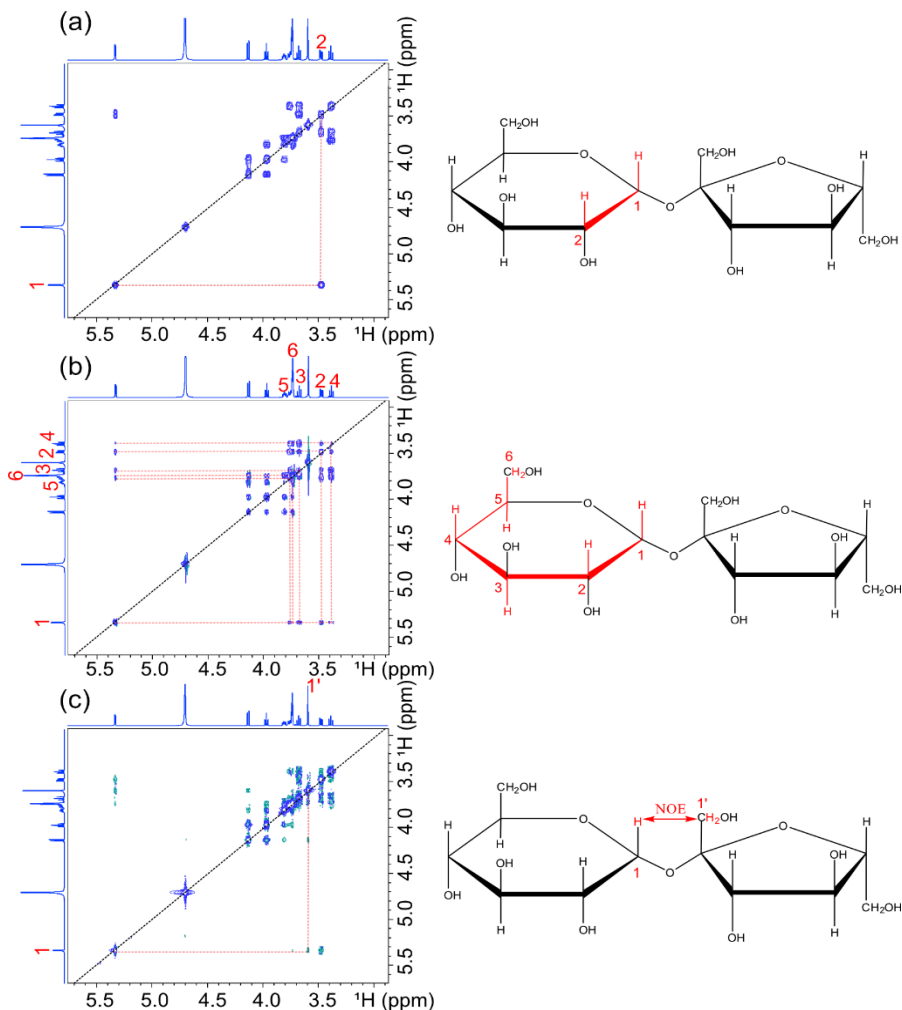


Figure 13. Homonuclear 2D NMR spectra of sucrose obtained by: (a) correlation spectroscopy (COSY), where the cross-peaks show the direct three-bond connectivity between protons, (b) total correlation spectroscopy (TOCSY) (mixing time = 80 ms), where the cross-peaks show proton connectivity (through chemical bonds) within the same spin system, and (c) nuclear Overhauser effect spectroscopy (NOESY) (mixing time = 400 ms), where the cross-peaks show dipolar cross-relaxation between two protons that are spatially close to each other. Key correlations in each spectrum are highlighted in red.

2D-[^1H , X]-heteronuclear single quantum coherence (HSQC) spectra are commonly used to identify heteronuclear correlations between spins coupled across one single bond. The HSQC pulse sequence is based on the insensitive nuclei enhanced by polarization transfer (INEPT) sequence, in which the transverse heteronuclear magnetization is generated and detected after the polarization transfers from the attached proton to the heteronucleus (Figure 14a). However, in HSQC, polarization is first transferred from the proton to the heteronucleus by one INEPT step and later back to the proton by an inverse INEPT step (Figure 14b). During the t_1 evolution period, X-nucleus magnetization evolves and the 180° pulse to the proton at the midpoint of t_1 inverts proton magnetization and refocuses heteronuclear coupling. Therefore heteronuclear chemical shifts can be observed in the F1 dimension without splitting or broadening from $^1J_{\text{CH}}$. X-spin decoupling is employed later in the acquisition period to avoid splitting from $^1J_{\text{CH}}$ and thereby increasing S/N . A typical $^1J_{\text{CH}}$ is around 145 Hz, so Δ ($\Delta = 1/(2^1J_{\text{XH}})$) is set to around 3.4 ms. A typical $^1J_{\text{NH}}$ is about 90 Hz, so Δ is set to 5.6 ms.

2D-HSQC plays an important role in chemical shift assignments of carbohydrates, especially in cases with overlapping signals in the ^1H dimension. Furthermore, multiplicity-edited-HSQC experiments can be used to identify carbons attached to an odd or even number of protons with opposite signs (marked in blue and green, respectively, in Figure 15a). Carbons without directly attached protons will not be visible in HSQC spectra.

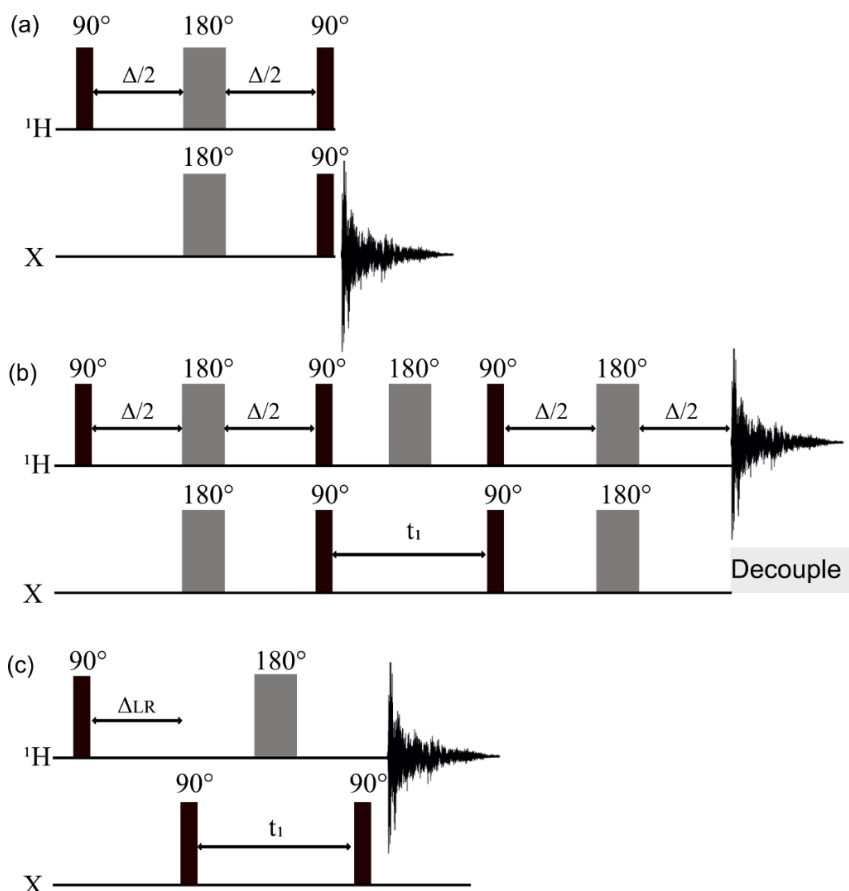


Figure 14. Schematic representations of the basic pulse sequences of (a) insensitive nuclei enhanced by polarization transfer (INEPT), (b) heteronuclear single quantum coherence (HSQC) and (c) heteronuclear multiple bond correlation (HMBC). t_1 = evolution time, $\Delta = 1/(2^1J_{\text{XH}})$; Δ_{LR} = coupling evolution time optimized for long-range coupling constants.

The 2D- $[^1\text{H}, \text{X}]$ -heteronuclear multiple bond correlation (HMBC) experiments reveal correlations between protons and heteronuclei separated by two or three chemical bonds ($^nJ_{\text{CH}}$, $n = 2, 3$) (Figure 14c). As in HSQC, the magnetization is transferred from the proton to the heteronucleus and then back to the proton. However, the magnetization transfer mechanism in HMBC is due to heteronuclear multiple-quantum coherence transfer rather than polarization transfer. The preparation period Δ_{LR} should be set long enough to allow the small long-range J_{CH} to evolve; in theory, Δ_{LR} should be at least 100 ms ($1/(2^nJ_{\text{CH}})$), but shorter delays are routinely employed to avoid

relaxation losses. The intensity of observed HMBC cross-peaks depends on the magnitude of both J_{CH} and Δ_{LR} . [^1H , ^{13}C]-HMBC experiments are used for determining the connectivity over the glycosidic linkages. Carbons without attached protons that are not visible in HSQC spectra can also be detected, such as carbon 2' in sucrose in Figure 15b.

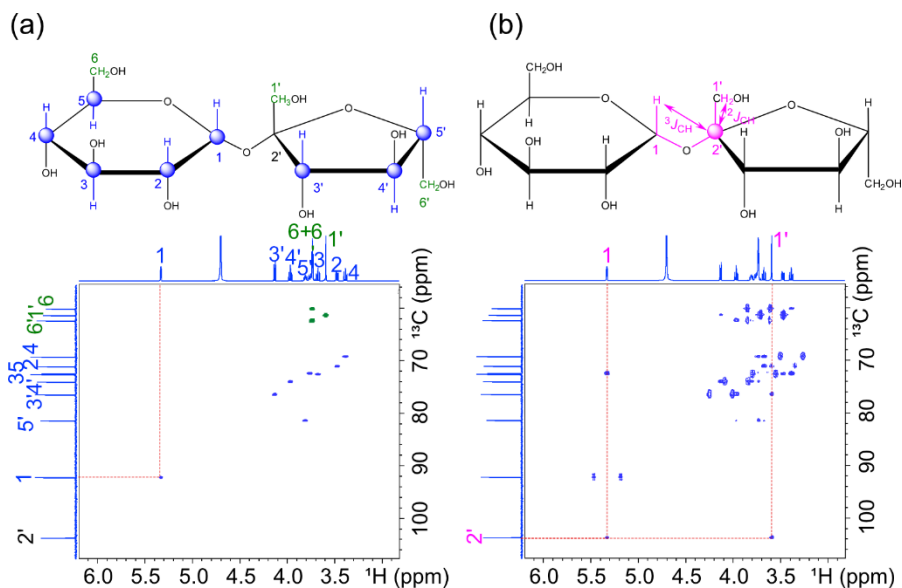


Figure 15. Heteronuclear 2D NMR spectra of sucrose: (a) multiplicity-edited [^1H , ^{13}C]-heteronuclear single quantum coherence (HSQC) with cross-peaks showing the one-bond proton-carbon correlations and (b) [^1H , ^{13}C]-heteronuclear multiple bond correlation (HMBC) with cross-peaks showing the 2- or 3-bond proton-carbon correlations.

Hybrid experiments such as [^1H , ^{13}C]-HSQC-TOCSY and [^1H , ^{13}C]-HSQC-NOESY, can further resolve the overlap of proton resonances observed in TOCSY/NOESY NMR spectra.

Isotope labeling

Carbohydrates exhibit high structural diversity (monosaccharides, glycosidic linkages, branching patterns, modifications) and great conformational flexibility. It is thus problematic to resolve all structures of carbohydrates by NMR due to the structural diversity, the limited ^1H chemical shift dispersion and the low natural abundance of ^{13}C (1.1%) and ^{15}N (0.35%) nuclei (Gimeno *et al.*, 2020). Incorporation of ^{13}C and/or ^{15}N isotopes into biomolecules, such as proteins, has improved sensitivity, reduced acquisition times and resolved

resonance overlap, leading to widespread use of isotope labeling methods in NMR studies of protein structure and dynamics. However, applications of isotope labeling in carbohydrate NMR remain limited.

In recent years, NMR spectroscopists and glycoscientists have started to develop new isotope labeling methods and new pulse sequences for glycans (Blundell *et al.*, 2004; Zhang *et al.*, 2008; Pomin *et al.*, 2010; Barb *et al.*, 2011). Incorporating ^{13}C and ^{15}N isotopic labeling in carbohydrates opens up the opportunity to utilize NMR experiments commonly used on proteins, such as triple-resonance and multi-dimensional experiments. This could reveal information previously not obtainable with unlabeled samples, such as overlapped chemical shifts of internal residues and long-range coupling constants across glycosidic linkages and in aldopyranosyl rings (Blundell *et al.*, 2006b; Zhu *et al.*, 2006; Bose-Basu *et al.*, 2007; Fontana *et al.*, 2014; Zhang *et al.*, 2017).

3.2 Mass spectrometry

Mass spectrometry is another useful analytical technique for identifying and quantifying the molecular composition of a sample, as it provides information complementary to that obtained by NMR. For example, the elemental composition of a compound can be determined by measuring its monoisotopic mass and its isotope distribution pattern, and structural information can be obtained by measuring masses of compound fragments formed inside the mass spectrometer.

Mass spectrometry is highly sensitive and capable of analyzing extremely small quantities of samples, sometimes with detection limits at picomolar to femtomolar level (Tunlid *et al.*, 1989; Bedair & Sumner, 2008; Hosu *et al.*, 2017), which makes it a valuable tool in fields such as metabolomics, proteomics and environmental analysis. The MS process consists of ionization, mass analysis and detection steps. The sample is initially ionized in an ion source to produce ions, which are separated in a mass analyzer based on their mass-to-charge ratio (m/z). The separated ions are then transported to a detector which, when hit by the ions, yields an electrical signal that measures the ion abundance. The detector signal as a function of m/z is referred to as a mass spectrum. There are many different types of ion sources and mass analyzers, each with its own advantages and disadvantages regarding detection sensitivity, mass resolution and mass accuracy. Ion

sources and mass analyzers can be combined in different ways, but each commercially available mass spectrometer typically provides one combination, and the mass spectrometer is often chosen according to the specific requirements of the analysis.

Mass spectrometry is usually coupled with a chromatographic separation system, such as gas chromatography (GC) or liquid chromatography (LC). In a chromatographic system, the sample compounds elute from the chromatographic column at their respective retention times and are detected. The retention time is typically a characteristic feature of the separation system, aiding in the identification of analytes based on their specific elution time. MS-detection generates an ion chromatogram composed of a large set of successively acquired mass spectra, each providing mass spectral data for the eluted compounds. Thus, the components can be identified one after the other by their respective mass spectra.

3.2.1 Ionization

Analytes can be ionized chemically, thermally, by electric fields or by exposure to laser light or energetic electrons. When the sample is volatile and thermally stable, MS is usually coupled with GC, so the sample is ionized in the gas phase. One classical procedure of ionization in the gas phase is called electron ionization (EI), in which energetic electrons impact the analyte molecules and produce positive molecular ions (M^+). EI is considered a hard ionization method due to the application of highly energetic electrons, which induces extensive fragmentation of the molecular ion. The resulting fragmentation patterns are reproducible and characteristic of the molecular structure of the analyte, allowing for structural elucidation of unknown compounds and identification of known compounds by comparison with spectra stored in libraries. Since EI leads to the fragmentation of molecular ions, which sometimes hinders the detection of the molecular mass, another complementary technique, namely chemical ionization (CI), can be used. In CI, a reagent gas (*e.g.* methane or ammonia) is first ionized to form reagent ions, which react with analyte molecules to produce analyte ions. CI is a softer ionization method that yields a spectrum with fewer fragment ion signals and with the molecular ion signal easily recognized.

For non-volatile samples, MS is typically coupled with LC, and electrospray ionization (ESI) is used to generate gas-phase ions from

solution-phase analytes. In ESI, the analyte-containing solution is pumped under high voltage through a capillary from which highly charged droplets are sprayed at atmospheric pressure. The droplets enter a narrow heated tube that transfers them into the mass analyzer, which is held under vacuum. The heat and lowering of the pressure through the tube allow the solvent to evaporate, leaving bare singly or multiply charged ions in the mass analyzer. The ions formed in ESI are adduct ions, with $[M\pm nH]^{n\pm}$ as the most common, and the polarity depends on the high voltage used. ESI can produce singly charged ions from small molecules up to multiply charged ions from large biomolecules (MW >130 kDa) including oligonucleotides and proteins (Fenn *et al.*, 1989). Another soft ionization technique, called matrix-assisted laser desorption/ionization (MALDI), is also commonly used for analysis of large biomolecules. In MALDI, the analyte is mixed with a matrix material (usually a small organic molecule) in solution, and the mixture is then applied to a metal plate to dry and form a thin layer of matrix crystals with the sample molecules embedded. The sample plate is introduced to the MALDI ion source, which is held under vacuum, and the analyte-containing crystals are exposed to a pulsed laser beam (typically UV). The laser light is absorbed by the matrix molecules, which are rapidly desorbed together with the analyte molecules from the crystal surface. A portion of the material is ionized and can be transferred to the mass analyzer using an electric field. Some advantages of MALDI are the simple sample preparation and relatively high tolerance to contamination.

3.2.2 Mass analyzers

In a mass analyzer, electric or magnetic fields are employed to separate the ions formed in the ion source according to their respective m/z -values. The quadrupole analyzer is probably the most common type, as it is used both separately (in single or multiple steps) and in combination with other types of mass analyzers. The quadrupole consists of four metal rods (electrodes) placed in a circular array. The electrodes are connected pairwise to an electric potential with both a static part and an alternating part (RF) and with one pair always having the opposite sign of potential to the other pair. Ions can enter the center of the array at one end of the rods and, for a specific combination of static and RF-potential amplitudes, ions with a specific m/z -value can exit at the other end of the rods, whereas all other ions instead collide with the electrodes. By sweeping both amplitudes over some range (keeping their

ratio constant), ions with different m/z will have stable trajectories through the quadrupole and can reach the detector. The detector signal as a function of the amplitude settings of the sweep scans the abundance of ions at different m/z -values and hence generates a mass spectrum. Quadrupole analyzers have relatively low resolution and accuracy.

The quadrupole ion trap analyzer operates according to the same basic principle as the quadrupole analyzer. The difference is that in the ion trap analyzer, all the ions of different m/z -values are trapped inside a volume with the electrodes as boundaries and are thereafter m/z -selectively expelled from the trap by manipulating the RF amplitude. The ion trap is capable of performing multiple MS (MS^n) by trapping and fragmenting ions in a controlled manner and expelling the fragment ions to the detector, yielding multidimensional mass spectra.

The orbitrap analyzer is an electrostatic ion trap based on a novel concept (Makarov, 2000) and launched on the market rather recently (Hu *et al.*, 2005). The orbitrap provided two outer electrodes and a central electrode held at a constant voltage. The electrodes have a specific rather complicated shape, and ions that enter the orbitrap radially at some distance from the central electrode are trapped in an orbital motion around the central electrode. Furthermore, the ions are separated into m/z -specific packets that oscillate along the central electrode axis. Thereby, a time-dependent image current is induced in the outer electrodes. The frequency of the axial motion is directly related to m/z and, by FT of the time-dependent image current, a mass spectrum is derived. The high resolution makes the orbitrap very useful for the accurate identification and quantification of complex mixtures and also for the quantification of the mass and abundance of isotopes in a compound.

The principle of the time-of-flight (TOF) analyzer is that all ions have the same kinetic energy after being initially accelerated in an electric field, and further separation is based on the differences in their velocity through the field-free drift zone toward the detector. The flight time of each ion to reach the detector is proportional to the square root of its m/z . The upper mass range of a TOF analyzer has no limit, which makes it ideal for analyzing large molecules. TOF requires a pulsed ion source, but a continuous ion source such as ESI can be used if the ions are first passed through a focusing device (quadrupole) and entered orthogonally into the TOF analyzer, where a high voltage pulse is applied to accelerate the ions through the analyzer at a well-

defined time. This arrangement is referred to as a quadrupole time-of-flight (QTOF) mass spectrometer and can provide high resolution and sensitivity.

4. Aims

The overall aim of the work described in this thesis was to gain a deeper understanding of the structural and dynamic characteristics associated with different forms of hyaluronan (HA) by using NMR-based methodologies. The work involved investigations of chemically modified HA, mono- and oligo-saccharides of HA and isotopically labeled HA using a wide range of NMR experiments. These experiments included relaxation and diffusion studies, analysis of correlations through chemical bonds and space (*J*-couplings and NOEs), adapted protein NMR experiments and quantitative NMR analysis.

Specific objectives were to:

- Study the relationship between the physicochemical properties of butanediol-diglycidyl ether (BDDE) cross-linked HA hydrogels and the relaxation and diffusion behaviors of their water protons using high-field NMR spectroscopy (Paper I)
- Analyze the first-observed amide *cis* conformation of *N*-acetylglucosamine (GlcNAc) and further investigate the conformation of the *N*-acetyl group by adapting protein NMR experiments for ¹³C, ¹⁵N labeled GlcNAc (Paper II)
- Compare the conformation of the glycosidic linkages and the *N*-acetyl group between different HA chain lengths by analyzing NOEs and *trans*-glycosidic ³*J*-couplings (Paper III)
- Determine the level of ¹³C and ¹⁵N isotope enrichment in biosynthetically produced HA (Paper IV)

5. Results and Discussion

The results reported in Papers I–IV are summarized and discussed in Sections 5.1–5.4.

5.1 Relaxation and diffusion of water protons in BDDE cross-linked hyaluronic acid hydrogels investigated by NMR spectroscopy - Comparison with physicochemical properties (Paper I)

The use of native hyaluronan (HA) as biomaterial or in biomedical applications is hampered by its rapid degradation *in vivo* (Stern *et al.*, 2006; Hwang *et al.*, 2012), and various cross-linking methods have been developed to address this problem (Segura *et al.*, 2005). The aim of cross-linking is to enhance viscoelasticity, increase resistance to degradation *in vivo* and uphold other innate properties of HA, such as biocompatibility and biodegradability. Butanediol-diglycidyl ether (BDDE) cross-linked HA hydrogels offer improved stability and mechanical properties that are expected to facilitate progress in various applications such as tissue engineering and drug delivery.

Since water is the major component of HA hydrogels, the behavior of water protons in hydrogels may show correlations with the physicochemical properties of HA. In this study, the longitudinal (T_1) and transverse (T_2) relaxation times and the diffusion coefficient (D) of water protons in BDDE cross-linked HA hydrogels and in native solutions were measured by high-field NMR spectroscopy.

Nine different hydrogels (A–I) with different degree of modification (MoD), degree of cross-linking (CrD) (Kenne *et al.*, 2013), gel content (GelC), swelling degree (SwD) and damping factor ($\tan \delta$) (Edsman *et al.*, 2012) were investigated (Table 1). Based on their physicochemical

properties, these nine hydrogels were divided into strong (D, H), medium (A, B, C, I), and weak (E, F, G) hydrogels. Three native solutions of HA with different MW (85 kDa, 172 kDa, and 3 MDa) were also studied. The samples were prepared in three concentration ranges, low (~2.5 mg/mL), medium (~5 mg/mL) and high (~10 mg/mL), and the NMR experiments were performed in the temperature interval 5–70 °C. A water reference sample was also analyzed.

Table 1. Degree of modification (MoD), degree of cross-linking (CrD), gel content (GelC), swelling degree (SwD) and damping factor (Tan δ) of hyaluronan-butenediol-diglycidyl ether (HA-BDDE) hydrogels A–I

Sample	MoD (%)	CrD (%)	GelC*(%)	SwD (g/g)	Tan δ
A	7.4	0.8	93.9	173	0.09
B	1.0	0.2	88.7	144	0.14
C	1.1	0.5	88.0	226	0.07
D	1.5	0.8	96.3	116	0.10
E	1.1	0.3	77.8	887	0.32
F	7.0	0.9	76.3	827	0.28
G	0.9	0.2	62.9	542	0.21
H	4.6	2.1	98.0	79	0.15
I	2.9	0.6	86.7	359	0.05

* Fraction of cross-linked to non-cross-linked HA.

5.1.1 Longitudinal relaxation and diffusion coefficient of water protons
 Longitudinal relaxation (T_1) and diffusion coefficient (D) of the water protons in the HA samples increased with temperature, and the behavior of water protons in HA samples was similar to that in pure water, although with slightly lower T_1 and D at high temperatures. No significant differences in T_1 and D were observed between the HA hydrogels and the native HA solutions (Figure 16).

However, on comparing the average values of T_1 and D of water protons in HA hydrogels and native solutions, slight dependence of T_1 and D on sample concentration was observed (see Table 2 in Paper I). The T_1 and D of water protons decreased with increasing concentration of HA sample, which is consistent with a higher degree of polymer-bound water molecules at higher concentrations.

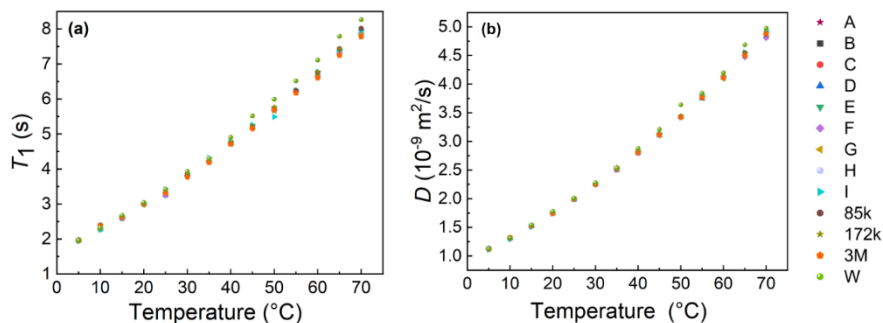


Figure 16. (a) Longitudinal relaxation (T_1 , s) and (b) diffusion coefficient (D , m^2/s) as a function of temperature (± 1 °C) at low HA concentration. A–I = hydrogels A–I (see Table 1); 85k, 172k and 3M = native HA solutions with molecular weight 85 kDa, 172 kDa and 3 MDa, respectively; W = water reference.

5.1.2 Transverse relaxation of water protons

While T_1 and D of water protons showed clear temperature dependence, the behavior of T_2 of water protons was more complex. At low HA concentrations, T_2 increased with temperature in all samples (Figure 17a). The T_2 values of the 85 kDa and 172 kDa solutions were higher than those of the other samples. All hydrogel samples behaved quite similarly, with the exception of hydrogel D (strong hydrogel), which had the lowest T_2 values of all samples. The 3 MDa HA solution had a temperature profile more similar to that of the hydrogels than to that of the 85 kDa and 172 kDa solutions.

At medium HA concentrations, different temperature profiles for T_2 of water protons were observed (Figure 17b). The T_2 values for the three native solutions first increased upon increasing temperature to reach a maximum at about 25 °C and then decreased. In contrast, the hydrogel samples were relatively insensitive to temperature change. Overall, the T_2 values of the water protons in the medium-concentration samples were smaller and varied less over the temperature range than those of the low-concentration samples.

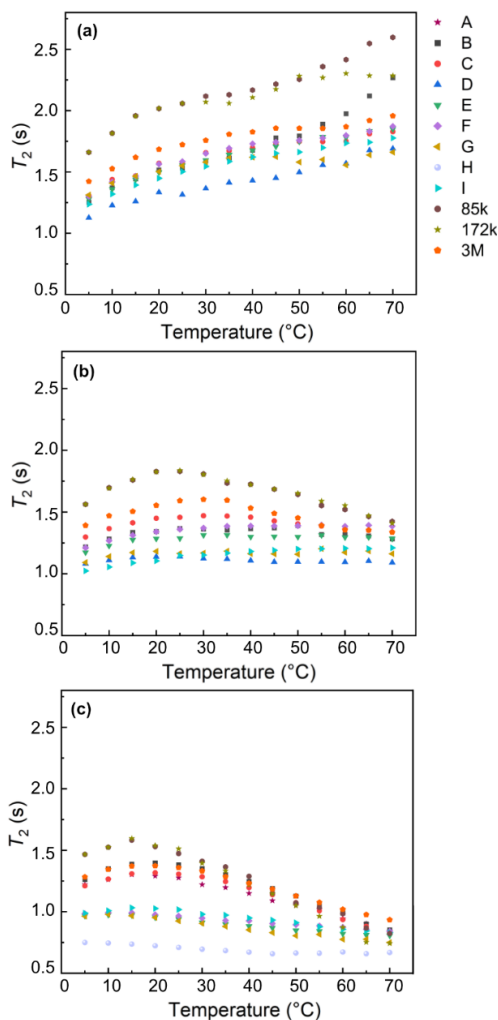


Figure 17. Transverse relaxation (T_2 , s) as a function of temperature (± 1 °C) at (a) low, (b) medium and (c) high HA concentration. A–I = hydrogels A–I (see Table 1); 85k, 172k and 3M = native HA solutions with molecular weight 85 kDa, 172 kDa and 3 MDa, respectively.

At high HA concentrations, the T_2 maximum for all samples was reached at lower temperatures (10–20 °C) (Figure 17c). The 85 kDa and 172 kDa solutions showed a strong decrease in the T_2 values of the water protons from 15 °C. The temperature profiles of the 3 MDa solution and of hydrogels A, B and C were quite similar, while the other hydrogels, particularly hydrogel

H, were rather insensitive to temperature changes. The average T_2 values at high HA concentrations were lower than those at the other concentrations.

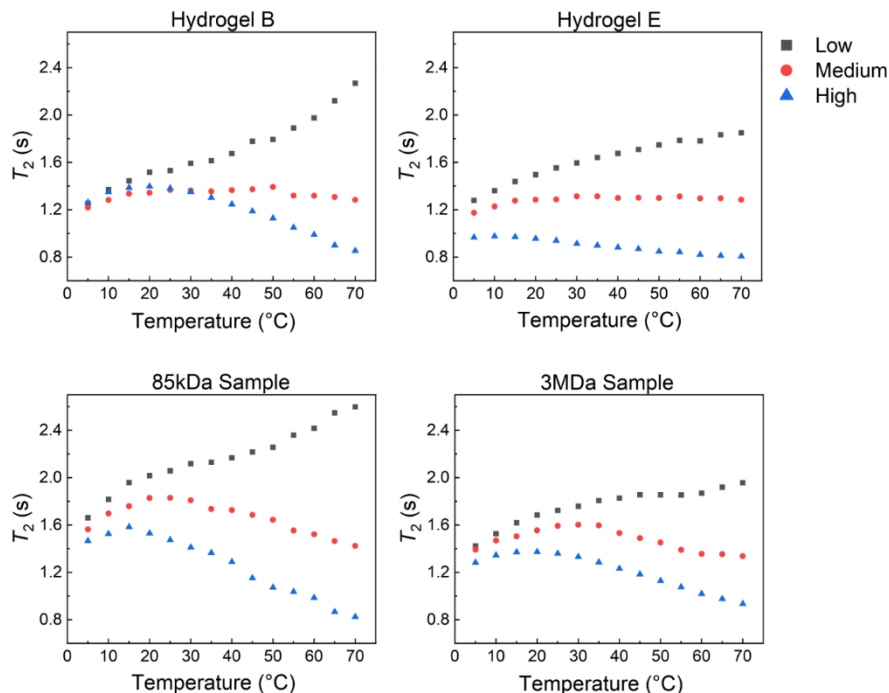


Figure 18. Transverse relaxation (T_2 , s) as a function of temperature for four representative samples at low, medium, and high HA concentrations.

Figure 18 shows the T_2 -temperature profile of four representative samples at different concentrations. The T_2 values of water protons in stronger hydrogels (e.g. hydrogel B) were less affected by concentration changes than those of water protons in weaker hydrogels (e.g. hydrogel E) in the temperature range 5–50 °C. For the native HA solutions, samples with low MW showed larger variations in T_2 for both concentration and temperature changes. In general, T_2 of water protons was more sensitive to temperature changes in the native HA solutions than the HA hydrogels.

Hills *et al.* have demonstrated that when exchangeable protons such as NH and OH are present in hydrogels, T_2 relaxation of water protons is dominated by the chemical exchange process between the exchangeable protons of the polymer and the water protons (Hills *et al.*, 1989; Hills, 1991).

During the chemical exchange process, the molecular spins exchange positions with other spins in the surrounding chemical environment, which can give insights into molecular mobility. Consequently, the presence or absence of exchangeable protons in hydrogels results in different temperature profiles of T_2 relaxation. Studies have shown that T_2 increases monotonically with temperature in hydrogels without exchangeable protons (McConville & Pope, 2001; McConville *et al.*, 2002), while more complex behaviors have been observed for hydrogels with exchangeable protons (McConville & Pope, 2001; Fabri *et al.*, 2005).

Assuming that the observed T_2 in HA samples has contributions from both water protons (T_{2b}) and exchangeable HA protons (T_{2c}): at low temperatures, T_{2c} is short due to the slow exchange rate. Therefore, T_{2b} dominates the observed T_2 , which increases with increasing temperature in a certain range. As the temperature continues to rise, the exchange rate increases and T_{2c} makes a larger contribution to the observed T_2 . Since T_{2c} is still shorter than T_{2b} , the observed T_2 at medium and high concentrations decreases at a specific point with increasing temperature. Meanwhile, because the water content decreases and the proportion of exchangeable HA protons increases at higher concentrations, the exchangeable protons will contribute more and more to the observed T_2 . This could explain why observed T_2 values at low concentrations are much more sensitive to temperature change than those at high concentrations.

The higher the concentration of the sample, the lower the value of T_2 , indicating that the fraction of exchangeable protons increases with HA concentration and that the mobility of exchangeable protons is more restricted at higher concentrations. Exchangeable protons in low-concentration samples and/or weak hydrogels, on the other hand, can be mobile enough to have a high exchange rate with water protons even at low temperatures.

In summary, T_1 and D showed very similar trends for all samples, while the behavior of T_2 was more complex and was dominated by the chemical exchange between water protons and exchangeable protons of HA. Thus T_2 measurements of water protons over a range of temperatures are able to distinguish between samples with different concentrations. In addition, based on the T_2 temperature profiles, some distinctions can be achieved between hydrogels with different physicochemical properties and native solutions.

5.2 Determination of amide *cis/trans* isomers in *N*-acetyl-D-glucosamine: Tailored NMR analysis of the *N*-acetyl group conformation (Paper II)

N-acetylglucosamine (GlcNAc) is a prevalent amino sugar in nature and one of the two monosaccharides constituting the repeating unit of HA. Because the conformation of polysaccharides containing GlcNAc sugars is mainly determined by the geometry of the glycosidic linkage and the conformation of the pyranose ring (Sattelle & Almond, 2011), the *N*-acetyl group and its amide linkage have received little attention. However, the *N*-acetyl group can have varied conformations in aqueous solution depending on its involvement in hydrogen bonds and water bridges, which may also influence the overall geometry of the polysaccharide. Amide linkages can undergo *cis-trans* isomerization (CTI), which is a key determinant of linkage conformation and a critical exchange process in many biological systems, particularly in peptide linkages (Dugave, 2006).

5.2.1 Conformation of the *N*-acetyl group

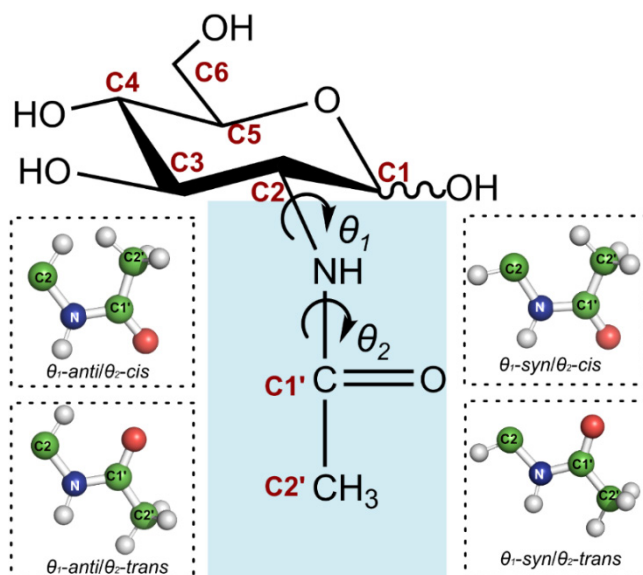


Figure 19. Chemical structure of *N*-acetylglucosamine (GlcNAc) with the two torsion angles θ_1 (H2-C2-N-H) and θ_2 (C2-N-C1'-C2') that define the conformation of the *N*-acetyl group. The four possible isomers of the *N*-acetyl group are shown in the dashed boxes.

The conformation of the *N*-acetyl group in GlcNAc is defined by two torsion angles θ_1 (H2-C2-N-H) and θ_2 (C2-N-C1'-C2'), as shown in Figure 19. The amide linkage that is defined by θ_2 has a partial double bond character and enables *trans* and *cis* conformations, where *trans* is the predominant conformation because it is energetically favored over *cis* (Fischer, 2000). The torsion angle θ_1 defines the C2-N bond geometry, which is more flexible than the amide bond. The relative orientation of H2 and NH enables *anti* and *syn* conformations, where the *anti* conformation is considered to be favored in GlcNAc mono- and polysaccharides (Cowman *et al.*, 1984; Donati *et al.*, 2001; Blundell *et al.*, 2006a; Mobli & Almond, 2007; Hu *et al.*, 2010a). Because the activation energy of the *cis-trans* interconversion is larger than that of the *syn-anti* interconversion, the exchange between the *cis* and *trans* isomers is slow enough for distinct NMR signals to be observed at room temperature, whereas no separate NMR signals of the *syn* and *anti* forms can be observed (Hu *et al.*, 2010b).

5.2.2 First observation of amide *cis* conformation by ¹H NMR

The amide protons of the α - and β -GlcNAc *cis* conformation were observed for the first time by NMR spectroscopy, with each accounting for less than 1% of the sum of the *trans* isomers (Figure 20). In addition, it was possible to assign other chemical shifts arising from the low-abundance *cis* form by utilizing the amide proton in a series of NMR experiments on uniformly labeled ¹³C,¹⁵N GlcNAc and unlabeled GlcNAc (Table 2).

Table 2. ¹H, ¹³C and ¹⁵N chemical shifts (ppm) that are sensitive to the amide *trans* and *cis* forms of α - and β -GlcNAc^[a]

	NH N	H1 C1	H2 C2	H3 C3	C1'	H2' C2'
<i>α-trans</i>	8.10 123.6	5.20 93.6	3.86 56.9	3.75 73.5		2.04 24.7
<i>α-cis</i>	7.12 123.5	5.26 94.3	3.58 60.7	3.74 74.1	177.3 179.5	2.03 22.6
<i>β-trans</i>	8.19 122.9	4.70 97.7	3.66 59.5	3.52 76.7		2.04 24.9
<i>β-cis</i>	7.53 124.3	4.70 97.9	3.30 64.0	3.47 77.1	180.4	2.03 23.0

[a] In 90% H₂O/10% D₂O at 25 °C; Chemical shifts relative to external DSS-*d*₆; ¹H and/or ¹³C chemical shifts of C4, C5 and C6 on the pyranose ring were not determined for their amide *cis* forms.

The chemical shifts of the different GlcNAc forms were influenced by both the α/β anomeric configuration and the *cis/trans* conformation (Table 2). The chemical shifts of the amide proton signals were the most affected, with the *cis* forms shifted upfield (up to 1.0 ppm) relative to the *trans* form with the same anomeric configuration. Similarly, the H2 signal was shifted upfield (0.3–0.4 ppm) in the *cis* form compared with the *trans* form. The NH and H2 protons are both close to the exocyclic carbonyl group and are most likely affected by the shielding anisotropy of the carbonyl bond. The amide proton is perpendicular to the carbonyl double bond in the *cis* conformation, which makes it more shielded than the *trans* form and causes an upfield shift. The most affected carbon chemical shift in the *cis* forms was that of C2 (up to 4.5 ppm) compared with the *trans* form. The chemical shifts of the carbons in the *N*-acetyl group C1' and C2' were more affected than C1 and C3 in the pyranose rings. There was no significant difference between the ^{15}N chemical shifts of the α -*cis* and α -*trans* forms, while the ^{15}N chemical shift of β -*cis* was more downfield than that of β -*trans*.

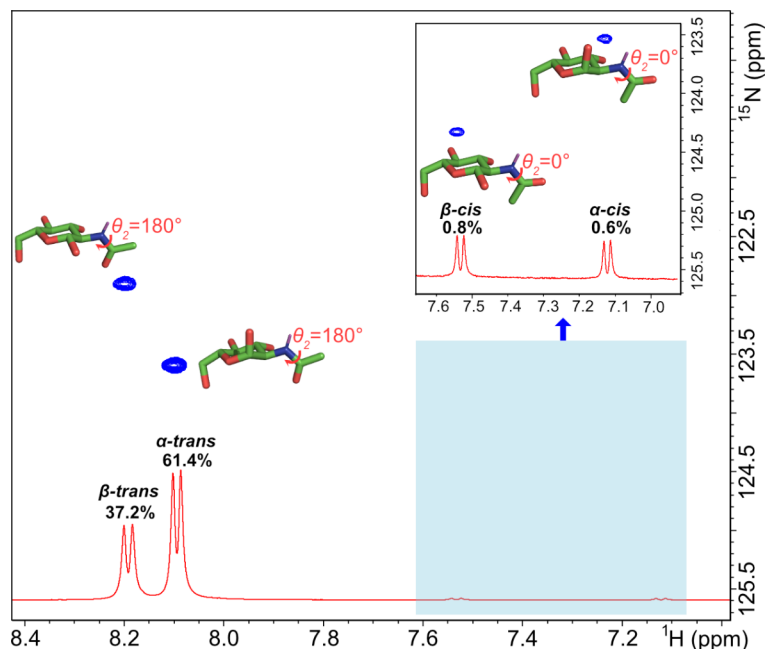


Figure 20. Selected region of 2D-[^1H , ^{15}N]-HSQC and 1D ^1H spectra of GlcNAc at 25 °C. Amide protons of α - and β -GlcNAc in the *cis* forms are highlighted and shown in the inset. The conformations of *trans* and *cis* isomers, with their corresponding anomeric configurations and relative percentages, are illustrated.

5.2.3 Tailored NMR experiments for GlcNAc conformation analysis

GlcNAc resembles the protein backbone with an amide function and with C α and C β replaced by C2 and C3, while C $_i$, C $_{i-1}$ and C α_{i-1} are replaced by GlcNAc C1, C1' and C2', respectively (Figure 21). The protein backbone angles φ and ω are replaced by the torsion angles θ_1 and θ_2 . Therefore, it was possible to employ modified versions of exclusive correlation spectroscopy (E.COSY) and J -quantitative protein NMR experiments to uniformly labeled ^{13}C , ^{15}N GlcNAc to measure eight 3J -couplings that are sensitive to the torsion angles θ_1 and θ_2 . Six 3J -couplings through the C2-N bond ($^3J_{\text{NH},\text{H}2}$, $^3J_{\text{NH},\text{C}1}$, $^3J_{\text{NH},\text{C}3}$, $^3J_{\text{H}2,\text{C}1'}$, $^3J_{\text{C}1,\text{C}1'}$ and $^3J_{\text{C}3,\text{C}1'}$) are sensitive to the θ_1 torsion angle, while two 3J -couplings through the N-C1' bond ($^3J_{\text{NH},\text{C}2'}$ and $^3J_{\text{C}2,\text{C}2'}$) are sensitive to the θ_2 torsion angle.

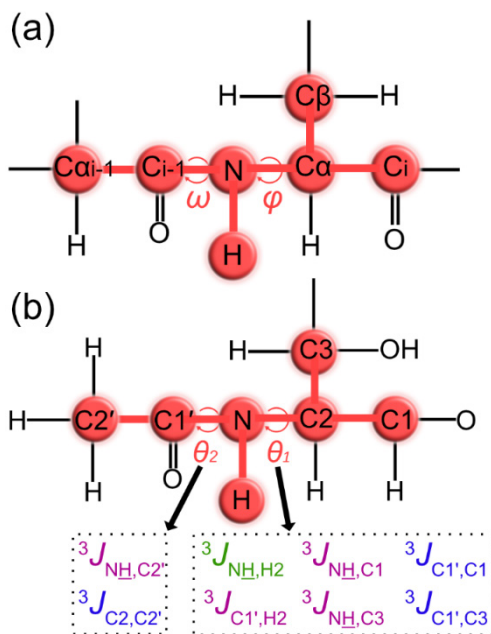


Figure 21. Comparison between (a) the protein backbone and (b) the *N*-acetyl group; Eight 3J -couplings associated with torsion angle θ_1 and θ_2 were measured by adapting protein NMR experiments.

5.2.4 3J -couplings sensitive to the θ_1 angle (H2-C2-N-NH)

$^3J_{\text{NH},\text{H}2}$ is the most commonly used coupling constant for assessing the conformation of the *N*-acetyl group and the generally held assumption is that

the *anti* conformation is more stable than the *syn* conformation in GlcNAc (Cowman *et al.*, 1984; Donati *et al.*, 2001; Blundell *et al.*, 2006a; Mobli & Almond, 2007; Hu *et al.*, 2010a). From the modified HNCA[HA]-E.COSY experiment, the $^3J_{\text{NH,H2}}$ value was measured to be 8.8 Hz for the α -*trans* form and 9.5 Hz for the β -*trans* form (Figure 22a). The *cis* forms of GlcNAc were also observed, despite the low intensity of the signals, and the $^3J_{\text{NH,H2}}$ value was determined to be 10.6 Hz for the α -*cis* form and 10.2 Hz for the β -*cis* form (Figure 22b). These results are in good agreement with previous findings on *N*-formyl substituted sugars in their *trans* and *cis* forms in DMSO- d_6 (Hu *et al.*, 2010b).

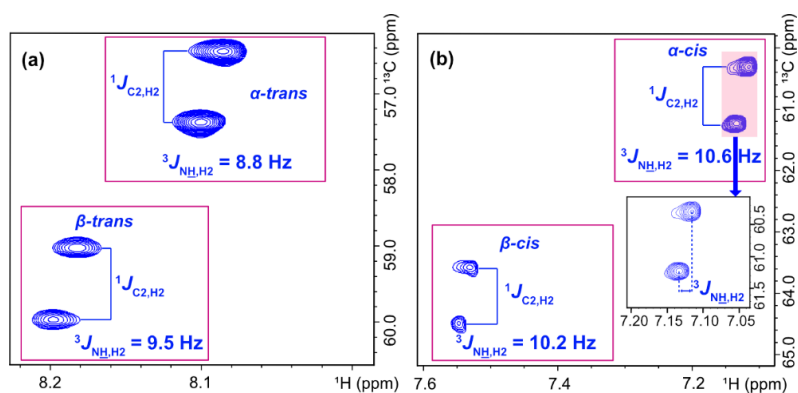


Figure 22. Selected regions of E.COSY spectra used to measure $^3J_{\text{NH,H2}}$ of (a) *trans* and (b) *cis* forms of the *N*-acetyl group with ^{15}N decoupling.

Parametrized Karplus equations for $^3J_{\text{NH,H2}}$ in GlcNAc model structures show maxima at 0° and 180° , corresponding to θ_1 -*syn* and θ_1 -*anti*, respectively (Hu *et al.*, 2010a). By calculating the difference between the experimental values of $^3J_{\text{NH,H2}}$ and values from the parametrized Karplus equations over the entire range of torsion angles, a minimization plot where the global minimum corresponds to the most probable torsion angle was generated (Figure 23a). However, the use of $^3J_{\text{NH,H2}}$ alone to distinguish between *syn* and *anti* forms was limited, since minima for all four forms were observed in both regions, *i.e.* near 0° and $\pm 180^\circ$. Therefore, five additional 3J -couplings that are sensitive to torsion angle θ_1 were measured, as shown in Table 3.

Table 3. 3J -coupling constants (Hz) that are sensitive to the torsion angle θ_1 in α - and β -GlcNAc ^[a]

	${}^3J_{\text{NH,H2}}$	${}^3J_{\text{H2,C1}'}$	${}^3J_{\text{NH,C1}}$	${}^3J_{\text{NH,C3}}$	${}^3J_{\text{C1,C1}'}$	${}^3J_{\text{C3,C1}'}$
<i>α-trans</i>	8.8 ± 0.1	2.8 ± 0.1	0.4 ± 0.1	0.9 ± 0.1	1.0 ± 0.1	1.4 ± 0.1
<i>α-cis</i>	10.6 ± 0.2	3.3 ± 0.1	0.7 ± 0.1	0.7 ± 0.1	1.6 ± 0.1	obs. ^[b]
<i>β-trans</i>	9.5 ± 0.1	3.4 ± 0.1	0.6 ± 0.1	0.8 ± 0.1	1.0 ± 0.2	1.0 ± 0.1
<i>β-cis</i>	10.2 ± 0.3	2.6 ± 0.2	0.7 ± 0.1	0.9 ± 0.2	obs. ^[b]	obs. ^[b]

[a] At 25 °C in 90% H₂O/10% D₂O. Data presented are from at least three measurements \pm one standard deviation; [b] Obscured signals.

The difference between each measured 3J -couplings and the values from the corresponding parametrized Karplus equations were first calculated. Then the six 3J -couplings were adjusted to the common torsion angle θ_1 and root mean square deviation (RMSD) of the full set of coupling constants was calculated over the entire range of torsion angles (Figure 23b). The global minimum was found in the region from 168° to 180° (*anti* conformation), more specifically *α -trans* at $(+170 \pm 10)^\circ$, *β -trans* at $(+178 \pm 6)^\circ$, *α -cis* at $(180 \pm 10)^\circ$ and *β -cis* at $(+168 \pm 19)^\circ$. Local minima were found in the region near 0° (*syn* conformation), but with relatively larger RMSD.

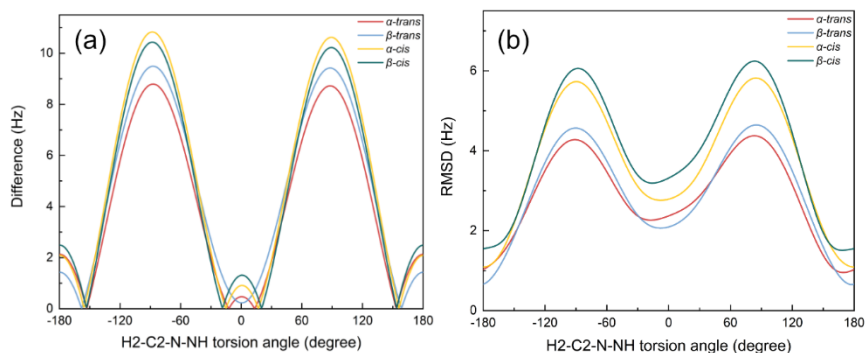


Figure 23. (a) Difference between the experimental values of ${}^3J_{\text{NH,H2}}$ and calculated values from the Karplus equations and (b) RMSD versus H2-C2-N-NH torsion angle using all six coupling constants that are sensitive to θ_1 .

These data are consistent with previous findings based on 3J -coupling measurements and MD simulations of GlcNAc in the *trans* forms that the θ_1 angle lies in the region $+160^\circ$ to 180° (Mobli & Almond, 2007; Hu *et al.*, 2010a; Sattelle & Almond, 2011). A two-state model was also generated and no major contribution of the *syn* conformation was found, except for the *β -trans* form where 2% of θ_1 -*syn* conformation was predicted.

5.2.5 3J -couplings sensitive to the θ_2 angle (C2-N-C1'-C2')

The orientation of the amide linkage for the *trans* and *cis* forms was evaluated by measuring two 3J -couplings ($^3J_{\text{NH},\text{C}2'}$ and $^3J_{\text{C}2,\text{C}2'}$) that are sensitive to the θ_2 torsion angle. The values of $^3J_{\text{NH},\text{C}2'}$ showed a clear difference between the *trans* and *cis* forms of GlcNAc, where both the α - and β -*trans* forms exhibited $^3J_{\text{NH},\text{C}2'}$ of 0.9 Hz, while $^3J_{\text{NH},\text{C}2'}$ was 4.5 Hz for α -*cis* and 4.0 Hz for β -*cis* (Figure 24). Thus, $^3J_{\text{NH},\text{C}2'}$ alone is sufficient to differentiate between *trans* and *cis* amide conformation.

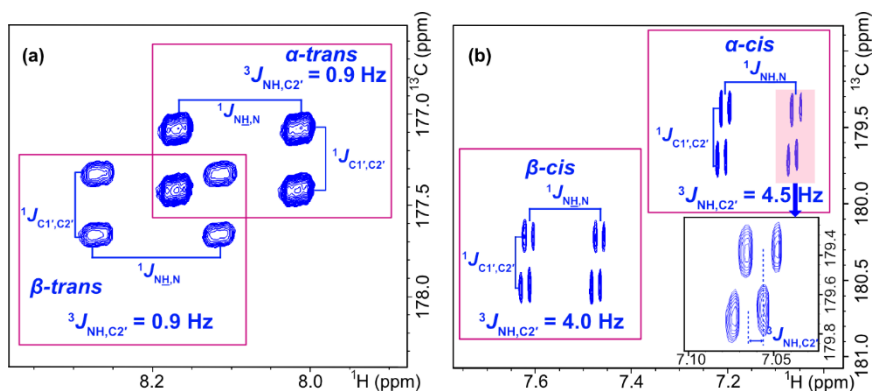


Figure 24. Selected regions of E.COSY spectra used to measure $^3J_{\text{NH},\text{C}2'}$ of (a) *trans* and (b) *cis* forms of the *N*-acetyl group without ^{15}N decoupling.

The values of $^3J_{\text{C}2,\text{C}2'}$ were determined to be 1.4 and 1.7 Hz for α - and β -*trans* forms, respectively (Table 4). However, the magnitude for *cis* forms was below the detection limit (<0.5 Hz). Parametrized Karplus equations have shown that $^3J_{\text{C}2,\text{C}2'}$ is affected by both θ_1 and θ_2 torsion angles, where *trans* forms are predicted to be 1.5 Hz in θ_1 -*anti* and 3.3 Hz in θ_1 -*syn*, whereas *cis* forms are predicted to be close to 0 Hz in both *syn* and *anti* conformations (Hu *et al.*, 2010a).

In a similar way, the differences between the two coupling constants and the values from the corresponding parametrized Karplus equations were calculated and adjusted to the torsion angle θ_2 . The RMSD plots of the θ_2 torsion angle showed global minima located as expected, *i.e.* close to 180° for the *trans* forms and close to 0° for the *cis* forms (Figure 25). More specifically, the minima of the *trans* forms were found at $\pm 172^\circ$. However, since the *cis* forms of $^3J_{\text{C}2,\text{C}2'}$ were set to 0 Hz (<0.5 Hz from experiments), the exact torsion angles could not be measured accurately due to broad minima near 0° . Although $^3J_{\text{NH},\text{C}2'}$ is sufficient to differentiate between *trans*

and *cis* amide conformation, both ${}^3J_{\text{NH},\text{C}2'}$ and ${}^3J_{\text{C}2,\text{C}2'}$ are necessary for detailed determination of the θ_2 torsion angle.

Table 4. 3J -coupling constants (Hz) that are sensitive to the torsion angle θ_2 in α - and β -GlcNAc ^[a]

	${}^3J_{\text{NH},\text{C}2'}$	${}^3J_{\text{C}2,\text{C}2'}$
<i>α-trans</i>	0.9 ± 0.1	1.4 ± 0.1
<i>α-cis</i>	4.5 ± 0.1	<0.5 ^[b]
<i>β-trans</i>	0.9 ± 0.1	1.7 ± 0.1
<i>β-cis</i>	4.0 ± 0.1	<0.5 ^[b]

[a] At 25 °C in 90% H₂O/10% D₂O. Data presented are from at least three measurements \pm one standard deviation; [b] Below the detection limit.

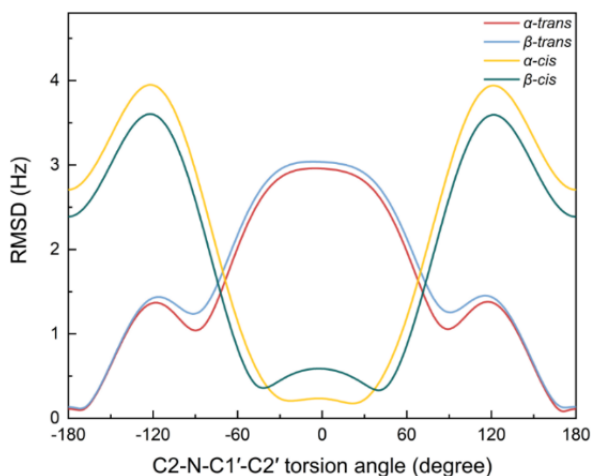


Figure 25. RMSD versus C2-N-C1'-C2' torsion angle using ${}^3J_{\text{NH},\text{C}2'}$ and ${}^3J_{\text{C}2,\text{C}2'}$ that are sensitive to θ_2 .

In summary, the first identification of NH protons of the amide *cis* forms of α - and β -GlcNAc was achieved by NMR spectroscopy. In comparison with the *trans* forms, the *cis* amide protons were distinguished by upfield chemical shifts and each of the *cis* forms accounted for less than 1% of the total. Modified protein NMR experiments were used to measure eight 3J -couplings that are sensitive to the torsion angles θ_1 and θ_2 of the *N*-acetyl group. θ_1 -*anti* and θ_2 -*trans* were determined to be the predominant conformations of GlcNAc. The use of ${}^3J_{\text{NH},\text{H}2}$ alone to distinguish *syn* and *anti* conformations of the torsion angles θ_1 proved to be limited and therefore an additional five 3J -coupling constants are required for detailed analysis. On the other hand, the orientation of the amide linkage could be distinguished

between *cis* and *trans* by one 3J -coupling constant, $^3J_{\text{NH},\text{C}2}$. This study provides tools for future conformational analysis of GlcNAc sugars in larger biomolecules such as polysaccharides and glycoproteins.

5.3 Solution conformational analysis of hyaluronan with different chain lengths by NMR spectroscopy (Paper III)

The preceding section presented a thorough investigation into the conformation of the *N*-acetyl group in the GlcNAc monosaccharide. However, when examining HA chains, the principal source of structural flexibility arises from the two glycosidic linkages, which are defined by the two torsion angles φ and ψ (Figure 26). This study aimed to investigate conformational differences between two HA chain lengths: HA-8mer and HA-20mer. To achieve this, a series of NMR experiments was conducted to assess NOEs and 3J -couplings of the $\beta(1\rightarrow3)$ and $\beta(1\rightarrow4)$ glycosidic linkages, and of the *N*-acetyl group.

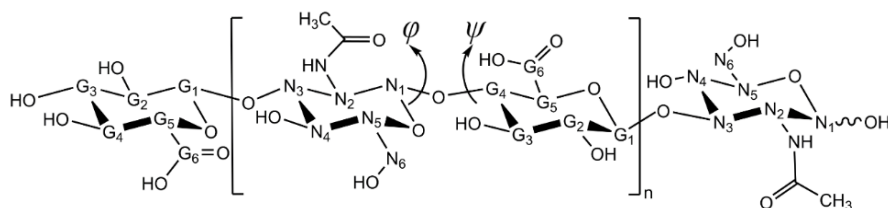


Figure 26. Schematic structure of HA oligomers: HA-8mer ($n = 3$) and HA-20mer ($n = 9$). Two torsion angles φ and ψ are shown over the $\beta(1\rightarrow4)$ glycosidic linkage between GlcNAc and GlcA. The monosaccharide residues within the chain are abbreviated N_x (GlcNAc $_x$) and G_x (GlcA $_x$) where x indicates the carbon position on the pyranosyl ring. The glycosidic linkage was defined by two dihedral angles, φ ($\text{H}_1\text{-C}_1\text{-O}_y\text{-C}_y$) and ψ ($\text{C}_1\text{-O}_y\text{-C}_y\text{-H}_y$), where y depends on the linkage ($1\rightarrow3$ or $1\rightarrow4$).

5.3.1 Experimental interproton distances and 3J -couplings

2D- $^1\text{H}, ^1\text{H}$ -NOESY spectra only provide limited information on conformation, due to the severe overlap of proton signals from medium-sized sugar molecules. Therefore 2D- $^1\text{H}, ^{13}\text{C}$ -HSQC-NOESY experiments were performed to alleviate signal overlap by exploiting the high dispersion in the ^{13}C dimension. Important inter-residue NOE cross-peaks of HA that convey conformational information appeared to be well separated in the ^{13}C

dimension (Figure 27). In particular, cross-peaks with similar proton chemical shifts (such as N₃/G₄/G₅) were well separated in the ¹³C dimension. Thus NOE cross-peaks can be used directly to determine the inter-proton distance, without subtraction of overlapping cross-peaks.

The [¹H,¹³C]-HSQC-NOESY spectra were recorded with a series of mixing times (20–300 ms, 8–10 spectra). The interproton distances associated with the glycosidic linkages and the *N*-acetyl group were calculated from the slope of the initial buildup rate. In addition, several ³J_{HH} and ³J_{CH} were obtained from 1D ¹H NMR and heteronuclear long-range *J*-HMBC spectra, respectively. The detailed conformation of the glycosidic linkages and the acetamido group were analyzed and compared between the two HA chain lengths.

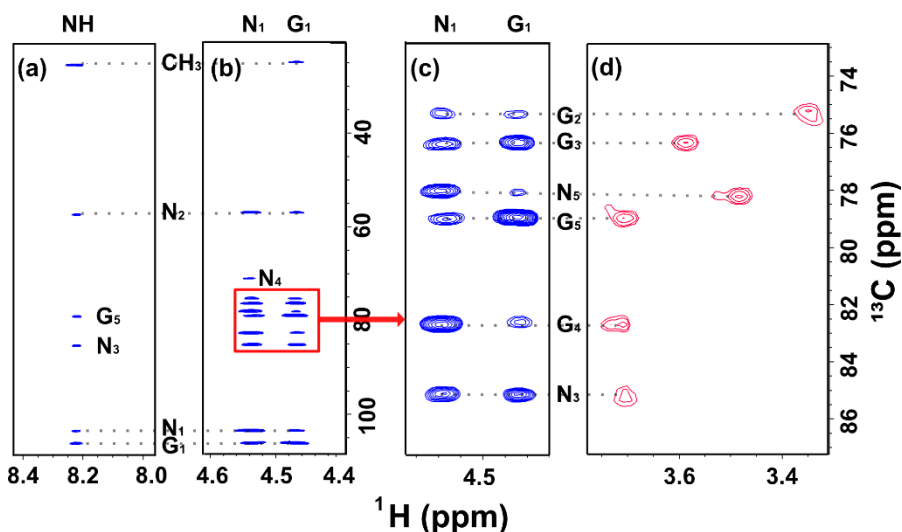


Figure 27. Selected regions of 2D NMR spectra for the interior residues of HA-20mer (8 mM) in 90% H₂O/10% D₂O at 5 °C: (a) GlcNAc amide proton region, (b, c) anomeric proton region of [¹H,¹³C]-HSQC-NOESY spectrum (mixing time (τ_m) = 0.3 s) and (d) corresponding cross-peaks in the [¹H,¹³C]-HSQC spectrum.

5.3.2 Conformation of the acetamido group

As mentioned in Section 5.2, the H2-C2-N-NH torsion angle (torsion angle θ_1) of the acetamido group is generally considered to be in the *anti* conformation in GlcNAc monosaccharide and in longer HA chains (Donati *et al.*, 2001; Blundell *et al.*, 2006a; Mobli & Almond, 2007; Hu *et al.*, 2010a). As shown in Figure 27a, most of the strong NOE cross-peaks to NH were

found to originate from the neighboring positions in GlcNAc (N_1 , N_2 and N_3). Together with two 3J -couplings ($^3J_{\text{NH-H}_2}$ and $^3J_{\text{H}_2\text{-CO}}$) that are sensitive to the θ_1 torsion angle, the five sets of experimental data were used to determine the geometry of the acetamido group in HA-8mer and HA-20mer (Table 5).

The absolute differences between experimental data and calculated distances and 3J -couplings from a model structure of HA-8mer (Protein Data Bank (PDB) accession code: 2BVK) and parameterized Karplus equations (Hu *et al.*, 2010a) were used to obtain RMSDs across the entire torsion angle range. Minimization plots were generated, where the global minimum corresponded to the most probable value of the torsion angle θ_1 (Figure 28). The global minima for HA-8mer and HA-20mer were found at $(165 \pm 5)^\circ$ and $(-167 \pm 10)^\circ$, respectively, which represents the average structure and is close to 180° , equivalent to a clear *anti* conformation. Thus, the orientation of the *N*-acetyl group was similar in HA-8mer and HA-20mer, which is consistent with earlier conclusions in NMR studies on HA oligo- and polysaccharides (Cowman *et al.*, 1984; Donati *et al.*, 2001; Blundell *et al.*, 2006a; Mobli & Almond, 2007).

Table 5. Interproton distances (\AA) and 3J -couplings (Hz) that are sensitive to torsion angle θ_1

		NH- N_1	NH- N_2	NH- N_3	$^3J_{\text{NH-H}_2}$	$^3J_{\text{H}_2\text{-CO}}$
Expt.	HA-8mer ^[a]	2.8±0.1	2.9±0.1	2.6±0.1	10.4±0.1	3.6±0.3 ^[b]
	HA-20mer ^[a]	2.7±0.1	3.0±0.1	2.8±0.1	10.1±0.1	2.8±0.3 ^[c]
Calc.	HA-8mer ^[d]	2.7	3.0	2.4	10.2	3.6
	HA-20mer ^[d]	2.5	3.0	2.6	10.4	3.7

[a] At 5 °C in 90% H₂O/10% D₂O; [b] At 5 °C in D₂O; [c] At 25 °C in D₂O; [d] Calculated interproton distances from the model structure and coupling constants from the parameterized Karplus equations after adjusting the torsion angle θ_1 to the global minimum.

The calculated interproton distances and 3J -couplings of HA-8mer and HA-20mer to their respective global minima are also listed in Table 5. The experimental data were in good agreement with the calculated values, and the only clear difference between experimental and calculated data was observed for $^3J_{\text{H}_2\text{-CO}}$ of HA-20mer (2.8 Hz from NMR data, 3.7 Hz from the parametrized equation). However, the parametrized Karplus equation was derived from the GlcNAc monosaccharide with an implicit water model, which may not accurately mimic real water-solute interactions (Hu *et al.*, 2010a). The glycosidic linkages on GlcNAc C₁ and C₃, dynamics of the

GlcNAc ring and the nearby sodium ion could all have affected the magnitude of the coupling constant compared with the calculated value.

The torsion angle corresponding to the global minimum for each condition was applied in subsequent glycosidic linkage calculations to ensure that the differences from the acetamide group were included.

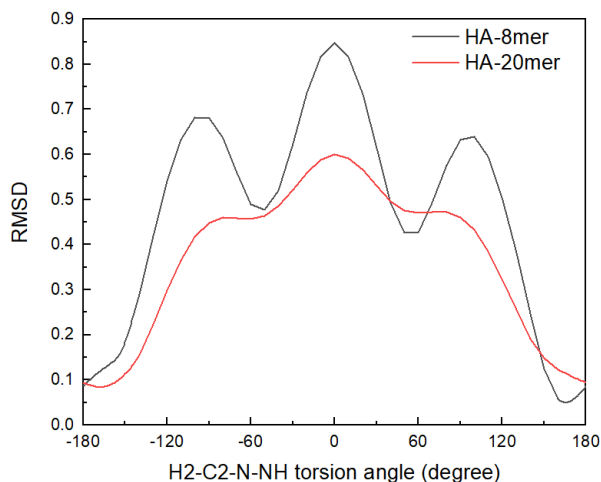


Figure 28. RMSD versus H2-C2-N-NH torsion angle.

5.3.3 Conformation of the $\beta(1\rightarrow3)$ glycosidic linkage

Three interproton distances (G_1-N_2 , G_1-N_3 , G_1-NH) and one *trans*-glycosidic coupling constant (${}^3J_{N(C3)-G(H1)}$) were obtained from NMR experiments to investigate the conformation of the $\beta(1\rightarrow3)$ glycosidic linkage (Table 6). In addition, two NOEs (G_1-N_4 and G_2-N_2) were added as constraints and their distances were set to be longer than 4 Å, as they did not show any NOE correlation in the HSQC-NOESY spectra.

Table 6. Interproton distances (Å) and *trans*-glycosidic 3J -coupling (Hz) that are sensitive to the $\beta(1\rightarrow3)$ glycosidic linkage

		G_1-N_3	G_1-N_2	G_1-NH	G_1-N_4	G_2-N_2	${}^3J_{N(C3)-G(H1)}$
Expt.	HA-8mer	$2.5\pm 0.1^{[a]}$	$3.4\pm 0.1^{[a]}$	$2.6\pm 0.1^{[a]}$	$>4^{[e]}$	$>4^{[e]}$	$3.9\pm 0.5^{[c]}$
	HA-20mer	$2.7\pm 0.1^{[a]}$	$3.1\pm 0.1^{[a]}$	$2.5\pm 0.1^{[b]}$	$>4^{[e]}$	$>4^{[e]}$	$3.3\pm 0.4^{[d]}$
Calc.	HA-8mer ^[f]	2.3	3.7	2.5	4.4	4.8	3.4
	HA-20mer ^[f]	2.7	3.1	2.5	4.4	4.8	3.4

[a] At 5 °C in 90% H₂O/10% D₂O and D₂O; [b] At 5 °C in 90% H₂O/10% D₂O; [c] At 5 °C in D₂O; [d] At 25 °C in D₂O; [e] Distances were set to be longer than 4 Å; [f] Calculated interproton distances from the model structure and coupling constants from the parameterized Karplus equations after adjusting the torsion angles ϕ and ψ to the global minima.

As done for the torsion angle θ_i , the experimental results (Table 6) were compared with distances and 3J -couplings obtained from the model structure and the parameterized Karplus equation (Säwén *et al.*, 2010). RMSDs between experimental and modeled data were calculated based on five interproton distances and one 3J -coupling, and minimization diagrams were plotted as shown in Figure 29.

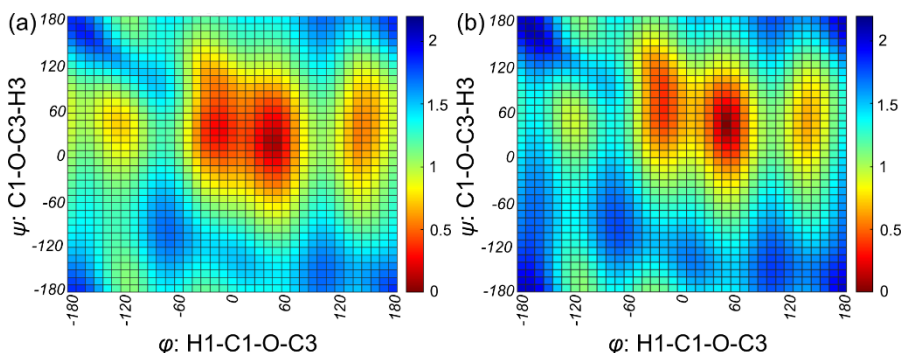


Figure 29. Conformational heatmaps showing the (φ, ψ) distribution with $10^\circ \times 10^\circ$ bins of the $\beta(1 \rightarrow 3)$ glycosidic linkage of (a) HA-8mer and (b) HA-20mer. Colors indicate RMSD value, ranging from highest (blue) to lowest (red).

The global minimum of $(\varphi_{13}, \psi_{13})$, corresponding to the smallest deviation between the experimental NMR data and the computed model, was located at $((50 \pm 10)^\circ, (10 \pm 10)^\circ)$ for HA-8mer (Figure 29a). This value is very close to the MD simulation results within HA-4mer and HA-6mer reported by Almond *et al.* (2006), with average $(\varphi_{13}, \psi_{13})$ angles of $(50.7^\circ, 9.7^\circ)$. Previous simulations gave generally consistent values of φ_{13} , typically between 46° and 52° , but values of ψ_{13} displayed significant variation, spanning from -10° to 25° (Holmbeck *et al.*, 1994; Kaufmann *et al.*, 1998; Donati *et al.*, 2001; Almond *et al.*, 2006; Taweechat *et al.*, 2020; Whitmore *et al.* 2020). The results in this study were based entirely on experimental data and provided experimental support for the $\beta(1 \rightarrow 3)$ conformation previously established by MD simulations.

In HA-20mer, the conformation of the glycosidic linkages was slightly altered, with $(\varphi_{13}, \psi_{13})$ angles of $((50 \pm 10)^\circ, (40 \pm 10)^\circ)$, as shown in Figure 29b. The theoretical and experimental values agreed very well, where the values of HA-20mer were almost identical. This consistency supports the presence of a predominant conformation observed in the $\beta(1 \rightarrow 3)$ glycosidic linkage.

5.3.4 Conformation of the $\beta(1\rightarrow4)$ glycosidic linkage

Three interproton distances (N_1-G_4 , N_1-G_3 , N_1-G_5) and one *trans*-glycosidic coupling constant (${}^3J_{G(C4)-N(H1)}$) obtained in NMR analysis were used to investigate the conformation of the $\beta(1\rightarrow4)$ glycosidic linkage (Table 7). The short N_1-G_4 distances obtained from HA-8mer and HA-20mer, which were equivalent to the expected *syn* conformation over the glycosidic linkage, were almost identical to the distance in the previous MD model (Almond *et al.*, 2006). However, the N_1-G_3 and N_1-G_5 distances obtained from HA-8mer and HA-20mer, respectively, were much shorter than predicted by the model. After repeating previous procedures, including the calculation of RMSD and global minima of $(\varphi_{14}, \psi_{14})$, it was observed that the theoretical and experimental values did not match when adjusting the $(\varphi_{14}, \psi_{14})$ torsion angles to the respective global minima. The lack of consistency between the theoretical and experimental values suggests that the experimental data do not support the presence of one predominant conformation of the $\beta(1\rightarrow4)$ glycosidic linkage. Instead, it suggests that two or more different conformations co-exist over the $\beta(1\rightarrow4)$ glycosidic linkage.

Table 7. Interproton distances (\AA) and *trans*-glycosidic 3J -coupling (Hz) that are sensitive to the $\beta(1\rightarrow4)$ glycosidic linkage

		N_1-G_4	N_1-G_3	N_1-G_5	${}^3J_{G(C4)-N(H1)}$
Expt.	HA-8mer	2.2±0.1 ^[a]	2.8±0.1 ^[a]	abs.	3.2±0.5 ^[c]
	HA-20mer	2.4±0.1 ^[a]	2.7±0.1 ^[b]	2.8±0.2 ^[b]	n.d.
Calc.	HA-8mer	2.3 ^[d]	4.4 ^[d]	3.9 ^[d]	3.6 ^[e]

[a] At 5 °C in 90% H₂O/10% D₂O and D₂O; [b] At 5 °C and 25 °C in 90% H₂O/10% D₂O and D₂O; [c] At 5 °C in D₂O; [d] Interproton distances from the model structure; [e] Calculated coupling constant from the parameterized Karplus equation based on the model structure $(\varphi_{14}, \psi_{14}) = (47.9^\circ, 8.0^\circ)$; abs. = absence; n.d. = not determined.

To explore the correlation between the experimental data and various conformations, conformations derived from MD simulations conducted by Whitmore *et al.* (2020) on HA-20mer were used. Their study assessed the $\beta(1\rightarrow4)$ glycosidic linkage based on Gibbs free energy ΔG (φ_{14}, ψ_{14}) minima and revealed one global minimum (conformation I: $\Delta G = 0$ kcal/mol) and two additional local minima (conformation II: $\Delta G = 1.31$ kcal/mol and conformation II': $\Delta G = 1.42$ kcal/mol). The global minimum conformation I (φ_{14}, ψ_{14}) = (50.0°, -3.1°; *syn* conformation) is similar to the MD simulation data reported by Almond *et al.* (2006), with average $(\varphi_{14}, \psi_{14})$ angles of (47.9°, 8.0°). The two minor conformations, II and II', were located at $(\varphi_{14},$

$\psi_{14}) = (35.0^\circ, 167.0^\circ)$ and $(\varphi_{14}, \psi_{14}) = (60.0^\circ, -153.1^\circ)$, respectively, both defined as *anti* conformations. The calculated interproton distances and 3J -coupling constant based on each of these conformations are presented in Table 8. Comparison of these three sets of values with the NMR data further confirmed the existence of an equilibrium between major and minor conformations across the $\beta(1\rightarrow4)$ glycosidic linkage. The expected ratio between the conformations at 5 °C was calculated based on the reported ΔG of each conformation and was determined to be 83%, 9% and 8%, respectively. The ratio of each conformation was taken into account by calculating the weighted interproton distances and 3J -coupling constant (Table 8). The calculated interproton distances showed a maximum deviation of 0.2 Å from the experimental data for HA-20mer (Table 7), suggesting that the experimental results were in good agreement with this distribution of conformations.

Table 8. Three minimal conformations from MD simulations (Whitmore et al., 2020) and two weighted ratios, along with their corresponding interproton distances (Å) and 3J -couplings (Hz)

Conformation	Percentage (%)			N ₁ -G ₄	N ₁ -G ₃	N ₁ -G ₅	$^3J_{G(C4)-N(H1)}$
	I	II	II'				
MD simulation ^[a]	100	0	0	2.2	4.4	4.0	3.4
	0	100	0	3.6	1.9	2.1	4.8
	0	0	100	3.4	1.8	3.5	2.3
Weighted calculation	83	9	8	2.3	2.5	3.0	3.4
	92	0	8	2.2	2.8	4.0	3.3

[a] In the MD simulation, the dihedrals were defined as φ (O₅-C₁-O₄-C₄) and ψ (C₁-O₄-C₄-C₃). For conversion to our definition, φ (H₁-C₁-O₄-C₄) = φ (O₅-C₁-O₄-C₄) + 118.7° and ψ (C₁-O₄-C₄-H₄) = ψ (C₁-O₄-C₄-C₃) - 119.3°.

By adjusting the distribution of the three conformations, a ratio that best fitted the HA-8mer experimental data was found. This ratio consisted of 92% of conformation I and 8% of conformation II', where the calculated interproton distances and 3J -couplings and the experimental data were almost identical. In addition, the weighted interproton distance of N₁-G₅ was calculated to be 4.0 Å, thus supporting the reason for the absence of N₁-G₅ cross-peaks in the HSQC-NOESY spectra of HA-8mer.

In summary, the NMR data and comparisons with model structures suggested that there was no significant difference in the conformation of the acetamide group in HA-8mer and HA-20mer, and the torsion angle θ_1 of both chain lengths had a clear *anti* conformation. As for the $\beta(1\rightarrow3)$

glycosidic linkage, the NMR data supported the presence of a single predominant conformation for both chain lengths. The global minima of $(\varphi_{13}, \psi_{13})$ for HA-8mer and HA-20mer were found to be located at $((50\pm 10)^\circ, (10\pm 10)^\circ)$ and $((50\pm 10)^\circ, (40\pm 10)^\circ)$, respectively. For the $\beta(1\rightarrow 4)$ glycosidic linkage, NMR and theoretical values did not match with one single conformation, indicating the presence of a conformational equilibrium at this linkage. By employing one *syn* and two *anti* conformations from MD simulations, the major conformation was predicted to be the same for both chain lengths. However, two minor *anti* conformations were equivalent to the NMR data of HA-20mer, accounting for 8% and 9%, respectively. In contrast, only one minor *anti* conformation was predicted from NMR data of HA-8mer, accounting for 8% of the total. Overall, the conformations of HA-8mer and HA-20mer at the glycosidic linkages exhibited subtle differences. This is the first NMR study to provide experimental support for the existence of minor conformations over the $\beta(1\rightarrow 4)$ glycosidic linkage, along with validation of the $\beta(1\rightarrow 3)$ conformation previously established by MD simulations.

5.4 Metabolic labeling of hyaluronan: Biosynthesis and quantitative analysis of ^{13}C , ^{15}N -enriched hyaluronan by NMR and MS-based methods (Paper IV)

A deeper understanding of HA structure at atomic resolution is essential to decipher its diverse biological functions (Dicker *et al.*, 2014; Rayahin *et al.*, 2015). As mentioned in previous chapters, NMR is the method of choice for conformational studies of complex biomolecules, but the sensitivity of heteronuclear NMR experiments is limited due to the low natural abundance of the NMR-active nuclei ^{13}C and ^{15}N . Stable isotope labeling has greatly enhanced the sensitivity of NMR experiments and holds great promise for revealing hidden structural information about glycans and advancing understanding of their various conformations. Almond and his colleagues have reported on the production of ^{15}N isotopically labeled HA oligomers using *E. coli* and have investigated the structure and dynamics of labeled HA using NMR (Blundell *et al.*, 2004; Almond *et al.*, 2005, 2006; Blundell *et al.*, 2006b). However, the use of isotope labeling techniques for determining structural details in carbohydrate research is still limited, and therefore

further exploration of effective methods for biosynthesis and structural analysis of isotopically labeled HA is required.

Streptococcus equi subsp. *zoepidemicus* has a native HA capsule biosynthesis system that does not require modified strains and is therefore widely utilized in various culturing protocols for biotechnological production of HA. Due to its prevalence in biotechnological applications, ease of isolation and relatively high HA yield, *Streptococcus zoepidemicus* was deemed to be the optimal bacterium for the intended isotope labeling approach. In this study, *Streptococcus zoepidemicus* was employed to produce ^{13}C , ^{15}N -labeled HA polysaccharides by using small-scale cultures and media with uniformly labeled ^{13}C -glucose and ^{15}N -glutamine as substrates. The ^{13}C and ^{15}N isotopically enriched HA polymer was further degraded with chondroitinase ABC (ChABC) to produce the disaccharide with an unsaturated uronic acid at the non-reducing end (ΔHA_2) (Figure 30). The isotope distribution and the extent of isotopic incorporation of ^{13}C and ^{15}N in ΔHA_2 were evaluated quantitatively by NMR and MS.

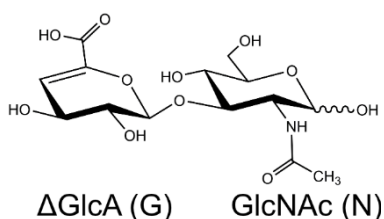


Figure 30. Schematic representation of ΔHA_2 obtained by degradation of HA with chondroitinase ABC (ChABC).

5.4.1 Quantitative 1D ^1H NMR

The characteristic amide proton (δ_{H} 8.0–8.5 ppm) and methyl protons (δ_{H} 1.8–2.1 ppm) of the *N*-acetyl group of GlcNAc and G4 proton (δ_{H} 5.5–6.0 ppm) of ΔGlcA were distinguished from the other overlapping signals in the 1D ^1H spectrum (highlighted in blue in Figure 31). However, signals from protons bound to unlabeled nuclei (*i.e.* ^{12}C and ^{14}N) and labeled nuclei (^{13}C and/or ^{15}N) were observed simultaneously, due to incomplete $^{13}\text{C}/^{15}\text{N}$ incorporation. Therefore, three ^{13}C - or ^{15}N -decoupled ^1H NMR spectra (red spectra in Figure 31a–c) were obtained to differentiate between the ^1H signals of isotopically labeled and unlabeled ΔHA_2 .

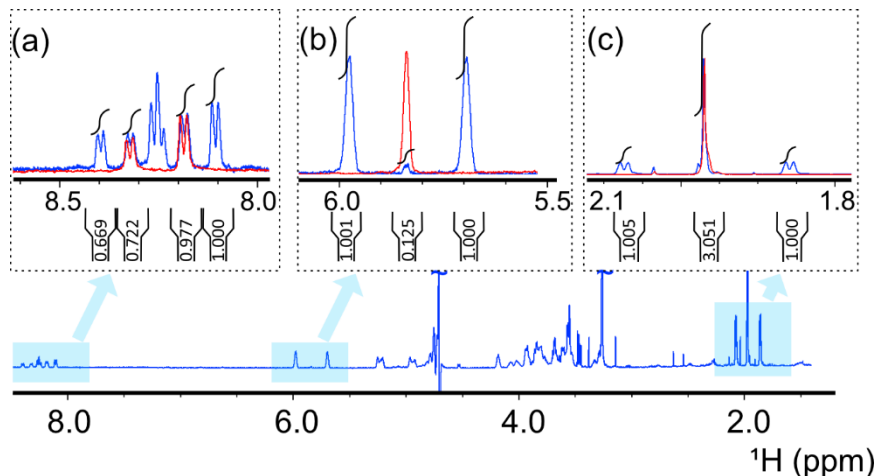


Figure 31. 1D ^1H NOESY pre-saturation spectrum (blue) of ^{13}C , ^{15}N -enriched ΔHA_2 at 25 °C. Highlighted regions in blue correspond to (a) amide protons with ^{15}N decoupling centered at 120 ppm (red), (b) G4 proton with ^{13}C decoupling centered at 110 ppm (red) and (c) methyl protons with ^{13}C decoupling centered at 30 ppm (red). The intensity of decoupled spectra was adjusted to match the NOESY pre-saturation spectrum. Integrals were measured from the NOESY pre-saturation spectrum.

The two doublets at δ_{H} 8.32 ppm and δ_{H} 8.18 ppm in the ^{15}N -decoupled spectrum corresponded to the amide proton of β - and α -GlcNAc, respectively (Figure 31a). In the absence of ^{15}N decoupling, the two doublets split and partially overlapped due to the ^1H - ^{15}N one-bond J -coupling. The signals from the protons bound to ^{14}N without splitting from the ^1H - ^{15}N coupling showed incomplete ^{15}N incorporation at the N -acetyl group. The average level of ^{15}N isotope enrichment estimated by integrating the NH proton signals in the ^1H spectrum without ^{15}N decoupling was found to be 66% using the α anomer and 63% using the β anomer (Table 9). Similarly, the average level of ^{13}C isotope enrichment on G4 was estimated to be 96%. The level of ^{13}C isotope enrichment of the methyl group was determined to be approximately 61% by 1D diffusion experiments (Table 9).

Table 9. Mean level of isotope enrichment (%) of ^{13}C and ^{15}N in ΔHA_2 determined by quantitative ^1H NMR ^[a]

Proton positions		
G4	NH (α/β)	Me
96±2	66±1/63±2	61±2

[a] Data with standard deviation are presented from at least three measurements and D1 was set to 25 s.

5.4.2 Quantitative 1D ^{13}C NMR

The extent of ^{13}C incorporation at each carbon in ΔHA_2 was obtained from quantitative 1D ^{13}C NMR (Figure 32) and the integration values are listed in Table 10. The isotopic purity of ^{13}C was determined to be between 80–100%, depending on the carbon. Given that ^{13}C -labeled glucose serves as the primary source of carbon for GlcA and GlcNAc in the biosynthesis of HA, all carbons in the pyranose rings were expected to have the same amount of ^{13}C enrichment. The discrepancies arising, which were more pronounced for the N2 position, were probably linked in part to a low signal-to-noise ratio (S/N) due to the low concentration of the sample and the subsequent integration errors.

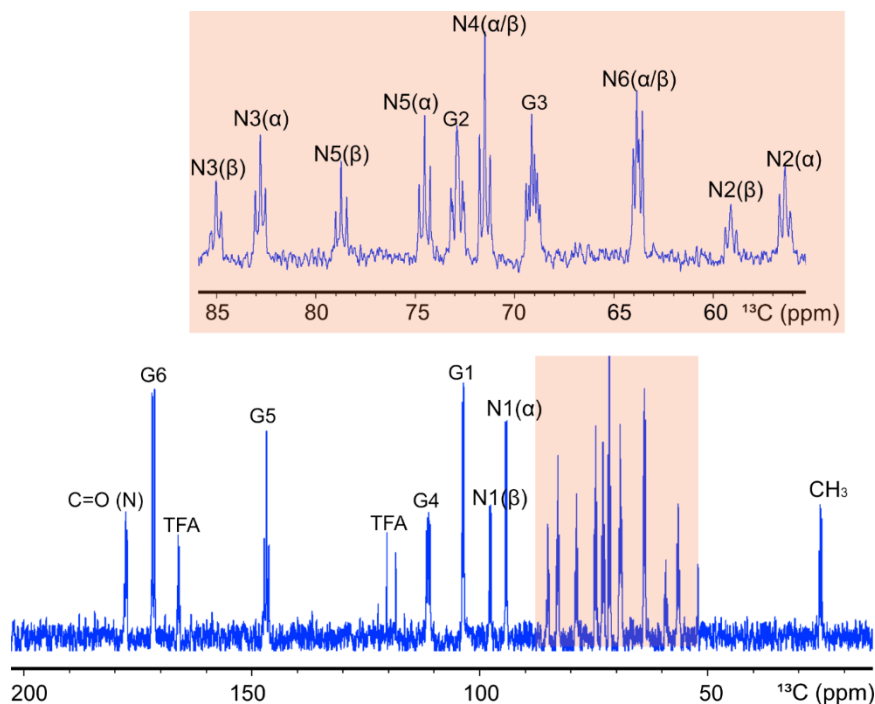


Figure 32. 1D ^{13}C NMR spectrum of $^{13}\text{C},^{15}\text{N}$ -enriched ΔHA_2 at 25 °C. TFA = trifluoroacetic acid.

For the *N*-acetyl group, the level of ^{13}C was determined to be 60–65% for the carbonyl and methyl groups. The good agreement with the level of ^{15}N obtained from quantitative ^1H NMR (65%) suggests possible isotopic dilution during the acetylation process of glucosamine-1-phosphate, leading to incomplete ^{13}C and ^{15}N incorporation (Liu *et al.*, 2011).

Table 10. Mean level of isotope enrichment (%) of ^{13}C at each carbon of ΔHA_2 determined by quantitative ^{13}C NMR ^[a]

	^{13}C isotope enrichment (%) at carbon positions							
	C-1	C-2	C-3	C-4	C-5	C-6	CO	Me
ΔGlcA	100 \pm 10	89 \pm 1	90 \pm 4	97 \pm 8	87 \pm 1	100 ^[b]	/	/
$\text{GlcNAc } (\alpha+\beta)$	90 \pm 10	77 \pm 3	86 \pm 5	83 \pm 1	90 \pm 8	100 \pm 4	59 \pm 1	64 \pm 3

[a] Data with standard deviation are presented from at least two measurements and D1 was set to 25 s; [b] The integration value was set as a reference.

5.4.3 Mass spectrometry analysis

The extent of ^{13}C and ^{15}N isotopic incorporation in ΔHA_2 was also evaluated by ESI-orbitrap-MS. A cluster of peaks of protonated molecular ions ($[\text{M}+\text{H}]^+$) from m/z 395 to 391 was observed in the extracted ion chromatogram (EIC) (Figure 33). The peak at m/z 395.1620 corresponded to $[\text{UL-}^{13}\text{C}_{14}; ^{15}\text{N}]\text{-}\Delta\text{HA}_2$ and the different mass shifts in the nearby regions corresponded to combinations of isotopic variants. By amplifying the mass shift regions (m/z 394, 393, 392 and 391), two peaks with different m/z values were observed at each site (highlighted in blue in Figure 33). The mass difference between the uniformly labeled peak and the remaining peaks was calculated. Subsequently, the isotopologue corresponding to each peak was assigned by comparing the mass differences between ^{15}N and ^{14}N (0.9970 Da) and ^{13}C and ^{12}C (1.0034 Da). The relative percentage of each peak and the assigned isotopologues are listed in Table 11.

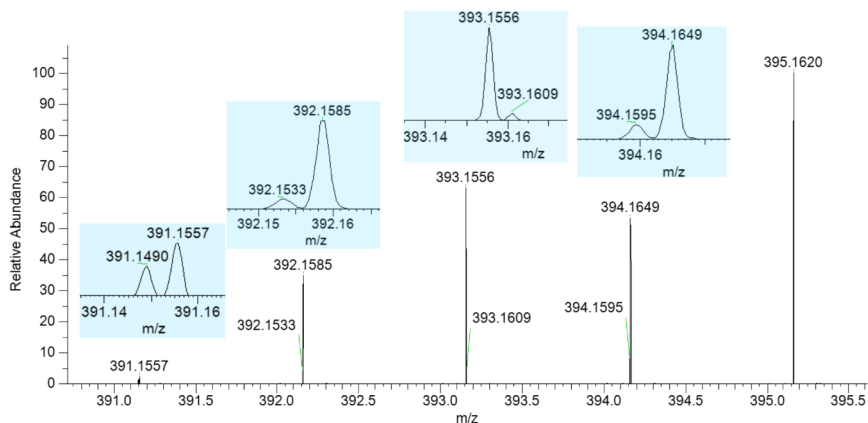


Figure 33. ESI-orbitrap-MS $[\text{M}+\text{H}]^+$ spectrum of $^{13}\text{C},^{15}\text{N}$ -enriched ΔHA_2 ; amplified mass shift regions are shown in the insets.

On adding the two peaks at m/z 395.1620 ($^{13}\text{C}_{14}$; ^{15}N) and m/z 394.1649 ($^{13}\text{C}_{14}$; ^{14}N) together, the percentage of complete ^{13}C incorporation of ΔHA_2 was at least 57.2% ($\geq 37.8\% + 19.4\%$), which is in good agreement with the conclusion from quantitative NMR that the ^{13}C level of isotope enrichment of the *N*-acetyl group was 59–64%. When the percentages of all peaks labeled with ^{15}N were combined ($37.8\% + 3.2\% + 23.1\% + 1.3\%$), ^{15}N incorporation of 65.4% was obtained. This also agrees well with the average value of amide ^{15}N determined from ^1H NMR spectra.

Table 11. Summary of the results of ESI-orbitrap-MS measurement of ^{13}C , ^{15}N -enriched ΔHA_2

[M+H]⁺ (<i>m/z</i>)	Isotopologue	Relative percentage (%)
395.1620	$^{13}\text{C}_{14}$, ^{15}N	37.8
394.1649	$^{13}\text{C}_{14}$, ^{14}N	19.4
394.1595	$^{13}\text{C}_{13}$, $^{12}\text{C}_1$, ^{15}N	3.2
393.1609	$^{13}\text{C}_{13}$, $^{12}\text{C}_1$, ^{14}N	1.6
393.1556	$^{13}\text{C}_{12}$, $^{12}\text{C}_2$, ^{15}N	23.1
392.1585	$^{13}\text{C}_{12}$, $^{12}\text{C}_2$, ^{14}N	13.6
392.1533	$^{13}\text{C}_{11}$, $^{12}\text{C}_3$, ^{15}N	1.3
391.1557	$^{13}\text{C}_{11}$, $^{12}\text{C}_3$, ^{14}N	<1
391.1490	$^{13}\text{C}_{10}$, $^{12}\text{C}_4$, ^{15}N	<1

In summary, ^{13}C , ^{15}N -enriched HA polymers were produced by *Streptococcus zooepidemicus* using small-scale cultures and media with defined carbon and nitrogen sources. The HA polymer was further degraded enzymatically by ChABC to the disaccharide ΔHA_2 to allow assessment of the level of ^{13}C and ^{15}N isotope enrichment at each position by quantitative NMR. This project provides an effective method that can be applied to the quantitative assessment of isotopically labeled glycans and the produced glycans will help to improve detection capabilities and facilitate future structure–function relationship analysis of HA.

6. Conclusions and Outlook

By applying NMR spectroscopy in different ways, this thesis made contributions to improving understanding of the structural and dynamic properties of various forms of HA. The main findings are as follows:

- Longitudinal relaxation (T_1) and diffusion coefficient (D) of water protons in HA-BDDE hydrogels and native HA solutions showed very similar trends, irrespective of physicochemical properties and sample concentration.
- Transverse relaxation (T_2) of water protons in HA-BDDE hydrogels and native HA solutions was dominated by the chemical exchange between water protons and exchangeable protons of HA. Using the temperature profile of T_2 , it was possible to distinguish between samples with different concentrations and in some cases between hydrogels with different physicochemical properties.
- The first identification of NH protons of the amide *cis* forms of α - and β -GlcNAc was achieved by ^1H NMR.
- Eight 3J -couplings that are sensitive to the torsion angles θ_1 and θ_2 of the *N*-acetyl group were measured using uniformly ^{13}C , ^{15}N -labeled GlcNAc with experiments originally developed for protein NMR studies.
- HA-8mer and HA-20mer had similar conformations of the acetamido group, with the torsion angle θ_1 adopting a clear *anti* conformation.
- HA-8mer and HA-20mer showed one similar predominant conformation of the $\beta(1\rightarrow3)$ glycosidic linkage and the presence of a conformational equilibrium at the $\beta(1\rightarrow4)$ glycosidic linkage with the same major *syn* conformation.

- ^{13}C , ^{15}N -enriched HA polymer was produced by *Streptococcus zooepidemicus* and degraded enzymatically to the disaccharide ΔHA_2 for quantitative assessment of isotope enrichment by NMR and MS.

Further studies of the diverse properties of HA and derivatives should encompass the following topics:

- Measurements of T_1 and T_2 of water protons in HA-BDDE hydrogels at low-field NMR would provide further insights into different components of relaxation.
- Employing a strictly chemically defined medium to produce uniformly ^{13}C and ^{15}N -labeled HA polysaccharides would help to address the issue of isotopic dilution.
- The use of size-defined uniformly ^{13}C - and ^{15}N -labeled HA oligo- and polysaccharides as substrates would greatly facilitate analysis of HA-protein interactions and provide further insights into the conformation of HA at different chain lengths.

References

- Afratis, N., Gialeli, C., Nikitovic, D., Tsegenidis, T., Karousou, E., Theocharis, A.D., Pavão, M.S., Tzanakakis, G.N. & Karamanos, N.K. (2012). Glycosaminoglycans: key players in cancer cell biology and treatment. *The FEBS Journal*, 279 (7), 1177–1197. <https://doi.org/10.1111/j.1742-4658.2012.08529.x>
- Almond, A., DeAngelis, P.L. & Blundell, C.D. (2005). Dynamics of hyaluronan oligosaccharides revealed by ^{15}N relaxation. *Journal of the American Chemical Society*, 127 (4), 1086–1087. <https://doi.org/10.1021/ja043526i>
- Almond, A., DeAngelis, P.L. & Blundell, C.D. (2006). Hyaluronan: The local solution conformation determined by NMR and computer modeling is close to a contracted left-handed 4-fold helix. *Journal of Molecular Biology*, 358 (5), 1256–1269. <https://doi.org/10.1016/j.jmb.2006.02.077>
- Atkins, E.D.T. & Sheehan, J.K. (1972). Structure for hyaluronic acid. *Nature New Biology*, 235 (60), 253–254. <https://doi.org/10.1038/newbio235253a0>
- Balazs, E.A., Laurent, T.C. & Jeanloz, R.W. (1986). Nomenclature of hyaluronic acid. *Biochemical Journal*, 235 (3), 903. <https://doi.org/10.1042/bj2350903>
- Barb, A.W., Freedberg, D.I., Battistel, M.D. & Prestegard, J.H. (2011). NMR detection and characterization of sialylated glycoproteins and cell surface polysaccharides. *Journal of biomolecular NMR*, 51 (1–2), 163–171. <https://doi.org/10.1007/s10858-011-9550-0>
- Bedair, M. & Sumner, L.W. (2008). Current and emerging mass-spectrometry technologies for metabolomics. *TrAC Trends in Analytical Chemistry*, 27 (3), 238–250. <https://doi.org/10.1016/j.trac.2008.01.006>
- Bloch, F., Hansen, W.W. & Packard, M. (1946). Nuclear induction. *Physical Review*, 69, 127. <https://doi.org/10.1103/PhysRev.69.127>
- Blundell, C., Deangelis, P., Day, A.J. & Almond, A. (2004). Use of ^{15}N -NMR to resolve molecular details in isotopically-enriched carbohydrates: sequence-specific observations in hyaluronan oligomers up to decasaccharides. *Glycobiology*, 14 (11), 999–1009. <https://doi.org/10.1093/glycob/cwh117>

- Blundell, C.D., Deangelis, P.L. & Almond, A. (2006a). Hyaluronan: the absence of amide–carboxylate hydrogen bonds and the chain conformation in aqueous solution are incompatible with stable secondary and tertiary structure models. *Biochemical Journal*, 396 (3), 487–498.
<https://doi.org/10.1042/BJ20060085>
- Blundell, C.D., Reed, M.A.C. & Almond, A. (2006b). Complete assignment of hyaluronan oligosaccharides up to hexasaccharides. *Carbohydrate Research*, 341 (17), 2803–2815.
<https://doi.org/10.1016/j.carres.2006.09.023>
- Bohaumilitzky, L., Huber, A.-K., Stork, E.M., Wengert, S., Woelfl, F. & Boehm, H. (2017). A Trickster in disguise: Hyaluronan’s ambivalent roles in the matrix. *Frontiers in Oncology*, 7, 242.
<https://doi.org/10.3389/fonc.2017.00242>
- Bose-Basu, B., Klepach, T., Bondo, G., Bondo, P.B., Zhang, W., Carmichael, I. & Serianni, A.S. (2007). ^{13}C – ^{13}C NMR spin–spin coupling constants in saccharides: Structural correlations involving all carbons in aldohexopyranosyl rings. *The Journal of Organic Chemistry*, 72 (20), 7511–7522. <https://doi.org/10.1021/jo0706776>
- Bubb, W.A. (2003). NMR spectroscopy in the study of carbohydrates: Characterizing the structural complexity. *Concepts in Magnetic Resonance Part A*, 19A (1), 1–19. <https://doi.org/10.1002/cmr.a.10080>
- Casale, J. & Crane, J.S. (2019). Biochemistry, Glycosaminoglycans. In *StatPearls*, Treasure Island (FL).
- Chen, H., Qin, J. & Hu, Y. (2019). Efficient degradation of high-molecular-weight hyaluronic acid by a combination of ultrasound, hydrogen peroxide, and copper ion. *Molecules*, 24 (3), 617.
<https://doi.org/10.3390/molecules24030617>
- Chien, L.-J. & Lee, C.-K. (2007). Enhanced hyaluronic acid production in *Bacillus subtilis* by coexpressing bacterial hemoglobin. *Biotechnology Progress*, 23 (5), 1017–1022. <https://doi.org/10.1021/bp070036w>
- Collins, M.N. & Birkinshaw, C. (2007). Comparison of the effectiveness of four different crosslinking agents with hyaluronic acid hydrogel films for tissue-culture applications. *Journal of Applied Polymer Science*, 104 (5), 3183–3191. <https://doi.org/10.1002/app.25993>
- Cowman, M.K. (2017). Hyaluronan and hyaluronan fragments. *Advances in Carbohydrate Chemistry and Biochemistry*, 74, 1–59.
<https://doi.org/10.1016/bs.accb.2017.10.001>
- Cowman, M.K., Cozart, D., Nakanishi, K. & Balazs, E.A. (1984). ^1H NMR of glycosaminoglycans and hyaluronic acid oligosaccharides in aqueous solution: The amide proton environment. *Archives of Biochemistry and Biophysics*, 230 (1), 203–212. [https://doi.org/10.1016/0003-9861\(84\)90101-2](https://doi.org/10.1016/0003-9861(84)90101-2)

- Cowman, M.K., Feder-Davis, J. & Hittner, D.M. (2001). ^{13}C NMR studies of hyaluronan. 2. Dependence of conformational dynamics on chain length and solvent. *Macromolecules*, 34 (1), 110–115.
<https://doi.org/10.1021/ma001082e>
- Cowman, M.K., Hittner, D.M. & Feder-Davis, J. (1996). ^{13}C -NMR studies of hyaluronan: Conformational sensitivity to varied environments. *Macromolecules*, 29 (8), 2894–2902. <https://doi.org/10.1021/ma951701x>
- Cowman, M.K. & Matsuoka, S. (2005). Experimental approaches to hyaluronan structure. *Carbohydrate Research*, 340 (5), 791–809.
<https://doi.org/10.1016/j.carres.2005.01.022>
- Cowman, M.K., Spagnoli, C., Kudasheva, D., Li, M., Dyal, A., Kanai, S. & Balazs, E.A. (2005). Extended, relaxed, and condensed conformations of hyaluronan observed by atomic force microscopy. *Biophysical Journal*, 88 (1), 590–602. <https://doi.org/10.1529/biophysj.104.049361>
- DeAngelis, P.L., Papaconstantinou, J. & Weigel, P.H. (1993). Molecular cloning, identification, and sequence of the hyaluronan synthase gene from group A *Streptococcus pyogenes*. *Journal of Biological Chemistry*, 268 (26), 19181–19184. [https://doi.org/10.1016/S0021-9258\(19\)36494-4](https://doi.org/10.1016/S0021-9258(19)36494-4)
- Dicker, K.T., Gurski, L.A., Pradhan-Bhatt, S., Witt, R.L., Farach-Carson, M.C. & Jia, X. (2014). Hyaluronan: A simple polysaccharide with diverse biological functions. *Acta Biomaterialia*, 10 (4), 1558–1570.
<https://doi.org/10.1016/j.actbio.2013.12.019>
- Donati, A., Magnani, A., Bonechi, C., Barbucci, R. & Rossi, C. (2001). Solution structure of hyaluronic acid oligomers by experimental and theoretical NMR, and molecular dynamics simulation. *Biopolymers*, 59 (6), 434–445.
[https://doi.org/10.1002/1097-0282\(200111\)59:6<434::AID-BIP1048>3.0.CO;2-4](https://doi.org/10.1002/1097-0282(200111)59:6<434::AID-BIP1048>3.0.CO;2-4)
- Dovedytis, M., Liu, Z.J. & Bartlett, S. (2020). Hyaluronic acid and its biomedical applications: A review. *Engineered Regeneration*, 1, 102–113.
<https://doi.org/10.1016/j.engreg.2020.10.001>
- Dugave, C. (2006). *cis-trans* Isomerization in Biochemistry. *Wiley-VCH*, Weinheim. <https://doi.org/10.1002/3527609334>
- Edsman, K., Nord, L.I., Öhrlund, Å., Lärkner, H. & Kenne, A.H. (2012). Gel properties of hyaluronic acid dermal fillers. *Dermatologic Surgery*, 38 (7pt2), 1170–1179. <https://doi.org/10.1111/j.1524-4725.2012.02472.x>
- El-Safory, N.S., Fazary, A.E. & Lee, C.-K. (2010). Hyaluronidases, a group of glycosidases: Current and future perspectives. *Carbohydrate Polymers*, 81 (2), 165–181. <https://doi.org/10.1016/j.carbpol.2010.02.047>
- Fabri, D., Williams, M.A.K. & Halstead, T.K. (2005). Water T_2 relaxation in sugar solutions. *Carbohydrate Research*, 340 (5), 889–905.
<https://doi.org/10.1016/j.carres.2005.01.034>

- Fakhari, A. & Berklund, C. (2013). Applications and emerging trends of hyaluronic acid in tissue engineering, as a dermal filler and in osteoarthritis treatment. *Acta Biomaterialia*, 9 (7), 7081–7092. <https://doi.org/10.1016/j.actbio.2013.03.005>
- Fallacara, A., Baldini, E., Manfredini, S. & Vertuani, S. (2018). Hyaluronic acid in the third millennium. *Polymers*, 10 (7), 701. <https://doi.org/10.3390/polym10070701>
- Fenn, J.B., Mann, M., Meng, C.K., Wong, S.F. & Whitehouse, C.M. (1989). Electrospray ionization for mass spectrometry of large biomolecules. *Science*, 246 (4926), 64–71. <https://doi.org/10.1126/science.2675315>
- Fischer, G. (2000). Chemical aspects of peptide bond isomerisation. *Chemical Society Reviews*, 29 (2), 119–127. <https://doi.org/10.1039/a803742f>
- Flitsch, S.L. & Ulijn R.V. (2003). Sugars tied to the spot. *Nature*, 421 (6920), 219–220. <https://doi.org/10.1038/421219a>
- Fontana, C., Kovacs, H. & Widmalm, G. (2014). NMR structure analysis of uniformly ¹³C-labeled carbohydrates. *Journal of Biomolecular NMR*, 59 (2), 95–110. <https://doi.org/10.1007/s10858-014-9830-6>
- Fontana, C. & Widmalm, G. (2023). Primary structure of glycans by NMR spectroscopy. *Chemical Reviews*, 123 (3), 1040–1102. <https://doi.org/10.1021/acs.chemrev.2c00580>
- Fraser, J.R.E., Laurent, T.C. & Laurent, U.B.G. (1997). Hyaluronan: its nature, distribution, functions and turnover. *Journal of Internal Medicine*, 242 (1), 27–33. <https://doi.org/10.1046/j.1365-2796.1997.00170.x>
- Furlan, S., La Penna, G., Perico, A. & Cesàro, A. (2005). Hyaluronan chain conformation and dynamics. *Carbohydrate Research*, 340 (5), 959–970. <https://doi.org/10.1016/j.carres.2005.01.030>
- Gargiulo, V., Morando, M.A., Silipo, A., Nurisso, A., Pérez, S., Imberty, A., Cañada, F.J., Parrilli, M., Jiménez-Barbero, J. & De Castro, C. (2010). Insights on the conformational properties of hyaluronic acid by using NMR residual dipolar couplings and MD simulations. *Glycobiology*, 20 (10), 1208–1216. <https://doi.org/10.1093/glycob/cwq067>
- Gimeno, A., Valverde, P., Ardá, A. & Jiménez-Barbero, J. (2020). Glycan structures and their interactions with proteins. A NMR view. *Current Opinion in Structural Biology*, 62, 22–30. <https://doi.org/10.1016/j.sbi.2019.11.004>
- Grabska, S. & Sionkowska, A. (2019). The influence of UV-radiation on hyaluronic acid and its blends with addition of collagen and chitosan. *International Journal of Polymer Analysis and Characterization*, 24 (4), 285–294. <https://doi.org/10.1080/1023666X.2019.1592899>
- Gray, C.J., Migas, L.G., Barran, P.E., Pagel, K., Seeberger, P.H., Eyers, C.E., Boons, G.-J., Pohl, N.L.B., Compagnon, I., Widmalm, G. & Flitsch, S.L. (2019). Advancing solutions to the carbohydrate sequencing challenge.

- Journal of the American Chemical Society*, 141 (37), 14463–14479.
<https://doi.org/10.1021/jacs.9b06406>
- Grøndahl, F., Tveit, H., Akslen-Hoel, L.K. & Prydz, K. (2011). Easy HPLC-based separation and quantitation of chondroitin sulphate and hyaluronan disaccharides after chondroitinase ABC treatment. *Carbohydrate Research*, 346 (1), 50–57. <https://doi.org/10.1016/j.carres.2010.10.025>
- Guss, J.M., Hukins, D.W.L., Smith, P.J.C., Winter, W.T., Arnott, S., Moorhouse, R. & Rees, D.A. (1975). Hyaluronic acid: Molecular conformations and interactions in two sodium salts. *Journal of Molecular Biology*, 95 (3), 359–384. [https://doi.org/10.1016/0022-2836\(75\)90196-5](https://doi.org/10.1016/0022-2836(75)90196-5)
- Guvench, O. (2022). Atomic-resolution experimental structural biology and molecular dynamics simulations of hyaluronan and its complexes. *Molecules*, 27 (21), 7276. <https://doi.org/10.3390/molecules27217276>
- Haasnoot, C.A.G., de Leeuw, F.A.A.M. & Altona, C. (1980). The relationship between proton-proton NMR coupling constants and substituent electronegativities—I: An empirical generalization of the Karplus equation. *Tetrahedron*, 36 (19), 2783–2792. [https://doi.org/10.1016/0040-4020\(80\)80155-4](https://doi.org/10.1016/0040-4020(80)80155-4)
- Hafsa, J., Chaouch, M.A., Charfeddine, B., Rihouey, C., Limem, K., Le Cerf, D., Rouatbi, S. & Majdoub, H. (2017). Effect of ultrasonic degradation of hyaluronic acid extracted from rooster comb on antioxidant and antiglycation activities. *Pharmaceutical Biology*, 55 (1), 156–163. <https://doi.org/10.1080/13880209.2016.1232740>
- Hargittai, I. & Hargittai, M. (2008). Molecular structure of hyaluronan: an introduction. *Structural Chemistry*, 19 (5), 697–717. <https://doi.org/10.1007/s11224-008-9370-3>
- Harris, R.K., Becker, E.D., Menezes, S.M.C. de, Goodfellow, R. & Granger, P. (2001). NMR nomenclature. Nuclear spin properties and conventions for chemical shifts (IUPAC Recommendations 2001). *Pure and Applied Chemistry*, 73 (11), 1795–1818. <https://doi.org/10.1351/pac200173111795>
- Heatley, F. & Scott, J.E. (1988). A water molecule participates in the secondary structure of hyaluronan. *Biochemical Journal*, 254 (2), 489–493. <https://doi.org/10.1042/bj2540489>
- Heatley, F., Scott, J.E. & Casu, B. (1979). ¹H-N.M.R. spectra of glycosaminoglycan monomers and dimers in solution in methyl sulphoxide and water. *Carbohydrate Research*, 72, 13–23. [https://doi.org/10.1016/S0008-6215\(00\)83919-1](https://doi.org/10.1016/S0008-6215(00)83919-1)
- Hills, B.P. (1991). Multinuclear NMR studies of water in solutions of simple carbohydrates. *Molecular Physics*, 72 (5), 1099–1121. <https://doi.org/10.1080/00268979100100791>

- Hills, B.P., Wright, K.M. & Belton, P.S. (1989). Proton N.M.R. studies of chemical and diffusive exchange in carbohydrate systems. *Molecular Physics*, 67 (6), 1309–1326. <https://doi.org/10.1080/00268978900101831>
- Holmbeck, S.M.A., Petillo, P.A. & Lerner, L.E. (1994). The solution conformation of hyaluronan: A combined NMR and molecular dynamics study. *Biochemistry*, 33 (47), 14246–14255. <https://doi.org/10.1021/bi00251a037>
- Hosu, I. S., Sobaszek, M., Ficek, M., Bogdanowicz, R., Drobecq, H., Boussekey, L., Barras, A., Melnyk, O., Boukherroub, R. & Coffinier, Y. (2017). Carbon nanowalls: A new versatile graphene based interface for the laser desorption/ionization-mass spectrometry detection of small compounds in real samples. *Nanoscale*, 9 (27), 9701–9715. <https://doi.org/10.1039/C7NR01069A>
- Hu, Q., Noll, R.J., Li, H., Makarov, A., Hardman, M. & Graham Cooks, R. (2005). The Orbitrap: a new mass spectrometer. *Journal of mass spectrometry: JMS*, 40 (4), 430–443. <https://doi.org/10.1002/jms.856>
- Hu, X., Carmichael, I. & Serianni, A.S. (2010a). *N*-acetyl side-chains in saccharides: NMR *J*-Coupling equations sensitive to CH-NH and NH-CO bond conformations in 2-acetamido-2-deoxy-aldohexopyranosyl rings. *The Journal of Organic Chemistry*, 75 (15), 4899–4910. <https://doi.org/10.1021/jo100521g>
- Hu, X., Zhang, W., Carmichael, I. & Serianni, A.S. (2010b). Amide *cis*–*trans* isomerization in aqueous solutions of methyl *N*-formyl-D-glucosaminides and methyl *N*-acetyl-D-glucosaminides: chemical equilibria and exchange kinetics. *Journal of the American Chemical Society*, 132 (13), 4641–4652. <https://doi.org/10.1021/ja9086787>
- Huin-Amargier, C., Marchal, P., Payan, E., Netter, P. & Dellacherie, E. (2006). New physically and chemically crosslinked hyaluronate (HA)-based hydrogels for cartilage repair. *Journal of Biomedical Materials Research Part A*, 76A (2), 416–424. <https://doi.org/10.1002/jbm.a.30536>
- Hwang, H.-D., Cho, H.-J., Balakrishnan, P., Chung, C.-W., Yoon, I.-S., Oh, Y.-K., Byun, Y. & Kim, D.-D. (2012). Cross-linked hyaluronic acid-based flexible cell delivery system: application for chondrogenic differentiation. *Colloids and surfaces B, Biointerfaces*, 91, 106–113. <https://doi.org/10.1016/j.colsurfb.2011.10.052>
- Jia, X., Colombo, G., Padera, R., Langer, R. & Kohane, D.S. (2004). Prolongation of sciatic nerve blockade by in situ cross-linked hyaluronic acid. *Biomaterials*, 25 (19), 4797–4804. <https://doi.org/10.1016/j.biomaterials.2003.12.012>
- Karplus, M. (1959). Contact electron-spin coupling of nuclear magnetic moments. *The Journal of Chemical Physics*, 30 (1), 11–15. <https://doi.org/10.1063/1.1729860>

- Kaufmann, J., Möhle, K., Hofmann, H.-J. & Arnold, K. (1998). Molecular dynamics study of hyaluronic acid in water. *Journal of Molecular Structure: THEOCHEM*, 422 (1-3), 109–121. [https://doi.org/10.1016/S0166-1280\(97\)00084-5](https://doi.org/10.1016/S0166-1280(97)00084-5)
- Kenne, L., Gohil, S., Nilsson, E.M., Karlsson, A., Ericsson, D., Helander Kenne, A. & Nord, L.I. (2013). Modification and cross-linking parameters in hyaluronic acid hydrogels—Definitions and analytical methods. *Carbohydrate Polymers*, 91 (1), 410–418. <https://doi.org/10.1016/j.carbpol.2012.08.066>
- Kiss, J. (1974). β -Eliminative degradation of carbohydrates containing uronic acid residues. *Advances in Carbohydrate Chemistry and Biochemistry*, 29, 229–303. [https://doi.org/10.1016/S0065-2318\(08\)60251-6](https://doi.org/10.1016/S0065-2318(08)60251-6)
- Kubo, K., Nakamura, T., Takagaki, K., Yoshida, Y. & Endo, M. (1993). Depolymerization of hyaluronan by sonication. *Glycoconjugate Journal*, 10 (6), 435–439. <https://doi.org/10.1007/BF00737963>
- Laine, R.A. (1997). Information capacity of the carbohydrate code. *Pure and Applied Chemistry*, 69 (9), 1867–1873. <https://doi.org/10.1351/pac199769091867>
- Lapčič, L., Lapčič, L., De Smedt, S., Demeester, J. & Chabreček, P. (1998). Hyaluronan: Preparation, structure, properties, and applications. *Chemical Reviews*, 98 (8), 2663–2684. <https://doi.org/10.1021/cr941199z>
- Larrañeta, E., Henry, M., Irwin, N.J., Trotter, J., Perminova, A.A. & Donnelly, R.F. (2018). Synthesis and characterization of hyaluronic acid hydrogels crosslinked using a solvent-free process for potential biomedical applications. *Carbohydrate Polymers*, 181, 1194–1205. <https://doi.org/10.1016/j.carbpol.2017.12.015>
- Lauder, R.M., Huckerby, T.N. & Nieduszynski, I.A. (2000). A fingerprinting method for chondroitin/dermatan sulfate and hyaluronan oligosaccharides. *Glycobiology*, 10 (4), 393–401. <https://doi.org/10.1093/glycob/10.4.393>
- Laurent, T.C. (1955). Studies on hyaluronic acid in the vitreous body. *Journal of Biological Chemistry*, 216 (1), 263–271. [https://doi.org/10.1016/S0021-9258\(19\)52303-1](https://doi.org/10.1016/S0021-9258(19)52303-1)
- Laurent, T.C. & Fraser, J.R.E. (1992). Hyaluronan. *The FASEB Journal*, 6 (7), 2397–2404. <https://doi.org/10.1096/fasebj.6.7.1563592>
- Laurent, T.C., Hellsing, K., Gelotte, B., Burton, J.S. & Stevens, R. (1964). Cross-linked gels of hyaluronic acid. *Acta Chemica Scandinavica*, 18, 274–275. <https://doi.org/10.3891/acta.chem.scand.18-0274>
- Laurent, T.C., Laurent, U.B. & Fraser, J.R.E. (1996). The structure and function of hyaluronan: An overview. *Immunology & Cell Biology*, 74 (2), a1–a7. <https://doi.org/10.1038/icb.1996.32>
- Laurent, T.C., Ryan, M. & Pietruszkiewicz, A. (1960). Fractionation of hyaluronic acid the polydispersity of hyaluronic acid from the bovine vitreous body.

- Biochimica et Biophysica Acta*, 42, 476–485.
[https://doi.org/10.1016/0006-3002\(60\)90826-X](https://doi.org/10.1016/0006-3002(60)90826-X).
- Linker, A., Hoffman, P. & Meyer, K. (1957). The hyaluronidase of the leech: an endoglucuronidase. *Nature*, 180 (4590), 810–811.
<https://doi.org/10.1038/180810b0>
- Linker, A. & Meyer, K. (1954). Production of unsaturated uronides by bacterial hyaluronidases. *Nature*, 174 (4443), 1192–1193.
<https://doi.org/10.1038/1741192a0>
- Liu, L., Liu, Y., Li, J., Du, G. & Chen, J. (2011). Microbial production of hyaluronic acid: current state, challenges, and perspectives. *Microbial Cell Factories*, 10 (1), 99. <https://doi.org/10.1186/1475-2859-10-99>
- Makarov, A. (2000). Electrostatic axially harmonic orbital trapping: A high-performance technique of mass analysis. *Analytical Chemistry*, 72 (6), 1156–1162. <https://doi.org/10.1021/ac991131p>
- Maleki, A., Kjøniksen, A.-L. & Nyström, B. (2007). Characterization of the chemical degradation of hyaluronic acid during chemical gelation in the presence of different cross-linker agents. *Carbohydrate Research*, 342 (18), 2776–2792. <https://doi.org/10.1016/j.carres.2007.08.021>
- Mao, Z. & Chen, R.R. (2007). Recombinant synthesis of hyaluronan by *Agrobacterium* sp. *Biotechnology Progress*, 23 (5), 1038–1042.
<https://doi.org/10.1021/bp070113n>
- Mao, Z., Shin, H.-D. & Chen, R. (2009). A recombinant *E. coli* bioprocess for hyaluronan synthesis. *Applied Microbiology and Biotechnology*, 84 (1), 63–69. <https://doi.org/10.1007/s00253-009-1963-2>
- Maytin, E.V. (2016). Hyaluronan: More than just a wrinkle filler. *Glycobiology*, 26 (6), 553–559. <https://doi.org/10.1093/glycob/cww033>
- McConville, P. & Pope, J.M. (2001). ¹H NMR *T*₂ relaxation in contact lens hydrogels as a probe of water mobility. *Polymer*, 42 (8), 3559–3568.
[https://doi.org/10.1016/S0032-3861\(00\)00714-X](https://doi.org/10.1016/S0032-3861(00)00714-X)
- McConville, P., Whittaker, M.K. & Pope, J.M. (2002). Water and polymer mobility in hydrogel biomaterials quantified by ¹H NMR: A simple model describing both *T*₁ and *T*₂ relaxation. *Macromolecules*, 35 (18), 6961–6969. <https://doi.org/10.1021/ma020539c>
- Meyer, K. & Palmer, J.W. (1934). The polysaccharide of the vitreous humor. *Journal of Biological Chemistry*, 107 (3), 629–634.
[https://doi.org/10.1016/S0021-9258\(18\)75338-6](https://doi.org/10.1016/S0021-9258(18)75338-6)
- Mobli, M. & Almond, A. (2007). *N*-Acetylated amino sugars: the dependence of NMR ³*J*_(HNH₂)-couplings on conformation, dynamics and solvent. *Organic & Biomolecular Chemistry*, 5 (14), 2243–2251.
<https://doi.org/10.1039/B705761J>
- Mondek, J., Kalina, M., Simulescu, V. & Pekař, M. (2015). Thermal degradation of high molar mass hyaluronan in solution and in powder; comparison

- with BSA. *Polymer Degradation and Stability*, 120, 107–113.
<https://doi.org/10.1016/j.polymdegradstab.2015.06.012>
- Necas, J., Bartosikova, L., Brauner, P. & Kolar, J. (2008). Hyaluronic acid (hyaluronan): a review. *Veterinárni medicína*, 53 (8), 397–411.
<https://doi.org/10.17221/1930-VETMED>
- Neelamegham, S., Aoki-Kinoshita, K., Bolton, E., Frank, M., Lisacek, F., Lütteke, T., O’Boyle, N., Packer, N.H., Stanley, P., Toukach, P., Varki, A., Woods, R.J., & SNFG Discussion Group (2019). Updates to the symbol nomenclature for glycans guidelines. *Glycobiology*, 29 (9), 620–624.
<https://doi.org/10.1093/glycob/cwz045>
- Pogány, P. & Kovács, A. (2010). Theoretical study of hyaluronan oligosaccharides. *Structural Chemistry*, 21 (6), 1185–1194. <https://doi.org/10.1007/s11224-010-9658-y>
- Pomin, V.H. (2014). NMR-based dynamics of free glycosaminoglycans in solution. *Analyst*, 139 (15), 3656–3665.
<https://doi.org/10.1039/C4AN00531G>
- Pomin, V.H., Sharp, J.S., Li, X., Wang, L. & Prestegard, J.H. (2010). Characterization of glycosaminoglycans by ¹⁵N NMR spectroscopy and in vivo isotopic labeling. *Analytical Chemistry*, 82 (10), 4078–4088.
<https://doi.org/10.1021/ac1001383>
- Purcell, E.M., Torrey, H.C. & Pound, R.V. (1946). Resonance absorption by nuclear magnetic moments in a solid. *Physical Review*, 69, 37–38.
<https://doi.org/10.1103/PhysRev.69.37>
- Rayahin, J.E., Buhrman, J.S., Zhang, Y., Koh, T.J. & Gemeinhart, R.A. (2015). High and low molecular weight hyaluronic acid differentially influence macrophage activation. *ACS Biomaterials Science & Engineering*, 1 (7), 481–493. <https://doi.org/10.1021/acsbiomaterials.5b00181>
- Saitoh, H., Takagaki, K., Majima, M., Nakamura, T., Matsuki, A., Kasai, M., Narita, H. & Endo, M. (1995). Enzymic reconstruction of glycosaminoglycan oligosaccharide chains using the transglycosylation reaction of bovine testicular hyaluronidase. *Journal of Biological Chemistry*, 270 (8), 3741–3747. <https://doi.org/10.1074/jbc.270.8.3741>
- Sattelle, B.M. & Almond, A. (2011). Is *N*-acetyl-D-glucosamine a rigid ⁴C₁ chair? *Glycobiology*, 21 (12), 1651–1662. <https://doi.org/10.1093/glycob/cwr101>
- Säwén, E., Massad, T., Landersjö, C., Damberg, P. & Widmalm, G. (2010). Population distribution of flexible molecules from maximum entropy analysis using different priors as background information: application to the ϕ , ψ -conformational space of the α -(1→2)-linked mannose disaccharide present in *N*- and *O*-linked glycoproteins. *Organic & Biomolecular Chemistry*, 8 (16), 3684–3695.
<https://doi.org/10.1039/c003958f>

- Schanté, C.E., Zuber, G., Herlin, C. & Vandamme, T.F. (2011). Chemical modifications of hyaluronic acid for the synthesis of derivatives for a broad range of biomedical applications. *Carbohydrate Polymers*, 85 (3), 469–489. <https://doi.org/10.1016/j.carbpol.2011.03.019>
- Scott, J.E., Heatley, F. & Hull, W.E. (1984). Secondary structure of hyaluronate in solution. A ^1H -n.m.r. investigation at 300 and 500 MHz in $[\text{D}_6]$ dimethyl sulphoxide solution. *Biochemical Journal*, 220 (1), 197–205. <https://doi.org/10.1042/bj2200197>
- Segura, T., Anderson, B.C., Chung, P.H., Webber, R.E., Shull, K.R. & Shea, L.D. (2005). Crosslinked hyaluronic acid hydrogels: a strategy to functionalize and pattern. *Biomaterials*, 26 (4), 359–371. <https://doi.org/10.1016/j.biomaterials.2004.02.067>
- Sheehan, J.K. & Atkins, E.D.T. (1983). X-ray fibre diffraction study of conformational changes in hyaluronate induced in the presence of sodium, potassium and calcium cations. *International Journal of Biological Macromolecules*, 5 (4), 215–221. [https://doi.org/10.1016/0141-8130\(83\)90005-3](https://doi.org/10.1016/0141-8130(83)90005-3)
- Shikina, E.V., Kovalevsky, R.A., Shirkovskaya, A.I. & Toukach, P.V. (2022). Prospective bacterial and fungal sources of hyaluronic acid: A review. *Computational and Structural Biotechnology Journal*, 20, 6214–6236. <https://doi.org/10.1016/j.csbj.2022.11.013>
- Šimek, M., Lemr, K., Hermannová, M. & Havlíček, V. (2020). Analysis of hyaluronan and its derivatives using chromatographic and mass spectrometric techniques. *Carbohydrate Polymers*, 250, 117014. <https://doi.org/10.1016/j.carbpol.2020.117014>
- Simulescu, V., Kalina, M., Mondek, J. & Pekař, M. (2016). Long-term degradation study of hyaluronic acid in aqueous solutions without protection against microorganisms. *Carbohydrate Polymers*, 137, 664–668. <https://doi.org/10.1016/j.carbpol.2015.10.101>
- Simulescu, V., Mondek, J., Kalina, M. & Pekař, M. (2015). Kinetics of long-term degradation of different molar mass hyaluronan solutions studied by SEC-MALLS. *Polymer Degradation and Stability*, 111, 257–262. <https://doi.org/10.1016/j.polymdegradstab.2014.12.005>
- Snetkov, P., Zakharova, K., Morozkina, S., Olekhovich, R. & Uspenskaya, M. (2020). Hyaluronic acid: the influence of molecular weight on structural, physical, physico-chemical, and degradable properties of biopolymer. *Polymers*, 12 (8), 1800. <https://doi.org/10.3390/polym12081800>
- Söderman, P., Jansson, P.-E. & Widmalm, G. (1998). Synthesis, NMR spectroscopy and conformational studies of the four anomeric methyl glycosides of the trisaccharide D-Glcp-(1→3)-[D-Glcp-(1→4)]- α -D-Glcp. *Journal of the Chemical Society, Perkin Transactions*, 2, 639–648. <https://doi.org/10.1039/A707346A>

- Song, Y., Zhang, F. & Linhardt, R.J. (2021) Analysis of the glycosaminoglycan chains of proteoglycans. *Journal of Histochemistry & Cytochemistry*, 69 (2), 121-135. <https://doi.org/10.1369/0022155420937154>
- Stern, R., Asari, A.A. & Sugahara, K.N. (2006). Hyaluronan fragments: an information-rich system. *European Journal of Cell Biology*, 85 (8), 699–715. <https://doi.org/10.1016/j.ejcb.2006.05.009>
- Stern, R., Kogan, G., Jedrzejas, M.J. & Šoltés, L. (2007). The many ways to cleave hyaluronan. *Biotechnology Advances*, 25 (6), 537–557. <https://doi.org/10.1016/j.biotechadv.2007.07.001>
- Suzuki, K., Terasaki, Y. & Uyeda, M. (2002). Inhibition of hyaluronidases and chondroitinases by fatty acids. *Journal of Enzyme Inhibition and Medicinal Chemistry*, 17 (3), 183–186. <https://doi.org/10.1080/14756360290032930>
- Sze, J.H., Brownlie, J.C. & Love, C.A. (2016). Biotechnological production of hyaluronic acid: a mini review. *3 Biotech*, 6 (1), 67. <https://doi.org/10.1007/s13205-016-0379-9>
- Tao, L., Song, F., Xu, N., Li, D., Linhardt, R.J. & Zhang, Z. (2017). New insights into the action of bacterial chondroitinase AC I and hyaluronidase on hyaluronic acid. *Carbohydrate Polymers*, 158, 85–92. <https://doi.org/10.1016/j.carbpol.2016.12.010>
- Taweechat, P., Pandey, R.B. & Sompornpisut, P. (2020). Conformation, flexibility and hydration of hyaluronic acid by molecular dynamics simulations. *Carbohydrate Research*, 493, 108026. <https://doi.org/10.1016/j.carres.2020.108026>
- Toffanin, R., Kvam, B.J., Flaibani, A., Atzori, M., Biviano, F. & Paoletti, S. (1993). NMR studies of oligosaccharides derived from hyaluronate: complete assignment of ¹H and ¹³C NMR spectra of aqueous di- and tetra-saccharides, and comparison of chemical shifts for oligosaccharides of increasing degree of polymerisation. *Carbohydrate Research*, 245 (1), 113–120. [https://doi.org/10.1016/0008-6215\(93\)80064-L](https://doi.org/10.1016/0008-6215(93)80064-L)
- Tokita, Y. & Okamoto, A. (1995). Hydrolytic degradation of hyaluronic acid. *Polymer Degradation and Stability*, 48 (2), 269–273. [https://doi.org/10.1016/0141-3910\(95\)00041-J](https://doi.org/10.1016/0141-3910(95)00041-J)
- Tomihata, K. & Ikada, Y. (1997). Crosslinking of hyaluronic acid with glutaraldehyde. *Journal of Polymer Science Part A: Polymer Chemistry*, 35 (16), 3553–3559. [https://doi.org/10.1002/\(SICI\)1099-0518\(19971130\)35:16<3553::AID-POLA22>3.0.CO;2-D](https://doi.org/10.1002/(SICI)1099-0518(19971130)35:16<3553::AID-POLA22>3.0.CO;2-D)
- Tunlid, A., Ringelberg, D., Phelps, T.J., Low, C. & White, D.C. (1989). Measurement of phospholipid fatty acids at picomolar concentrations in biofilms and deep subsurface sediments using gas chromatography and chemical ionization mass spectrometry. *Journal of Microbiological Methods*, 10 (2), 139–153. [https://doi.org/10.1016/0167-7012\(89\)90010-9](https://doi.org/10.1016/0167-7012(89)90010-9)

- Weigel, P.H. (2015). Hyaluronan Synthase: The mechanism of initiation at the reducing end and a pendulum model for polysaccharide translocation to the cell exterior. *International Journal of Cell Biology*, 2015, 367579. <https://doi.org/10.1155/2015/367579>
- Weigel, P.H. & DeAngelis, P.L. (2007). Hyaluronan synthases: A decade-plus of novel glycosyltransferases. *Journal of Biological Chemistry*, 282 (51), 36777–36781. <https://doi.org/10.1074/jbc.R700036200>
- Weigel, P.H., Hascall, V.C. & Tammi, M. (1997). Hyaluronan synthases. *Journal of Biological Chemistry*, 272 (22), 13997–14000. <https://doi.org/10.1074/jbc.272.22.13997>
- Wende, F.J., Gohil, S., Mojarradi, H., Gerfaud, T., Nord, L.I., Karlsson, A., Boiteau, J.-G., Kenne, A.H. & Sandström, C. (2016). Determination of substitution positions in hyaluronic acid hydrogels using NMR and MS based methods. *Carbohydrate Polymers*, 136, 1348–1357. <https://doi.org/10.1016/j.carbpol.2015.09.112>
- Wende, F.J., Gohil, S., Nord, L.I., Helander Kenne, A. & Sandström, C. (2017). 1D NMR methods for determination of degree of cross-linking and BDDE substitution positions in HA hydrogels. *Carbohydrate Polymers*, 157, 1525–1530. <https://doi.org/10.1016/j.carbpol.2016.11.029>
- Whitmore, E.K., Martin, D. & Guvench, O. (2020). Constructing 3-dimensional atomic-resolution models of nonsulfated glycosaminoglycans with arbitrary lengths using conformations from molecular dynamics. *International Journal of Molecular Sciences*, 21 (20), 7699. <https://doi.org/10.3390/ijms21207699>
- Widner, B., Behr, R., Von Dollen, S., Tang, M., Heu, T., Sloma, A., Sternberg, D., Deangelis, P.L., Weigel, P.H. & Brown, S. (2005). Hyaluronic acid production in *Bacillus subtilis*. *Applied and Environmental Microbiology*, 71 (7), 3747–3752. <https://doi.org/10.1128/AEM.71.7.3747-3752.2005>
- Wu, Y. (2012). Preparation of low-molecular-weight hyaluronic acid by ozone treatment. *Carbohydrate Polymers*, 89 (2), 709–712. <https://doi.org/10.1016/j.carbpol.2012.03.081>
- Xu, X., Jha, A.K., Harrington, D.A., Farach-Carson, M.C. & Jia, X. (2012). Hyaluronic acid-based hydrogels: from a natural polysaccharide to complex networks. *Soft Matter*, 8 (12), 3280–3294. <https://doi.org/10.1039/C2SM06463D>
- Young, J.-J., Cheng, K.-M., Tsou, T.-L., Liu, H.-W. & Wang, H.-J. (2004). Preparation of cross-linked hyaluronic acid film using 2-chloro-1-methylpyridinium iodide or water-soluble 1-ethyl-(3,3-dimethylaminopropyl)carbodiimide. *Journal of Biomaterials Science, Polymer Edition*, 15 (6), 767–780. <https://doi.org/10.1163/156856204774196153>

- Zhang, T., Zhao, S., Chen, Y., Wang, J., Zhang, W., Liu, J., Kan, Y., Li, J., Guo, X. & Li, H. (2023). In-depth characterization of 1,4-butanediol diglycidyl ether substituted hyaluronic acid hydrogels. *Carbohydrate Polymers*, 307, 120611. <https://doi.org/10.1016/j.carbpol.2023.120611>
- Zhang, W., Turney, T., Meredith, R., Pan, Q., Sernau, L., Wang, X., Hu, X., Woods, R.J., Carmichael, I. & Serianni, A.S. (2017). Conformational populations of β -(1 \rightarrow 4) *O*-glycosidic linkages using redundant NMR *J*-couplings and circular statistics. *The Journal of Physical Chemistry B*, 121 (14), 3042–3058. <https://doi.org/10.1021/acs.jpcc.7b02252>
- Zhang, Z., McCallum, S.A., Xie, J., Nieto, L., Corzana, F., Jiménez-Barbero, J., Chen, M., Liu, J. & Linhardt, R.J. (2008). Solution structures of chemoenzymatically synthesized heparin and its precursors. *Journal of the American Chemical Society*, 130 (39), 12998–13007. <https://doi.org/10.1021/ja8026345>
- Zhao, X. (2006). Synthesis and characterization of a novel hyaluronic acid hydrogel. *Journal of Biomaterials Science, Polymer Edition*, 17 (4), 419–433. <https://doi.org/10.1163/156856206776374115>
- Zhu, Y., Pan, Q., Thibaudeau, C., Zhao, S., Carmichael, I. & Serianni, A.S. (2006). [^{13}C , ^{15}N]2-Acetamido-2-deoxy-D-aldohexoses and their methyl glycosides: synthesis and NMR investigations of *J*-couplings involving ^1H , ^{13}C , and ^{15}N . *The Journal of Organic Chemistry*, 71 (2), 466–479. <https://doi.org/10.1021/jo051510k>

Popular science summary

Hyaluronic acid (HA) was first discovered in the vitreous of bovine eyes by Karl Meyer and John Palmer in 1934. Subsequent analyzes revealed many unique properties of this new biopolymer, such as high viscoelasticity, high water retention capacity, and wide distribution in various living organisms. It is present in high concentrations in the skin, joints and eyes, and plays a critical role in maintaining hydration, tissue repair and overall skin health. HA is a linear polysaccharide and its primary structure consists of repeating units of two monosaccharides (glucuronic acid (GlcA) and *N*-acetylglucosamine (GlcNAc)), which are linked by $\beta(1\rightarrow4)$ and $\beta(1\rightarrow3)$ glycosidic linkages. The primary structure of HA is relatively simple, but its secondary and tertiary structures are complex and dynamic and can change depending on the environment and interactions with other molecules. Many studies have investigated the behavior of HA in different environments, but its structure-function relationship is difficult to establish because it is affected by many variables. At the same time, potential biomedical applications for this compound have been emerging rapidly in the past decade. Therefore, there is a need to improve understanding of its structure-function relationship and to further explore its potential.

In this thesis, nuclear magnetic resonance (NMR) spectroscopy was used to study the structure and properties of HA. NMR works by applying a strong magnetic field to a sample with NMR-active nuclei (such as ^1H , ^{13}C and ^{15}N), which are held in equilibrium parallel or anti-parallel to the magnetic field. When radiofrequency pulses are applied to the sample, the nuclei absorb and re-emit electromagnetic energy at characteristic frequencies according to their chemical environment. The radiofrequency signals emitted by the excited nuclei are then transformed by Fourier transformation to frequency domain spectra. The advantage of NMR is that it can provide detailed

structural and dynamic information at atomic level. Another analytical technique, called mass spectrometry (MS), is also widely used to identify and quantify the composition of samples by measuring the mass-to-charge ratio (m/z) of sample components. The sample is first ionized and then sorted and separated by different m/z . The resulting mass spectra provide detailed "fingerprints" that can be used to study the structure of molecules.

Studies of HA and its related structures by NMR in this thesis identified correlations between the physicochemical properties of cross-linked HA hydrogels and dynamic behavior of their water molecules. By studying the relaxation and diffusion behavior of water protons in the hydrogels, the relationship between hydrogel strength and water proton exchange with the surroundings was determined.

Hyaluronan with different chain lengths may exhibit different conformations in solution, so conformations in the glycosidic linkages and the acetamido group of HA with two different molecular weights were compared and studied. A minor conformation of GlcNAc (one of the repeating units of HA) was observed for the first time using ^1H NMR. To fully investigate this minor conformation, experiments for protein NMR analysis were adapted to study GlcNAc, to gain insights into different conformational changes. This was done using an isotope labeling technique that compensates for the low sensitivity of NMR.

Overall, the results revealed some limitations of NMR in revealing hidden information about HA, so isotope labeling was tested as a pivotal approach. ^{13}C , ^{15}N -enriched HA polysaccharide was produced biosynthetically and the level of ^{13}C and ^{15}N isotope incorporation was determined quantitatively by NMR and confirmed by high-resolution MS.

Collectively, the results in this thesis improve understanding of HA and its related structures by providing insights into their structural and dynamic behaviors, and demonstrate good potential of isotope labeling in enhancing analysis of these complex systems.

Populärvetenskaplig sammanfattning

Hyaluronsyra (HA) upptäcktes först i glaskroppen hos nötdjursögon av Karl Meyer och John Palmer år 1934. Efterföljande analyser avslöjade att denna nya biopolymer har många unika egenskaper, såsom hög viskoelasticitet och hög vattenretention. HA återfinns i många olika levande organismer och förekommer i höga koncentrationer i huden, lederna och ögonen där den spelar en avgörande roll för att bibehålla hydrering, vävnadsreparation och den övergripande hudhälsan. HA är en linjär polysackarid och dess primära struktur består av upprepade enheter av två monosackarider (glukuronsyra (GlcA) och *N*-acetylglukosamin (GlcNAc)), som är sammankopplade med $\beta(1\rightarrow4)$ - och $\beta(1\rightarrow3)$ -glykosidbindningar. HA:s primära struktur är relativt okomplicerad, men dess sekundära och tertiära strukturer är komplexa och dynamiska och kan förändras beroende på miljön och interaktioner med andra molekyler. Många studier har undersökt HA:s beteende i olika miljöer, men dess struktur-funktionsförhållande är svårt att fastställa eftersom det påverkas av många variabler. Samtidigt har potentiella biomedicinska tillämpningar för denna förening blivit allt vanligare under det senaste decenniet. Därför behövs förbättrad förståelse av förhållandet mellan HA:s struktur och funktion, samt ytterligare utforskning av dess potential.

I denna avhandling användes kärnmagnetisk resonans (NMR)-spektroskopi för att studera HA:s struktur och egenskaper. NMR fungerar genom att applicera ett starkt magnetfält på ett prov med NMR-aktiva kärnor (som ^1H , ^{13}C och ^{15}N), vilka befinner sig i jämvikt parallellt eller antiparallellt med det magnetiska fältet. När radiofrekvenspulser appliceras på provet absorberar och sänder kärnorna ut elektromagnetisk energi vid karakteristiska frekvenser beroende på deras kemiska miljö. De radiofrekvenssignaler som sänds ut av de exciterade kärnorna omvandlas sedan genom Fouriertransformering till frekvensspektra. Fördelen med

NMR är att den kan ge detaljerad strukturell och dynamisk information på atomnivå. En annan analytisk teknik, masspektrometri (MS), används också brett för att identifiera och kvantifiera sammansättningen av prover genom att mäta förhållandet mellan massa och laddning (m/z) för provkomponenterna. Provet joniseras först och sorteras sedan och separeras efter olika m/z . De resulterande masspektrumen ger detaljerade "fingeravtryck" som kan användas för att studera molekylers struktur.

NMR-studier av HA och dess relaterade strukturer i denna avhandling identifierade korrelationer mellan de fysikalisk-kemiska egenskaper och det dynamiska beteendet hos korsbundna HA-hydrogeler och nativa HA-lösningar. Genom att studera vattenprotoners relaxations- och diffusionsbeteende i hydrogelerna kunde sambandet mellan hydrogelens styrka och vattenprotonernas utbyte med omgivningen fastställas.

Hyaluronan med olika kedjelängder kan uppvisa olika konformationer i lösning, så konformationsförändringar i glykosidbindningar och sidogrupper hos HA med två olika molekylvikter jämfördes och studerades. En mindre vanlig konformation av GlcNAc (en av HA:s upprepade enheter) observerades för första gången med hjälp av ^1H NMR. För att fullt ut undersöka denna ovanliga konformation anpassades experiment för protein-NMR-analys för att studera GlcNAc och dess olika konformationsförändringar. Detta gjordes med hjälp av en isotopmärkningsmetod som kompenserar för NMR:s låga känslighet.

Sammanfattningsvis visade resultaten i denna avhandling att NMR har vissa begränsningar när det kommer till att avslöja dold information om HA, så isotopmärkning testades som en central metod. Genom att använda detta tillvägagångssätt biosyntetiserades ^{13}C , ^{15}N -berikad HA, och nivån av isotopinkorporering bestämdes kvantitativt.

Resultaten i denna avhandling förbättrar förståelsen av HA och andra relaterade strukturer genom att ge kunskap om deras strukturella och dynamiska egenskaper. Dessutom visar resultaten att isotopmärkning är en lovande metod för att förbättra analysen av dessa komplexa system.

Acknowledgements

At last, we have reached the final phase of this thesis, a stage that I find particularly challenging to write. I am deeply grateful to all the individuals involved, as each of you has played a crucial role in making this journey possible.

First of all, I would like to express my utmost gratitude to my main supervisor, **Corine Sandström**. Thank you for giving me this opportunity to be your Ph.D. student five years ago; it has been a real pleasure to learn from you, work with you, and get to know you along this journey. You are not only a great scientist, but more importantly, a warm and kind person who is always there for me and willing to selflessly help me. I am very thankful for everything.

Thank you, my co-supervisor **Gustav Nestor**. I have always been impressed by your passion for science and am grateful for the invaluable support and patience you have shown me over the years. Thank you for teaching me about NMR, sugars, and many other things. Thank you for the countless hours you invested in our work and for always coming up with solutions and ideas when I am at my wit's end.

Thank you, my co-supervisor **Frida Wende**, for your help with our first paper at the beginning of my Ph.D. studies. Thank you for inviting us to visit Galderma's laboratory and for providing me with the opportunity to present my research. Also, I want to express my appreciation for the time we spent together in Portugal—it was a lot of fun!

Suresh Gohil, what would we do without you? Thank you for still being willing to work and for not choosing to retire. Thank you for all your help and support with MS and HA. **Jan Eriksson**, thank you for teaching me how

to use the Orbitrap and for assisting me in crafting the MS section. Additionally, thank you for sharing all the enjoyable and entertaining stories.

I would like to thank my co-authors: **Tomasz Niedziela**, **Karolina Ucieklak**, and **Åke Öhrlund**, for providing the research material and support throughout the manuscript submission process.

Hanna, an unknown student once used the phrase “ett ljus i mörket” to describe you, which I find so accurate. Thank you for being a wonderful office mate and for being there for me over the past five years. Your strong empathy for others and constant kindness and helpfulness have made a significant difference. To my former office mate, **Johnny**, ever since you left, our thermophilic office has turned into a 20.5 °C ice cube. Your absence is deeply felt, especially since no one is willing to play the silly 'you know who' game with me anymore. **Elin**, it has been a pleasure to share the entire journey at SLU with you from day one. I wish you the best of luck as you approach the final stages. **Mathilde**, thank you for all the engaging discussions in the Fika room and for always responding so quickly to my thesis-related questions.

Peter and **Tatiana**, thank you for all the help with NMR. It was a very nice experience with the protein structure NMR course, and thanks for showing me the outside world of carbohydrate NMR. **Anders S.**, thank you for all the assistance with teaching and proofreading the MS section in my kappa. Also, thank you for always being so positive and cheerful. **Lena** and **Christina**, thank you for your help with the SEC and HPLC systems. **Christina**, we missed you a lot in the lab, but not as much as the drinks you prepared! **Anders B.**, thank you for your help with the analytical natural product course. **Janicka**, thank you for taking on the responsibility of ordering the chemicals and lab equipment. **Nazila**, welcome to the group, and I hope you have a pleasant stay in Sweden.

The 2D corridor has the reputation of being a 'happy' corridor (or maybe we're the only ones who think so), which can be attributed to all the wonderful colleagues. Thank you, **Anja**, **Solja**, and **Klara**, for being so outgoing and social, and for bringing so much energy to the lunchroom. **Mathias**, thank you for always participating in the silly and sometimes ridiculous events we came up with, and for always being so nice and considerate to everyone. **Jaqueline**, thank you for having lunches with me over the past few weeks when our corridor was practically deserted, and for

discussing all sorts of topics. **Troy**, thanks for being so easy to talk to and for sharing/complaining about things. **Jing**, it is always delightful to be able to converse in Chinese with you, and thanks for always having a smile on your face. A big thank you to **Ani** for caring about me and encouraging me in the final stage, and even for dreaming about my manuscript ☺. Thanks for teaching me how to do macramé; I promise to teach you mahjong this autumn!

Thank you, **Maud, Galia, Henrik, Gulaim, Vadim, Ingmar, Saeid, Ali, Fredric, Ning, Björn, Filip, Alejandra, Johanna, Oksana, Marijana, and Tahereh**, for creating such a pleasant working environment in the corridor throughout the years.

Thank you, **Monika**, for your consistent support and care for all your Ph.D. students. I would also like to extend my gratitude to **all my fellow Ph.D. students** at the Department of Molecular Sciences for their support and help.

Gunilla, thank you for your assistance in preparing the MEKÖL lab. **Nils, Mikolaj**, and **Leslie**, thank you for helping with IT-related issues. **Robert** and **Magnus**, thank you for your support in resolving building-related problems.

I would like to express my gratitude to **all my friends** back home and in Sweden. A special thanks to **Alice** and **Lexi**. I am appreciative of the meaningful connections we have made and all the unforgettable memories we have created together.

Gaby, thank you for introducing me to the best parts of Brilon and for making me feel at home there. Your thoughtful letters, cards, and gifts throughout the years have meant a lot to me.

感谢我所有的家人对我无私的支持和鼓励。感谢我的**爷爷**,尽管你在我读博士的最后一年离开了我们,但我时常会想起小时候我们在一起的时光和你带给我生命中的温暖。感谢我的**奶奶**,谢谢你总是牵挂着我,爱着我,用你独有的方式保护着我。感谢我的爸爸妈妈:**薛保平**和**张丰爱**。感谢你们对我毫无保留的爱和包容。是你们所付出的一切才让我有机会去选择和实现自己想要的人生。所以我把这篇博士文献给你们。期待我们分离 1356 天后的再次相聚!

Finally, to **Tim**. Thank you for your patience, your advice, and most importantly, your faith in us. I have mulled this paragraph over and over but cannot find the right words precisely convey my feelings. So this is just a little reminder of how much you mean to me. I look forward to the times ahead, to the two of us navigating through thick and thin.



Relaxation and diffusion of water protons in BDDE cross-linked hyaluronic acid hydrogels investigated by NMR spectroscopy—Comparison with physicochemical properties

Frida J. Wende^{a,1,2}, Yan Xue^{a,2}, Gustav Nestor^a, Åke Öhrlund^b, Corine Sandström^{a,*}

^a Department of Molecular Sciences, Uppsala BioCenter, Swedish University of Agricultural Sciences, P.O. Box 7015, SE-750 07 Uppsala, Sweden

^b Development Galderma, Seminariegatan 21, SE-752 28 Uppsala, Sweden

ARTICLE INFO

Keywords:
Hyaluronic acid
Hydrogel
NMR
Water
Relaxation
Diffusion

ABSTRACT

Cross-linked hyaluronic acid (HA) hydrogels are used in many biomedical applications but their characterization in order to distinguish between physicochemical properties is challenging. Longitudinal (T_1) and transverse (T_2) relaxation times and diffusion coefficient (D) of water protons in diepoxide 1,4-butanediol diglycidyl ether (BDDE)-cross-linked HA hydrogels were analyzed by high-field NMR spectroscopy to distinguish between different physicochemical properties. Hydrogels of different degrees of modification and cross-linking, representing a range of gel content, swelling ability, elastic and viscous behavior were studied, as well as solutions of native HA of different molecular weights. T_1 , T_2 and D were measured for several concentrations of HA and as a function of temperature. D and T_1 showed a weak concentration dependence, but did not differ between the hydrogels. T_2 , dominated by chemical exchange between water protons and exchangeable protons of HA, varied significantly between the different hydrogels and the temperature profiles changed dramatically between different concentrations.

1. Introduction

The high water holding capacity and high viscoelasticity of hyaluronic acid (HA) together with its biocompatibility and biodegradability make it suitable for many biomedical applications (Burdick & Prestwich, 2011; Lapčík, Lapčík, De Smedt, Demeester, & Chabreček, 1998; Schanté, Zuber, Herlin, & Vandamme, 2011). However, the rapid *in vivo* degradation by enzymes and reactive oxygen species considerably limits the applications of native HA (Fraser, Laurent, & Laurent, 1997). Wide varieties of cross-linking strategies have thus been employed to create materials that are less susceptible to *in vivo* degradation (Schanté et al., 2011; Segura et al., 2005). The objective of cross-linking is also to preserve the biocompatibility and physical functionality of unmodified HA (Fig. 1a), while improving the viscoelastic properties and long-lasting effect (Baek et al., 2018).

The chemical and physicochemical properties of hydrogels are characterized by the degree of modification (MoD), the degree of cross-linking (CrD) (Kenne et al., 2013), the swelling degree (SwD), as well as

the gel strength defined as the elastic modulus (G'), viscous modulus (G'') and damping ($\tan \delta$). Gel concentration and particle size might also affect the properties. The mechanical, rheological and swelling properties of the hydrogel depend on the nature of the cross-linker and on the extent of modification. The diepoxide 1,4-butanediol diglycidyl ether (BDDE) (Fig. 1b) is one of the most commonly used HA cross-linkers due to the high reactivity of the epoxide, the biostability of the formed ether linkages, and the mechanical properties of the hydrogel (Ågerup, Berg, & Åkermark, 2005; Segura et al., 2005).

The characterization of HA hydrogels is often challenging and there is a need for simple methods that can be used to discriminate between hydrogels with different MoD and CrD or between strong and weak hydrogels in terms of viscoelastic properties. Since water is the main component of polysaccharide-based hydrogels, studying the behavior of water protons in the hydrogels might show correlations with, or provide information on these physicochemical properties.

In this work, the longitudinal (T_1) and transverse (T_2) relaxation times, and the diffusion coefficient (D) of water protons in HA

* Corresponding author: Department of Molecular Sciences, Swedish University of Agricultural Sciences, P.O. Box 7015, 750 07 Uppsala, Sweden.

E-mail addresses: Frida.wende@slu.se, Frida.Wende@galderma.com (F.J. Wende), Yan.xue@slu.se (Y. Xue), gustav.nestor@slu.se (G. Nestor), ake.ohrlund@galderma.com (Å. Öhrlund), corine.sandstrom@slu.se (C. Sandström).

¹ Present address: Development Galderma, Seminariegatan 21, SE-752 28 Uppsala, Sweden.

² Both authors contributed equally to the work.

<https://doi.org/10.1016/j.carbpol.2020.116768>

Received 3 May 2020; Received in revised form 23 June 2020; Accepted 12 July 2020

Available online 15 July 2020

0144-8617/ © 2020 Published by Elsevier Ltd.

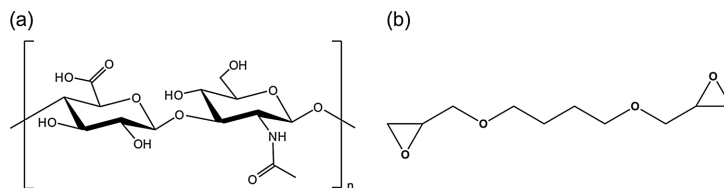


Fig. 1. (a) Repeating unit of hyaluronic acid polysaccharide; (b) Chemical structure of BDDE.

hydrogels cross-linked with BDDE and with different MoD and CrD were measured with high-field NMR spectroscopy. Swelling ability, elastic and viscous behavior of the hydrogels as well as the intrinsic viscosity of the starting material were also determined. The aim of this work was to determine how the diffusion and relaxation behavior of water protons vary in the different hydrogels and whether NMR data can be used to discriminate between the different hydrogels and native HA solutions.

2. Experimental

2.1. Sample preparation

The HA-BDDE hydrogels were produced by cross-linking HA (from *Streptococcus zooepidemicus*) with BDDE under alkaline conditions at room temperature. The reaction was quenched by neutralization of pH and heat treatment at 70 °C. Variation of some parameters such as intrinsic viscosity of HA, concentration of HA, BDDE and NaOH as well as time for the cross-linking reactions provided nine hydrogels with different chemical and physicochemical properties (A–I; see Table 1). The particle size of the hydrogels was reduced by pressing them through a metal mesh. The hydrogels were then precipitated in ethanol and stored in a freezer until use. Three unmodified HA samples with different molecular weights (85 kDa, 172 kDa, and 3 MDa) were also used. Dried hydrogels and unmodified HA powders were dissolved in 90 % H₂O/10 % D₂O directly in the 5 mm NMR tubes for three concentration ranges, low (ca. 2.5 mg/mL), medium (ca. 5 mg/mL) and high (ca. 10 mg/mL). The pH of the samples was measured to be between 6 and 7. The exact concentration of HA in each sample was determined by NMR analysis of enzymatic digests (*vide infra*) after completion of all T_1 , T_2 and D measurements. Swelling of the hydrogels was allowed for at least one month prior to NMR analysis. Hydrogels A and H had a low swelling degree and could not swell to reach low or medium concentration levels. Hydrogel D at high concentration was not analyzed due to persistent air bubbles in the sample. A water reference sample containing 90 % H₂O and 10 % D₂O was also prepared.

2.2. NMR spectroscopy

NMR spectra were recorded on a Bruker Avance III 600 MHz spectrometer using a 5mm broadband observe detection SmartProbe equipped with z-gradient. The temperature (5–70 °C) was controlled with methanol and/or ethylene glycol reference samples and was within ± 1 °C.

T_1 was determined from a saturation recovery experiment, where the water signal was presaturated by continuous-wave (CW) irradiation with a weak radiofrequency field (60 Hz) during 10 s after a relaxation delay of 30 s. A variable delay list of 14 points between 0.15 and 7 s was used. One scan was recorded for each point. The saturation recovery experiment was chosen instead of the inversion recovery experiment to avoid the effects of radiation damping (Mao et al., 1994).

T_2 was determined from a conventional Carr-Purcell-Meiboom-Gill (CPMG) sequence (relaxation delay-90°-(τ -180°- τ)_n-acquire), with 8 scans collected for each spin echo time. A number of 14 total spin echo times between 21 ms and 6.7 s were sampled, with a pulse spacing τ of 1.3 ms and a relaxation delay of 30 s.

D was determined from a bipolar-pair longitudinal-eddy-current delay (BPP-LED) DOSY experiment (Bruker pulse sequence ledbpgp2s) using a diffusion delay (Δ) of 50 ms, an effective gradient pulse duration (δ) of 2 ms, and a relaxation delay of 20 s. The gradient amplitude (g) was varied in 16 steps from 2.4–45.7 G/cm (scaled to rectangular gradients), with 16 scans acquired for each step.

Topspin 4.0 (Bruker) was used for processing and calculation of relaxation times and diffusion coefficients. Integrals of the water signal were fitted to Eq. (1) for T_1 , Eq. (2) for T_2 and Eq. (3) for D :

$$I(t) = I_0 + P \cdot e^{-t/T_1} \quad (1)$$

$$I(t) = P \cdot e^{-t/T_2} \quad (2)$$

$$I(g) = I_0 \cdot e^{-D \gamma^2 g^2 \delta^2 \left(\Delta - \frac{\delta}{3}\right)} \quad (3)$$

where γ is the gyromagnetic ratio. The decay curves from D and T_2 measurements and the build-up curves from saturation-recovery T_1 measurements were inspected for possible two-component behavior, but mono-component exponential fitting was found to give an excellent fit for most samples and was used on all measurements to avoid

Table 1
Modification, cross-linking, rheological and swelling parameters for HA-BDDE hydrogels A-I.

Sample	MoD (%)	CrR	CrD (%)	GelC* (%)	SwD (g/g)	G' (Pa)	G'' (Pa)	Tan δ	$[\eta]$ ** (m ³ /kg)
A	7.4	0.1	0.8	93.9	173	870	75	0.09	2.77
B	1.0	0.2	0.2	88.7	144	741	101	0.14	1.70
C	1.1	0.5	0.5	88.0	226	401	27	0.07	1.76
D	1.5	0.5	0.8	96.3	116	1845	188	0.10	1.78
E	1.1	0.3	0.3	77.8	887	45	14	0.32	1.80
F	7.0	0.1	0.9	76.3	827	66	18	0.28	2.94
G	0.9	0.3	0.2	62.9	542	109	23	0.21	1.92
H	4.6	0.5	2.1	98.0	79	2053	304	0.15	0.26
I	2.9	0.2	0.6	86.7	359	288	15	0.05	2.77

* Fraction of non-extractable (cross-linked) HA to total amount of HA gel.

** The intrinsic viscosity of the HA starting material.

overfitting. The water signal always appeared as a symmetric signal without shoulders and there was no indication of distinct water signals (Fig. 1, SI). The standard error of T_1 , T_2 and D from the nonlinear fitting were estimated by an iterative approach, where the parameter of interest was varied to define a 95 % confidence interval from the sum of squared residuals (Kemmer & Keller, 2010). Experiments performed on the same NMR samples were run in duplicates for determination of D and in triplicates for determination of T_1 and T_2 . The standard deviation between experiments was generally lower than the error from the fitting procedure. The estimated relative standard errors were on average < 0.7 % for T_1 , < 1.0 % for T_2 , and < 0.3 % for D . A few samples showed larger T_2 relative standard errors, but < 4.5 %.

2.3. Determination of HA concentration

After completion of the NMR measurements, an aqueous solution of chondroitinase ABC (70 μ L, 4 units/mL from *Proteus vulgaris* (Sigma Aldrich, art. No. C2905) was added to the NMR tube. The sample was incubated at 37 °C for 24 h to allow for degradation (Fig. 2, SI). The solvent was removed by freeze-drying and the dried sample was dissolved in D₂O (0.6 mL) containing TSP (trimethylsilylpropanoic acid) as an internal standard (4.2 mM). Quantitative 1D ¹H NMR spectra (Fig. 2, SI) were obtained using a relaxation delay of 30 s and 128 scans. After phase and baseline correction, the integral of the signal corresponding to the *N*-acetyl methyl resonance at 2.1 ppm (3 H) and to the TSP resonance at 0.0 ppm (9 H) were used to calculate the concentration of HA.

2.4. Analysis of physicochemical properties of hydrogels (A–I)

Determination of MoD, CrR and CrD was performed by enzymatic degradation followed by ¹H NMR spectroscopy and liquid chromatography–mass spectrometry (LC–MS) analysis according to the methods described by Kenne et al. (2013).

Rheological analysis (G' , G'' , $\tan \delta$), determination of gel content and swelling degree (SwD) followed the procedures described by Edsman, Nord, Öhrlund, Lärkner, and Kenne (2012)). SwD is the swelling degree measured as the ratio between weights of swollen hydrogel to weight of dried hydrogel. The concentration of the hydrogels was 20 mg/mL for the rheological analysis.

The intrinsic viscosity of the HA raw materials was determined according to principle as described in Ph.Eur. monograph 1472, using an automated Ubbelohde capillary viscometer Lauda PVS1/4 (Lauda-Königshofen, Germany).

3. Results

Nine HA-BDDE hydrogels (A–I) with different physicochemical properties were investigated. Table 1 shows the chemical properties represented by MoD, CrR and CrD of the hydrogels, and the intrinsic viscosity of HA prior to cross-linking (as a measure of the molecular weight of the HA raw material). The physical properties, represented by SwD and gel strength (G' , G'' and $\tan \delta$) of the hydrogels are also presented in Table 1.

The NMR study, including measurement of T_1 , T_2 and D of water protons in the hydrogels, was performed for three concentration ranges, low, medium and high concentration of HA, and in the temperature interval 5–70 °C (Table 2). Solutions of three native HA polysaccharides with molecular weights of 85 kDa, 172 kDa and 3 MDa were also analyzed by NMR.

3.1. Physicochemical properties (degree of modification, cross-linking, rheological parameters, swelling degree) of the HA hydrogels A–I

Hydrogels A–I had a broad variety of physicochemical properties. Inspection of Table 1 shows the relationship between G' , G'' and SwD.

Hydrogels with higher G' and G'' had lower SwD. For example hydrogel H, which had the highest G' and G'' , had the lowest SwD while hydrogel E, which had the lowest G' and G'' , had the highest SwD. From these data, the hydrogels can be divided into strong (D and H), medium (A, B, C and I) and weak (E, F and G) viscoelasticity. The MoD of the hydrogels (Table 1) varied from 1 to 7% whereas the CrD varied from 0.2 to 2.1 %.

3.2. NMR analysis of D , T_1 and T_2 of water protons in the HA samples

Figs. 2 and 3 show the temperature dependence of T_1 and D of water protons in hydrogels A–I and in the three native HA samples. Both D and T_1 increase with temperature and have very similar values for all samples. The water reference is included in Figs. 2 and 3 showing that the behavior of water protons in the HA samples is similar to that of pure water, but with lower T_1 and D especially at higher temperatures. Small decreases in T_1 and D were observed when increasing the concentration (see Table 2), but there is no significant difference in T_1 or D between HA hydrogels and native HA solutions.

Fig. 4 depicts the temperature dependence of T_2 of water protons for the HA samples in the temperature range 5–70 °C. For comparison, the T_2 of the pure water reference sample is plotted together with the T_2 of the low concentration HA samples in Fig. 3, SI.

At the lowest HA concentration (Fig. 4a), the T_2 of the water protons increases with temperature for all samples, but less than in pure water. In the temperature range of 5–45 °C, the 85 and 172 kDa samples have a very similar profile and are clearly separated from the other samples by higher T_2 . The 3 MDa HA is clearly different from the hydrogels, although with T_2 closer to that of the hydrogels than to that of the 85 and 172 kDa samples. The hydrogels do not show any significant difference in T_2 values in the temperature range of 5–45 °C, except for hydrogel D, which has a lower T_2 . Inspection of Table 1 shows that D has together with H (which could not be analyzed at low HA concentration, see experimental) the lowest swelling degree and highest G' and G'' . Above 45 °C, hydrogel B has a more steep increase of T_2 , whereas T_2 of hydrogel G and the 172 kDa sample level off and do not increase further.

As the HA concentration is increased, different temperature profiles are observed for T_2 of water protons (Fig. 4b). In the three solutions of native HA, an increase in T_2 is first observed upon an elevation of the temperature. After reaching a maximum, further increases of temperature result in a decrease in T_2 . For the 85 and 172 kDa samples, the T_2 values are nearly identical over the entire temperature range with a maximum around 20–25 °C. The T_2 values are shorter for the 3 MDa sample and a maximum is reached at 30–35 °C. In most of the HA hydrogels, a smaller continuous increase of T_2 up to 15–30 °C and an unchanged or slightly increasing T_2 at higher temperatures is observed. Thus, the hydrogels are relatively insensitive to variation in temperature whereas the 85 and 172 kDa samples show the largest T_2 changes. Overall, T_2 values are smaller and the amplitude of the changes over the temperature range is lower than for the low concentration solutions.

For the highest concentration (Fig. 4c), a T_2 maximum is reached at a lower temperature (10–20 °C). Hydrogel H, which has the highest G' , G'' and CrD and the lowest SwD, has the lowest T_2 with a relatively flat temperature profile when compared to the other hydrogels. Hydrogel E, F, G, and I are clustered at low T_2 and with a relatively flat temperature profile similar to that of hydrogel H. Also the A, B, and C hydrogels are clustered, but at higher T_2 and exhibit temperature profiles similar to that of native HA solutions, especially the 3 MDa sample. The A, B, and C hydrogels are higher in G' and G'' and lower in SwD compared to the E, F, G, and I hydrogels (Table 1). The 85 and 172 kDa HA solutions exhibit a strong drop in T_2 from 15 °C.

4. Discussion

Possible relationships between degree of cross-linking, rheological parameters and NMR parameters such as D , T_1 and T_2 (Barbucci et al.,

Table 2
Average water T_1 and D (\pm standard deviation) of water protons in HA hydrogels and native HA solutions at different temperatures and concentrations.

Temp. (°C)	T_1 (s)			D (10^{-9} m ² /s)		
	Low Conc.	Medium Conc.	High Conc.	Low Conc.	Medium Conc.	High Conc.
5	1.96 ± 0.01	1.94 ± 0.01	1.93 ± 0.01	1.12 ± 0.007	1.10 ± 0.003	1.09 ± 0.011
10	2.31 ± 0.05	2.28 ± 0.01	2.27 ± 0.03	1.31 ± 0.009	1.30 ± 0.005	1.29 ± 0.005
15	2.62 ± 0.02	2.64 ± 0.01	2.58 ± 0.02	1.52 ± 0.006	1.51 ± 0.006	1.49 ± 0.012
20	3.00 ± 0.01	3.00 ± 0.02	2.96 ± 0.03	1.75 ± 0.008	1.74 ± 0.005	1.72 ± 0.008
25	3.31 ± 0.06	3.39 ± 0.05	3.30 ± 0.05	1.99 ± 0.006	1.97 ± 0.005	1.95 ± 0.010
30	3.82 ± 0.02	3.84 ± 0.01	3.76 ± 0.02	2.25 ± 0.005	2.24 ± 0.005	2.21 ± 0.009
35	4.24 ± 0.04	4.25 ± 0.03	4.18 ± 0.04	2.52 ± 0.014	2.50 ± 0.008	2.48 ± 0.012
40	4.74 ± 0.02	4.77 ± 0.02	4.68 ± 0.03	2.81 ± 0.009	2.82 ± 0.008	2.76 ± 0.016
45	5.19 ± 0.04	5.24 ± 0.02	5.12 ± 0.06	3.12 ± 0.012	3.13 ± 0.015	3.06 ± 0.024
50	5.68 ± 0.07	5.77 ± 0.02	5.64 ± 0.05	3.43 ± 0.008	3.47 ± 0.018	3.38 ± 0.031
55	6.21 ± 0.03	6.19 ± 0.05	6.14 ± 0.05	3.77 ± 0.014	3.74 ± 0.025	3.70 ± 0.019
60	6.71 ± 0.06	6.70 ± 0.05	6.63 ± 0.09	4.12 ± 0.023	4.08 ± 0.022	4.05 ± 0.041
65	7.34 ± 0.07	7.31 ± 0.08	7.25 ± 0.06	4.51 ± 0.028	4.46 ± 0.025	4.42 ± 0.025
70	7.88 ± 0.08	7.80 ± 0.10	7.77 ± 0.09	4.88 ± 0.034	4.84 ± 0.017	4.79 ± 0.051

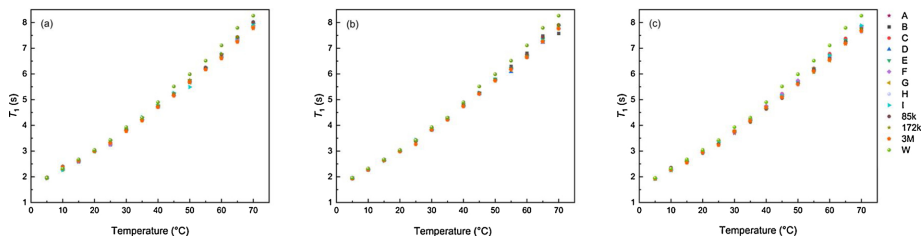


Fig. 2. Longitudinal relaxation, T_1 (s) as a function of temperature (± 1 °C) at (a) low, (b) medium and (c) high HA concentration. A–I: Hydrogel A–I; 85k, 172k and 3 M – Unmodified HA with molecular weight of 85 kDa, 172 kDa, and 3 MDa; W – Water reference.

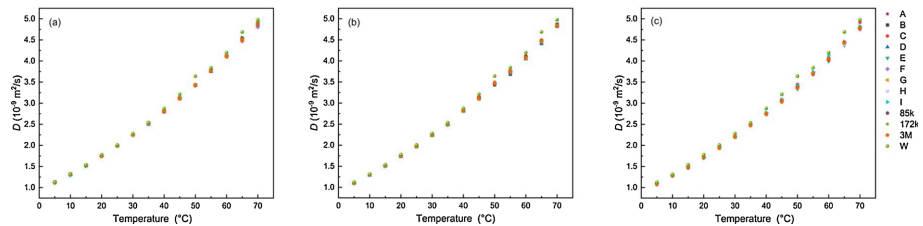


Fig. 3. Diffusion coefficients, D (m^2/s) as a function of temperature (± 1 °C) at (a) low, (b) medium and (c) high HA concentration. A–I: Hydrogel A–I; 85k, 172k and 3 M – Unmodified HA with molecular weight of 85 kDa, 172 kDa, and 3 MDa; W – Water reference.

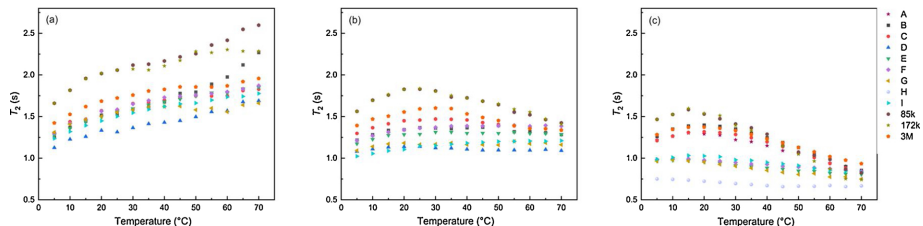


Fig. 4. Transverse relaxation, T_2 (s) as a function of temperature at (a) low, (b) medium and (c) high HA concentration. A–I: Hydrogel A–I; 85k, 172k and 3 M – Unmodified HA with molecular weight of 85 kDa, 172 kDa, and 3 MDa.

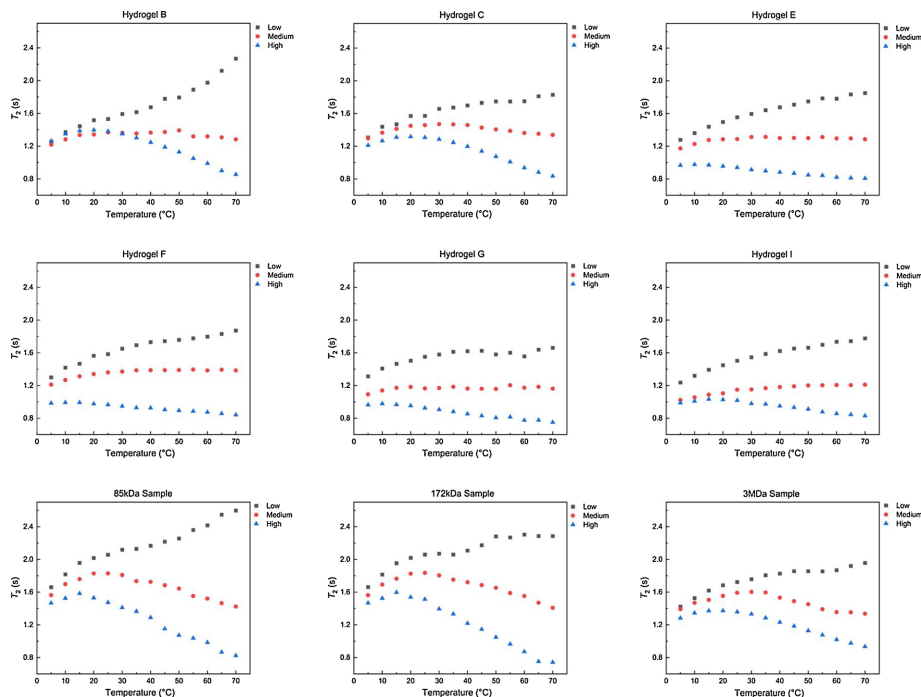


Fig. 5. Transverse relaxation, T_2 (s) as a function of temperature for individual sample at low, medium and high concentrations.

2006) were investigated in the present study. Hydrogel H had the lowest SwD and the highest G' together with the highest CrD but no clear correlations between CrD and rheological properties were observed for the other hydrogels. An inverse relationship between cross-linker ratio and SwD, sometimes shown for polymer gels (La Gatta et al., 2013; Ström, Larsson, & Okay, 2015) is not evident here, but the degree of cross-linking in the hydrogels investigated in the present work was much lower (0.2–2.1 %). Other parameters such as gel content, apparent molecular weight and the intrinsic viscosity of the starting material will also affect the relationship.

Water T_1 and D of the hydrogels and of the native HA samples correlated with temperature and to some extent with concentration. Figs. 2, 3 and Table 2 show that the T_1 and D of water protons decreased with increasing concentration of hydrogel, which is in accordance with a higher degree of polymer-bound water molecules at higher concentrations. A study on water in aggrecan solutions performed at low and high field has shown that D was approximately proportional to the longitudinal relaxation rate such that the quotient D/T_1 was constant for all temperatures (8–38 °C) and concentrations (Foster, Damion, Baboolal, Smye, & Ries, 2016). This was attributed to local microviscosity controlling both processes. The same behavior was earlier shown for pure water from 0 to 40 °C (Simpson & Carr, 1958). Above this temperature, T_1 did not follow the viscosity in the predicted manner (Simpson & Carr, 1958). In the present study, an increase of D/T_1 with temperature was observed (Fig. 4, SI) suggesting that other factors than the local microviscosity are important in the HA hydrogels. However, variations of the apparent D with Δ indicated that some convection occurred at 50 °C or higher temperature, leading to an overestimation of D (Fig. 4, SI) at the highest temperatures.

While the spin-lattice relaxation and the diffusion coefficients show

a simple behavior at high magnetic field, the spin-spin relaxation is more complex (Fig. 4). Hills and coworkers (Hills, Wright, & Belton, 1989; Hills, 1991) have demonstrated that the dominant mechanism of water proton transverse relaxation in hydrogels is that of chemical exchange between water protons and exchangeable protons (OH and NH protons) of the polymers. The cross relaxation of water with hydrogel is negligible compared to chemical exchange even at low temperatures. The chemical exchange, defined as molecular spins exchanging position with others in their surrounding chemical environment, may affect the frequency and linewidth of the corresponding signal in the NMR spectra, but it can also give insight on molecular structures. Since water spin-spin relaxation in hydrogels is dominated by the chemical exchange between water and exchangeable polymer protons, the polymer protons will contribute increasingly to the measured T_2 as the water content decreases and the proportion of polymer protons increase. Hence, the overall behavior observed in Fig. 4a–c is representative of the water content dependencies on both the water proton and HA proton motions.

Consequently, different behaviors have been observed upon temperature changes for hydrogels containing exchangeable protons or not. For hydrogels without exchangeable protons, such as co-polymers of methyl methacrylate, T_2 increased monotonically with temperature (McConville & Pope, 2001; McConville, Whittaker, & Pope, 2002). More complex behavior was observed for hydrogels with exchangeable protons with local T_2 minima and maxima depending on the temperature (Fabri, Williams, & Halstead, 2005; McConville & Pope, 2001). For agarose and kappa carrageenan's, an increase in linewidth or transverse relaxation rate of water protons has been shown from low temperature to ca. 40 °C, followed by a decrease (Ablett, Lillford, Baghdadi, & Derbyshire, 1978; Aizawa et al., 1973; Andrasko, 1975; Child & Pryce,

1972). Such behavior was not observed for polymers without exchangeable protons. Assuming a two-component system, the components being the water protons (b) and the exchangeable polymer protons (c), the T_2 observed in HA hydrogels A-H and the three native HA solutions at medium and high concentrations could be explained as follows: At low temperature, T_{2c} is very short and the exchange correlation time τ_{ex} is very long. The measured T_2 can therefore be approximated by T_{2b} , which increases with increasing temperature. As the temperature increases, the exchange rate increases and T_{2c} makes a larger contribution to the observed T_2 . Since T_{2c} is significantly shorter than T_{2b} , the measured T_2 at a certain point actually decreases with increasing temperature.

Fig. 4a–c shows that for a specific temperature and sample, T_2 values of water protons decreases as the concentration increased and thus as the number of exchangeable protons increases. T_2 also decreased as the molecular weight of HA increased (from 85 kDa to 3 MDa).

Hydrogels E, F and G are more sensitive to concentration changes than B, C and D (Fig. 5). Thus, T_2 values of water protons in stronger hydrogels are less affected by concentration changes than in weaker hydrogels. Concerning temperature effects, the samples of the lowest concentration and/or the lowest molecular weight have larger variations in T_2 over the temperature range 5–50 °C. The T_2 of water is much less sensitive to temperature changes in most of the HA-BDDE hydrogels as compared to the native HA solutions or the water reference. For example, at the highest concentration, T_2 in the cross-linked hydrogel H is almost unchanged in the temperature range 5–50 °C (0.79 to 0.75 s), while T_2 in HA 172 kDa decreases from 1.4 to 0.8 s. Differences among the cross-linked HA are also observed. The T_2 of water protons in hydrogel D and H are relatively insensitive to temperature changes. These are the strongest of the analyzed hydrogels with the highest CrD, G' and G'' and the lowest SwD.

The decrease in T_2 with concentration indicates that the fraction of exchangeable protons in states with restricted motion increases with hyaluronic acid concentration. The lower response of some hydrogels to temperature change might be due to the fact that the mobility of these large polymers is less affected by temperature change if compared to smaller or more flexible polymers. Lower temperatures are sufficient for HA of low concentration or for weaker hydrogel to be mobile and thereby to have a high rate of hydroxyl proton exchange with water protons.

A mechanical and optical rheological study showed that for a HA polymer of 1.43 MDa, an increase in temperature from 20 to 60 °C decreases the viscosity corresponding to a large increase in chain mobility. The relaxation of the system became faster as the temperature was increased and there was no indication of large structural or conformational change in this temperature change (Cowman, Schmidt, Raghavan, & Stecco, 2015; Oelschlaeger, Cota Pinto Coelho, & Willenbacher, 2013). Thus, to attribute the shape of the T_2 curves in terms of increasingly effective exchange process instead of in terms of temperature dependent conformational changes would be in good agreement with studies on the viscoelastic properties of HA (Oelschlaeger et al., 2013).

5. Conclusion

The aim of this work was to investigate if the T_1 , T_2 and D of water protons in BDDE cross-linked HA hydrogels could be correlated to physicochemical properties such as CrD and rheological properties. Three native HA of different molecular weights were also investigated. D and T_1 were very similar for all compounds investigated while T_2 , which at high magnetic field is dominated by the chemical exchange between water protons and exchangeable protons of HA, showed significant variations between samples. Thus, T_2 measurements of water, at different HA concentrations and over a range of temperatures, allowed to distinguish between cross-linked and non-cross-linked HA. Some distinction between strong, medium and weak hydrogels could be

achieved based on the T_2 temperature profiles but the relationship to CrD was not straightforward. This might be due to the fact that all hydrogels but one had a low CrD (< 1 %). The sample with a higher CrD (2.1 %) displayed significantly lower T_2 mostly independent of temperature changes. That the T_2 behavior can be explained in terms of exchange process between water and hyaluronan protons instead of in terms of a temperature dependent conformational change could be investigated by changing the H₂O/D₂O ratio. Complementary studies involving measurements of T_1 and T_2 at low-field NMR could also be performed to differentiate between the different components of relaxation. Beside these experiments, ¹³C CPMAS NMR studies of native and cross-linked HA-BDDE hydrogels could provide information on the hydration of the polymers (Brus et al., 2017).

Author's contributions

All authors have contributed to the manuscript

Appendix A. Supplementary data

Supplementary material related to this article can be found, in the online version, at doi:<https://doi.org/10.1016/j.carbpol.2020.116768>.

References

- Ablett, S., Lillford, P. J., Baghdadi, S. M. A., & Derbyshire, W. (1978). Nuclear magnetic resonance investigations of polysaccharide films, sols, and gels. I. Agarose. *Journal of Colloid and Interface Science*, 67(2), 355–377. [https://doi.org/10.1016/0021-9797\(78\)90020-6](https://doi.org/10.1016/0021-9797(78)90020-6).
- Ågerup, B., Berg, P., & Åkermark, C. (2005). Non-animal stabilized hyaluronic acid: A new formulation for the treatment of osteoarthritis. *BioDrugs*, 19(1), 23–30. <https://doi.org/10.2165/00063030-20051901-00003>.
- Aizawa, M., Suzuki, S., Suzuki, T., & Toyama, H. (1973). Properties of water in macromolecular gels. V. anomalous temperature dependence of the nuclear magnetic resonance line-width of water in macromolecular gels. *Bulletin of the Chemical Society of Japan*, 46(1), 116–119. <https://doi.org/10.1246/bcsj.46.116>.
- Andrasko, J. (1975). Water in agarose gels studied by nuclear magnetic resonance relaxation in the rotating frame. *Biophysical Journal*, 15(12), 1235–1243. [https://doi.org/10.1016/S0006-3495\(75\)85896-6](https://doi.org/10.1016/S0006-3495(75)85896-6).
- Baek, J., Fan, Y., Jeong, S.-H., Lee, H.-Y., Jung, H.-D., Kim, H.-E., et al. (2018). Facile strategy involving low-temperature chemical cross-linking to enhance the physical and biological properties of hyaluronic acid hydrogel. *Carbohydrate Polymers*, 202, 545–553. <https://doi.org/10.1016/j.carbpol.2018.09.014>.
- Barbucci, R., Leone, G., Chiumentoni, A., Di Cocco, M. E., D'Orazio, G., Gianferri, R., et al. (2006). Low- and high-resolution nuclear magnetic resonance (NMR) characterization of hyaluronan-based native and sulfated hydrogels. *Carbohydrate Research*, 341, 1848–1858. <https://doi.org/10.1016/j.carres.2006.04.046>.
- Brus, J., Urbanova, M., Czernek, J., Pavelkova, M., Kubova, K., Vyslouliz, J., et al. (2017). Structure and dynamics of alginate gels cross-linked by polyvalent ions probed via solid state NMR spectroscopy. *Biomacromolecules*, 18, 2478–2488. <https://doi.org/10.1021/acs.biomac.7b00627>.
- Burdick, J. A., & Prestwich, G. D. (2011). Hyaluronic acid hydrogels for biomedical applications. *Advanced Materials*, 23(12), H41–H56. <https://doi.org/10.1002/adma.201003963>.
- Child, T. F., & Pryce, N. G. (1972). Steady-state and pulsed NMR studies of gelation in aqueous agarose. *Biopolymers*, 11(2), 409–429. <https://doi.org/10.1002/bip.1972.360110208>.
- Cowman, M. K., Schmidt, T. A., Raghavan, P., & Stecco, A. (2015). Viscoelastic properties of hyaluronan in physiological conditions. *F1000Research*, 4, 622. <https://doi.org/10.12688/f1000research.6885.1>.
- Edsman, K., Nord, L. I., Öhrlund, Å., Lärkner, H., & Kenne, A. H. (2012). Gel properties of hyaluronic acid dermal fillers. *Dermatologic Surgery*, 38(7pt2), 1170–1179. <https://doi.org/10.1111/j.1524-4725.2012.02472.x>.
- Fabri, D., Williams, M. A. K., & Halstead, T. K. (2005). Water T2 relaxation in sugar solutions. *Carbohydrate Research*, 340(5), 889–905. <https://doi.org/10.1016/j.carres.2005.01.034>.
- Foster, R. J., Damion, R. A., Baboolal, T. G., Smye, S. W., & Ries, M. E. (2016). A nuclear magnetic resonance study of water in agarose solutions. *Royal Society Open Science*, 3(3), 150705. <https://doi.org/10.1098/rsos.150705>.
- Fraser, J. R. E., Laurent, T. C., & Laurent, U. B. G. (1997). Hyaluronan: Its nature, distribution, functions and turnover. *Journal of Internal Medicine*, 242(1), 27–33. <https://doi.org/10.1046/j.1365-2796.1997.00170.x>.
- Hills, B. P. (1991). Multinuclear NMR studies of water in solutions of simple carbohydrates. *Molecular Physics*, 72(5), 1099–1121. <https://doi.org/10.1080/00268979100100791>.
- Hills, B. P., Wright, K. M., & Belton, P. S. (1989). Proton N.M.R. studies of chemical and diffusive exchange in carbohydrate systems. *Molecular Physics*, 67(6), 1309–1326. <https://doi.org/10.1080/00268978900101831>.

- Kemmer, G., & Keller, S. (2010). Nonlinear least-squares data fitting in excel spreadsheets. *Nature Protocols*, 5(2), 267–281. <https://doi.org/10.1038/nprot.2009.182>.
- Kenne, L., Gohil, S., Nilsson, E. M., Karlsson, A., Ericsson, D., Helander Kenne, A., et al. (2013). Modification and cross-linking parameters in hyaluronic acid hydrogels—Definitions and analytical methods. *Carbohydrate Polymers*, 91(1), 410–418. <https://doi.org/10.1016/j.carbpol.2012.08.066>.
- La Gatta, A., Schiraldi, C., Papa, A., D'Agostino, A., Cammarota, M., De Rosa, A., et al. (2013). Hyaluronan scaffolds via diglycidyl ether crosslinking: Toward improvements in composition and performance. *Carbohydrate Polymers*, 96(2), 536–544. <https://doi.org/10.1016/j.carbpol.2013.04.022>.
- Lapčík, L., Lapčík, L., De Smedt, S., Demeester, J., & Chabreček, P. (1998). Hyaluronan: Preparation, structure, properties, and applications. *Chemical Reviews*, 98(8), 2663–2684. <https://doi.org/10.1021/cr941199z>.
- Mao, X., Guo, J., & Ye, C. (1994). Radiation damping effects on spin-lattice relaxation time measurements. *Chemical Physics Letters*, 222(5), 417–421. [https://doi.org/10.1016/0009-2614\(94\)00388-2](https://doi.org/10.1016/0009-2614(94)00388-2).
- McConville, P., & Pope, J. M. (2001). ¹H NMR T2 relaxation in contact lens hydrogels as a probe of water mobility. *Polymer*, 42(8), 3559–3568. [https://doi.org/10.1016/S0032-3861\(00\)00714-X](https://doi.org/10.1016/S0032-3861(00)00714-X).
- McConville, P., Whittaker, M. K., & Pope, J. M. (2002). Water and polymer mobility in hydrogel biomaterials quantified by ¹H NMR: A simple model describing both T1 and T2 relaxation. *Macromolecules*, 35(18), 6961–6969. <https://doi.org/10.1021/ma020539c>.
- Oelschlaeger, C., Cota Pinto Coelho, M., & Willenbacher, N. (2013). Chain flexibility and dynamics of polysaccharide hyaluronan in entangled solutions: A high frequency rheology and diffusing wave spectroscopy study. *Biomacromolecules*, 14(10), 3689–3696. <https://doi.org/10.1021/bm4010436>.
- Schanté, C. E., Zuber, G., Herlin, C., & Vandamme, T. F. (2011). Chemical modifications of hyaluronic acid for the synthesis of derivatives for a broad range of biomedical applications. *Carbohydrate Polymers*, 85(3), 469–489. <https://doi.org/10.1016/j.carbpol.2011.03.019>.
- Segura, T., Anderson, B. C., Chung, P. H., Webber, R. E., Shull, K. R., & Shea, L. D. (2005). Crosslinked hyaluronic acid hydrogels: A strategy to functionalize and pattern. *Biomaterials*, 26(4), 359–371. <https://doi.org/10.1016/j.biomaterials.2004.02.067>.
- Simpson, J. H., & Carr, H. Y. (1958). Diffusion and nuclear spin relaxation in water. *The Physical Review*, 111(5), 1201–1202. <https://doi.org/10.1103/PhysRev.111.1201>.
- Ström, A., Larsson, A., & Okay, O. (2015). Preparation and physical properties of hyaluronic acid-based cryogels. *Journal of Applied Polymer Science*, 132(29). <https://doi.org/10.1002/app.42194>.

Supplementary Material

Relaxation and diffusion of water protons in BDDE cross-linked hyaluronic acid hydrogels investigated by NMR spectroscopy – comparison with physicochemical properties

Frida J Wende^a, Yan Xue^a, Gustav Nestor^a, Åke Öhrlund^b, Corine Sandström^{a*}

^a Department of Molecular Sciences, Uppsala BioCenter, Swedish University of Agricultural Sciences, P.O. Box 7015, SE-750 07 Uppsala, Sweden

^b Development Galderma, Seminariegatan 21, SE-752 28 Uppsala, Sweden

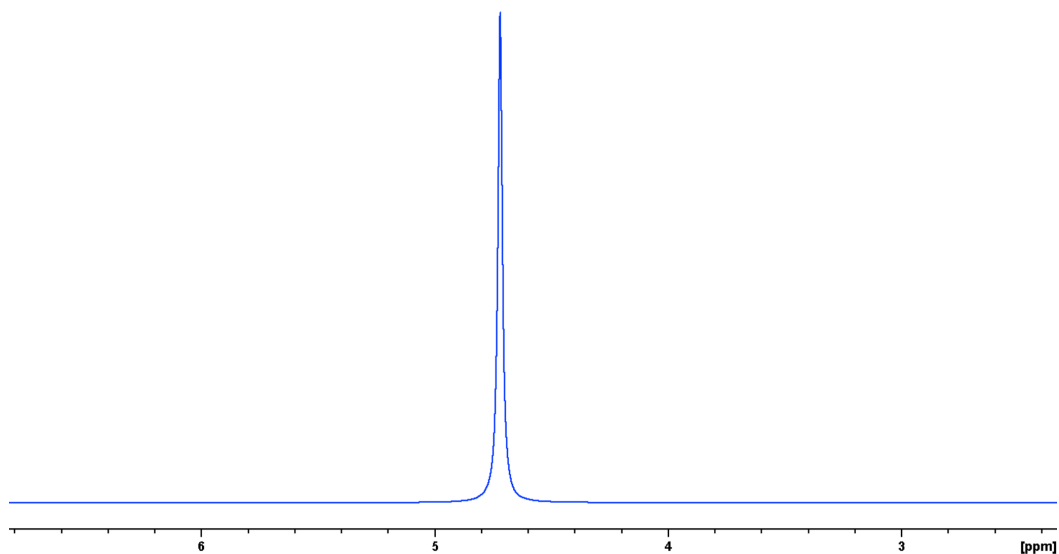


Figure 1. 1D ¹H NMR spectrum of hydrogel **B** dissolved in 90% H₂O/10% D₂O at medium concentration.

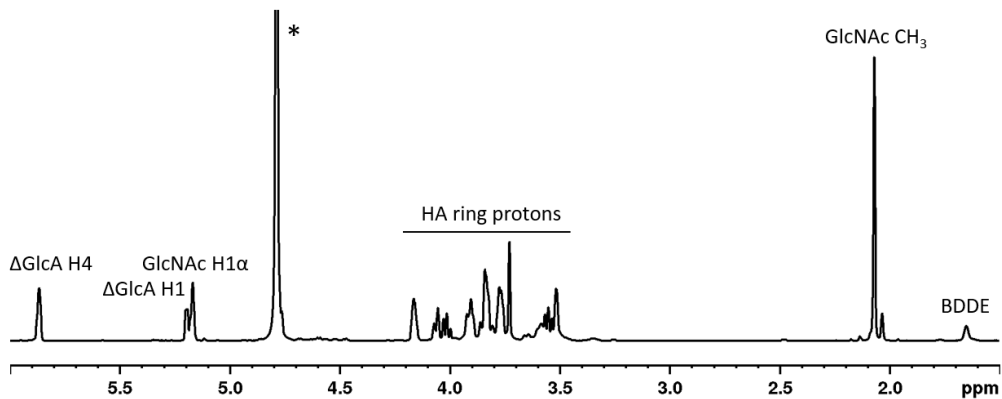
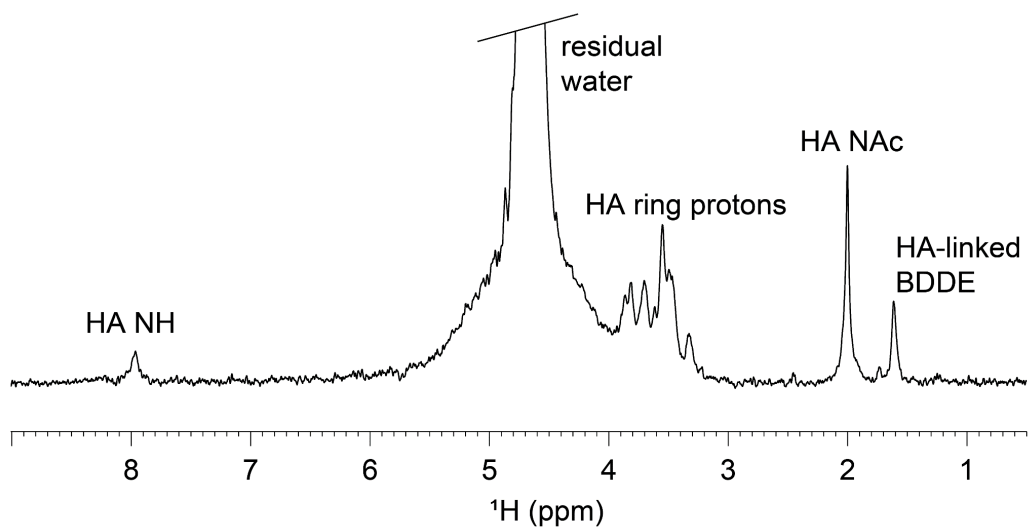


Figure 2. 1D ^1H NMR spectra of HA-BDDE hydrogel (top) intact in 90% $\text{H}_2\text{O}/10\%$ D_2O and (bottom) in D_2O after enzymatic hydrolysis by chondroitinase (done to calculate the exact hydrogel concentration). The spectrum in 90% $\text{H}_2\text{O}/10\%$ D_2O was obtained using a water pre-saturation scheme.

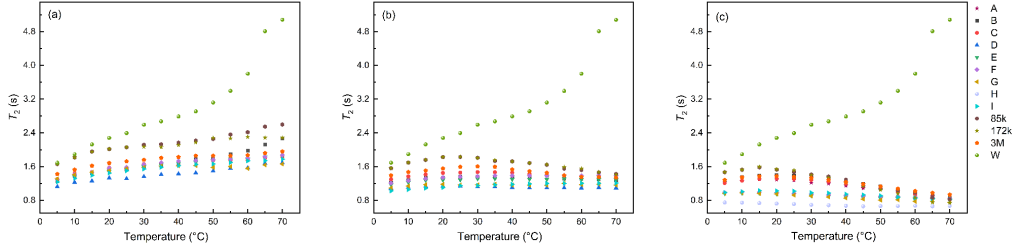


Figure 3. Transverse relaxation, T_2 (s) as a function of temperature (± 1 °C) at (a) low, (b) medium and (c) high HA concentration. A- I: Hydrogel A- I; 85k, 172k and 3M – solution **85k**, **172k** and **3M**; W – Water reference.

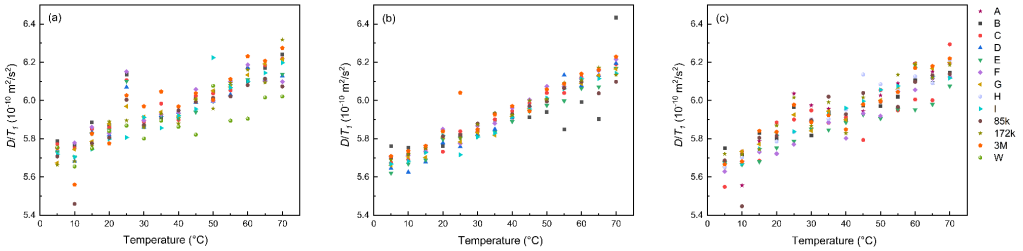


Figure 4. The ratio between self-diffusion coefficient D (m^2/s) and longitudinal relaxation time T_1 (s) as a function of temperature (± 1 °C) at (a) low, (b) medium and (c) high HA concentration. A- I: Hydrogel A- I; 85k, 172k and 3M – solution **85k**, **172k** and **3M**; W – Water reference.

Table 1. The calculated concentrations of HA hydrogels **A-I** and HA solutions (of MW **85k**, **172k** and **3M**).

Sample	Calculated Concentration (mg/ml)		
	Low	Medium	High
Hydrogel A	/	/	9.23
Hydrogel B	2.12	5.42	9.10
Hydrogel C	2.14	4.38	9.19
Hydrogel D	2.28	4.84	/
Hydrogel E	2.56	4.60	9.25
Hydrogel F	2.37	2.14	8.83
Hydrogel G	2.72	5.52	9.95
Hydrogel H	/	/	9.20
Hydrogel I	2.63	4.63	9.20
Solution 85k	1.99	3.89	7.80
Solution 172k	2.22	4.13	8.93
Solution 3M	2.03	4.65	8.37

Determination of Amide *cis/trans* Isomers in *N*-Acetyl-D-glucosamine: Tailored NMR Analysis of the *N*-Acetyl Group Conformation

Yan Xue^[a] and Gustav Nestor^{*[a]}

N-Acetyl-D-glucosamine (GlcNAc) is one of the most common amino sugars in nature, but the conformation of its *N*-acetyl group has drawn little attention. We report herein the first identification of NH protons of the amide *cis* forms of α - and β -GlcNAc by NMR spectroscopy. Relative quantification and thermodynamic analysis of both *cis* and *trans* forms was carried out in aqueous solution. The NH protons were further utilized by adapting protein NMR experiments to measure eight *J*-

couplings within the *N*-acetyl group, of which six are sensitive to the H2-NH conformation and two are sensitive to the amide conformation. For amide *cis* and *trans* forms, the orientation between H2 and NH was determined as *anti* conformation, while a small percentage of *syn* conformation was predicted for the amide *trans* form of β -GlcNAc. This approach holds great promise for the detailed conformational analysis of GlcNAc in larger biomolecules, such as glycoproteins and polysaccharides.

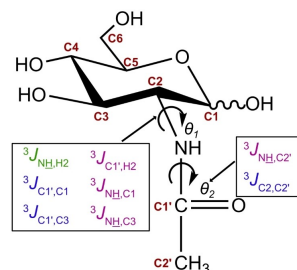
Introduction

Amino sugars are widely distributed in nature and function as key components of glycoproteins, glycolipids, and glycosaminoglycans.^[1] *N*-Acetyl-D-glucosamine (GlcNAc), one of the most common amino sugars in nature, appears as building blocks in many polysaccharides and glycoconjugates such as chitin, hyaluronic acid (HA), and peptidoglycan, which are broadly involved as biological and structural components of cell walls and extracellular matrices.^[2,3] GlcNAc is an essential constituent in both O- and N-glycosylation and it is involved in accommodating various biosynthesis and signaling pathways in diverse organisms including animals, bacteria, and fungi.^[4–7] Moreover, GlcNAc is tightly associated with a large number of human diseases, for example as a modulator of intracellular signaling, where GlcNAc regulates the insulin pathway in adipocytes.^[2]

Since the conformations of GlcNAc polysaccharides mainly depend on glycosidic-linkage geometry and pyranosyl ring conformation,^[8] structural changes and kinetics of the *N*-acetyl group of GlcNAc and its amide linkage have drawn little attention.^[9] However, the *N*-acetyl group can adopt different conformations that will determine its participation in both intra- and intermolecular hydrogen bonds and water bridges, which might also be critical for the general geometry of polysaccharides. Amide *cis-trans* conformation is a key determinant for

amide linkages and *cis-trans* isomerization (CTI) is considered a crucial biological exchange process, especially in peptide linkages.^[10] The ability of the amide nitrogen atom to delocalize its electron lone pair and the consequent partial double bond character between nitrogen and carbonyl carbon hinder free rotation around the C–N bond, resulting in *cis* and *trans* isomers, where *trans* is energetically favored over *cis*.^[11] However, it has been shown that a certain amount of amide *cis* conformation exists in small organic compounds as well as in larger biomolecules.^[12–14]

In GlcNAc, the two torsion angles θ_1 (H2–C2–N–H) and θ_2 (C2–N–C1'–C2'), as shown in Scheme 1, define the conformation of the *N*-acetyl group. The amide bond defined by θ_2 enables CTI and the activation energy for *cis-trans* interconversion has been determined to about 20 kcal/mol in GlcNAc methyl glycosides,^[9] which makes the exchange slow enough to observe separate NMR signals for the *cis* and *trans* forms at room temperature. Prior studies show that the amide bond in GlcNAc is predominantly in the *trans* conformation (the relative orientation of C2 and C2', see Scheme 2), with only about 1.8%



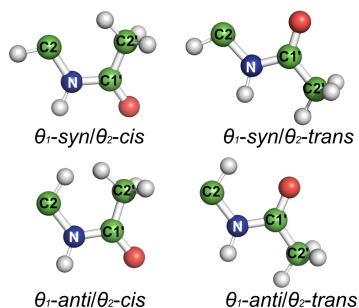
Scheme 1. *J*-couplings related to the torsion angles θ_1 and θ_2 in α - and β -GlcNAc.

[a] Y. Xue, Dr. G. Nestor

Department of Molecular Sciences
Swedish University of Agricultural Sciences
Uppsala BioCenter, P.O. Box 7015, 750 07, Uppsala (Sweden)
E-mail: gustav.nestor@slu.se

Supporting information for this article is available on the WWW under <https://doi.org/10.1002/cbic.202200338>

© 2022 The Authors. ChemBioChem published by Wiley-VCH GmbH. This is an open access article under the terms of the Creative Commons Attribution License, which permits use, distribution and reproduction in any medium, provided the original work is properly cited.



Scheme 2. Four conformations that are related to the torsion angles θ_1 and θ_2 in the *N*-acetyl side chain.

in the *cis* conformation at 42 °C.^[9] However, surveys on glycoprotein X-ray crystal structures found that as much as 6–12% of the GlcNAc residues populate the *cis* conformation,^[9,15] although a substantial amount of these structures are severely twisted or may be due to an erroneous interchange of the carbonyl oxygen and the methyl carbon, which indicates an overestimation of the amount of *cis* conformations.^[15,16] Thus the amide *cis* conformation may play an important role in certain glycoconjugates, although characterization of the *cis* form in monomeric GlcNAc remains challenging due to the low abundance in aqueous solution.

The C2-N bond, on the other hand, is more flexible than the amide bond. The *anti* conformation (defined by the relative orientation of H2 and NH, see Scheme 2) is considered to be the preferred one in GlcNAc monomers, as predicted by molecular dynamic (MD) simulations and NMR data.^[9,17] However, deviations from the *anti* conformation can be crucial for the possibility of NH hydrogen bond interactions. For example, GlcNAc in HA oligosaccharides is known to be in a H2-NH *anti* conformation,^[18] but it is still unclear to what extent the polymer deviates from the *anti* conformation to form a hydrogen bond between the amide proton and a neighboring carboxylate group,^[19] or even contain a significant fraction of *syn* conformation.^[20] The activation energy for *anti-syn* interconversion of GlcNAc was determined by density functional theory (DFT) calculations to 5–10 kcal/mol,^[9] and with small chemical shift differences between the two forms, no separate NMR signals of the two forms can be observed.

Spin-spin coupling constants (also known as *J*-couplings), together with NOEs, are the most important NMR tools for 3D structure determination of biomolecules. Previous work on GlcNAc has focused on the homonuclear H2-NH coupling constant ($^3J_{\text{NH,H2}}$) to distinguish between *anti* and *syn* conformation.^[17,21–23] More recently, Hu et al. showed the advantage of using a set of *J*-couplings to determine the conformation of both torsion angles (θ_1 and θ_2).^[24] The same group also showed the presence of the amide *cis* conformation from ¹³C NMR spectra of GlcNAc methyl glycosides with site-

specific ¹³C-labeling and characterized the *cis-trans* equilibrium and the exchange kinetics.^[9]

In this study, the amide protons of the GlcNAc *cis* forms were observed for the first time and amide protons of both *cis* and *trans* forms were investigated by NMR spectroscopy. A series of NMR experiments were utilized to measure *J*-couplings within the *N*-acetyl group of uniformly ¹³C,¹⁵N-labeled GlcNAc. ¹³C,¹⁵N-labeling enabled the measurement of eight vicinal scalar coupling constants (one $^3J_{\text{HH}}$, three $^3J_{\text{CC}}$, and four $^3J_{\text{CH}}$) within the *N*-acetyl group, of which six are sensitive to the θ_1 angle and two are sensitive to the θ_2 angle (Scheme 1). The *J*-couplings were used to identify the preferred *N*-acetyl conformation of both *cis* and *trans* forms of GlcNAc.

Results and Discussion

Amide protons of minor *cis* conformers

The *trans* conformers of the α - and β -anomer of GlcNAc, which constitute >98% at room temperature, could readily be identified from amide proton cross-peaks in the ¹H,¹⁵N-HSQC spectrum (Figure 1) of uniformly ¹³C,¹⁵N-labeled GlcNAc in 90% H₂O/10% D₂O. This pattern is similar to previous studies on GlcNAc using ¹H,¹⁵N-HSQC.^[25,26] However, closer examination of the GlcNAc ¹H,¹⁵N-HSQC revealed two weak cross-peaks, which correlated with doublets at 7.12 and 7.53 ppm in the ¹H NMR spectrum (Figure 1). These species constituted about 0.5% each, compared to the sum of the *trans* forms. By performing 1D selective EXSY experiments, exchange correlations with the *trans* forms could be observed (Figure 2), so that the doublet at 7.12 ppm correlated with the α -*trans* form and the doublet at 7.53 ppm correlated with the β -*trans* form. Comparison of the ¹³C chemical shifts of the *cis* forms (*vide infra*) with the earlier observation of the *cis* forms^[9] showed identical results and we could thus assign the two weak ¹H,¹⁵N cross-peaks to the α -*cis* (7.12 ppm) and β -*cis* (7.53 ppm) forms of GlcNAc.

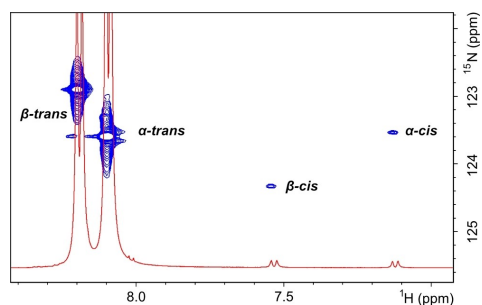


Figure 1. Selected region of 2D-[¹H, ¹⁵N] HSQC and 1D-¹H spectra of GlcNAc at 25 °C. Amide protons of α - and β -GlcNAc in *cis* and *trans* forms are highlighted.

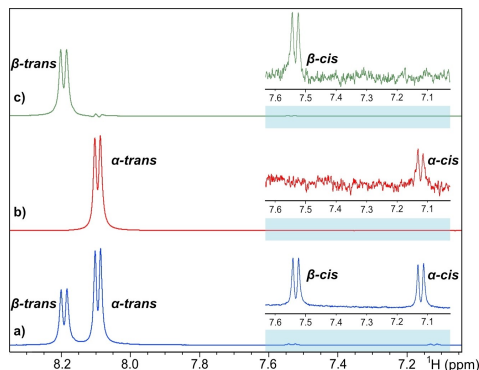


Figure 2. Selected region of a) 1D- ^1H spectrum with excitation sculpting; b) 1D selective EXSY spectrum targeted at the α -*trans* signal; c) 1D selective EXSY spectrum targeted at the β -*trans* signal.

Chemical shifts

In order to distinguish signals arising from *cis* forms with very low abundance, several NMR experiments were conducted to assign the chemical shifts of the different GlcNAc forms. The assignments of ^{13}C resonances were obtained from ^1H , ^{13}C -CT-HSQC, (H)C(C)H-TOCSY and HNCACB experiments, whereas the assignments of ^1H resonances were also obtained from ^1H , ^{15}N -HSQC-TOCSY and ^1H -selective experiments (Figure S1).

The ^1H chemical shifts are affected by the conformation of the *N*-acetyl side chain and the α/β anomeric configuration as shown in Tables 1 and 2. Amide protons were most affected and the amide *cis* forms shift upfield (up to 1.0 ppm) compared to the *trans* form with the same anomeric configuration. Meanwhile, amide protons of the β anomer have higher chemical shifts compared to α anomer with the same amide conformation. Similarly, the H2 signals of the *cis* forms are shifted upfield (0.3–0.4 ppm) compared to the *trans* forms. However, H2 resonances of both *trans* and *cis* forms experienced more downfield chemical shifts in the α anomer than in the β anomer, which is the opposite of the amide protons. The H2 and NH protons are close to the exocyclic carbonyl group

and are most likely affected by the shielding anisotropy of the carbonyl bond. In the *cis* form, the amide proton is perpendicular to the carbonyl double bond, which makes it shielded and leads to an upfield shift.

The most affected carbon chemical shifts of the *cis* forms were those of C2, C1' and C2', with a downfield shift of C2 and C1' resonances (~4 ppm and 2–3 ppm, respectively) and an upfield shift (~2 ppm) of C2' resonances, compared to the *trans* forms (Table 1). These differences in ^{13}C chemical shifts between *cis* and *trans* forms are consistent with previously determined rules for assignment of *Z* and *E* isomers of various sugar amides.^[27] The ^{15}N chemical shift of the β -*cis* isomer was shifted downfield (1.4 ppm) compared to the β -*trans* isomer, but the ^{15}N chemical shift of the α -*cis* isomer was almost identical to the α -*trans* isomer (Table 2).

Temperature coefficients ($d\delta/dT$) of amide protons are used to indicate the existence of hydrogen bonds or reduced hydration in proteins^[28] and $d\delta/dT$ have also been measured from amide protons of GlcNAc and other *N*-acetylated sugars.^[29] The temperature coefficients of *trans* and *cis* amide protons in α - and β -GlcNAc were determined over the range of 3 to 40 °C (Table 2). The values vary from –6.9 to –9.1 ppb/°C, which indicates that the amide protons do not form intramolecular hydrogen bonds to a large extent in aqueous solution, since temperature coefficients from –10 to –6 ppb/°C are usually indicative of the lack of intramolecular hydrogen bonds.^[30] However, the slightly less negative $d\delta/dT$ of α -*cis* NH (–6.9 ppb/°C) compared to α -*trans* NH (–9.1 ppb/°C) suggests that the α -*cis* amide proton is less solvated, which could be due to steric effects, transient intramolecular hydrogen bonds or transient hydrogen bonds to water molecules.

The one-bond coupling constant, $^1J_{\text{NH}}$, was determined from coupled ^1H , ^{15}N -HSQC spectra and showed lower values for the *cis* forms (87–89 Hz) than the *trans* forms (91–93 Hz). This is in accordance with peptide linkages, where $^1J_{\text{NH}}$ are typically in the range 92–94 Hz and 89–91 Hz for a *trans* and a *cis* conformation, respectively.^[31] The α -*trans* NH showed a larger $^1J_{\text{NH}}$ than β -*trans* NH, which is equivalent to previously reported $^1J_{\text{NH}}$ on GlcNAc.^[32]

Table 1. Non-exchangeable ^1H and ^{13}C chemical shifts (ppm) of α - and β -GlcNAc in *trans* and *cis* amide forms.^[34]

	H1 C1	H2 C2	H3 C3	H4 C4	H5 C5	H6a/b C6	C1'	H2' C2'
α - <i>trans</i>	5.20	3.86	3.75	3.47	3.84	3.83/3.78		2.04
	93.6	56.9	73.5	72.8	74.3	63.4	177.3	24.7
α - <i>cis</i>	5.26	3.58	3.74	3.51	3.86	3.80/3.78		2.03
	94.3	60.7	74.1	n.d.	n.d.	n.d.	179.5	22.6
β - <i>trans</i>	4.70	3.66	3.52	3.45	3.45	3.89/3.74		2.04
	97.7	59.5	76.7	72.6	78.6	63.5	177.5	24.9
β - <i>cis</i>	4.70	3.30	3.47	n.d.	n.d.	3.92/3.75		2.03
	97.9	64.0	77.1	n.d.	n.d.	n.d.	180.4	23.0

[a] In 90% $\text{H}_2\text{O}/10\%$ D_2O at 25 °C; chemical shifts relative to $\text{DSS-}d_6$; n.d. = not determined.

Table 2. $^1\text{H}/^{15}\text{N}$ chemical shifts (ppm), one-bond coupling constants (Hz), and temperature coefficients ($d\delta/dT$, ppb/ $^{\circ}\text{C}$) of *trans* and *cis* amide groups in α - and β -GlcNAc.^[6]

	δ_{NH}	δ_{NH}	$^1J_{\text{NH}}$	$d\delta/dT$
α - <i>trans</i>	8.10	123.6	(-) 92.8	-9.1
α - <i>cis</i>	7.12	123.5	(-) 88.6	-6.9
β - <i>trans</i>	8.19	122.9	(-) 91.5	-7.9
β - <i>cis</i>	7.53	124.3	(-) 87.4	-8.5

[a] In 90% $\text{H}_2\text{O}/10\%$ D_2O , pH 6.7 ± 0.1 , at 25°C ; ppm relative to $\text{DSS-}d_6$.

Relative quantification of GlcNAc isomers

Relative quantification of the four GlcNAc isomers (*trans* and *cis* amides of the α - and β -anomer, respectively) was obtained by integration of amide proton signals from 1D spectra of unlabeled GlcNAc over a temperature range from 3 to 40°C (Figure S2). The GlcNAc α -pyranoside dominates over the β -pyranoside in their amide *trans* forms and it increases with temperature, which is consistent with earlier reports of 68% α - and 32% β -pyranoside at 70°C .^[33]

The relative amount of amide *cis* forms increased with temperature. In contrast to the *trans* forms, the β -*cis* isomer (0.6–1.2%) is more populated than the α -*cis* isomer (0.3–1.0%) at all temperatures investigated. The equilibrium constants $K_{\text{trans/cis}}$ were calculated and used to construct van't Hoff plots (see Table S1 and Figure S3), from which $\Delta H^{\circ}_{\text{cis} \rightarrow \text{trans}}$ were extracted and determined to -12.8 kJ/mol and -15.6 kJ/mol for the α - and the β -pyranoside, respectively. $\Delta S^{\circ}_{\text{cis} \rightarrow \text{trans}}$ were determined to -3.9 J/K/mol for α -pyranoside and -20.2 J/K/mol for β -pyranoside. Amide *trans* forms in both α - and β -pyranosides are enthalpically favored but entropically disfavored and $\Delta G^{\circ}_{\text{cis} \rightarrow \text{trans}}$ was calculated to -11.6 kJ/mol and -8.9 kJ/mol at 25°C for the α - and the β -pyranoside, respectively; thus amide *trans* forms are thermodynamically favored. Moreover, compared with β -pyranoside, α -pyranoside has higher equilibrium constants $K_{\text{trans/cis}}$ and more negative Gibbs free energy. The results are in the same order of magnitude as earlier investigations on GlcNAc methyl glycosides by Hu et al., except a more negative $\Delta S^{\circ}_{\text{cis} \rightarrow \text{trans}}$ for the β -pyranoside (-20.2 J/K/mol) compared to the methyl glycoside (-2.9 J/K/mol).^[9]

NMR experiments for determination of GlcNAc N-acetyl J-coupling constants

By utilizing the GlcNAc amide protons, we could use protein NMR experiments on uniformly $^{13}\text{C},^{15}\text{N}$ -labeled GlcNAc for determination of eight three-bond J -coupling constants within the N -acetyl group. The N -acetyl group of GlcNAc resembles the protein backbone with an amide function, C α replaced by C2, and C β replaced by C3 (Figure 3). Since the protein backbone is a repeat of NH, C α , and CO, but GlcNAc is not, CO $_1$, corresponds to GlcNAc C1', whereas CO $_2$ is replaced by C1, and C α_{i-1} is replaced by C2'. Thus, E-COSY-type and J -quantitative protein NMR experiments for coupling constants over the ϕ and ω

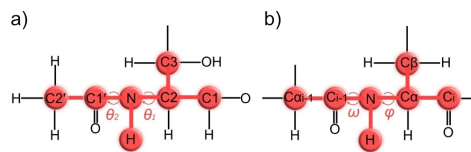


Figure 3. Comparison between a) the N -acetyl group of GlcNAc and b) the protein backbone.

backbone angles could be adapted and utilized for the θ_1 , and θ_2 torsion angles of the N -acetyl group.

Six vicinal coupling constants through the C2-N bond are sensitive to the θ_1 torsion angle, $^3J_{\text{NH,H2}}$, $^3J_{\text{NH,C1}}$, $^3J_{\text{NH,C3}}$, $^3J_{\text{H2,C1}}$, $^3J_{\text{C1,C1}}$, and $^3J_{\text{C3,C1}}$, whereas two vicinal coupling constants can be extracted over the N-CO bond, which are sensitive to the θ_2 torsion angle, namely $^3J_{\text{NH,C2}}$ and $^3J_{\text{C2,C2}}$. The experiments are summarized in Table S2 and presented in detail in the experimental section. The standard deviation of the J -couplings was typically 0.1 Hz for the *trans* forms and up to 0.3 Hz for the *cis* forms due to the low abundance of amide *cis* forms.

J -couplings sensitive to the θ_1 angle (H2-C2-N-H)

The HNCA[HA]-E-COSY experiment was used to determine $^3J_{\text{NH,H2}}$ with selective ^{13}C pulses and delays adjusted for GlcNAc (see experimental). The GlcNAc *trans* forms exhibited $^3J_{\text{NH,H2}}$ of 8.8 Hz for the α -anomer and 9.5 Hz for the β -anomer (Figure 4a), which is equivalent to earlier reported values of 8.7–8.9 Hz for α -GlcNAc and 9.1–9.8 Hz for β -GlcNAc.^[17,18,32] In addition, $^3J_{\text{NH,H2}}$ of the GlcNAc *cis* forms could be measured, despite the much lower intensity. The *cis* forms exhibited 10.6 Hz for the α -anomer and 10.2 Hz for the β -anomer (Figure 4b), which is 1.8 Hz and 0.7 Hz larger compared to the *trans* form of α - and β -GlcNAc, respectively. Earlier reported $^3J_{\text{NH,H2}}$ from *cis* forms of N -formyl substituted sugars in DMSO- d_6 have shown very similar values for *trans* and *cis* forms^[9] or a larger coupling constant of the *cis* form by 1.3 Hz.^[34]

Karplus equations that were parametrized for $^3J_{\text{NH,H2}}$ by Hu, et al.^[24] on GlcNAc model structures show maxima at 0° and 180° , corresponding to θ_1 -*syn* and θ_1 -*anti*, respectively. Separate Karplus equations were determined for *trans* and *cis* forms, where the *cis* forms have larger $^3J_{\text{NH,H2}}$ than the *trans* forms of about 2 Hz.^[24] Our results are in agreement with these parametrizations, assuming that the *trans* and *cis* forms have the same conformation over the θ_1 linkage. By calculating the difference between observed $^3J_{\text{NH,H2}}$ and the values from the parametrized Karplus equations over the whole span of torsion angles, a minimization plot is generated, where the global minimum corresponds to the most likely torsion angle (Figure S4a). However, for α - and β -GlcNAc (*trans* as well as *cis* forms) minima are observed in two regions, around 0° and 180° , which cannot be distinguished. The calculated $^3J_{\text{NH,H2}}$ is consistently higher in magnitude compared to experimental

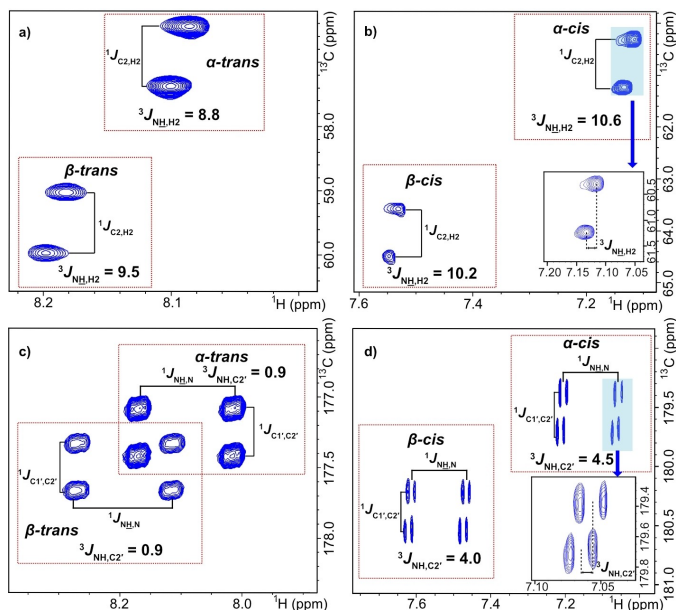


Figure 4. E-COSY spectra used to measure ${}^3J_{\text{NH},\text{H}_2}$ of a) *trans* and b) *cis* forms, and ${}^3J_{\text{NH},\text{C}_2'}$ of c) *trans* and d) *cis* forms. The spectra in a) and b) were recorded with ${}^{15}\text{N}$ decoupling whereas the spectra in c) and d) were recorded without decoupling.

data (about 1–2 Hz), which has been attributed to the internal dynamics of the pyranose ring.^[17] This inconsistency between experimental and calculated ${}^3J_{\text{NH},\text{H}_2}$ is in the same order of magnitude as the difference between the maxima in the Karplus curves corresponding to *syn* and *anti* conformation, which is 1.2–2.3 Hz depending on the parametrized equation. Consequently, the use of ${}^3J_{\text{NH},\text{H}_2}$ alone to distinguish between *anti* and *syn* conformations is limited, as shown by our minimization plot, and additional *J*-coupling constants are needed for the analysis.

The ${}^3J_{\text{H}_2,\text{C}_1'}$ coupling constant was measured from the (H)NCAHA(CO)-E-COSY experiment to 2.8 and 3.4 Hz for the *trans* forms of α - and β -GlcNAc, respectively (Table 3; Figure S5). This can be compared with earlier reported ${}^3J_{\text{H}_2,\text{C}_1'}$ of 3.1 for the methyl glycoside of α -GlcNAc^[24] and 3.5 Hz for β -GlcNAc.^[32] The

cis forms showed similar ${}^3J_{\text{H}_2,\text{C}_1'}$ with 3.3 and 2.6 Hz for α - and β -GlcNAc, respectively.

In contrast to ${}^3J_{\text{NH},\text{H}_2}$, ${}^3J_{\text{H}_2,\text{C}_1'}$ values differ clearly between 0° and 180° , corresponding to *anti* and *syn* conformation, respectively. Calculated Karplus equations show much larger ${}^3J_{\text{H}_2,\text{C}_1'}$ at 180° (8.0–8.5 Hz) compared to 0° (4.0–4.4 Hz) and thus the observed ${}^3J_{\text{H}_2,\text{C}_1'}$ for both *trans* and *cis* forms are consistent with θ_1 -*anti* rather than θ_1 -*syn* conformation. However, due to the symmetrical shape of the Karplus curve, ${}^3J_{\text{H}_2,\text{C}_1'}$ alone cannot be used to determine torsion angles in-between *anti* and *syn* conformation, which might be populated if the *N*-acetyl group is involved in hydrogen bonding. For an accurate determination of the torsion angle, a set of several coupling constants is necessary.

The ${}^3J_{\text{NH},\text{C}_1}$ and ${}^3J_{\text{NH},\text{C}_3}$ coupling constants were measured from HNCA[CB]-E-COSY experiments with off-resonance carbon pulses on C3 and C1, respectively. Both *trans* and *cis* forms of α -

Table 3. 3J and 2J coupling constants (Hz) that are sensitive to the θ_1 and θ_2 angles in α - and β -GlcNAc.^[a]

	${}^3J_{\text{NH},\text{H}_2}$	${}^3J_{\text{H}_2,\text{C}_1'}$	${}^3J_{\text{NH},\text{C}_1}$	${}^3J_{\text{NH},\text{C}_3}$	${}^3J_{\text{C}_1,\text{C}_1'}$	${}^3J_{\text{C}_3,\text{C}_1'}$	${}^3J_{\text{NH},\text{C}_2'}$	${}^3J_{\text{C}_2,\text{C}_2'}$	${}^2J_{\text{C}_2,\text{C}_1'}$ ^[b]
α - <i>trans</i>	8.8 ± 0.02	2.8 ± 0.11	0.4 ± 0.01	0.9 ± 0.02	1.0 ± 0.01	1.4 ± 0.03	0.9 ± 0.05	1.4 ± 0.04	0.5 ± 0.13
α - <i>cis</i>	10.6 ± 0.18	3.3 ± 0.02	0.7 ± 0.09	0.7 ± 0.11	1.6 ± 0.03	obs. ^[c]	4.5 ± 0.11	< 0.5 ^[d]	1.1 ± 0.31
β - <i>trans</i>	9.5 ± 0.01	3.4 ± 0.04	0.6 ± 0.02	0.8 ± 0.01	1.0 ± 0.23	1.0 ± 0.04	0.9 ± 0.06	1.7 ± 0.06	0.9 ± 0.03
β - <i>cis</i>	10.2 ± 0.26	2.6 ± 0.23	0.7 ± 0.06	0.9 ± 0.24	obs. ^[c]	obs. ^[c]	4.0 ± 0.07	< 0.5 ^[d]	1.2 ± 0.20

[a] At 25 °C in 90% H₂O/10% D₂O. Data are presented from at least three measurements with ± one standard deviation. [b] Sign unknown. [c] Obscured signals. [d] Below the detection limit.

and β -GlcNAc exhibited $^3J_{\text{NH},\text{C}1}$ and $^3J_{\text{NH},\text{C}3}$ in the range 0.4–0.9 Hz (Table 3; Figure S5). This is consistent with an *anti* conformation, with calculated $^3J_{\text{NH},\text{C}1}$ and $^3J_{\text{NH},\text{C}3}$ of 0.8–1.2 Hz from parametrized Karplus equations.^[24] The same equations predict 1.7–2.8 Hz for *syn* conformations, with $^3J_{\text{NH},\text{C}1}$ slightly larger than $^3J_{\text{NH},\text{C}3}$. Since the amide proton in the *anti* conformation is in a *gauche* position to C1 and C3 (-60° and $+60^\circ$, respectively), the $^3J_{\text{NH},\text{C}1}$ and $^3J_{\text{NH},\text{C}3}$ coupling constants are close to minima at $\pm 90^\circ$ in the Karplus curve and similarly the *syn* conformation, which corresponds to $+120^\circ$ and -120° , respectively, are close to the minima. However, if the θ_1 torsion angle deviates from the *anti* and *syn* conformations, $^3J_{\text{NH},\text{C}1}$ and $^3J_{\text{NH},\text{C}3}$ are predicted to be much larger, up to 6–9 Hz for $\theta_1 = \pm 60^\circ$ (corresponding to 180° in the C1–C2–N–H or C3–C2–N–H Karplus curve).

Finally, a spin-echo difference CT-HSQC experiment was used to determine the $^3J_{\text{C}1,\text{C}1'}$ and $^3J_{\text{C}3,\text{C}1'}$ coupling constants. The 2D spectrum is identical to a $^1\text{H},^{13}\text{C}$ -HSQC spectrum, but with intensities affected by the C–CO couplings in a *J*-quantitative manner.^[35] Since GlcNAc C1 and C3 cross-peaks were well resolved (at least for the *trans* forms), $^3J_{\text{C}1,\text{C}1'}$ and $^3J_{\text{C}3,\text{C}1'}$ could be measured from the same experiment (Table 3). However, the C3 cross-peaks of the *cis* forms were obscured by the much more intense *trans* forms, which prevented the measurement of $^3J_{\text{C}3,\text{C}1'}$. Similarly, $^3J_{\text{C}1,\text{C}1'}$ of the α -GlcNAc *cis* form could not be determined due to the overlap of the C1 cross-peak with the *trans* form. The cross-peak from the *trans* β -GlcNAc C1 was close to the residual water signal and therefore the standard deviation for this measurement was significantly higher (0.23 Hz).

All $^3J_{\text{C}1,\text{C}1'}$ and $^3J_{\text{C}3,\text{C}1'}$ were in the range 1.0–1.6 Hz, which is consistent with previously reported data.^[9,32] According to parametrized Karplus equations,^[24] a θ_1 -*anti* conformation corresponds to $^3J_{\text{C}1,\text{C}1'}$ and $^3J_{\text{C}3,\text{C}1'}$ in the range 1.1–1.5 Hz, whereas a *syn* conformation corresponds to $^3J_{\text{C}1,\text{C}1'}$ and $^3J_{\text{C}3,\text{C}1'}$ close to zero. Thus, the obtained *J* couplings are consistent with a θ_1 -*anti* conformation. As for $^3J_{\text{NH},\text{C}1}$ and $^3J_{\text{NH},\text{C}3}$, the orientation of C1 and C3 in relation to the amide proton (and C1') implies that $^3J_{\text{C}1,\text{C}1'}$ and $^3J_{\text{C}3,\text{C}1'}$ are close to the minima at $\pm 90^\circ$ in the θ_1 -*anti* and *syn* conformations. However, deviations from θ_1 -*anti* and *syn* conformations would result in larger $^3J_{\text{C}1,\text{C}1'}$ and $^3J_{\text{C}3,\text{C}1'}$ of up to 3–4.5 Hz.

Other C–C couplings involving C1' could also be measured using the spin-echo difference CT-HSQC experiment, including the two-bond coupling $^2J_{\text{C}2,\text{C}1'}$, which was in the range of 0.5–1.2 Hz (Table 3). This is in accordance with earlier reports of 0.8–1.1 Hz,^[9] but there is no obvious correlation between $^2J_{\text{C}2,\text{C}1'}$ and the θ_1 or θ_2 torsion angle conformation.

J-couplings sensitive to the θ_2 angle (C2–N–C1'–C2)

$^3J_{\text{NH},\text{C}2}$ was measured from the HNC[C(A)]-E.COSY experiment with selective pulses on the methyl carbon rather than $\text{C}\alpha$ (see experimental). A clear difference was observed between GlcNAc *trans* conformations, with $^3J_{\text{NH},\text{C}2}$ of 0.9 Hz for both anomers, and GlcNAc *cis* conformations, with $^3J_{\text{NH},\text{C}2}$ of 4.5 and 4.0 Hz for α - and β -GlcNAc, respectively (Figure 4c and d). This is close to predicted values from parametrized Karplus equations, which

are 1.0 Hz for a *trans* conformation and 4.8 Hz for a *cis* conformation.^[24] Thus, $^3J_{\text{NH},\text{C}2}$ can be successfully used to distinguish between *trans* and *cis* amide conformation and, in the case of GlcNAc, it confirms the *cis* conformation of the minor GlcNAc species.

$^3J_{\text{C}2,\text{C}2'}$ was measured by a *J*-quantitative long-range (H)C(C)H experiment, which can be used to measure several *J*_{CC} couplings within the ring or, in the case of oligosaccharides, over the glycosidic linkage.^[36] The *trans* forms showed $^3J_{\text{C}2,\text{C}2'}$ of 1.4 and 1.7 Hz for α - and β -GlcNAc, respectively (Table 3; Figure S6), but the *cis* forms were below the detection limit (<0.5 Hz). These values are in agreement with previously measured $^3J_{\text{C}2,\text{C}2'}$ of 1.6–1.8 Hz from GlcNAc.^[9] Parametrized Karplus equations have shown that $^3J_{\text{C}2,\text{C}2'}$ is affected by both the θ_1 and the θ_2 angle.^[24] *Trans* forms are predicted to 3.3 Hz in θ_1 -*syn* conformation and 1.5 Hz in the θ_1 -*anti* conformation, whereas *cis* forms are predicted to have $^3J_{\text{C}2,\text{C}2'}$ close to 0 Hz in both θ_1 -*syn* and *anti* conformations. Thus, our observed values for the *trans* forms are equivalent to the θ_1 -*anti* conformation and $^3J_{\text{C}2,\text{C}2'}$ for the *cis* forms are not detected because it is probably close to 0 Hz.

The overall geometry of the *N*-acetyl group

In order to generate single-state models for the torsion angles θ_1 (H2–C2–N–H) and θ_2 (C2–N–C1'–C2), absolute differences were calculated between our experimental results (Table 3) and the values from parametrized Karplus equations (Table S3). The differences were then normalized to a common torsion angle (θ_1 and θ_2) and root-mean-square deviations (RMSD) were calculated over the full range of torsion angles for the full ensemble of coupling constants (six coupling constants related to θ_1 and two coupling constants related to θ_2).

The plots of RMSD versus torsion angles H2–C2–N–H and C2–N–C1'–C2' are presented in Figure 5. For the θ_1 torsion angle (Figure 5a) the global minimum, corresponding to the smallest deviation between calculated and experimental *J*-couplings, can be found in the region from 168° to 180° (*anti* conformation) with α -*trans* at $(+170 \pm 10)^\circ$, β -*trans* at $(+178 \pm 6)^\circ$, α -*cis* at $(180 \pm 10)^\circ$ and β -*cis* at $(+168 \pm 19)^\circ$. Other local minima are located in the region near 0° (*syn* conformation), but with RMSD that are about 1.5 Hz larger. The results are consistent with earlier reports on θ_2 -*trans* forms of GlcNAc, where a similar treatment of *J*-couplings on the α -GlcNAc methyl glycoside was used to identify a global RMSD minimum at $+160^\circ$,^[24] whereas MD simulations found an average θ_1 angle at $+165^\circ$ for α -GlcNAc^[8] or $+161^\circ$ and 180° for α - and β -GlcNAc, respectively.^[17]

The *J*-couplings were also subdivided into four groups to obtain individual RMSD plots: Group 1 with $^3J_{\text{NH},\text{H}2}$ and $^3J_{\text{H}2,\text{C}1}$; Group 2 with $^3J_{\text{NH},\text{C}1}$ and $^3J_{\text{NH},\text{C}3}$; Group 3 with $^3J_{\text{C}1,\text{C}1'}$ and $^3J_{\text{C}3,\text{C}1'}$; and Group 4 with $^3J_{\text{NH},\text{C}1}$, $^3J_{\text{NH},\text{C}3}$, $^3J_{\text{NH},\text{H}2}$ and $^3J_{\text{H}2,\text{C}1}$ (Figure S7). The *anti* and *syn* conformation can be most clearly distinguished from Group 1, where the difference in RMSD between the two rotamers is about 3 Hz for all the GlcNAc forms. Also, Group 2 can be used to distinguish between *anti* and *syn* conformation, though with a smaller difference in RMSD of about 1 Hz. Group

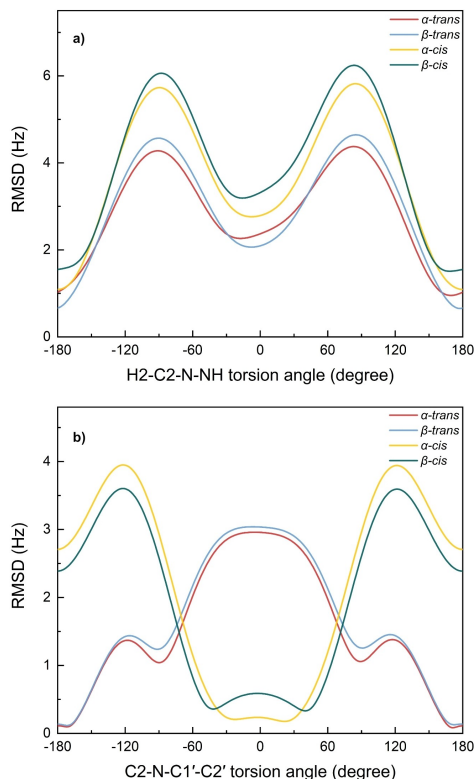


Figure 5. The overall single-state plots of a) RMSD versus H2–C2–N–NH torsion angle using all six coupling constants that are sensitive to θ_1 , and b) RMSD versus C2–N–C1'–C2' torsion angle using ${}^3J_{\text{C2,C2}'}$ and ${}^3J_{\text{NH,C2}'}$ that are sensitive to θ_2 .

3, on the other hand, cannot be used to find the correct conformation, whereas Group 4 is almost identical to the plot of all six J -couplings. In conclusion, ${}^3J_{\text{NH,H2}}$ and ${}^3J_{\text{H2,C1}'}$ are enough to distinguish between *anti* and *syn* conformation. To determine the exact θ_1 angle, the addition of ${}^3J_{\text{NH,C1}'}$ and ${}^3J_{\text{NH,C3}}$ is necessary, since ${}^3J_{\text{NH,H2}}$ and ${}^3J_{\text{H2,C1}'}$ cannot be used to differentiate between positive and negative θ_1 due to the symmetry of the Karplus curves. Finally, the entire set of J -couplings may be necessary in the rare case of θ_1 around $\pm 90^\circ$ (in between *anti* and *syn* conformation), where ${}^3J_{\text{NH,H2}}$ and ${}^3J_{\text{H2,C1}'}$ are close to 0 Hz and ${}^3J_{\text{NH,C1}'}$ and ${}^3J_{\text{NH,C3}}$ are similar for $+90^\circ$ and -90° .

In order to investigate minor contribution of *syn* conformation, a two-state model for the θ_1 torsion angle was generated (Figure S8). The torsion angle was fixed at 180° (*anti*) and 0° (*syn*) and the relative contribution of the two conformations was optimized by minimizing the RMSD between experimental and calculated J -couplings, as in the single-state model. For α -

trans, α -*cis*, and β -*cis* forms, the lowest RMSD was found at 100% *anti* conformation, but for β -*trans* a small contribution of *syn* conformation was obtained (2% *syn*, 98% *anti*). Interestingly, MD simulations on GlcNAc *trans* forms have shown a similar tendency with 100% *anti* conformation of α -GlcNAc, but 87% *anti* and 13% *syn* conformation of β -GlcNAc.^[17]

A single-state model of the θ_2 torsion angle exhibited RMSD plots (Figure 5b) with global minima located as expected, close to 180° for *trans* conformation and close to 0° for *cis* conformation. The minima of the *trans* amides were located at $\pm 172^\circ$, but due to an almost flat RMSD curve around 180° , it is not possible to distinguish between $+172^\circ$ and -172° or to exclude a planar 180° conformation. For the *cis* forms, ${}^3J_{\text{C2,C2}'}$ was set to 0 Hz (< 0.5 Hz from experiments) and the exact torsion angles could not be determined accurately due to broad minima around 0° . Overall, ${}^3J_{\text{NH,C2}'}$ is enough to differentiate between *trans* and *cis* amide conformation (Figure S4b), whereas both coupling constants (${}^3J_{\text{NH,C2}'}$ and ${}^3J_{\text{C2,C2}'}$) are necessary to determine the θ_2 torsion angle in detail.

It is noteworthy that the RMSD in the global minima of the single-state models are considerable for the θ_1 torsion angle (0.6–1.5 Hz), but much lower for the θ_2 torsion angle (0.1–0.3 Hz), despite up to six J -couplings used for θ_1 , and only two for θ_2 . This could be explained by 1) contribution from a less populated θ_1 -*syn* conformation, 2) experimental errors, and 3) limitations of the parametrized Karplus equations. However, our two-state model incorporating both *anti* and *syn* conformation did not improve the RMSD since the *syn* conformation was only populated by 0–2%. Experimental errors of the measured coupling constants probably contribute to the RMSD, but the use of several different coupling constants with different torsion angle dependencies should minimize this effect so that the global minimum is detected with higher accuracy. Finally, the parametrized Karplus equations derived for GlcNAc model structures may have limitations due to the use of an implicit water model, which may not accurately mimic the real water-solute interactions.^[24] It should also be mentioned that the dynamics of the GlcNAc ring is not included in the models and could affect the J -couplings.^[17] Actually, the two most deviating J -couplings, ${}^3J_{\text{NH,H2}}$ and ${}^3J_{\text{H2,C1}'}$, both involve H2, which is probably most affected by ring puckering and other dynamic effects.

The preference for the α -anomeric configuration of GlcNAc, in contrast to glucose, where the β -anomeric configuration is preferred, is not well understood. It has been hypothesized that hydrogen bonding between NH and O1 would stabilize the α -pyranoside^[37] and that unfavorable electrostatic interaction between O1 and C1'O is minimized in the α -pyranoside.^[38] From our data, there is no indication of direct NH–O1 hydrogen bonding in α -GlcNAc, based on the NH temperature coefficients showing similar values for the two anomers, and the average θ_1 torsion angle, which predicts that the amide proton is pointing away from O1. However, the interaction between NH and O1 through water bridges is likely to be significant in α -GlcNAc as earlier reported from MD simulations.^[17] Such interaction may stabilize the α -GlcNAc θ_1 -*anti* conformation, which could explain why the α -GlcNAc θ_1 -*syn* conformation was not detected by our two-state model. In addition, the θ_1 -*syn*

conformation of α -GlcNAc exhibits a possibly unfavorable steric interaction between the axial O1 and the carbonyl oxygen. The β -pyranoside, on the other hand, showed a more diverse appearance with a small fraction of θ_1 -*syn* conformation and a larger proportion of amide *cis* conformation, compared to the α -pyranoside. Given that β -GlcNAc θ_1 -*syn* conformation is free from steric hindrance, this conformation is expected in minor amounts. The reason for a larger proportion of *cis* conformation in β -GlcNAc is less evident, but the more negative $\Delta S^\circ_{cis \rightarrow trans}$ for β -GlcNAc, compared to α -GlcNAc, suggests that differences in the water-solute interactions of the two anomers might be an important factor for the *cis-trans* equilibria.

Conclusions

In this study, we report the first identification of NH protons of the amide *cis* forms of α - and β -GlcNAc by NMR spectroscopy. The *cis* amide protons were distinguished by upfield chemical shifts and smaller $^1J_{NH}$, compared to the *trans* forms. The chemical shifts of the *cis* forms in aqueous solution were assigned and the temperature coefficients ($d\delta/dT$) of amide protons were measured. The amide proton signals were also used for the relative quantification of each isomer over a temperature range from 3 °C to 40 °C, showing that the β -*cis* isomer (0.6–1.2%) is more populated than the α -*cis* isomer (0.3–1.0%) with an increasing amount of *cis* forms at higher temperatures. Thermodynamic analysis showed that amide *trans* forms in both α and β pyranosides are enthalpically favored but entropically disfavored, which might be due to solvation effects.

The amide protons of GlcNAc were further utilized by adapting E.COSY and *J*-quantitative protein NMR experiments for ^{13}C , ^{15}N -labelled GlcNAc to measure eight *J*-couplings along the *N*-acetyl side chain. The experimental data were compared with parametrized Karplus equations and the full set of *J*-couplings was used to identify the most probable conformation. For both *trans* and *cis* amide forms, the orientation between H2 and NH was determined as *anti* with a torsion angle (θ_1) of $+168^\circ$ – 180° . A two-state model was also generated, showing no contribution of the *syn* conformation except for the *trans* form of β -GlcNAc, where 2% of θ_1 -*syn* conformation was predicted. The orientation of the amide linkage for the *trans* and *cis* forms was confirmed by two *J*-couplings that are sensitive to the θ_2 torsion angle. The $^3J_{NH,C2}$ coupling constant was found to be particularly useful to distinguish between amide *cis* and *trans* conformation.

The larger proportion of *cis* amide and θ_1 -*syn* conformation in β -GlcNAc suggests higher flexibility of the *N*-acetyl group of β -GlcNAc compared to α -GlcNAc. This fact is of special interest in studies on glycans and glycoconjugates containing β -GlcNAc, such as chitin, hyaluronic acid and *N*- and *O*-glycosylated proteins. The presence of *cis* amide and/or θ_1 -*syn* conformation in these biologically important molecules may have crucial effects on the overall conformation and the physicochemical properties. The tailored *J*-coupling NMR experiments utilized herein for *N*-acetyl

conformation analysis provide tools for detecting these forms in complex glycoconjugates with isotopic labeling.

Experimental Section

Syn and *anti* conformations are related to the torsion angle θ_1 (H2–C2–N–H) so that *syn* and *anti* conformation correspond to 0° and 180° , respectively. *Cis* and *trans* conformations are related to the torsion angle θ_2 (C2–N–C1'–C2'), so that *cis* and *trans* conformation correspond to 0° and 180° , respectively (Scheme 2). See Table S3 for relations to other torsion angles within the *N*-acetyl group.

Sample preparation: Unlabeled *N*-acetyl-D-glucosamine (CAS.RN 7512-17-6) was purchased from Sigma-Aldrich and was dissolved in 90% H₂O/10% D₂O (600 μ L) to obtain a 57 mM solution. The pH of the sample was adjusted to 7.0 with HCl or NaOH solutions and DSS-*d*₆ (0.5 mM) was added as a chemical shift reference (δ_H 0.00 ppm). The sample was transferred into a 5 mm NMR sample tube for further analysis.

N-[1, 2- ^{13}C] acetyl-D-[UL- ^{13}C , ^{15}N] glucosamine (CAS.RN 478529-44-1) was purchased from Omicron Biochemicals, Inc. (South Bend, IN, USA) and was used without further purification. UL-GlcNAc (1 mg) was dissolved in 90% H₂O/10% D₂O (160 μ L) to obtain a 27 mM solution. The pH of the sample was adjusted to 6.7 with HCl or NaOH solutions. The sample was transferred into a 3 mm NMR sample tube for further analysis.

NMR Spectroscopy: NMR spectra were recorded at 25 °C, unless otherwise stated, on a Bruker Avance III 600 MHz spectrometer using a 5 mm $^1H/^{13}C/^{15}N/^{31}P$ inverse detection CryoProbe equipped with a *z*-gradient. Parameter settings for the NMR experiments are summarized in Table S4. NMR spectra were processed with TopSpin 4.0.6 (Bruker).

1H NMR experiments with water suppression using excitation sculpting were recorded on the unlabeled GlcNAc sample at 5 °C intervals from 3 to 40 °C to determine amide proton temperature coefficients and the percentages of *cis* and *trans* amide. Automatic phase correction, baseline correction and linear prediction were conducted prior to peak integration of *cis* and *trans* amide protons. For each temperature, at least three spectra were recorded and the average values were calculated. The temperature was controlled with 4% MeOH in methanol-*d*₄ and was within $\pm 1^\circ C$.

1D EXSY experiments were performed on unlabeled GlcNAc to detect the exchange between *cis* and *trans* conformation. A Gaussian 180° pulse (80 ms) was used for excitation of selected amide protons and excitation sculpting was used for water suppression.

For resonance assignments of GlcNAc *cis* and *trans* forms, the UL-GlcNAc sample was used for 1H , ^{13}C -constant time (CT)-HSQC, 1H , ^{15}N -HSQC, 1H , ^{15}N -HSQC-TOCSY, HNCACB, and (H)C(C)H-TOCSY experiments. In addition, 1D and 2D TOCSY experiments with selective excitation³⁹ of the *cis* form amide protons were recorded on unlabeled GlcNAc to visualize the 1H spin systems of the *cis* forms without spectral overlap with the much more abundant *trans* forms.

The NMR experiments for spin-spin coupling constants are described in detail in the Supporting Information with changes of delays and carbon pulses compared to the default protein NMR experiments. All the experiments were recorded as 2D experiments since the four GlcNAc amide proton signals could be resolved in the 1D 1H spectrum.

The homonuclear coupling constant ${}^3J_{\text{NH}_2\text{H}_2}$ was extracted from the HNCA[HA]-E.COSY experiment,^[40] where H2 becomes the passive spin with ${}^1J_{\text{C}_2\text{H}_2}$ of about 145 Hz as associated coupling. Selective carbon pulses were adjusted for C2 and C1', instead of C α and CO.

${}^3J_{\text{NH}_2\text{C}_1}$ and ${}^3J_{\text{NH}_2\text{C}_3}$ were measured from HNCA[CB]-E.COSY experiments,^[41] with C1 and C3, respectively, becoming the passive spin instead of C β . The two coupling constants were differentiated by carbon pulses selective on either C3 to yield ${}^3J_{\text{NH}_2\text{C}_1}$ or on C1 to yield ${}^3J_{\text{NH}_2\text{C}_3}$, instead of CO pulses in the original experiment. Fortunately, the C1, C2, and C3 carbons of GlcNAc resonate in different spectral regions (at about 95, 60 and 75 ppm, see Table 1), which allows selective pulses that can be distinguished between these different carbons. The associated coupling in the indirect dimension are ${}^1J_{\text{C}_1\text{C}_2}$ and ${}^1J_{\text{C}_2\text{C}_3}$ of about 45 and 35 Hz, respectively, which makes them easily resolved.

The ${}^3J_{\text{H}_2\text{C}_1'}$ coupling constant was measured from the (H)NCAHA(CO)-E.COSY experiment,^[42] where C1' becomes the passive spin with ${}^1J_{\text{N}_\text{C}_1'}$ of about 15 Hz as associated coupling.

The homonuclear carbon coupling constants, ${}^3J_{\text{C}_1\text{C}_1'}$, ${}^2J_{\text{C}_2\text{C}_1'}$, and ${}^3J_{\text{C}_3\text{C}_1'}$, were measured from the spin-echo difference CT-HSQC experiment.^[35] The experiment is run in an interleaved manner, between a reference spectrum that equals a normal CT-HSQC and the second experiment where ${}^3J_{\text{C}_1\text{C}_1'}$ couplings are active during the constant time period. The coupling constants are calculated from the relation between the cross-peak intensities in the two spectra in a J-quantitative manner.

${}^3J_{\text{NH}_2\text{C}_2'}$ was measured from a HNCO[CA]-E.COSY experiment,^[43] where the methyl carbon becomes the passive spin with the associated coupling ${}^1J_{\text{C}_1'\text{C}_2'}$ of about 50 Hz. Carbon pulses selective on C α were exchanged to C2' at 23–25 ppm, which resonate in a region that is clearly distinguished from all other GlcNAc carbons.

A J-quantitative long-range (H)C(C)H experiment was used to measure ${}^3J_{\text{C}_2'\text{C}_2'}$.^[44] It is a COSY-type experiment where the correlation is related to the size of the J_{CC} coupling. Since C2' chemical shifts are different from other carbons, the correlations to C2 could be resolved.

Acknowledgements

The Carl Trygger Foundation is acknowledged for financial support.

Conflict of Interest

The authors declare no conflict of interest.

Data Availability Statement

The data that support the findings of this study are available in the supplementary material of this article.

Keywords: conformational analysis · isotopic labelling · N-acetylglucosamine · NMR spectroscopy

- [1] A. S. Cole, J. E. Eastoe, *Biochemistry and Oral Biology*, Butterworth-Heinemann, Oxford, 1988.
- [2] B. Mousstaf, *Comp. Biochem. Physiol.* **2008**, *149*, 215–226.
- [3] J.-K. Chen, C.-R. Shen, C.-L. Liu, *Mar. Drugs* **2010**, *8*, 2493–2516.
- [4] E. Weerapana, B. Imperiali, *Glycobiology* **2006**, *16*, 91R–101R.
- [5] H. E. Murrey, L. C. Hsieh-Wilson, *Chem. Rev.* **2008**, *108*, 1708–1731.
- [6] K. Mariño, J. Bones, J. J. Kattla, P. M. Rudd, *Nat. Chem. Biol.* **2010**, *6*, 713–723.
- [7] K. Skarbek, M. J. Milewska, *Carbohydr. Res.* **2016**, *434*, 44–71.
- [8] B. M. Sattelle, A. Almond, *Glycobiology* **2011**, *21*, 1651–1662.
- [9] X. Hu, W. Zhang, I. Carmichael, A. S. Serianni, *J. Am. Chem. Soc.* **2010**, *132*, 4641–4652.
- [10] C. Dugave, *cis-trans Isomerization in Biochemistry*, Wiley-VCH, Weinheim, 2006.
- [11] G. Fischer, *Chem. Soc. Rev.* **2000**, *29*, 119–127.
- [12] G. V. Garner, O. Meth-Cohn, H. Suschitzky, *J. Chem. Soc. C* **1971**, 1234–1236.
- [13] E. Beausoleil, W. D. Lubell, *J. Am. Chem. Soc.* **1996**, *118*, 12902–12908.
- [14] G. Scherer, M. L. Kramer, M. Schutkowski, U. Reimer, G. Fischer, *J. Am. Chem. Soc.* **1998**, *120*, 5568–5574.
- [15] J. Hendrickx, V. Tran, Y. Sanejouand, *Proteins* **2020**, *88*, 1376–1383.
- [16] T. Lütteke, M. Frank, C.-W. von der Lieth, *Carbohydr. Res.* **2004**, *339*, 1015–1020.
- [17] M. Mobli, A. Almond, *Org. Biomol. Chem.* **2007**, *5*, 2243–2251.
- [18] C. D. Blundell, P. L. Deangelis, A. Almond, *Biochem. J.* **2006**, *396*, 487–498.
- [19] G. Giubertoni, G. H. Koenderink, H. J. Bakker, *J. Phys. Chem. A* **2019**, *123*, 8220–8225.
- [20] G. Nestor, C. Sandström, *Carbohydr. Polym.* **2017**, *157*, 920–928.
- [21] M. K. Cowman, D. Cozart, K. Nakanishi, E. A. Balazs, *Arch. Biochem. Biophys.* **1984**, *230*, 203–212.
- [22] A. Almond, P. L. Deangelis, C. D. Blundell, *J. Mol. Biol.* **2006**, *358*, 1256–1269.
- [23] J. T. Davis, S. Hirani, C. Bartlett, B. R. Reid, *J. Biol. Chem.* **1994**, *269*, 3331–3338.
- [24] X. Hu, I. Carmichael, A. S. Serianni, *J. Org. Chem.* **2010**, *75*, 4899–4910.
- [25] D. J. Langeslay, S. Beni, C. K. Larive, *J. Magn. Reson.* **2012**, *216*, 169–174.
- [26] V. H. Pomin, J. S. Sharp, X. Li, L. Wang, J. H. Prestegard, *Anal. Chem.* **2010**, *82*, 4078–4088.
- [27] M. Avalos, R. Babiano, C. J. Durán, J. L. Jiménez, J. C. Palacios, *J. Chem. Soc. Perkin Trans. 2* **1992**, 2205–2215.
- [28] T. Cierpicki, J. Otlewski, *J. Biomol. NMR* **2001**, *21*, 249–261.
- [29] C. D. Blundell, A. Almond, *Magn. Reson. Chem.* **2007**, *45*, 430–433.
- [30] S. Rothmund, H. Weißhoff, M. Beyermann, E. Krause, M. Bienert, C. Mügge, B. D. Sykes, F. D. Sönnichsen, *J. Biomol. NMR* **1996**, *8*, 93–97.
- [31] J. A. Sogn, W. A. Gibbons, E. W. Randall, *Biochemistry* **1973**, *12*, 2100–2105.
- [32] Y. Zhu, Q. Pan, C. Thibaudeau, S. Zhao, I. Carmichael, A. S. Serianni, *J. Org. Chem.* **2006**, *71*, 466–479.
- [33] D. Horton, J. S. Jewell, *Carbohydr. Res.* **1966**, *2*, 251–260.
- [34] O. Engström, H. Mobarak, J. Stähle, G. Widmalm, *J. Phys. Chem. B* **2017**, *121*, 9487–9497.
- [35] S. Grzesiek, A. Bax, *J. Biomol. NMR* **1993**, *3*, 185–204.
- [36] Q. Xu, C. A. Bush, *Carbohydr. Res.* **1998**, *306*, 335–339.
- [37] D. Horton, J. S. Jewell, K. D. Phillips, *J. Org. Chem.* **1966**, *31*, 4022–4025.
- [38] A. Neuberger, A. P. Fletcher, *Carbohydr. Res.* **1971**, *17*, 79–88.
- [39] E. Alexandersson, C. Sandström, L. C. E. Lundqvist, G. Nestor, *RSC Adv.* **2020**, *10*, 32511–32515.
- [40] R. Weisemann, H. Rüterjans, H. Schwalbe, J. Schleucher, W. Bermel, C. Griesinger, *J. Biomol. NMR* **1994**, *4*, 231–240.
- [41] A. C. Wang, A. Bax, *J. Am. Chem. Soc.* **1996**, *118*, 2483–2494.
- [42] F. Löhr, H. Rüterjans, *J. Biomol. NMR* **1995**, *5*, 25–36.
- [43] M. Hennig, W. Bermel, H. Schwalbe, C. Griesinger, *J. Am. Chem. Soc.* **2000**, *122*, 6268–6277.
- [44] A. Bax, D. Max, D. Zax, *J. Am. Chem. Soc.* **1992**, *114*, 6923–6925.

Manuscript received: June 14, 2022
 Revised manuscript received: June 17, 2022
 Accepted manuscript online: June 17, 2022
 Version of record online: July 11, 2022

ChemBioChem

Supporting Information

Determination of Amide *cis/trans* Isomers in *N*-Acetyl-D-glucosamine: Tailored NMR Analysis of the *N*-Acetyl Group Conformation

Yan Xue and Gustav Nestor*

1. Supplementary Methods	
Spin-spin coupling constant experiments	S2
2. Supplementary Figures	
Figure S1	S4
Figure S2.....	S4
Figure S3.....	S4
Figure S4.....	S5
Figure S5.....	S6
Figure S6.....	S7
Figure S7.....	S7
Figure S8.....	S8
3. Supplementary Tables	
Table S1	S9
Table S2.....	S9
Table S3	S10
Table S4.....	S11
4. References.....	S12

Supplementary Methods

Spin-spin coupling constant experiments

See also Table S4 for additional parameters.

HNCA[HA]-E.COSY (${}^3J_{\text{NH,H2}}$)

The carrier frequency was positioned at 56 ppm (C2) for ${}^{13}\text{C}$ and 123 ppm for ${}^{15}\text{N}$. Off-resonance 180° shaped carbon pulses were positioned at 83 ppm to cover C1 and C3, but not C2. Pulse durations were 800 μs for off-resonance 180° Q3-surbop, 1.4 ms for on-resonance 180° Q3-surbop and 1.5 ms for 90° Q5-sebop pulses. Simultaneous decoupling of C2 and C1' was achieved with an MLEV-16 expansion of Q3 pulses of 768 μs length. ${}^{15}\text{N}$ was decoupled using the GARP decoupling sequence. The delays were set as follows: $\Delta/2 = 2.3$ ms, $\Delta' = 2.7$ ms, $\tau/2 = 13$ ms, $\tau'/2 = 11.1$ ms, and $\varepsilon = 1.2$ ms. Delay notations are referred to Weisemann et al. (1994).^[1]

HNCA[CB]-E.COSY (${}^3J_{\text{NH,C1}}$ and ${}^3J_{\text{NH,C3}}$)

Off-resonance 180° shaped carbon pulses were positioned at C3 (76 ppm) and C1 (95 ppm) for measuring ${}^3J_{\text{NH,C1}}$ and ${}^3J_{\text{NH,C3}}$, respectively. On-resonance shaped pulses were positioned at C2 (56 ppm). To make the pulses selective on either C1, C2, or C3, the pulse duration was set to 1.4 ms for 180° Q3-surbop and 1.5 ms for 90° Q5-sebop pulses. The carrier for the ${}^{15}\text{N}$ pulses was positioned at 123 ppm and ${}^{15}\text{N}$ GARP4 decoupling was applied during the acquisition with 567 μs pulse duration to allow for a long acquisition time (854 ms). Delay durations were $\tau = 2.3$ ms, $\Delta = 5.4$ ms, and $T = 13$ ms. Delay notations are referred to Wang and Bax (1996).^[2]

(H)NCAHA(CO)-E.COSY (${}^3J_{\text{H2,C1'}}$)

The carrier frequency was positioned at 55 ppm (C2) for ${}^{13}\text{C}$ and 123.2 ppm for ${}^{15}\text{N}$. Off-resonance 180° shaped carbon pulses were positioned at C1' (180 ppm) and the 180° pulse on aliphatic carbons during the ${}^{13}\text{C}$ constant-time evolution period was centered at 65 ppm. Pulse durations were 270 μs for 180° Q3-surbop and 350 μs for 90° Q5-sebop pulses. No ${}^{13}\text{C}$ or ${}^{15}\text{N}$ decoupling was used during the acquisition. Delay durations were $\tau = 2.3$ ms, $\eta = 5.4$ ms, $T_{\text{N}}/2 = 15.5$ ms, $T_{\text{C}}/2 = 11.1$ ms, $\kappa = 2.1$ ms, and $\delta = 1.7$ ms. Delay notations are referred to Löhner and Rüterjans (1995).^[3]

Spin-echo difference CT-HSQC (${}^3J_{\text{C1,C1'}}$, and ${}^3J_{\text{C3,C1'}}$)

The carrier frequency was positioned at 80 ppm for ${}^{13}\text{C}$ and 117 ppm for ${}^{15}\text{N}$. Off-resonance 180° shaped carbon pulses were positioned at C1' (178 ppm) and the pulse durations for shaped carbon pulses were 270 μs (180° Q3-surbop). ${}^{13}\text{C}$ was decoupled using the GARP decoupling sequence. The delays were set as follows: $\tau = 1.7$ ms and $T = 27$ ms, where the constant-time delay ($2T = n/{}^1J_{\text{CC}}$) was a compromise between ${}^1J_{\text{C1,C2}} = 45$ Hz and ${}^1J_{\text{C2,C3}} = 35$ Hz.

HNCO[CA]-E.COSY (${}^3J_{\text{NH,C2'}}$)

The carrier frequency was positioned at 174.8 ppm (C1') for ${}^{13}\text{C}$ and 123 ppm for ${}^{15}\text{N}$. Off-resonance 180° shaped carbon pulses were positioned close to C2' (10 ppm). Pulse durations were 500 μs for off-resonance 180° Q3-surbop, 270 μs for on-resonance 180° Q3-surbop and 350 μs for 90° Q5-sebop pulses. No ${}^{13}\text{C}$ or ${}^{15}\text{N}$ decoupling was used during the acquisition. The delays were set according to the default values in the pulse program.

***J*-quantitative long-range (H)C(C)H ($^3J_{C_2,C_2}$)**

The carrier frequency was positioned at 98 ppm for ^{13}C and 123 ppm for ^{15}N . Off-resonance 180° Q3-surbop carbon pulses were positioned at C1' (180 ppm) and 180° Q3-surbop pulses for aliphatic carbons were positioned at 63 ppm, both pulses with a duration of 270 μs . In addition, on-resonance ^{13}C inversion was achieved with a 60 kHz smoothed Chirp pulse (0.5 ms, 20.1% smoothing). ^{13}C was decoupled using the GARP decoupling sequence. The delays were set as follows: $\tau = 1.6$ ms and T = 22.2 ms.

Supplementary Figures

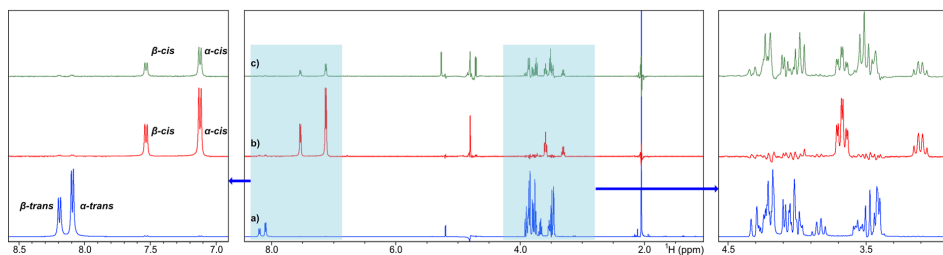


Figure S1. ^1H NMR spectrum with excitation sculpting a) and bandselective 1D TOCSY spectra with excitation of the *cis* amide protons and a mixing time of 20 ms b) and 120 ms c).

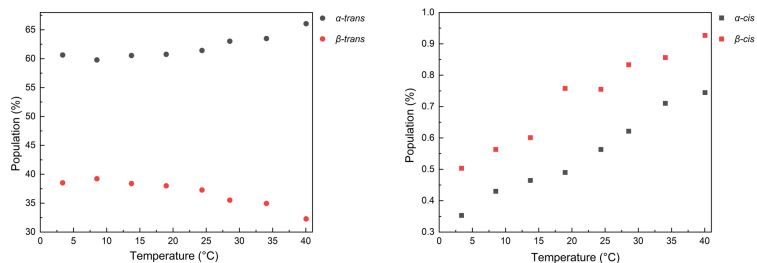


Figure S2. The relative concentration of *trans* and *cis* amide of α - and β -GlcNAc over a temperature range from 3 to 40 $^{\circ}\text{C}$.

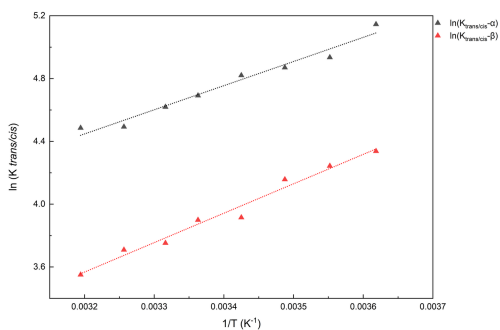


Figure S3. Van't Hoff plots for α - (black triangles) and β -GlcNAc (red triangles) using data from **Table SI 1**. $\Delta H^{\circ}_{cis \rightarrow trans}$, $\Delta S^{\circ}_{cis \rightarrow trans}$ and $\Delta G^{\circ}_{cis \rightarrow trans}$ values for the conversion of *cis* to *trans* amide in α - and β -pyranosides were determined (see text).

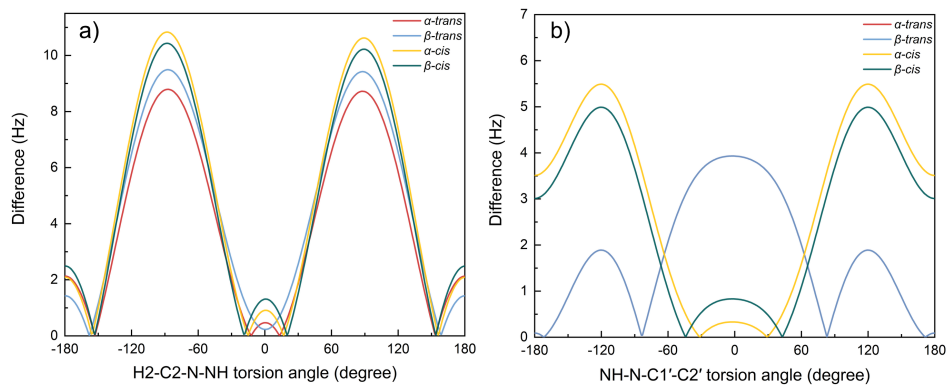


Figure S4. The difference between the experimental value of a) ${}^3J_{\text{NH},\text{H}2}$ and b) ${}^3J_{\text{NH},\text{C}2'}$ and the calculated values from the Karplus equations. In b), the curves for α -trans and β -trans are identical since the experimental values were the same (0.9 Hz).

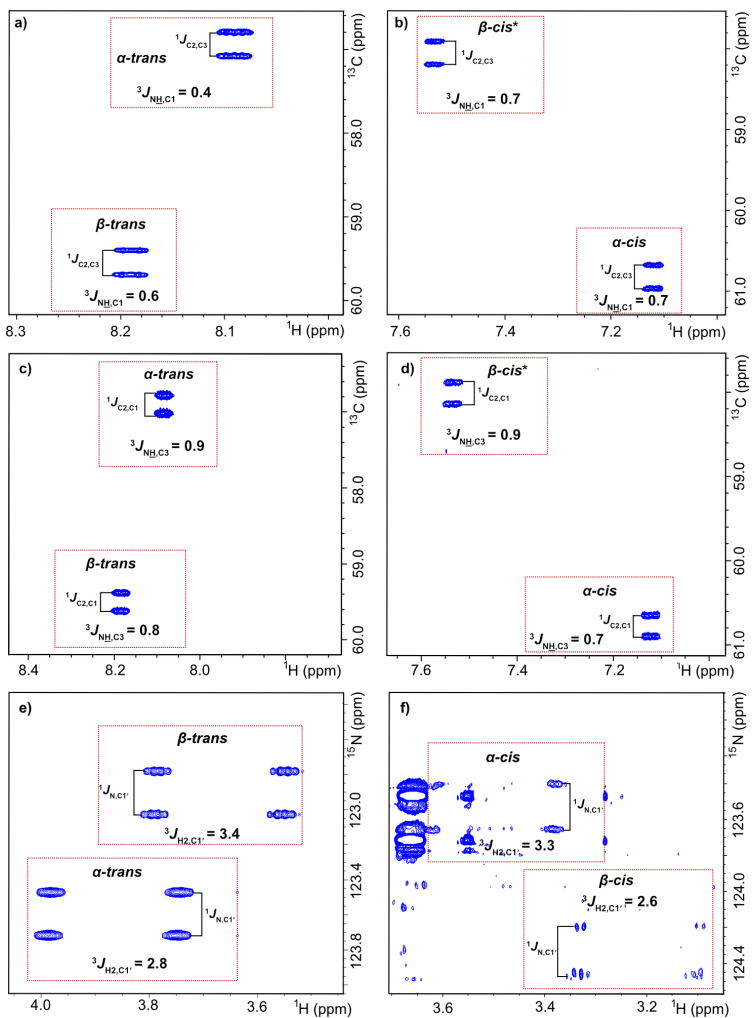


Figure S5. E-COSY spectra used to measure $^3J_{\text{NH,C1}}$ (a and b), $^3J_{\text{NH,C3}}$ (c and d), and $^3J_{\text{H2,C1}}$ (e and f). Cross-peaks that are folded in the spectra are indicated by an asterisk (*).

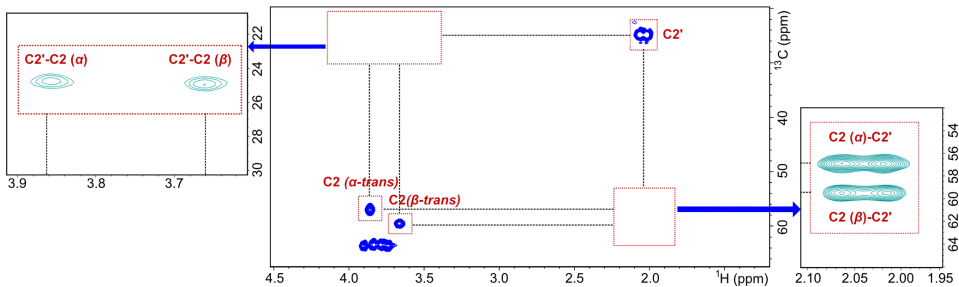


Figure S6. J -quantitative long-range (H)C(C)H spectrum used to measure ${}^3J_{C_2,C_2'}$. The J -couplings were measured from the cross-peaks corresponding to C2/H2' (f1/f2).

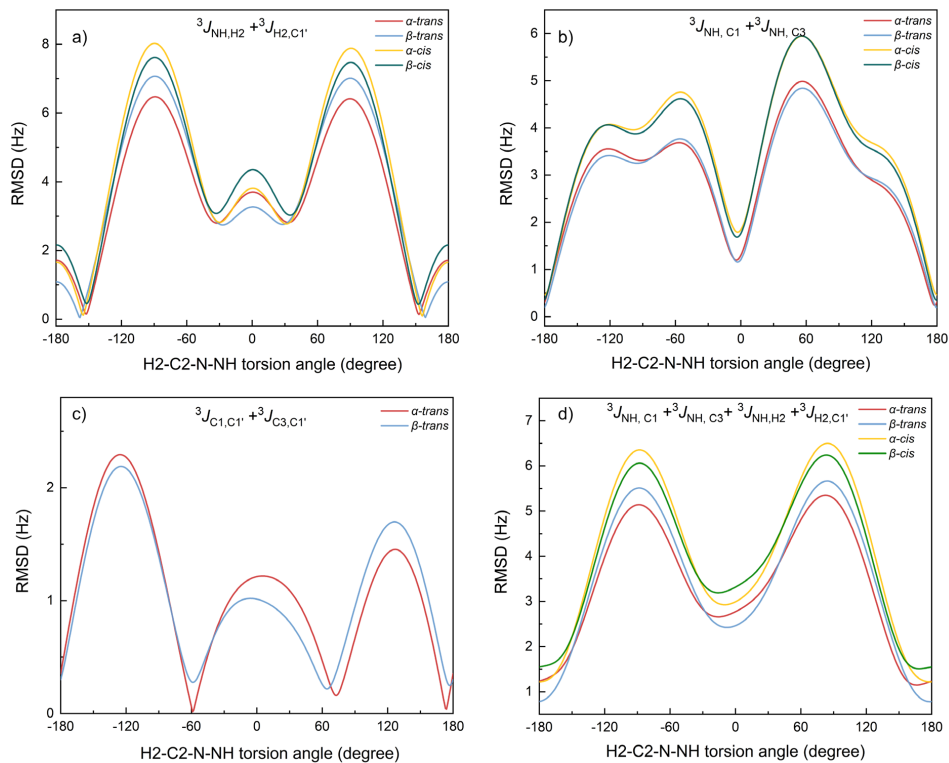


Figure S7. Plots of RMSD versus four groups of coupling constants that are sensitive to θ_1 : a) Group 1 with ${}^3J_{NH,H_2}$ and ${}^3J_{H_2,C_1'}$; b) Group 2 with ${}^3J_{NH,C_1}$ and ${}^3J_{NH,C_3}$; c) Group 3 with ${}^3J_{C_1,C_1'}$ and ${}^3J_{C_3,C_1'}$; and d) Group 4 with ${}^3J_{NH,C_1}$, ${}^3J_{NH,C_3}$, ${}^3J_{NH,H_2}$, and ${}^3J_{H_2,C_1'}$.

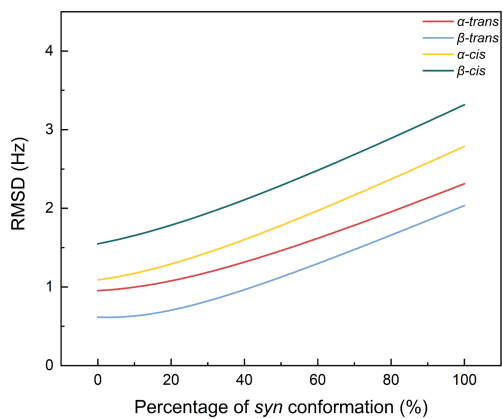


Figure S8. The overall two-state plot of RMSD versus percentage of *syn* conformation using all coupling constants that are sensitive to θ_1 .

Supplementary Tables

Table S1. The equilibrium constants $K_{trans/cis}$ of GlcNAc at different solution temperatures and thermodynamic parameters derived from $K_{trans/cis}$.

T (°C)	$K_{trans/cis}$	
	α - pyranoside	β - pyranoside
3.4	171.7	76.5
8.5	139.0	69.6
13.7	130.3	63.9
19.0	124.0	50.1
24.4	109.0	49.3
28.6	101.4	42.6
34.1	89.4	40.8
40.0	88.7	34.8

	Thermodynamic parameter ($cis \rightarrow trans$)	
	α - pyranoside	β - pyranoside
ΔH° (kJ* mol ⁻¹)	-12.8 ± 0.92	-15.6 ± 0.94
ΔS° (J*K ⁻¹ *mol ⁻¹)	-3.9 ± 3.13	-20.2 ± 3.21
ΔG° (kJ*mol ⁻¹)	-11.6 ± 0.01	-8.9 ± 0.01

Table S2. A summary of NMR experiments that were used to measure 3J coupling constants.

	E.COSY				J-Quantitative	
Multiplet pattern						
Coupling constant	$^3J_{NH,H2}$	$^3J_{H2,C1'}$	$^3J_{NH,C1}$ and $^3J_{NH,C3}$	$^3J_{NH,C2'}$	$^3J_{C1,C1'}$ and $^3J_{C3,C1'}$	$^3J_{C2,C2'}$
Original pulse program	HNCA[HA]-E.COSY	(H)NCAHA[CO]-E.COSY	HNCA[CB]-E.COSY	HNCO[CA]-E.COSY	Spin-echo difference CT-HSQC	J-quantitative long-range (H)C(C)H
Adjusted name for aminosugars	HNC2[H2]-E.COSY	(H)NC2H2[C1]-E.COSY	HNC2[C1/C3]-E.COSY	HNC1'[C2]-E.COSY	/	/

Table S3. Karplus equation coefficients on the formula ${}^3J = \mathbf{A} + \mathbf{B} \cos \theta + \mathbf{C} \cos(2\theta) + \mathbf{D} \sin \theta + \mathbf{E} \sin(2\theta)$ for θ_1 and the formula ${}^3J = \mathbf{A} + \mathbf{B} \cos \theta + \mathbf{C} \cos(2\theta) + \mathbf{D} \cos(3\theta) + \mathbf{E} \sin(\theta) + \mathbf{F} \sin(2\theta) + \mathbf{G} \sin(3\theta)$ for θ_2 , as well as torsion angle differences of θ_1 and θ_2 .^a

		θ_1					
		H2-C2-N-H	H2-C2-N-C1'	C1-C2-N-H	C3-C2-N-H	C1-C2-N-C1'	C3-C2-N-C1'
θ_2 - <i>trans</i>	A	5.08	3.11	2.94	2.57	1.27	1.11
	B	-0.83	-2.02	-1.00	-0.61	-1.31	-0.87
	C	5.02	2.88	3.48	2.92	1.36	1.15
	D	0.03	-0.04	0.12	-0.09	0.12	-0.09
	E	0.06	0.05	-0.27	0.27	-0.07	0.08
θ_2 - <i>cis</i>	A	5.99	3.19	3.62	3.14	1.37	
	B	-0.59	-2.12	-1.32	-0.78	-1.52	
	C	6.11	3.30	4.13	3.47	1.62	
	D	0.10	-0.02	0.20	-0.16	0.10	
	E	0.12	0.06	-0.46	0.37	-0.15	
Angles	θ_1 - <i>syn</i> (°)	0	180	120	-120	-60	60
	θ_1 - <i>anti</i> (°)	180	0	-60	60	120	-120
	Difference (°) ^b	0	180	120	-120	-60	60

		θ_2	
		H-N-C1'-C2'	C2-N-C1'-C2'
θ_1 - <i>anti</i>	A	1.62	0.39
	B	-2.59	-1.03
	C	1.29	0.36
	D	0.67	0.25
	E	0.02	-0.01
	F	-0.02	0.02
	G	0.003	-0.004
θ_1 - <i>syn</i>	A	1.62	0.84
	B	-2.59	-2.03
	C	1.29	0.60
	D	0.67	0.13
	E	0.02	0.04
	F	-0.02	-0.02
	G	0.003	0.002
Angles	θ_2 - <i>cis</i> (°)	180	0
	θ_2 - <i>trans</i> (°)	0	180
	Difference (°) ^c	180	0

^aThe Karplus equations are from Hu et al.^[4]

^b Compared to H2-C2-N-H.

^c Compared to C2-N-C1'-C2'.

Table S4. Parameter settings for all NMR experiments.

Sample	Fig.	J	Experiment	Pulse sequence	NS	Dimensions	SW (ppm)	TD	AQ (ms)	T (°C)	Comments ^d	Exp. time
GlcNAc (unlabeled)	1		1D ¹ H	zgpgp	8	12	32k		2,272	25 ^b		1.5 min
GlcNAc (unlabeled)	S1		1D sel. TOCSY	b	256	10	32k		2,726	25	$\tau_{\text{mix}} = 120$ ms	17 min
GlcNAc (unlabeled)			2D sel. TOCSY	b	64	F2-F1	8×8	2k×128	213×13	25	$\tau_{\text{mix}} = 120$ ms	4 h
GlcNAc (unlabeled)	2		1D sel. EXSY	c	2k	8	32k		3,412	25	$\tau_{\text{mix}} = 400$ ms	2.8 h
UL- ¹³ C, ¹⁵ N-GlcNAc	1		¹ H, ¹⁵ N-HSQC	hscqcf3gpqh	16	F2-F1	17×6	2k×128	100×175	25		48 min
UL- ¹³ C, ¹⁵ N-GlcNAc			¹ H, ¹³ C-CT-HSQC	hscqctetgpsi	32	F2-F1	8×86	1k×256	107×10	25	2T = 22 ms	3.7 h
UL- ¹³ C, ¹⁵ N-GlcNAc			2D (H)(C)H-TOCSY	hcbhfgp3d2	64	F3-F1	8×100	1k×512	107×17	25	$\tau_{\text{mix}} = 11$ ms	15.4 h
UL- ¹³ C, ¹⁵ N-GlcNAc			2D ¹ H, ¹⁵ N-HSQC-TOCSY	hscqctetf3gpsi	16	F2-F1	8×4	1k×128	107×263	25	$\tau_{\text{mix}} = 100$ ms	1 h
UL- ¹³ C, ¹⁵ N-GlcNAc			2D HNCACB	hncatcbgwg3d	32	F3-F1	7.5×90	1k×128	114×5	25		2 h
UL- ¹³ C, ¹⁵ N-GlcNAc	4	³ J _{AG,H2}	2D HNC[HA]-E-COSY	hncatcosgp3d2	32	F3-F1	7.4×14	1k×128	116×30	25		1.5 h
UL- ¹³ C, ¹⁵ N-GlcNAc	S4	³ J _{AG,C1}	2D HNC[CB]-E-COSY	hncatjgp3d	64	F3-F1	8×6	8k×128	854×71	25		7 h
UL- ¹³ C, ¹⁵ N-GlcNAc	S4	³ J _{AG,C3}	2D HNC[CB]-E-COSY	hncatjgp3d	64	F3-F1	8×6	8k×128	854×71	25		7 h
UL- ¹³ C, ¹⁵ N-GlcNAc	S4	³ J _{H2,C1}	2D (H)NCA(HA)(CO)-E-COSY	hncatagp3d	256	F3-F1	7×4	4k×128	487×263	25		25 h
UL- ¹³ C, ¹⁵ N-GlcNAc		³ J _{C1,C1} , ³ J _{C3,C1}	2D spin-echo diff. CT-HSQC	hscqctetgpijlr	64	F2-F1	8×60	2k×256	214×14	25		10.5 h
UL- ¹³ C, ¹⁵ N-GlcNAc	4	³ J _{AG,C2}	2D HNC[CA]-E-COSY	hncatcosgp3d	32	F3-F1	8×2	4k×64	427×106	25		1.5h
UL- ¹³ C, ¹⁵ N-GlcNAc	S5	³ J _{C3,C2}	2D J -quant. long-range (H)(C)H	hcbctagplr	32	F2-F1	7.5×164	1k×256	114×5	25		4h

^a A series of experiments were also performed at different temperatures (5–40 °C) to obtain temperature coefficients.

^b In-house pulse sequences from Alexandersson et al.^[6] Bandselective ¹H pulses covering *cis* amide protons (6.9 ppm) were achieved with IBURP-2, shapes of 6.45 ms duration and a bandwidth of 770 Hz.

^c In-house pulse sequence based on the Bruker pulse sequence *seltrngp*, with the inclusion of excitation sculpting for water suppression.

^d The relaxation delay was set to 1.5 s or larger.

References

- [1] R. Weisemann, H. Rüterjans, H. Schwalbe, J. Schleucher, W. Bermel, C. Griesinger, *J. Biomol. NMR* **1994**, *4*, 231–240.
- [2] A. C. Wang, A. Bax, *J. Am. Chem. Soc.* **1996**, *118*, 2483–2494.
- [3] F. Löhr, H. Rüterjans, *J. Biomol. NMR* **1995**, *5*, 25–36.
- [4] X. Hu, I. Carmichael, A. S. Serianni, *J. Org. Chem.* **2010**, *75*, 4899–4910.
- [5] E. Alexandersson, C. Sandström, L. C. E. Lundqvist, G. Nestor, *RSC Adv.* **2020**, *10*, 32511–32515.

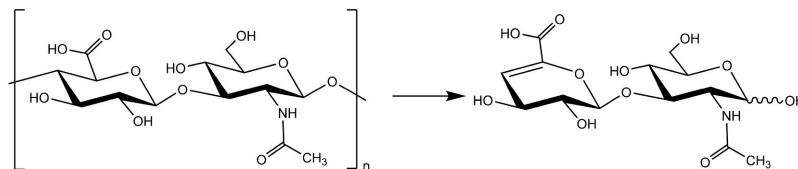


Fig. 1. Schematic representation of HA polysaccharide built by repeating disaccharide unit of $\rightarrow 4$ -D-GlcP- β (1 \rightarrow 3)-D-GlcPNAc- β (1 \rightarrow (left) and Δ HA₂ obtained by degradation with chondroitinase ABC (right).

hydroxyl protons involved in hydrogen bonds with the protein [13]. Such experiments have been used more often on protein-ligand interactions in general [14] and on protein-RNA interactions [15], but an easier access to ¹³C-labeled glycans has the potential for a more frequent use of these experiments on protein-glycan interactions [16].

In recent years, NMR spectroscopists and glycoscientists have started to explore the development of new isotope labeling methods. The preparation of ¹³C and/or ¹⁵N enriched heparin, its precursors and unsulfated chondroitin from *E. coli* K5 has been reported [17–20], as well as the *in vivo* ¹⁵N-labeling of GAG oligosaccharides [21]. Glycoproteins containing uniformly and site-specifically ¹³C-enriched *N*-acetylneuraminic acid have been produced and NMR pulse sequences tailored for sialylated biomolecules were reported [22]. Furthermore, ¹⁵N NMR has been exploited on oligomers of glycosaminoglycan, which resulted in resolved NH signals owing to the enhanced chemical shift dispersion in ¹⁵N compared to ¹H [23,24]. The use of ¹⁵N labeling together with ¹³C labeling not only enables ¹⁵N-edited 3D NMR experiments to resolve resonance overlap but also provides valuable sequence-specific information of the inter-residues of nitrogen-containing glycans. However, the use of isotope labeling methods to establish structural information from glycan is still very limited compared to the widespread applications of isotope labeling in protein NMR.

Since the 1980s, microbial-derived biotechnology has been developed for the production of HA. Among the bacteria capable of synthesizing HA, there are both Gram-positive Streptococci of groups A and C (e.g. *Streptococcus equi* subsp. *zooepidemicus*) and Gram-negative pathogenic bacteria (e.g. *Pasteurella multocida*). In comparison with previously reported *E. coli* K5 strain transfected with the recombinant HA synthase from *Pasteurella multocida*, *Streptococcus equi* subsp. *Zooepidemicus* is a natural producer of HA as a capsule of the bacteria and it is commonly used in a variety of culturing protocols employed for the biotechnological production of HA. Therefore, it allows to exploit the native biosynthetic pathways of *Streptococci* for the production of HA, using ¹³C- and ¹⁵N-labeled substrate replacement in the culturing medium. The prevalence in the biotechnological applications, the ease of isolation, and a relatively high yield of the obtained HA made the *Streptococcus zooepidemicus* the optimal bacterium for the purposed approach of isotopic labeling.

We herein report on the biosynthetic production of ¹³C,¹⁵N-labeled HA polysaccharides by *Streptococcus zooepidemicus* using small-scale cultures and media with defined carbon and nitrogen sources. The isotopic distribution and the extent of isotopic enrichment of the labeled HA polysaccharide were assessed quantitatively by NMR and mass spectrometry (MS). Performing analysis on intact HA polymer of high molecular weight is difficult or even not feasible due to high viscosity that leads to poor sensitivity and severe line broadening of NMR resonances resulting in inaccurate signal integration. Therefore, the polysaccharide was enzymatically digested to disaccharide prior to NMR and MS analysis. This study provides a valid methodological approach that can be applied to the quantitative assessment of isotopically labeled glycans and will help improve detection capabilities and facilitate future structure-function relationship analysis of complex glycans.

2. Results and discussion

2.1. Biosynthesis of isotopically labeled HA polysaccharide

For the production of the bio-synthetically ¹³C and ¹⁵N-labeled HA, *Streptococcus equi* subsp. *Zooepidemicus* - a bacterium that is commonly used in the biotechnological production of HA was employed. The biosynthesis pathways of HA have already been well-established: glucose in the source medium enters the bacterial metabolic pathways through enzymatic conversion to glucose-6-phosphate, followed by isomerization to fructose-6-phosphate. The fructose-6-phosphate is directly involved in the synthesis of acetamido sugars using *L*-glutamine as the source of amine and an acetyl-CoA as a source of the *N*-acetyl group [25]. Thus, GlcA and GlcNAc are derived from glucose-6-phosphate and fructose-6-phosphate, respectively, and UDP-GlcNAc and UDP-GlcA become the direct precursors of HA [26]. However, the synthesis of HA competes constantly with cell growth. The metabolic pathways of glucose provide also the building blocks that constitute bacterial cell wall polysaccharides, teichoic acids, and bacterial biomass in general. Consequently, only 10% of the initial glucose ends up in HA [27]. The metabolic labeling used in this study relied on the initial assumptions that, first, glucose is a primary carbon source for both D-GlcA and D-GlcNAc during the HA biosynthesis; second, *L*-glutamine provides the amino group for the Glc-6-P \rightarrow Fru-6-P \rightarrow GlcN-6-P conversion pathway that leads to D-GlcNAc formation; and third, the complete replacement of D-glucose and *L*-glutamine in the medium with U-¹³C₆-D-glucose and *L*-glutamine-(amide-¹⁵N) should yield the ¹³C,¹⁵N-labeled HA.

2.2. Isolation of ¹³C,¹⁵N-enriched Δ HA₂

The HA polysaccharide was digested using chondroitinase ABC. This lyase can cleave via a β -elimination reaction all 1 \rightarrow 4 linkages between GlcNAc and GlcA to generate the disaccharide Δ HA₂ with an unsaturated uronic acid at the non-reducing end [28,29] (Fig. 1). The products of the digestion were fractionated by HPLC and the α and β anomers of the disaccharides were well separated as two chromatographic peaks (Fig. S1). The fractions containing Δ HA₂ were lyophilized and further analyzed by NMR spectroscopy and MS.

2.3. NMR analyses of ¹³C,¹⁵N-enriched Δ HA₂

2.3.1. Chemical shift assignment

The ¹H, ¹³C, and ¹⁵N resonances of Δ HA₂ were assigned from a series of 1D and 2D NMR experiments including ¹H,¹³C-HSQC, ¹H,¹⁵N-HSQC, and ¹H,¹³C-HMBC. The data are in good agreement with previously published results on HA oligosaccharides [23,30,31]. In aqueous solution, the GlcNAc reducing end of Δ HA₂ is present in equilibrium between the α - and β -anomers in a 62/38% ratio due to mutarotation. Therefore, signals arising from both α - and β -anomers should be observed for all protons and carbons on both the reducing and non-reducing sugars. However, due to the negligible effect of anomeric configuration on the neighboring sugar and the limited spectral resolution, the ¹H and ¹³C signals for the α - and β -form of the disaccharide

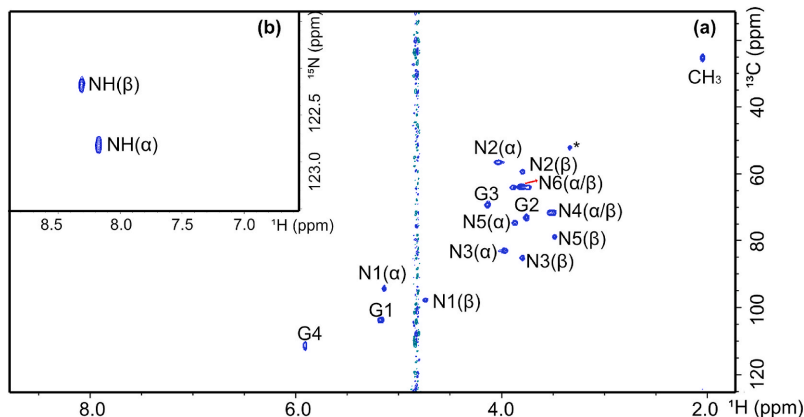


Fig. 2. 2D (a) ^1H , ^{13}C -HSQC and (b) ^1H , ^{15}N -HSQC spectra of ^{13}C , ^{15}N -enriched ΔHA_2 at 25 °C. Cross-peaks are annotated with G representing GlcA and N representing GlcNAc followed by a number indicating the position giving rise to the signal. NH and CH₃ represent signals arising from the amide and methyl protons of the *N*-acetyl group on GlcNAc, respectively. α and β represent the anomeric configuration of GlcNAc. *: Methanol.

can only be differentiated on the reducing sugar as shown in Fig. 2a. Similarly, the amide proton cross-peaks of α - and β -anomers could be identified in the ^1H , ^{15}N -HSQC spectrum (Fig. 2b).

2.3.2. Quantitative NMR analysis

The level of isotope enrichment in ΔHA_2 was determined from a combination of 1D and 2D quantitative NMR experiments. Since data reliability in quantitative NMR analysis is influenced by many factors, such as the relaxation delay, NOE, signal-to-noise ratio (S/N), and digitization, the acquisition and processing parameters must be treated with caution. Based on previous relaxation time measurements [32–34], a relaxation delay of 25 s was chosen for both ^1H and ^{13}C experiments to ensure complete nuclear relaxation, and 16 k scans were acquired for ^{13}C experiments to obtain a sufficient S/N. In addition, quantitative determination of isotopic enrichment in a commercially purchased [UL- $^{13}\text{C}_8$; ^{15}N]-GlcNAc sample was conducted to validate our NMR methods based on 1D ^1H , 1D ^{13}C , and 2D ^1H , ^{13}C -HSQC (see more information in Experimental and Supporting Information).

The characteristic amide proton (δ 8.0–8.5 ppm) and methyl protons (δ 1.8–2.1 ppm) of the *N*-acetyl group of GlcNAc and the G4 proton (δ 5.5–6.0 ppm) of ΔGlcA can be differentiated from the other overlapping

signals in the 1D ^1H spectrum (Fig. 3, highlighted in red). However, signals from protons bound to unlabelled nuclei (i.e., ^{12}C and ^{14}N) and labeled nuclei (^{13}C and/or ^{15}N) are observed simultaneously. Therefore, three ^{13}C - or ^{15}N -decoupled ^1H NMR spectra were acquired to distinguish between the ^1H signals of isotopically labeled and unlabelled ΔHA_2 (Fig. 3a, b, and c). In Fig. 3a, the ^1H spectrum with ^{15}N decoupling shows two doublets at 8.32 and 8.18 ppm, corresponding to the amide proton of β - and α -GlcNAc, respectively. Without ^{15}N decoupling, the two doublets are split and partially overlapped due to the ^1H - ^{15}N one-bond *J*-coupling. The signals from the proton bound to ^{14}N without splitting from the ^1H - ^{15}N coupling show incomplete ^{15}N incorporation

Table 1

Mean level of isotope enrichment (%) of ^{13}C and ^{15}N in ΔHA_2 determined by quantitative ^1H NMR.^a

Proton positions		
G4	NH (α/β)	Me
96 ± 2	66 ± 1/63 ± 2	61 ± 2

^a Data with standard deviation are presented from at least three measurements and D1 was set to 25 s.

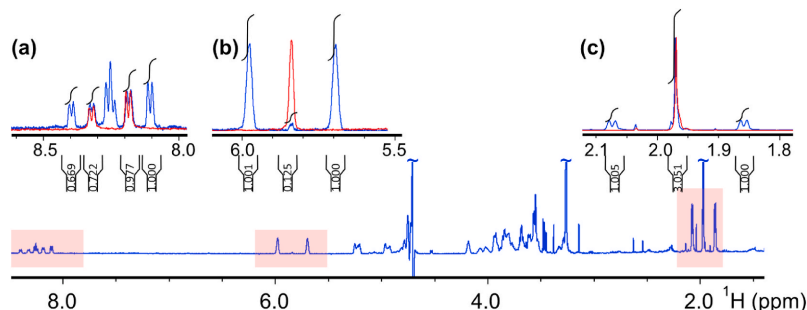


Fig. 3. 1D ^1H NOESY presaturation spectrum (blue) of ^{13}C , ^{15}N -enriched ΔHA_2 at 25 °C. Highlighted regions correspond to (a) amide protons with ^{15}N decoupling centered at 120 ppm (red); (b) G4 proton with ^{13}C decoupling centered at 110 ppm (red); (c) methyl protons with ^{13}C decoupling centered at 30 ppm (red). The intensity of decoupled spectra was adjusted to match the NOESY presaturation spectrum. The water suppression was achieved by presaturation during relaxation delay ($d1 = 25\text{ s}$) and mixing time ($d8 = 50\text{ ms}$).

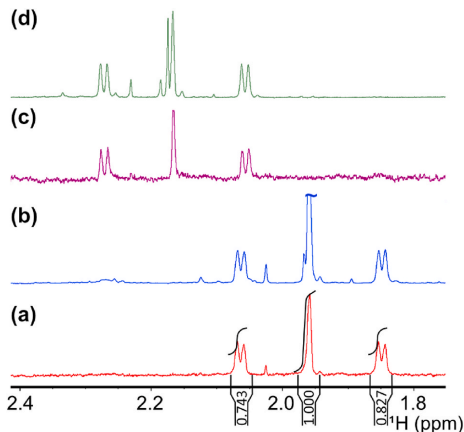


Fig. 4. 1D diffusion NMR of ^{13}C , ^{15}N -enriched ΔHA_2 with 95% gradient strength at (a) 25 °C and (c) 45 °C and 1D NOESY saturation at (b) 25 °C and (d) 45 °C. 1D diffusion experiments filtered out the signals of low-molecular-weight impurities lying around the methyl signal at 1.97 ppm. Two impurity signals superimposed with the methyl signal at 25 °C could be separated at 45 °C (Fig. 4d).

at the acetamido group. By integrating the NH proton signals in the 1D ^1H spectrum without ^{15}N decoupling (^1H - ^{14}N and ^1H - ^{15}N signals, respectively), the average level of ^{15}N isotope enrichment was estimated to be 66% from the NH signal associated with the α anomer and 63% from the NH signal associated with the β anomer (Table 1). In Fig. 3b, the ^1H spectrum with ^{13}C decoupling has a singlet at 5.84 ppm,

corresponding to the G4 proton. The singlet is split by the $^1J_{\text{CH}}$ coupling when recorded in the absence of ^{13}C decoupling. However, a minor signal remains at 5.84 ppm, which corresponds to the proton bound to ^{12}C and which therefore shows incomplete ^{13}C incorporation on the GlcA pyranose ring. Integration of the signals gave an average level of ^{13}C isotope enrichment on G4 of 96% (Table 1).

Using the same approach, the level of ^{13}C isotope enrichment on the methyl group was determined to be 40% by integrating the ^1H - ^{12}C signal and the ^1H - ^{13}C signal split by $^1J_{\text{CH}}$ respectively (Fig. 3c). This value was significantly lower than the one obtained from quantitative 1D ^{13}C and 2D ^1H , ^{13}C -HSQC NMR experiments and from MS data (*vide infra*). This discrepancy was due to the presence of traces of two impurities lying under the methyl signal at 1.97 ppm as demonstrated by 1D ^1H diffusion experiments that filter out signals from low molecular weight compounds as well as 1D ^1H spectra recorded at several temperatures. (see Fig. 4 for details). The average level of isotope enrichment of ^{13}C on the methyl group was then determined by 1D diffusion experiments to be about 61%.

Quantitative 1D ^{13}C NMR experiments were then performed to determine the extent of ^{13}C incorporation in ΔHA_2 (Fig. 5). The integration values at each carbon site are listed in Table 2. The discrepancies obtained by 1D ^{13}C NMR are attributed in part to the low S/N ratio due to the small amount of sample, which is more pronounced for the N2 position of GlcNAc (see Fig. 5). Quantitative HSQC experiments were also performed to further corroborate the ^{13}C results (Table S1). The intensity of cross-peaks in 2D HSQC is not directly proportional to the concentration but is highly signal specific and is affected by several different parameters such as T_1 and T_2 relaxation times, off-resonance effects, $^1J_{\text{CH}}$ coupling, J_{HH} couplings, and peak multiplicity [35–37]. In addition, ^{13}C -labeled compounds introduce the effect of $^1J_{\text{CC}}$ couplings, which evolve when magnetization has been transferred to ^{13}C and will affect the relative intensities. Similarly, ^{13}C decoupling could have an impact on the intensity of HSQC cross-peaks, especially for ^{13}C -labeled compounds [38]. Therefore, the quantitative HSQC results

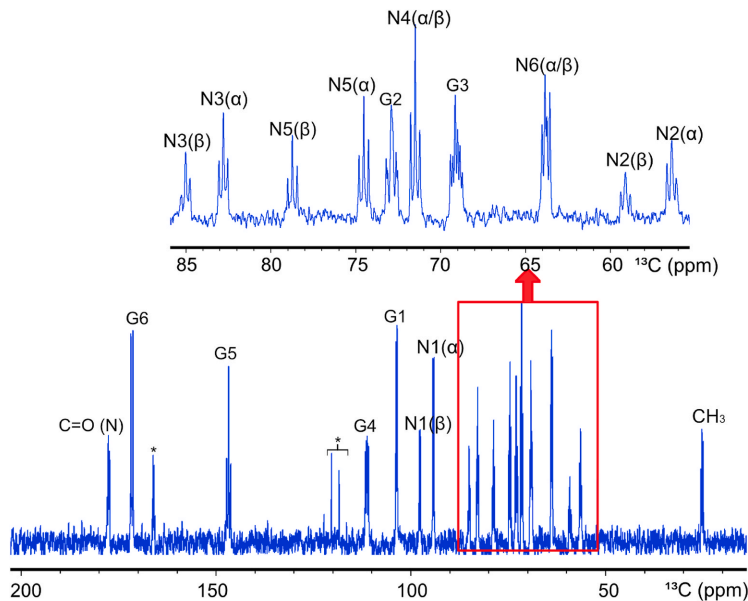


Fig. 5. 1D ^{13}C NMR spectrum of ^{13}C , ^{15}N -enriched ΔHA_2 at 25 °C. *: Trifluoroacetic acid (TFA).

Table 2

Mean level of isotope enrichment (%) of ^{13}C at each carbon of ΔHA_2 determined by quantitative ^{13}C NMR.^a

	^{13}C isotope enrichment (%) at carbon positions							
	C-1	C-2	C-3	C-4	C-5	C-6	CO	Me
ΔGlcA	100	89	90	97	87	100 ^b	/	/
	± 10	± 1	± 4	± 8	± 1			
GlcNAc	90	77	86	83	90	100	59	64
($\alpha+\beta$)	10	± 3	± 5	± 1	± 8	± 4	± 1	± 3

^a Data with standard deviation are presented from at least two measurements and D1 was set to 25 s.

^b The integration value was set as a reference.

were used as additional experimental data, while the 1D ^{13}C NMR data provided more reliable quantitative measurements. However, inspection of Table 2 and Table S1 shows relatively good agreement between data obtained from 1D ^{13}C NMR and 2D HSQC.

Thus, the isotopic purity of ^{13}C in the two pyranose rings was determined to be 80–100%. Since glucose is the primary carbon source for both GlcA and GlcNAc during HA biosynthesis, it is expected that all carbon within a sugar ring will have the same amount of ^{13}C enrichment and the range of ^{13}C enrichment 80–100% obtained for the different carbon atoms must be therefore inherent to errors from the ^{13}C NMR measurements.

For the *N*-acetyl group, the level of isotope enrichment of both ^{13}C and ^{15}N was determined to be 60–65%, which may be due to isotopic dilution during the acetylation of glucosamine-1-phosphate, resulting in incomplete ^{13}C and ^{15}N incorporation [39].

2.4. MS analysis of ^{13}C , ^{15}N -enriched ΔHA_2

^{13}C , ^{15}N incorporation and their isotopic distribution in the isolated ΔHA_2 product were also assessed by ESI-orbitrap-MS in addition to NMR analyses. ESI-orbitrap-MS revealed a cluster of peaks of protonated molecular ions ($[\text{M}+\text{H}]^+$) from m/z 395 to 391 in the extracted ion chromatogram (EIC) (Fig. 6a). A distinct peak was present at m/z 395.1620 corresponding to $[\text{UL-}^{13}\text{C}_{14}; ^{15}\text{N}]$ - ΔHA_2 . The different mass shifts that occur in the nearby region correspond to combinations of isotopic variants. By amplifying the mass shift regions (m/z 392, 393, and 394, respectively), two peaks with different m/z values can be found at each site (dash boxes in Fig. 6a). The mass difference between the uniformly labeled peak and the remaining peaks was first calculated, after which the isotopologue of each peak was assigned by comparing the mass differences between ^{15}N and ^{14}N (0.9970 Da), and ^{13}C and ^{12}C (1.0034 Da) as shown in Fig. 6b. The observed m/z values, the measured and expected mass differences, the relative percentage of each peak, as well as the isotopologues are also summarized in Table 3. The maximum deviation of the measured and expected mass difference is 1.5×10^{-3} Da, which can be explained by the very low abundance of the peak and the limited number of data points used for curve fitting.

In summary, the fully ^{13}C , ^{15}N -labeled ΔHA_2 peak at m/z 395.1620 accounted for 37.8% of the total. The neighboring peak at m/z 394.1649 corresponds to the complete ^{13}C incorporation (one ^{15}N loss) of ΔHA_2 , accounting for 19.4% of the total. Adding these two peaks together, the percentage of complete ^{13}C incorporation of ΔHA_2 should be at least 57.2% ($\geq 37.8\% + 19.4\%$). This is in good agreement with our conclusion from quantitative NMR that the ^{13}C level of isotope enrichment of

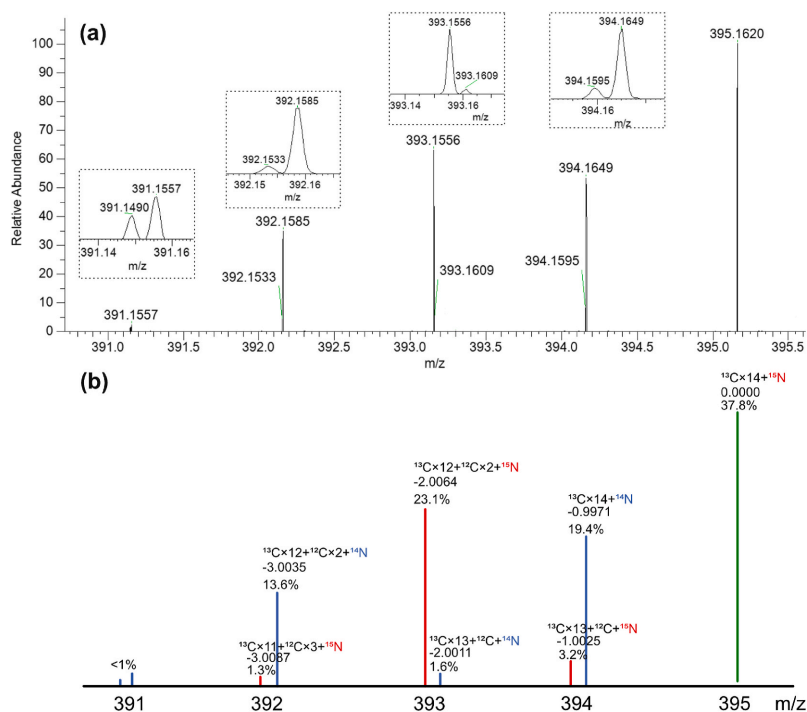


Fig. 6. (a) ESI-orbitrap-MS $[\text{M}+\text{H}]^+$ spectrum of ^{13}C , ^{15}N -enriched ΔHA_2 ; amplified mass shift regions are shown in the dash boxes; (b) Schematic illustration of the isotope distribution and relative percentages of each peak.

Table 3
Summary of the results of ESI-orbitrap-MS measurement of ^{13}C , ^{15}N -enriched ΔHA_2 .

[M+H] ⁺ (m/z)	Measured mass difference (Da) ^a	Expected mass difference (Da) ^b	Isotopologue	Relative percentage (%)
395.1620	0.0000	0.0000	$^{13}\text{C}_{14}$, ^{15}N	37.8
394.1649	-0.9971	-0.9970	$^{13}\text{C}_{14}$, ^{14}N	19.4
394.1595	-1.0025	-1.0034	$^{13}\text{C}_{13}$, $^{12}\text{C}_1$, ^{15}N	3.2
393.1609	-2.0011	-2.0004	$^{13}\text{C}_{13}$, $^{12}\text{C}_1$, ^{14}N	1.6
393.1556	-2.0064	-2.0068	$^{13}\text{C}_{12}$, $^{12}\text{C}_2$, ^{15}N	23.1
392.1585	-3.0035	-3.0038	$^{13}\text{C}_{12}$, $^{12}\text{C}_2$, ^{14}N	13.6
392.1533	-3.0087	-3.0102	$^{13}\text{C}_{11}$, $^{12}\text{C}_3$, ^{15}N	1.3
391.1557	-4.0063	-4.0072	$^{13}\text{C}_{11}$, $^{12}\text{C}_3$, ^{14}N	<1
391.1490	-4.0130	-4.0136	$^{13}\text{C}_{10}$, $^{12}\text{C}_4$, ^{15}N	<1

^a Mass difference from [M+H]⁺ = 395.1620.

^b Expected difference to obtain the respective isotopologue.

the *N*-acetyl group was 59–64%. Moreover, combining the percentages of all peaks labeled with ^{15}N yields 65.4% ^{15}N incorporation (37.8% + 3.2% + 23.1% + 1.3%), which agrees well with the average value of amide ^{15}N determined from ^1H NMR spectra.

3. Conclusion

In this work, ^{13}C , ^{15}N -labeled HA polysaccharides were biosynthetically produced by *Streptococcus zooepidemicus* using small-scale cultures and media with defined carbon and nitrogen sources. The HA polymer was enzymatically digested by chondroitinase ABC to the disaccharide repeating unit and the level of ^{13}C and ^{15}N isotope enrichment at each position was determined quantitatively using different types of NMR experiments. The ^{13}C level of the two pyranose rings was determined to be 80–100%, while the ^{13}C and ^{15}N level in the *N*-acetyl group was determined to be 60–65%. These results were further confirmed by high-resolution mass spectrometry. Stable isotope labeling can significantly improve sensitivity and offers the possibility of employing different NMR experiments in carbohydrate research. This work provides an effective method that can be applied to the quantitative assessment of isotopically labeled glycans. As a potential future direction, employing a strictly chemically defined medium to produce uniformly ^{13}C and ^{15}N -labeled HA polysaccharides would help address the issue of isotopic dilution and further enhance detection capabilities by NMR spectroscopy. HA polysaccharides could be submitted to partial enzymatic hydrolysis using chondroitinase or hyaluronidase followed by product separation using HPLC to obtain HA oligosaccharides of defined sizes [40]. The use of size-defined uniformly ^{13}C and ^{15}N -labeled HA oligosaccharides as substrates would greatly facilitate the study of HA-protein interactions and open avenues for comprehensive structure-function analysis in the future.

4. Experimental

4.1. Materials

Chondroitinase ABC from *Proteus vulgaris* (CAS No. 9024-13-9, Product Number: C2905), *D*-Glucose- $^{13}\text{C}_6$ (CAS No. 110187-42-3, Product Number: 389,374) with 99 atom-% ^{13}C , and *L*-Glutamine-(amide- ^{15}N) with 98 atom-% ^{15}N (CAS No. 59681-32-2, Product Number: 490,024) were all purchased from Sigma Aldrich (Darmstadt, Germany). *Streptococcus equi* subsp. *Zooepidemicus* strain DSM No. 20727 was purchased from the DSMZ collection (Leibniz-Institute DSMZ GmbH, Braunschweig, Germany). *N*-[1, 2- $^{13}\text{C}_2$] acetyl-D-[UL- $^{13}\text{C}_6$, ^{15}N] glucosamine (CAS No. 478529-44-1, Catalog GLC-054) with 99 atom-% ^{13}C and 98 atom-% ^{15}N was purchased from Omicron Biochemicals, Inc. (South Bend, IN, USA). D_2O (99.96% D) was purchased from Cambridge Isotope Laboratories, Inc. (Tewksbury, MA, USA). Water was

purified with Milli-Q® filtration apparatus (Millipore Co., Bedford, MA, USA).

4.2. Preparation of ^{13}C , ^{15}N -labeled HA polysaccharide

4.2.1. *Streptococcus zooepidemicus* growth conditions and production of ^{13}C , ^{15}N -labeled HA

Streptococcus equi subsp. *Zooepidemicus* was used in this study for small-scale production of the ^{13}C , ^{15}N -labeled HA. Bacteria were reconstituted from the locally maintained stock. Initially, the bacteria were grown on agar plates, followed by transfer to an inoculation medium (brain heart infusion broth, BHI, ~4 ml) and preincubated for 18 h at 37 °C. The inoculum (~1.5 ml) was then transferred to a liquid culture medium.

For the control set-up, the modified culture medium [41] was prepared. It contained peptone (1 g), yeast extract (0.5 g), *L*-glutamine (500 mg), and *D*-glucose (~3.2 g) in a final volume of 100 ml. The control culture with no labeled compounds was done to test the HA preparation procedures. For the metabolic labeling, the *D*-glucose was replaced by the U- $^{13}\text{C}_6$ -*D*-glucose and the *L*-glutamine was replaced by the *L*-glutamine-(amide- ^{15}N) in the liquid medium.

The liquid cultures were carried out for 24 h at 37 °C, using an incubator shaker operated at 100 rpm with natural aeration. The bacteria were harvested by centrifugation (8000 × g, 30 min) and the supernatant was collected.

4.2.2. Isolation and purification of ^{13}C , ^{15}N -labeled HA polysaccharide

HA polysaccharide was isolated using previously described procedures with modifications [42,43]. Following the separation of bacterial cells, active carbon powder (5.6 g/100 ml) was added and mixed thoroughly with the preserved supernatant. The mixture was incubated for 1 h and filtered. Cold ethanol (96%, stored at -20 °C) was added to the filtrate in a proportion of 1.5:1 (v/v) ethanol/supernatant and incubated at 4 °C, overnight. Subsequently, the white HA precipitate was collected by centrifugation (16,000 × g, 30 min). The precipitation step was repeated thrice. The collected precipitates of HA were freeze-dried. To remove the low-molecular-weight contaminants (medium ingredients and metabolites), the HA fractions were subjected to ultrafiltration (centrifugal filters, cut-off 3 kDa) and the retentate was freeze-dried. In total, a liquid culture of 100 ml yielded ~11.9 mg of ^{13}C , ^{15}N -labeled HA polysaccharide.

4.3. Degradation, separation, and purification

A solution of ^{13}C , ^{15}N -labeled HA polysaccharide (3.5 mg/ml) was prepared in Milli-Q® water, and the pH was adjusted to 7.0 with HCl or NaOH solutions. The aqueous solution was heated to 80 °C for 1 h to aid in the further enzymatic breakdown process. After cooling to room temperature, the HA solution was treated with 0.5 ml of chondroitinase ABC (1.26–12.6 units/ml) at 37 °C for full degradation to disaccharide. The degraded sample was then lyophilized, separated and mass analyzed on a Maxis Impact Q-TOF-MS (Bruker Daltonics GmbH & Co. KG, Bremen, Germany) coupled to a 1290 Infinity II LC system (Agilent Technologies, Santa Clara, CA, USA). The separation was performed across a porous graphite-based Hypercarb™ 4.6 × 100 mm column with a particle size of 3 μm (Thermo Scientific, Waltham, MA, USA) kept at 40 °C. The mobile phases employed were (A) water and (B) acetonitrile, both containing 0.05% trifluoroacetic acid, and a flow rate of 0.5 ml/min was used. A linear gradient from 20 to 40% mobile phase B in 15 min followed by a 5 min wash step with 20% mobile phase B was used. The MS was operated in the full scan positive ion mode. The α and β anomers of the disaccharide could be well separated as two chromatographic peaks and were identified from their labeled protonated molecular ion clusters. The same protocol was used to fractionate the two peaks on a micro-scale. A post-column splitter at the entrance to the MS was used to collect the eluents from several injections (20 μl each). The

pooled eluents were combined, lyophilized, and subjected to further analyses.

4.4. ESI-orbitrap-MS

The high-resolution capability of the Orbitrap QExactive mass spectrometer (Thermo Fisher Scientific) was exploited to obtain the spectra depicted in Fig. 6a. The chromatographic separation was performed on a Vanquish Horizon UHPLC system (Thermo Fisher Scientific) having a porous graphite-based Hypercarb™ 4.6 × 100 mm column with a particle size of 3 μm (Thermo Scientific, Waltham, MA, USA), maintained at a temperature of 40 °C. The mobile phases employed were (A) water and (B) acetonitrile, both containing 0.2% formic acid, and a flow rate of 0.5 ml/min was used. A linear gradient from 20 to 40% mobile phase B in 15 min followed by a 5-min wash step with 20% mobile phase B was used. The QExactive HF mass spectrometer was operated in the full scan positive ion mode (scan 70–1050 Da) with a spray voltage of 3.5 kV, a capillary temperature of 350 °C, and sheath and aux pressures of 50 and 15 arbitrary units respectively. Profile MS spectra were obtained at a resolution of 240,000 and an auto-gain control target of 3 × 10⁶.

4.5. NMR spectroscopy

The freeze-dried disaccharide sample was dissolved in 160 μl 90% H₂O/10% D₂O and transferred into a 3 mm NMR sample tube. NMR spectra were recorded on a Bruker Avance III 600 MHz spectrometer using a 5 mm ¹H/¹³C/¹⁵N/³¹P inverse detection CryoProbe equipped with a z-gradient (Bruker BioSpin GmbH, Ettlingen, Germany). The chemical shifts for NMR signals were referenced by using DSS-d₆ as an internal reference (δ_H 0.0 ppm δ_C 0.0 ppm). NMR spectra were processed with TopSpin 4.0.6 (Bruker). The ¹H NMR spectra were recorded using the pulse sequences *zgesp*, *noesygppr1d*, *ledbpgp2s1d* and *zggpw5* from the Bruker pulse sequence library. ¹³C- or ¹⁵N-decoupled spectra were acquired with a modified excitation sculpting pulse sequence (*zgesgp*) with decoupling during the acquisition time, which was limited to 0.85 s. Decoupling was obtained with the GARP-4 decoupling sequence, using a pulse length of 148.3 μs for ¹³C decoupling (equivalent to a bandwidth of 9.3 kHz) and 547.5 μs for ¹⁵N decoupling (equivalent to a bandwidth of 2.5 kHz). The ¹⁵N decoupling was centered at 120 ppm and the ¹³C decoupling was centered at 30 and 110 ppm for decoupling of methyl and G4 carbons, respectively. To obtain quantitative ¹H spectra, the relaxation delay (D1) was set to at least 25 s. Phase correction, baseline correction, and line broadening with a factor of 0.3 Hz were conducted prior to peak integration of the ¹H NMR signals. Quantitative 1D ¹³C spectra were recorded with the inverse-gated decoupling experiment *zgg30* from the Bruker pulse sequence library with a relaxation delay (D1) of 25 s and 16 k scans. A spectral width of 240 ppm and an acquisition time of 0.9 s was applied. Automatic baseline correction was performed with the command *c13cryo*. Phase correction and a line broadening factor of 5 Hz were used prior to peak integration. Quantitative 2D ¹H, ¹³C-HSQC spectra (*hsqcetgpsp.3* from Bruker pulse sequence library) were recorded with 1 k data points in t₂ and 256 increments in t₁, 16 dummy scans, 32 scans, and 5–20 s relaxation delay. A spectral width of 8 ppm in F₂ and 120 ppm in F₁ was used and the transmitter offset was set at 4.7 ppm in F₂ and 62 ppm in F₁. The integration of 2D peak volumes was performed after a 90° shifted squared sine bell function and automatic baseline correction in both dimensions. 2D ¹H, ¹³C-HMBC and ¹H, ¹⁵N-HSQC (*hmbcctetgpnid* and *fhscqf3gpph* from the Bruker pulse sequence library) spectra were recorded with 2 k data points in t₂ and 128 to 256 increments in t₁, with a minimum of 16 scans per increment and a relaxation delay of 1.0–1.2 s ¹³C T₁ was determined from an inversion recovery experiment (*t1irg* from the Bruker pulse sequence library) after a relaxation delay of 30 s. A variable delay list of 9 points between 0.05 and 30 s was used. 16 scans were recorded for each point.

Declaration of competing interest

The authors declare that they have no known competing financial interests or personal relationships that could have appeared to influence the work reported in this paper.

Data availability

Data will be made available on request.

Appendix A. Supplementary data

Supplementary data to this article can be found online at <https://doi.org/10.1016/j.carres.2023.108888>.

References

- Hargittai, M. Hargittai, Molecular structure of hyaluronan: an introduction, *Struct. Chem.* 19 (2008) 697–717, <https://doi.org/10.1007/s11224-008-9370-3>.
- A. Lierova, J. Kasparova, A. Filipova, J. Cizkova, L. Pekarova, L. Korecka, N. Mannova, Z. Bilkova, Z. Sinkorova, Hyaluronic acid: known for almost a century, but still in vogue, *Pharmaceutics* 14 (2022) 838, <https://doi.org/10.3390/pharmaceutics14040838>.
- K.T. Dicker, L.A. Gurski, S. Pradhan-Bhatt, R.L. Witt, M.C. Farach-Carson, X. Jia, Hyaluronan: a simple polysaccharide with diverse biological functions, *Acta Biomater.* 10 (2014) 1558–1570, <https://doi.org/10.1016/j.actbio.2013.12.019>.
- M.K. Cowman, Hyaluronan and hyaluronan fragments, *Adv. Carbohydr. Chem. Biochem.* 74 (2017) 1–59, <https://doi.org/10.1016/bs.accb.2017.10.001>.
- S. Garantziotis, R.C. Savani, Hyaluronan biology: a complex balancing act of structure, function, location and context, *Matrix Biol.* 78 (2019) 1–10, <https://doi.org/10.1016/j.matbio.2019.02.002>.
- T.N. Wight, Provisional matrix: a role for versican and hyaluronan, *Matrix Biol.* 60 (2017) 38–56, <https://doi.org/10.1016/j.matbio.2016.12.001>.
- J.E. Rayahin, J.S. Buhman, Y. Zhang, T.J. Koh, R.A. Gemeinhart, High and low molecular weight hyaluronic acid differentially influence macrophage activation, *ACS Biomater. Sci. Eng.* 1 (2015) 481–493, <https://doi.org/10.1021/acsbomater.5b00181>.
- O. Guvench, Atomic-resolution experimental structural biology and molecular dynamics simulations of hyaluronan and its complexes, *Molecules* 27 (2022) 7276, <https://doi.org/10.3390/molecules27217276>.
- M.D. Battistel, D.I. Freedberg, Dispersing the crowd: adopting 13C direct detection for glycans, *J. Magn. Reson.* 318 (2020), 106792, <https://doi.org/10.1016/j.jmr.2020.106792>.
- L. Paudel, R.W. Adams, P. Kiraly, J.A. Aguilar, M. Foroozandeh, M.J. Clif, M. Nilsson, P. Sándor, J.P. Waltho, G.A. Morris, Simultaneously enhancing spectral resolution and sensitivity in heteronuclear correlation NMR spectroscopy, *Angew. Chem., Int. Ed.* 52 (2013) 11616–11619, <https://doi.org/10.1002/anie.201305709>.
- G. Nestor, T. Anderson, S. Oscarson, A.M. Gronenborn, Exploiting uniformly 13C-labeled carbohydrates for probing carbohydrate–protein interactions by NMR spectroscopy, *J. Am. Chem. Soc.* 139 (2017) 6210–6216, <https://doi.org/10.1021/jacs.7b01929>.
- A. Gimeno, P. Valverde, A. Ardá, J. Jiménez-Barbero, Glycan structures and their interactions with proteins. A NMR view, *Curr. Opin. Struct. Biol.* 62 (2020) 22–30, <https://doi.org/10.1016/j.sbi.2019.11.004>.
- G. Nestor, T. Anderson, S. Oscarson, A.M. Gronenborn, Direct observation of carbohydrate hydroxyl protons in hydrogen bonds with a protein, *J. Am. Chem. Soc.* 140 (2018) 339–345, <https://doi.org/10.1021/jacs.7b10595>.
- J. Orts, A.D. Gossert, Structure determination of protein–ligand complexes by NMR in solution, *Methods* 138–139 (2018) 3–25, <https://doi.org/10.1016/j.ymeth.2018.01.019>.
- C. Dominguez, M. Schubert, O. Duss, S. Ravindranathan, F.H.-T. Allain, Structure determination and dynamics of protein–RNA complexes by NMR spectroscopy, *Prog. Nucl. Magn. Reson. Spectrosc.* 58 (2011) 1–61, <https://doi.org/10.1016/j.pnmrs.2010.10.001>.
- M. Schubert, Insights into carbohydrate recognition by 3D structure determination of protein–carbohydrate complexes using NMR, <https://doi.org/10.1039/9781782623946-00101>, 2017.
- Z. Zhang, S.A. McCallum, J. Xie, L. Nieto, F. Corzana, J. Jiménez-Barbero, M. Chen, J. Liu, R.J. Linhardt, Solution structures of chemoenzymatically synthesized heparin and its precursors, *J. Am. Chem. Soc.* 130 (2008) 12998–13007, <https://doi.org/10.1021/ja8026345>.
- C. Sigulinsky, P. Babu, X.V. Victor, B. Kuberan, Preparation and characterization of 15N-enriched, size-defined heparan sulfate precursor oligosaccharides, *Carbohydr. Res.* 345 (2010) 250–256, <https://doi.org/10.1016/j.carres.2009.10.024>.
- T.K.N. Nguyen, Characterization of uniformly and atom-specifically 13C-labeled heparin and heparan sulfate polysaccharide precursors using 13C NMR spectroscopy and ESI mass spectrometry, *Carbohydr. Res.* 345 (2010) 2228–2232, <https://doi.org/10.1016/j.carres.2010.08.011>.
- B.M. Sattelle, J. Shakeri, I.S. Roberts, A. Almond, A 3D-structural model of unsulfated chondroitin from high-field NMR: 4-sulfation has little effect on

- backbone conformation, *Carbohydr. Res.* 345 (2010) 291–302, <https://doi.org/10.1016/j.carres.2009.11.013>.
- [21] V.H. Pomin, J.S. Sharp, X. Li, L. Wang, J.H. Prestegard, Characterization of glycosaminoglycans by 15N NMR spectroscopy and in vivo isotopic labeling, *Anal. Chem.* 82 (2010) 4078–4088, <https://doi.org/10.1021/ac1001383>.
- [22] A.W. Barb, D.I. Freedberg, M.D. Battistel, J.H. Prestegard, NMR detection and characterization of sialylated glycoproteins and cell surface polysaccharides, *J. Biomol. NMR* 51 (2011) 163–171, <https://doi.org/10.1007/s10858-011-9550-0>.
- [23] C. Blundell, P. Deangelis, A.J. Day, A. Almond, Use of 15N-NMR to resolve molecular details in isotopically-enriched carbohydrates: sequence-specific observations in hyaluronan oligomers up to decasaccharides, *Glycobiology* 14 (2004) 999–1009, <https://doi.org/10.1093/GLYCOB/CWH117>.
- [24] M. Mobli, M. Nilsson, A. Almond, The structural plasticity of heparan sulfate NA-domains and hence their role in mediating multivalent interactions is confirmed by high-accuracy (15)N-NMR relaxation studies, *Glycoconj. J.* 25 (2008) 401–414, <https://doi.org/10.1007/s10719-007-9081-9>.
- [25] S.C. Namboori, D.E. Graham, Acetamido sugar biosynthesis in the euryarchaea, *J. Bacteriol.* 190.8 (2008) 2987–2996.
- [26] B.F. Chong, L.M. Blank, R. McLaughlin, L.K. Nielsen, Microbial hyaluronic acid production, *Appl. Microbiol. Biotechnol.* 66 (2005) 341–351, <https://doi.org/10.1007/s00253-004-1774-4>.
- [27] B.F. Chong, L.K. Nielsen, Amplifying the cellular reduction potential of *Streptococcus zoepidemicus*, *J. Biotechnol.* 100 (2003) 33–41, [https://doi.org/10.1016/S0168-1656\(02\)00239-0](https://doi.org/10.1016/S0168-1656(02)00239-0).
- [28] T. Yamagata, H. Saito, O. Habuchi, S. Suzuki, Purification and properties of bacterial chondroitinases and chondrosulfatases, *J. Biol. Chem.* 243 (1968) 1523–1535, [https://doi.org/10.1016/S0021-9258\(18\)93574-X](https://doi.org/10.1016/S0021-9258(18)93574-X).
- [29] A. Hamai, N. Hashimoto, H. Mochizuki, F. Kato, Y. Makiguchi, K. Horie, S. Suzuki, Two distinct chondroitin sulfate ABC lyases: an endoeliminase yielding tetrasaccharides and an exoeliminase preferentially acting on oligosaccharides, *J. Biol. Chem.* 272 (1997) 9123–9130, <https://doi.org/10.1074/jbc.272.14.9123>.
- [30] C.D. Blundell, M.A.C. Reed, A. Almond, Complete assignment of hyaluronan oligosaccharides up to hexasaccharides, *Carbohydr. Res.* 341 (2006) 2803–2815, <https://doi.org/10.1016/j.carres.2006.09.023>.
- [31] G. Nestor, L. Kenne, C. Sandström, Experimental evidence of chemical exchange over the $\beta(1\rightarrow3)$ glycosidic linkage and hydrogen bonding involving hydroxy protons in hyaluronan oligosaccharides by NMR spectroscopy, *Org. Biomol. Chem.* 8 (2010) 2795, <https://doi.org/10.1039/b927159g>.
- [32] M.K. Cowman, J. Feder-Davis, D.M. Hittner, 13C NMR studies of hyaluronan. 2. Dependence of conformational dynamics on chain length and solvent, *Macromolecules* 34 (2001) 110–115, <https://doi.org/10.1021/ma001082e>.
- [33] A. Donati, A. Magnani, C. Bonechi, R. Barbucci, C. Rossi, Solution structure of hyaluronic acid oligomers by experimental and theoretical NMR, and molecular dynamics simulation, *Biopolymers* 59 (2001) 434–445, [https://doi.org/10.1002/1097-0282\(200111\)59:6<434::AID-BIP1048>3.0.CO;2-4](https://doi.org/10.1002/1097-0282(200111)59:6<434::AID-BIP1048>3.0.CO;2-4).
- [34] H. Hofmann, O. Schmut, H. Sterk, H. Pölzler, Relaxation time measurements of hyaluronic acid, *J. Biol. Macromol.* 5.4 (1983) 229–232, [https://doi.org/10.1016/0141-8130\(83\)90007-7](https://doi.org/10.1016/0141-8130(83)90007-7).
- [35] P. Giraudeau, Challenges and perspectives in quantitative NMR, *Magn. Reson. Chem.* 55 (2017) 61–69, <https://doi.org/10.1002/mrc.4475>.
- [36] H. Koskela, Annual Reports on NMR Spectroscopy, Chapter 1 Quantitative 2D NMR Studies, vol. 66, Academic Press, 2009, pp. 1–31, [https://doi.org/10.1016/S0066-4103\(08\)00401-8](https://doi.org/10.1016/S0066-4103(08)00401-8).
- [37] L. Zhang, G. Gellerstedt, Quantitative 2D HSQC NMR determination of polymer structures by selecting suitable internal standard references, *Magn. Reson. Chem.* 45 (2007) 37–45, <https://doi.org/10.1002/mrc.1914>.
- [38] D. Lane, T.E. Skinner, N.I. Gershenzon, W. Bernmel, R. Soong, R. Dutta Majumdar, Y. Liaghati Mobarhan, S. Schmidt, H. Heumann, M. Monette, M.J. Simpson, A. J. Simpson, Assessing the potential of quantitative 2D HSQC NMR in 13C enriched living organisms, *J. Biomol. NMR* 73 (2019) 31–42, <https://doi.org/10.1007/s10858-018-0221-2>.
- [39] L. Liu, Y. Liu, J. Li, G. Du, J. Chen, Microbial production of hyaluronic acid: current state, challenges, and perspectives, *Microb. Cell Factories* 10 (2011) 99, <https://doi.org/10.1186/1475-2859-10-99>.
- [40] A. Tawada, T. Masa, Y. Oonuki, A. Watanabe, Y. Matsuzaki, A. Asari, Large-scale preparation, purification, and characterization of hyaluronan oligosaccharides from 4-mers to 52-mers, *Glycobiology* 12 (2002) 421–426, <https://doi.org/10.1093/glycob/cw0048>.
- [41] C. Matsubara, M. Kajiwara, H. Akasaka, S. Haze, Carbon-13 nuclear magnetic resonance studies of the biosynthesis of hyaluronic acid, *Chem. Pharm. Bull.* 39 (1991) 2446–2448, <https://doi.org/10.1248/cpb.39.2446>.
- [42] A.M.B. Pires, M.H.A. Santana, Metabolic effects of the initial glucose concentration on microbial production of hyaluronic acid, *Appl. Biochem. Biotechnol.* 162 (2010) 1751–1761, <https://doi.org/10.1007/s12010-010-8956-6>.
- [43] V. Rangaswamy, D. Jain, An efficient process for production and purification of hyaluronic acid from *Streptococcus equi* subsp. *zoepidemicus*, *Biotechnol. Lett.* 30 (2008) 493–496, <https://doi.org/10.1007/s10529-007-9562-8>.

Supporting Information

Metabolic Labeling of Hyaluronan: Biosynthesis and Quantitative Analysis of ^{13}C , ^{15}N -enriched Hyaluronan by NMR and MS-based Methods

Yan Xue^{a*}, Karolina Ucieklak^b, Suresh Gohil^a, Tomasz Niedziela^b, Gustav Nestor^a and Corine Sandström^a

^a Department of Molecular Sciences, Uppsala BioCenter, Swedish University of Agricultural Sciences, P.O. Box 7015, SE-750 07 Uppsala, Sweden

^b Hirszfeld Institute of Immunology and Experimental Therapy, 53-114 Wrocław, Poland

1. Supplementary Figures	
Figure S1.....	S2
Figure S2.....	S2
Figure S3.....	S3
Figure S4.....	S3
Figure S5.....	S4
2. Supplementary Tables	
Table S1.....	S5
Table S2.....	S5
Table S3.....	S5
Table S4.....	S6
3. Reference	S6

Supplementary Figures

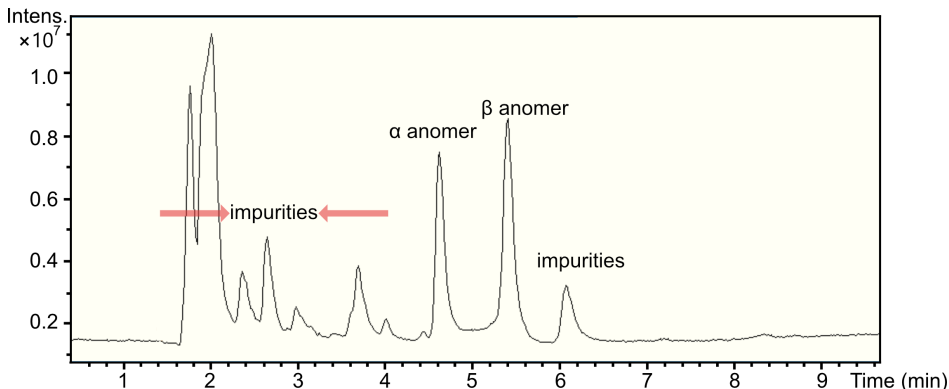


Figure S1. Total ion current (TIC) chromatogram obtained after an HPLC-MS analysis of fully degraded HA polysaccharide. The retention time of α - and β -anomers of ΔHA_2 is at 4.8 min and 5.6 min, respectively.

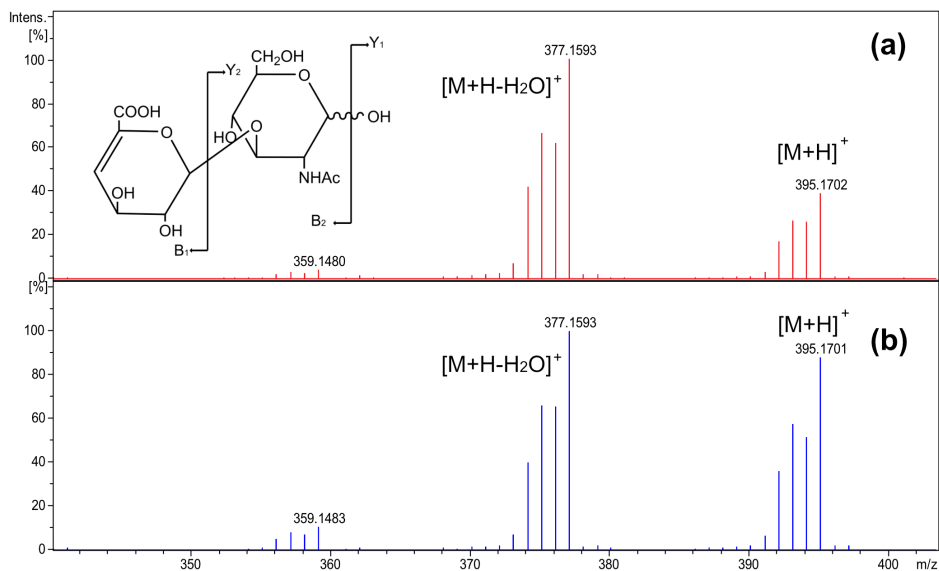


Figure S2. ESI-QTOF-MS spectra of ^{13}C , ^{15}N -enriched ΔHA_2 (a) α anomer (b) β anomer. The suggested water loss position is at B_2/Y_1 , where B_2 fragment corresponds to $m/z = 377$ and Y_1 fragment corresponds to the water loss. The fragments are described using the nomenclature of Domon and Costello [1].

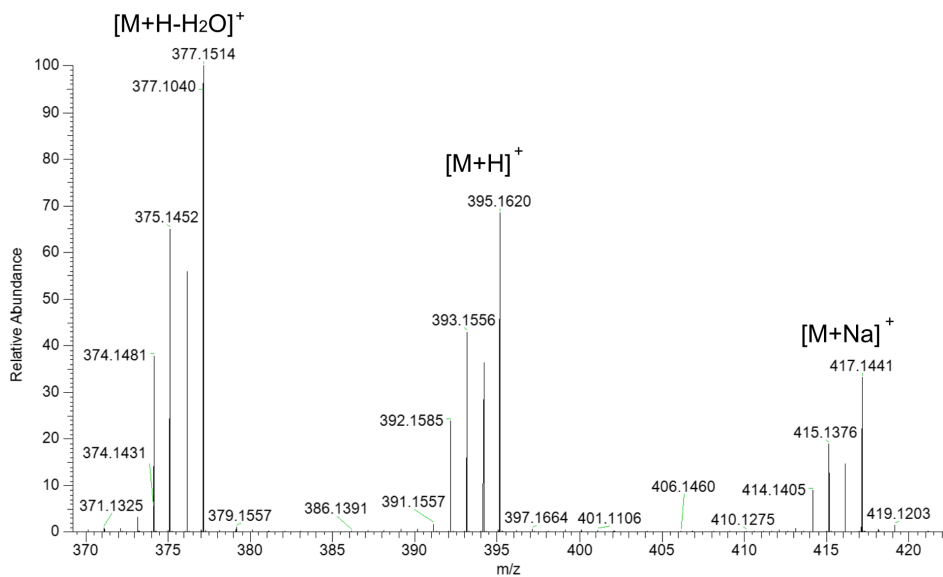


Figure S3. ESI-Orbitrap-MS spectrum of $^{13}\text{C}, ^{15}\text{N}$ -enriched ΔHA_2 .

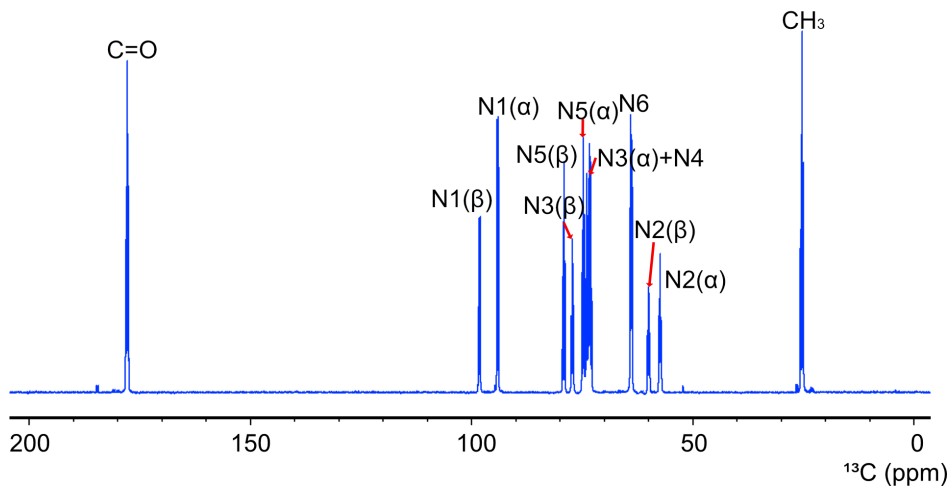


Figure S4. 1D ^{13}C NMR spectrum of $[\text{UL}-^{13}\text{C}_8; ^{15}\text{N}]$ GlcNAc at 25°C .

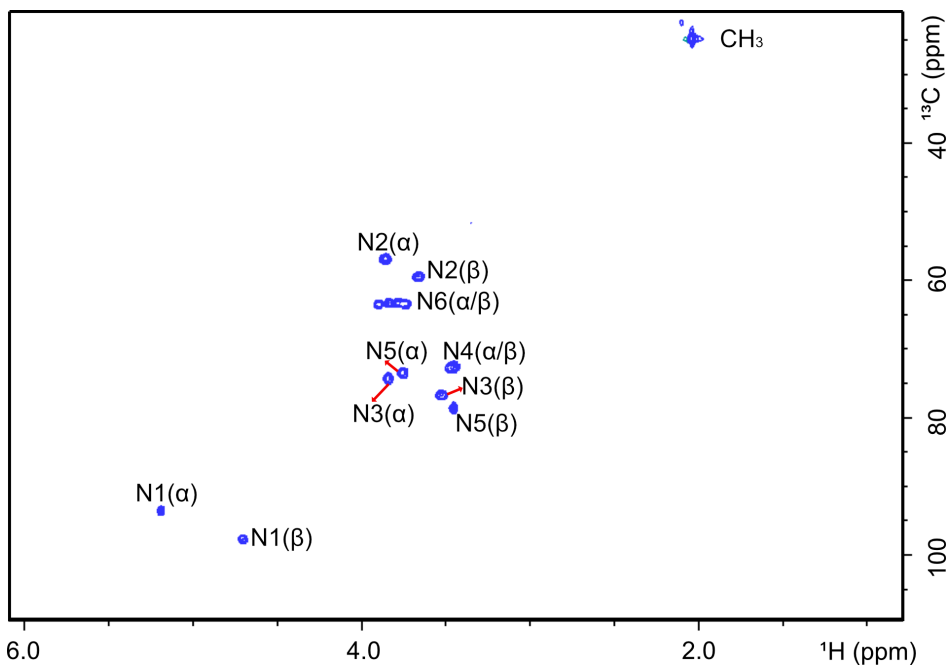


Figure S5. 2D ^1H , ^{13}C -HSQC spectrum of $[\text{UL-}^{13}\text{C}_8; ^{15}\text{N}]$ GlcNAc at 25 $^\circ\text{C}$.

Supplementary Tables

Table S1. Mean level of isotope enrichment (%) of ^{13}C at each carbon of ΔHA_2 determined by quantitative $^1\text{H},^{13}\text{C}$ -HSQC.^[a]

^{13}C isotope enrichment (%) at carbon positions							
	C-1	C-2	C-3	C-4	C-5	C-6	Me
ΔGlcA	92	85	94	78 ^[c]	/	/	/
$\text{GlcNAc } (\alpha+\beta)$	89	83	86	91	90	100 ^[b]	64

[a] D1 was set between 10-15s. All values are $\pm 15\%$. Data obtained from three measurements with standard deviation $\pm 2\%$.

Note: Quantitative HSQC experiments rely on the measurement of proton T_1 relaxation time instead of carbon T_1 . T_1 measurements on uniformly labeled GlcNAc reveal an average proton T_1 relaxation time of approximately 600 ms, whereas the methyl group protons exhibit the longest T_1 relaxation time of 1000 ms. Therefore, a relaxation delay of 10-15 seconds was selected for ΔHA_2 that is larger than monosaccharide GlcNAc to ensure complete proton relaxation. D1 between 10s and 15s were evaluated and found negligible variations between the different experiments. The effect of T_2 relaxation should also be negligible for small molecules such as ΔHA_2 .

[b] The integration value was set as a reference.

[c] The ΔGlcA has double bond at C4 position with $^1J_{\text{CH}} = 170\text{Hz}$, which differs from the $^1J_{\text{CH}} = 145\text{Hz}$ (cnst2 in HSQC) at other positions.

Table S2. Mean level of isotope enrichment (%) of ^{13}C at each carbon of $[\text{UL-}^{13}\text{C}_8; ^{15}\text{N}]$ -GlcNAc determined by quantitative ^{13}C NMR.^[a]

^{13}C isotope enrichment (%) at carbon positions								
	C-1	C-2	C-3	C-4	C-5	C-6	CO	Me
$\text{GlcNAc } (\alpha+\beta)$	102	92	overlap ^[c]	overlap ^[c]	100	100 ^[b]	102	99

[a] D1 was set at 15s. All values are $\pm 10\%$.

[b] The integration value was set as a reference.

[c] Signals from C3 (α) and C4 overlap and the total integration value is 196.3.

Table S3. Mean level of isotope enrichment (%) of ^{13}C at each carbon of $[\text{UL-}^{13}\text{C}_8; ^{15}\text{N}]$ -GlcNAc determined by quantitative $^1\text{H},^{13}\text{C}$ -HSQC.^[a]

^{13}C isotope enrichment (%) at carbon positions							
	C-1	C-2	C-3	C-4	C-5	C-6	Me
$\text{GlcNAc } (\alpha+\beta)$	99	85	93	98	90	100 ^[b]	99

[a] D1 was set at 20s. All values are $\pm 15\%$.

[b] The integration value was set as a reference.

Table S4. Average ^{13}C T_1 values at each carbon of [UL- $^{13}\text{C}_8$; ^{15}N]-GlcNAc.^[a]

	^{13}C T_1 (ms)							
	C-1	C-2	C-3	C-4	C-5	C-6	CO	Me
GlcNAc	969	906	956 ^[b]		974	565	4700	2631

[a] D1 was set at 30s. All values are \pm 10-25 ms.

[b] Overlapped signals

Reference

- [1] B. Domon, C.E. Costello, A systematic nomenclature for carbohydrate fragmentations in FAB-MS/MS spectra of glycoconjugates, *Glycoconj. J.* 5 (1988) 397–409.
<https://doi.org/10.1007/BF01049915>.

ACTA UNIVERSITATIS AGRICULTURAE SUECIAE

DOCTORAL THESIS No. 2023:57

This thesis investigated various forms of hyaluronan in aqueous solution using NMR spectroscopy, to gain insights into structural and dynamic behaviors. Correlations between the physicochemical properties of hyaluronan hydrogels and the dynamic behavior of water in the samples were examined. Detailed conformational studies of mono- and oligo-saccharides of hyaluronan were conducted, focusing on the glycosidic linkages and the *N*-acetyl group. The level of isotopic incorporation was assessed in biosynthetically obtained ¹³C,¹⁵N-enriched hyaluronan.

Yan Xue received her graduate education at the Department of Molecular Sciences, SLU, Uppsala. She attained her M.Sc. degree in Chemistry at Uppsala University.

Acta Universitatis Agriculturae Sueciae presents doctoral theses from the Swedish University of Agricultural Sciences (SLU).

SLU generates knowledge for the sustainable use of biological natural resources. Research, education, extension, as well as environmental monitoring and assessment are used to achieve this goal.

ISSN 1652-6880

ISBN (print version) 978-91-8046-166-5

ISBN (electronic version) 978-91-8046-167-2